

Durham E-Theses

The Mauritius radio telescope and a study of selected super nova remnants associated with pulsars

Dodson, R.G.

How to cite:

Dodson, R.G. (1997) *The Mauritius radio telescope and a study of selected super nova remnants associated with pulsars*, Durham theses, Durham University. Available at Durham E-Theses Online: <http://etheses.dur.ac.uk/4707/>

Use policy

The full-text may be used and/or reproduced, and given to third parties in any format or medium, without prior permission or charge, for personal research or study, educational, or not-for-profit purposes provided that:

- a full bibliographic reference is made to the original source
- a [link](#) is made to the metadata record in Durham E-Theses
- the full-text is not changed in any way

The full-text must not be sold in any format or medium without the formal permission of the copyright holders.

Please consult the [full Durham E-Theses policy](#) for further details.

The Mauritius Radio Telescope and a Study of
Selected Super Nova Remnants Associated with
Pulsars

R.G. Dodson

A thesis submitted to the University of Durham
in accordance with the regulations for
admittance to the Degree of Doctor of Philosophy.

The copyright of this thesis rests with the author. No quotation from it
should be published without his prior written consent and
information derived from it should be acknowledged.

Department of Physics
University of Durham
September 1997

The copyright of this thesis rests
with the author. No quotation
from it should be published
without the written consent of the
author and information derived
from it should be acknowledged.



19 FEB 1998

Contents

| | | |
|----------|--|-------------|
| 1 | Introduction | I-1 |
| 1.1 | Beginnings of Radio Astronomy | I-1 |
| 1.2 | Astronomy Transformed | I-3 |
| 1.3 | An overview of the Mauritius Radio Telescope | I-3 |
| 1.3.1 | The Telescope | I-5 |
| 1.3.2 | Scientific Objectives | I-6 |
| 1.4 | Structure of the thesis | I-7 |
| 1.5 | Some Interferometric Theory | I-7 |
| 1.6 | Digital Signals | I-10 |
| 1.7 | What do we see, why do we look? | I-13 |
| 1.8 | The Development of Supernova Remnants | I-14 |
| 1.8.1 | The Sedov Description of SNRs | I-15 |
| 1.8.2 | The Four Phases of SNR development | I-17 |
| 1.9 | Types of Emission from Supernova Remnants | I-19 |
| 1.9.1 | Radio | I-19 |
| 1.9.2 | Optical | I-20 |
| 1.9.3 | X-ray | I-20 |
| 1.10 | Some Emission Theory | I-20 |
| 1.10.1 | Synchrotron | I-20 |
| 1.10.2 | Bremsstrahlung | I-23 |
| 1.11 | Criteria for the acceptance of Associations | I-24 |
| 2 | Hardware | II-1 |
| 2.1 | Design criteria | II-1 |
| 2.1.1 | Description of MRT | II-2 |
| 2.2 | Hardware description and design | II-7 |
| 2.2.1 | The Helix | II-7 |
| 2.2.2 | Pre-Filter amplifier | II-10 |
| 2.2.3 | The 4-way and 8-way combiners | II-11 |
| 2.2.4 | The Mixer Module | II-11 |
| 2.2.5 | Transmission of the signals to the receiver room | II-13 |

| | | |
|--------|--|-------|
| 2.2.6 | The RF back end | II-13 |
| 2.2.7 | The Second Mixer Modules | II-13 |
| 2.2.8 | The 2-bits 3-levels samplers | II-15 |
| 2.2.9 | The 1088 channels correlator | II-17 |
| 2.2.10 | Data collection and storage | II-19 |
| 2.2.11 | The Walsh switching | II-19 |
| 2.2.12 | The recirculator | II-20 |

3 The MARMOSAT Suite: Programs for the Mauritius Radio

| | | |
|-------|---|--------------|
| | Telescope | III-1 |
| 3.1 | Introduction | III-1 |
| 3.2 | Tasks that MARMOSAT has to accomplish | III-2 |
| 3.2.1 | Documentation | III-2 |
| 3.2.2 | Data Management | III-2 |
| 3.2.3 | Data Storage | III-3 |
| 3.2.4 | Calibration of the signals | III-4 |
| 3.2.5 | Generation of the Images | III-4 |
| 3.2.6 | Others | III-4 |
| 3.3 | Recognising Spurious Data | III-4 |
| 3.4 | Coordinates | III-6 |
| 3.5 | Further remarks on transforms and the coordinate system | III-8 |
| 3.6 | Calculating the instrument phase | III-11 |
| 3.7 | Improving the calculated calibration | III-12 |
| 3.8 | Further improvement of the calibration values | III-15 |
| 3.9 | Applying the calculated calibration | III-20 |
| 3.10 | Transforming from visibilities | III-20 |

4 Our Maps **IV-1**

| | | |
|-------|--|------|
| 4.1 | Introduction | IV-1 |
| 4.2 | Phase stability | IV-1 |
| 4.2.1 | Day to Day Phase Differences | IV-2 |
| 4.2.2 | Source to Source Phase Differences | IV-2 |
| 4.2.3 | Zone to Zone Phase Differences | IV-3 |
| 4.2.4 | Improvement of phases by Base to Antenna reduction | IV-4 |
| 4.3 | Other unexpected errors | IV-4 |
| 4.4 | Maps of the 150 MHz sky from Mauritius | IV-6 |
| 4.4.1 | Flux scale at the instrument Zenith | IV-6 |
| 4.4.2 | The whole sky and the galactic plane | IV-6 |
| 4.4.3 | Higher resolution map of sections the 150 MHz sky | IV-7 |

| | | |
|----------|---|-------------|
| 5 | Methods | V-1 |
| 5.1 | Introduction | V-1 |
| 5.2 | Distance indicators for both pulsars and SNR's | V-2 |
| 5.2.1 | Kinematic methods | V-2 |
| 5.2.2 | Column density methods | V-9 |
| 5.3 | Supernova Remnant Distance indicators | V-9 |
| 5.3.1 | Historical Methods | V-9 |
| 5.3.2 | Σ - D relationship. | V-11 |
| 5.3.3 | Filament Velocities | V-12 |
| 5.3.4 | Derivation of the distance from X ray emission | V-15 |
| 5.4 | Pulsar Distances | V-16 |
| 5.4.1 | Models of Electron Density | V-16 |
| 5.4.2 | Taylor and Cordes Model of electron density in our galaxy | V-17 |
| 5.4.3 | Parallax Observations of Pulsars | V-20 |
| 5.4.4 | Associations with pulsars | V-20 |
| 5.5 | Related techniques | V-21 |
| 5.5.1 | Proper Motion of the Pulsar | V-21 |
| 5.5.2 | Scintillation velocity | V-21 |
| 5.5.3 | Pulsar velocity from the Pulsar Wind Nebula | V-23 |
| 5.5.4 | The Pulsar Age, τ_c | V-25 |
| 5.5.5 | Morphology | V-27 |
| 5.6 | Conclusions | V-29 |
| | | |
| 6 | Description of some selected SNRs | VI-1 |
| 6.1 | Introduction | VI-1 |
| 6.2 | The SNR G5.4-1.2 | VI-3 |
| 6.2.1 | First Observations of the Shell and the Pulsar | VI-3 |
| 6.2.2 | Emission driven by the pulsar | VI-6 |
| 6.2.3 | Interaction of the pulsar with the SNR shell as a whole | VI-6 |
| 6.2.4 | Estimates of the Pulsar Velocity | VI-6 |
| 6.2.5 | Other Observations | VI-7 |
| 6.2.6 | Conclusions | VI-8 |
| 6.3 | G8.7-0.1 | VI-9 |
| 6.3.1 | Previous Observations of the Shell | VI-9 |
| 6.3.2 | The Pulsar, and the required Velocity | VI-13 |
| 6.3.3 | Evidence for a reflection of the Shock Front | VI-15 |
| 6.3.4 | Effect of a misshapen shell on the X-ray plasma model | VI-16 |
| 6.3.5 | Conclusions and Difficulties | VI-16 |
| 6.4 | G315.4-2.3 | VI-17 |
| 6.4.1 | The Chinese Records | VI-17 |
| 6.4.2 | The optical data on G315.4-2.3 | VI-22 |

| | | |
|----------|--|--------------|
| 6.4.3 | The <i>ROSAT</i> data on G315.4-2.3 | VI-22 |
| 6.4.4 | The association; conclusion | VI-24 |
| 6.5 | G320.4-1.2 | VI-24 |
| 6.5.1 | The Chinese Records | VI-25 |
| 6.5.2 | Previous distance measurements | VI-27 |
| 6.5.3 | Radio and X-ray observations | VI-27 |
| 6.5.4 | The Optical observations | VI-34 |
| 6.5.5 | The Association with SN185 | VI-35 |
| 6.6 | G343.1-2.3 | VI-36 |
| 6.6.1 | First Observations | VI-36 |
| 6.6.2 | Refinement of the conclusions based on the MRT results | VI-39 |
| 6.6.3 | Results from the <i>ROSAT</i> data | VI-40 |
| 6.6.4 | Discussion of the <i>ROSAT</i> fit | VI-42 |
| 6.6.5 | Conclusion | VI-45 |
| 6.7 | Summary for our selected Associations | VI-46 |
| 7 | Conclusions | VII-1 |
| 7.1 | The Present Status of the Telescope | VII-1 |
| 7.2 | Results on Pulsar SNR Associations | VII-2 |
| 7.2.1 | G5.4-1.2 | VII-2 |
| 7.2.2 | G8.7-0.1 | VII-2 |
| 7.2.3 | G315.4-2.3 | VII-3 |
| 7.2.4 | G320.4-1.2 | VII-3 |
| 7.2.5 | G343.1-2.3 | VII-4 |
| 7.2.6 | Conclusions on Association | VII-4 |
| 7.3 | Methods | VII-5 |
| 7.3.1 | The X-ray plasma model | VII-5 |
| 7.3.2 | The pulsar wind nebula model | VII-6 |
| 7.4 | Pulsars and SNRs | VII-6 |
| 7.5 | Further work on the MRT maps | VII-7 |
| A | Appendix: MARMOSAT | A-1 |
| A.1 | Definition of Marmosat | A-1 |
| A.1.1 | Where to find the Marmosat | A-1 |
| A.1.2 | Compatibility with other libraries | A-2 |
| A.1.3 | Allied libraries used in the MARMOSAT | A-2 |
| A.2 | Introduction to MRT | A-2 |
| A.2.1 | online | A-2 |
| A.2.2 | fringe_cal | A-3 |
| A.2.3 | base2antenna | A-4 |
| A.2.4 | 1D and track | A-4 |
| A.2.5 | apply_cal | A-4 |

| | |
|--|------------|
| A.2.6 transform | A-4 |
| A.3 Utility programs | A-4 |
| B Appendix: Library routines | B-1 |
| C The Geminga Pulsar | C-1 |
| D A search for Fossil Radio Lines | D-1 |

List of Figures

| | | |
|------|--|-------|
| 1.1 | Radiation from two sources, separated by the resolution, arriving at a single dish | I-2 |
| 1.2 | Radiation from two sources arriving at an interferometer baseline. | I-4 |
| 1.3 | EW baseline rotating under the north pole to trace out circles on the uv plane. | I-9 |
| 1.4 | T style array, with the un-necessary Mills Cross style extension shown dotted in. The vectors are 180° rotations around the centre and therefore are conjugate (for a real sky). | I-11 |
| 1.5 | Delays along the signal path for a correlated baseline using an LO | I-12 |
| 1.6 | Shell formed from the supernova explosion | I-16 |
| 1.7 | An electron travelling into the page and spiralling around the magnetic field lines | I-21 |
| 1.8 | An electron travelling across the page | I-23 |
| 2.1 | The basic helix element | II-3 |
| 2.2 | MRT Field signal path for EW groups | II-4 |
| 2.3 | Schematic signal paths for both the EW and S groups to the correlator | II-5 |
| 2.4 | Heights of EW groups across the EW arm | II-7 |
| 2.5 | The R1 emission mode for a helix. | II-8 |
| 2.6 | Voltage Standing Wave Ratio for a typical element. | II-10 |
| 2.7 | First Stage Mixer Module | II-12 |
| 2.8 | Band rejection with a power combiner. | II-14 |
| 2.9 | Second stage mixer module, adapted from the CLRO module | II-16 |
| 2.10 | Change of signal recovery efficiency with V_{th} for a two bit three level correlator, From Bowers 1974 | II-17 |
| 2.11 | The MRT/CLRO correlator; a schematic matrix showing 32 real and 16 complex signals being feed into the correlator array. | II-18 |
| 2.12 | Fringes from the transit of Hydra A, with a 1km and 2km EW baseline | II-21 |

| | | |
|------|--|--------|
| 2.13 | Signal recovery with the sampling lower than the carrier frequency. | II-22 |
| 3.1 | Flow Diagram for MARMOSAT | III-5 |
| 3.2 | Two types of coordinate system in the MARMOSAT software. The tilt of the NS arm is exaggerated. | III-8 |
| 3.3 | A representation of the <i>uvw</i> coverage at MRT | III-10 |
| 3.4 | Rejection of confusing fringe frequencies in the fringe_cal program. Instrument phase is plotted against hour angle in radians | III-12 |
| 3.5 | Closure baselines on MRT, allowing the gains of the short EW baselines to be covered | III-14 |
| 3.6 | A typical 8.5 second time error showing up as a phase error along the EW arm | III-17 |
| 3.7 | The MRT_METER measured directly | III-18 |
| 3.8 | The theoretical phase difference when PKS1929-45 is a quar- ter of the strength of PKS1936-46 | III-19 |
| 4.1 | Phase differences for the calibrator source PKS1932-46, both before and after passing through base2antenna | IV-2 |
| 4.2 | Time errors found for the first 100 days of observation | IV-3 |
| 4.3 | Delay phases for zone 1 to zone 2, for Hydra on TJD10022 . . | IV-4 |
| 4.4 | The array response for a single EW group (32 helices) at 151.5MHz | IV-5 |
| 4.5 | Parkes flux values against the flux from MRT maps | IV-7 |
| 4.6 | the MRT 15' map of the whole sky | IV-8 |
| 4.7 | the MRT 15' map of the galactic plane | IV-9 |
| 4.8 | The MRT map of G5.4-1.2, the Duck | IV-13 |
| 4.9 | The MRT map of G8.7-0.1, W30 | IV-14 |
| 4.10 | The MRT map of G315.4-2.3, possible site of SN185 | IV-15 |
| 4.11 | The MRT map of G320.4-1.2, MSH15-52 and possible site of SN185 | IV-16 |
| 4.12 | Lower resolution map of G343.1-2.3 | IV-17 |
| 4.13 | Higher resolution map of G343.1-2.3 | IV-18 |
| 5.1 | Conversion of galactic rotation to line of sight velocity, after Galactic Radio Astronomy 1988 | V-3 |
| 5.2 | Plots of the rotation speed, Ω , versus galacto-centric radius(Taken from Clemens, 1985). The solid line correspond to the poly- nomials in equation 5.2. | V-5 |

| | | |
|------|---|-------|
| 5.3 | Velocity to distance conversion for pulsar PSR1706-44, from HI measurements of Radio Pulsars, Koribalski et al. 1995. The picture is of a) The total sky brightness with velocity, b) the ratio of the brightness with pulsar on over that with the pulsar off, and c) the rotation curve | V-8 |
| 5.4 | Light Curves of type 1 and 2 SNe. From Schaefer 1996 | V-10 |
| 5.5 | Surface brightness and Luminosity with Diameter, from Green 1991 | V-13 |
| 5.6 | Distance from the filament proper motions and line velocities | V-14 |
| 5.7 | The electron density in our galaxy from the model of Taylor and Cordes 1993. | V-19 |
| 5.8 | Autocorrelation of the pulsar signal with frequency and time. Figure 1 from Evidence again the PSR1706 association, Nicastro et al. 1996 | V-23 |
| 5.9 | Efficiency of PWN generation, with rate of energy loss, from the survey of Frail 1997. The dotted line represents 100% efficiency. All new results from that paper are upper limits. Labelled PSR are from other works. | V-25 |
| 5.10 | Fitting timing residuals to get a proper motions, from Pulsar Astronomy, 1990 | V-27 |
| 6.1 | The MOST image of G5.4-1.2 that first showed the far side of the remnant, Caswell et al. 1987 | VI-4 |
| 6.2 | The progression of images of the PSR nebula. The Caswell et al image from MOST (a) with a beam size of $110'' \times 42''$. Expanded from the marked region is the second image (b) from Becker and Helfand ($7'' \times 4''$), and expanded from that is the highest resolution image of Frail et al (c) $2'' \times 1.3''$. . . | VI-5 |
| 6.3 | The cumulative distribution of pulsar velocities, and the derived velocity distributions in one, two and three dimensions; from Lyne and Lorimer JApA 1995 | VI-8 |
| 6.4 | The VLA 327 MHz map from Kassim and Weiler (1990), that first showed the full extent of W30. The HII regions that were all that was seen at high frequencies and absorbed at low frequencies are labelled with the letters A through to G. The pulsar position is marked with a star. | VI-10 |
| 6.5 | The TPT 57.5 MHz map by Ödegard, from Kassim and Weiler (1990) | VI-11 |
| 6.6 | Overlay of the ROSAT emission with the MRT brightness contours. | VI-14 |
| 6.7 | The geometry of a reflection such as might be occurring in W30. | VI-15 |

| | | |
|------|--|-------|
| 6.8 | MOST image of G315.4-2.3. | VI-18 |
| 6.9 | <i>ROSAT</i> image of G315.4-2.3, showing the subsections selected for individual analysis. | VI-23 |
| 6.10 | High Resolution X-ray contours overlayed on the MOST image of G320.4-1.2, after Brazier and Becker 1997 | VI-26 |
| 6.11 | Supernova remnant G320.4-1.2 as seen by <i>ROSAT</i> . From Trussoni et al 1996. | VI-28 |
| 6.12 | IRAS and 2.4GHz contour maps. IRAS has been smoothed to the radio resolution, and a 1 degree smoothed version has been subtracted to remove the galactic ridge. | VI-29 |
| 6.13 | <i>ASCA</i> image of centre of G320.4-1.2 from Tamura et al. a) is mapped in the Mg K_{α} excess b) is with the highest (and therefore non-thermal) energies ($E > 2.2\text{keV}$), and also has the contours from a) in red. | VI-32 |
| 6.14 | Proposed model and track of the PSR jet scoring an ellipse on RCW89. Taken from Brazier and Becker 1997. | VI-33 |
| 6.15 | Proper motion of wisps (with reference to the PSR1509-58) against distance from the pulsar. | VI-35 |
| 6.16 | The MOST image from McAdam et al. 1993 of G343.1-2.3 | VI-38 |
| 6.17 | Supernova Remnant G343.1-2.3 in X-rays | VI-40 |
| 6.18 | Xspec fit to the counts from the assumed SNR, the model is the solid line and the crosses are the <i>ROSAT</i> data | VI-42 |
| 6.19 | Xspec confidence with Temperature and Column density on the <i>ROSAT</i> data | VI-43 |
| 6.20 | Derived distances and ages for SNR G343.1-2.3 | VI-44 |
| D.1 | Part a) Line to continuum contrast. Part b) The lines with wavelength. From Dubrovich et al. 1995 | D-3 |

List of Tables

| | | |
|-----|--|-------|
| 1.1 | Fundamental parameters of a developing SNR | I-19 |
| 5.1 | Coefficients of the Rotation Curves | V-6 |
| 5.2 | Coordinates of Fiducial points defining shapes of the model spiral arms, from Taylor and Cordes 1993. | V-17 |
| 5.3 | Parameters for electron density model, $n_e(x, y, z)$, from Tay- lor and Cordes 1993 | V-19 |
| 6.1 | Radio Telescopes, their frequency and resolution | VI-2 |
| 6.2 | Estimates for the Absolute Magnitudes for the two candidates for SN185 | VI-25 |
| 6.3 | Results from ROSAT observations on MSH15-52, Trussoni et al. 1996 | VI-30 |

List of symbols in general use in this thesis

| | |
|-------------------|--|
| B | Brightness of the sky |
| b | galactic latitude |
| β | Ratio of SNR centre to pulsar distance to centre to edge distance. |
| c | velocity of light |
| δ | declination |
| e | electron charge |
| I | Visibility intensity |
| k | Boltzmann constant |
| l | galactic longitude |
| m_e | electron mass |
| n_e | electron number density |
| n_i | ion number density |
| N_e | column electron density |
| N_H | column neutral hydrogen density |
| R | Radius, either from the Galactic centre or of SNR |
| R_\odot | distance of the Sun from the Galactic centre |
| D | distance from the Sun in kiloparsecs |
| T_e | electron temperature |
| T_b | brightness temperature |
| v | velocity |
| V | Voltage |
| Ω | Rotational velocity |
| ω | angular frequency |
| $P(\omega)$ | Power with frequency |
| z | height above the Galactic plane |
| Z | atomic number |
| Z | Zenith Angle |
| α | spectral index |
| ν | frequency |
| ϵ | emissivity |
| ϵ_0 | Initial energy loss of SN |
| ϵ | The dielectric constant |
| τ_i | Instrumental delay |
| τ_s | Geometric delay |
| \vec{u} | spatial separation in wavelengths |
| \vec{l} | cosine direction |
| λ | wavelength |
| μ | milliarcseconds |
| M_\perp | magnetic field |
| M_* | mass ejected in SN |
| P_0 | Pressure in ISM |
| P_* | Pressure in SNR |
| ρ | density |
| m_e | mass of an electron |
| t | time |
| Instrument Zenith | Peak of instrumental response |
| Local Zenith | Normal to the NS trolley arm and the EW horizontal |
| H | LO frequency |
| IF | Intermediate frequency |
| TJD | Truncated Julian date, Julian date - 2440000 |
| HPBW | Half Power Beam Width |
| PSF | Point spread function |
| \mathcal{F} | Fourier transform |

Acknowledgments

My supervisor, John Osborne and Uday Shankar, who played the role of thesis supervisor during the 12 months of my research studentship spent at the MRT site, have had the near impossible task of directing my research. They have ridden me with a long rein but were always there when I had difficulties, for which I am very grateful.

While in Mauritius we lived and worked in a very small circle, the intensity of this academic (well, not totally academic) cloister left one buzzing with wildfire ideas. Therefore I whole heartedly thank Kumar Golap, Sandeep Sachdev, Uday Shankar, Aswatapa and Raju for the excitement they all generated. It is amazing that in this very small group, living and working together seven days a week, we did not have more major fallings-out. That we didn't I put down to the regular - and bloody - games of Doom with which we worked out all our frustrations.

It was working with the whole MRT team, explicitly Nalini, Dinesh and Mahen, plus the staff and students who soldiered on in our little forest enclave (really far too many to name individually), that made me believe that it would be fun to quit the real world, and work on this project. In that they have succeeded, and I think I am grateful.

Being in such a small group in Durham has allowed me to tote my ideas and results around the department without fear nor favour. Regular victims of such carpet bagging have been all those in Rooms 4 and 6 and the X-ray group. Naun brought the question of the GEETEE errors to my attention. John Steele, working on the Babylonian records, was responsible for the inclusion of the discussion of the Chinese records. It has been an unmitigated pleasure being in the "broom cupboard" with all the other swept-up odd balls.

Durham's X-ray group, Chris Done and Karen Brazier, probably felt that they saw too much of me at times, but were always too scrupulously polite to say so.

A fair amount of family work went into this, my parents read all of it and introduced me to the idea of consistent grammatical constructs. I preferred a little of everything. Uncle Maurice, checked (as in stopped) some of the

madder mathematical ideas. Mohammed must be thanked for assistance on the acknowledgments, as he pointed out that is the only part most will read.

The department of Physics in Durham provided me with desk space and other facilities. Starlink and the local system manager, Alan Lotts, provided computing facilities. The last year has been entirely funded by the DSS.

The archaeology dept has housed a bolt hole to flee to when things got too rough, or boring.

Sally Hales at MRAO, Cambridge, has been another 'hand-holder'. Peter Warner of the same gave me the idea for looking for GARB's, based on the CLFO setup. We visited Jodrell Bank twice, which was nice.

The project began at the Raman Institute, and I must thank Rad for allowing me to work there on it. The new director, N. Kumar, has also been very supportive of both the project and myself. Ch. V. Sastry, of IIA (Bangalore) was the initiator of the project, and has been continually involved.

The University of Mauritius has also supported both the project and myself, and I must thank the Dean, Prof I. Fagoonee and the head of the Physics dept. Dr S. Rughooputh.

This research has made heavy use of the Bath Information Data Services (BIDS) ISI database, NASA's Astrophysics Data System (ADS) Abstract Service, the SIMBAD database, operated by CDS, Strasbourg, France, and the online Green SNR catalogue.

Abstract

The Mauritius Radio Telescope and a Study of Selected Super Nova Remnants Associated with Pulsars

Richard Dodson

The just completed Mauritius Radio Telescope, a 2km by 1km T shaped synthesis array designed to repeat the 6C survey but for the Southern hemisphere, is described. Full details of the instrument hardware, and the software designed to interpret the output of the hardware are presented.

The early results from the instrument, in the shape of maps of known SNR with possibly associated pulsars, are shown. In combination with publicly available X-ray data and published maps at other frequencies, conclusions on the associations are drawn. The sources described are G5.4-2.3 with PSR 1757-23, G8.7-0.1 with PSR 1800-21, G315.4-2.3 with SN 185, G320.4-1.2 with PSR 1509-58 and G343.1-2.3 with PSR 1706-44.

The MRT project is an example of hardware simplifications being made possible by the increasing power and sophistication of software and computation. The sheer speed with which calculations can be done nowadays has allowed corrections to be applied post factum, where previously it would have to be fixed in hardware (at much greater cost).

Preface

The work described in this thesis was undertaken between 1991 and 1997. Between 1991 and 1993 the author was a research assistant at the Raman Research Institute, Bangalore for one year and at the University of Mauritius for four months. Between 1993 and 1997 the author was a PPARC research student under the supervision of Dr. J.L. Osborne in the department of Physics at the University of Durham. This work has not been submitted for any other degree at Durham, nor at any other University.

Chapter 2 describes the hardware of the instrument, which many people were involved, many more deeply than the author. Chapter 6 calls on understanding for X-ray emission processes and benefited considerably from discussions with the experts at Durham, Drs Done and Brazier. Access to Dr Brazier's recent work on MSH15-52 was extremely helpful. However the large majority of the material presented therein is the author's own work. Maps prepared by K. Golap of the whole sky observable from Mauritius were used in Chapter 4 to show details of the difficulties with terrestrial and sublunar interference, the remainder of the images are the authors own.

A number of the results presented here have appeared in the following papers and proceedings:

Golap, K., Issur, N.H., Somanah, R., Dodson, R., Modgekar, M., Sachdev, S., Shankar, N.U. and Sastry, C.V. 1995, *Astrophysics and Space Science*, 228, 373

Golap, K., Issur, N.H., Somanah, R., Dodson, R., Modgekar, M., Sachdev, S., Shankar, N.U. and Sastry, C.V. 1995, *Journal of Astrophysics and Astronomy*, 16, 447

Golap, K. and Dodson, R. and Udaya Shankar, N., 1995, *Astron. Soc. of India. Bulletin*, 23, 574.

Udaya Shankar, N. and Dodson, R. and Osborne, J.L. 1997, *Proc. 25th Int. Cosmic Ray Conf.*, Durban, 3, 197

Chapter 1

Introduction

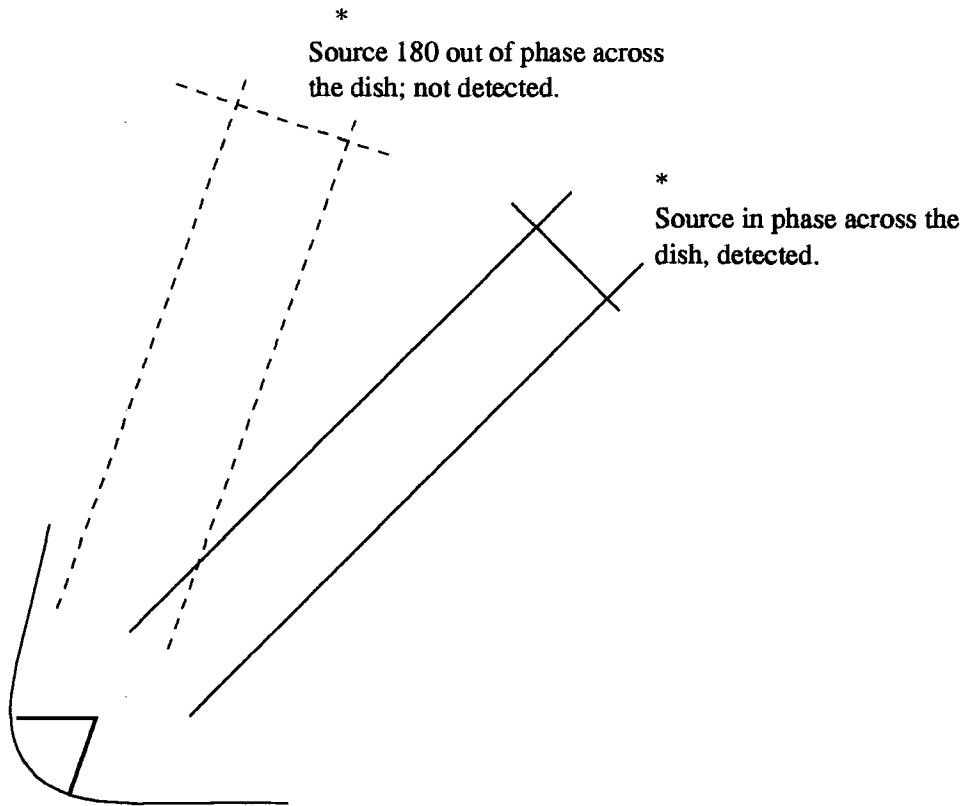
The Tragedy of King Richard III Act 1.1 line 19-21

1.1 Beginnings of Radio Astronomy

One of the youngest branches of astronomy, the oldest of the sciences, is radio astronomy. Its beginnings were in the serendipitous discovery of the Galactic plane, accomplished by Karl Jansky in 1931 while looking for the radio noise of thunderstorms. However it was Reber's follow-up analysis of these observations which deserves the credit for creating the field. A science is born only when there is systematic investigation of testable assumptions.

Reber's search for the same radio noise seen by Jansky was done in the face of massive indifference if not ridicule. His search was initially unsuccessful, as he had assumed that the signal would follow that of a black body in spectral index, and had built an instrument that looked at the higher frequencies of 330 and 910 MHz. He continued with his investigation, despite the lack of response at these shorter wavelengths, and moved into the longer wavelengths of 162 MHz where sky brightness became observable with the sensitivity of his receiver. It is the non-thermal nature of most radio emission that drives us to work at the lower frequencies. One can argue (particularly if one wishes to irritate the optical astronomers) that all the interesting phenomena are best viewed at the radio frequencies, as that is where the physics is occurring.

Reber used a type of radio astronomical dish shown in figure 1.1, a design which was to remain standard until the sixties. This can be simply described as a total power instrument. One builds the largest receiver that can be afforded and simply collects everything that rains down into it by bringing the photons at the focal point where a single feed is placed. Hence the telescope will measure the flux density from a certain region of the sky



Large single dish

Figure 1.1: Radiation from two sources, separated by the resolution, arriving at a single dish

centred at the direction towards which the telescope is pointed. Those wave fronts arriving from other directions will either be stopped by the edge of the dish, or be canceled out by the same wave arriving on the other side of the dish, but 180 degrees out of phase. Only those which arrive with zero phase difference will add together coherently. The consequence of this rejection is that the field of view of a single dish telescope is very limited; it is exactly the resolution. A beam shape is defined by the combination of the wavefronts across it. When either side of the wave front are exactly out of phase of the centre the resolution of the dish has been reached. This is simply λ/D , where D is the diameter of the dish and λ is the wavelength.

With the resolution and field of view being equal the mode of observation

is very simple, called a pencil beam for obvious reasons. The sky or source is mapped with multiple pointings of the beam.

1.2 Astronomy Transformed

Everyone was aware that this limitation, in which the non-aligned pairs cancel in the square law power detector, was not desirable. Martin Ryle (Ryle, 1952) proposed that, as at the radio frequencies one can measure both phase and magnitude¹, it was straight forward to reconstruct the field of view of the largest individually measured element. This field of view is where the rejection will take place in the same fashion as in the single dish. Furthermore he noted that this method was at least as efficient in observing time as a single dish. While many correlations have to be done with an array, up to $N*(N-1)/2$ for N antennas, the whole visible sky can be reconstructed from each run. If the array is filled, each group will have a size which defines this field of view, and this size will be $1/N^{th}$ of the full size of the instrument while the pixel size of the produced map will depend on the largest baselines. For the single dish only a single measurement needs be done (per some interval which is a function of sensitivity), but this is for a single pixel (size defined by the resolution). To cover the same area as available to the single dish would require N^2 observations. Therefore the interferometer can survey the sky more efficiently than the single dish can. Of course this is not true for certain kinds of observation, where only a single point, or a few points in the sky are of interest, such as pulsar observations. Also single dishes give the total power in the sky on all resolutions, including the broadscale. In an interferometer there has to be a minimum separation, which leads to the loss of what is called the zeroth baseline.

The theory of image reconstruction from the interferometric measurements is the Van Citter-Zernike theorem, originally developed in Fourier optics. The full theory will be approached in stages.

1.3 An overview of the Mauritius Radio Telescope

The Mauritius Radio Telescope (MRT) is the latest interferometric radio telescope to be built, and is a joint project of the University of Mauritius, the Indian Institute of Astrophysics and the Raman Research Institute. Prof. Ch. V. Sastry initiated this project. He conceived the idea of a low frequency telescope for the southern hemisphere and was in charge of the telescope during 1990-1992. Dr. N. Udaya Shankar has been in charge since 1992.

¹The power interferometer is an example of image reconstruction from magnitude only.

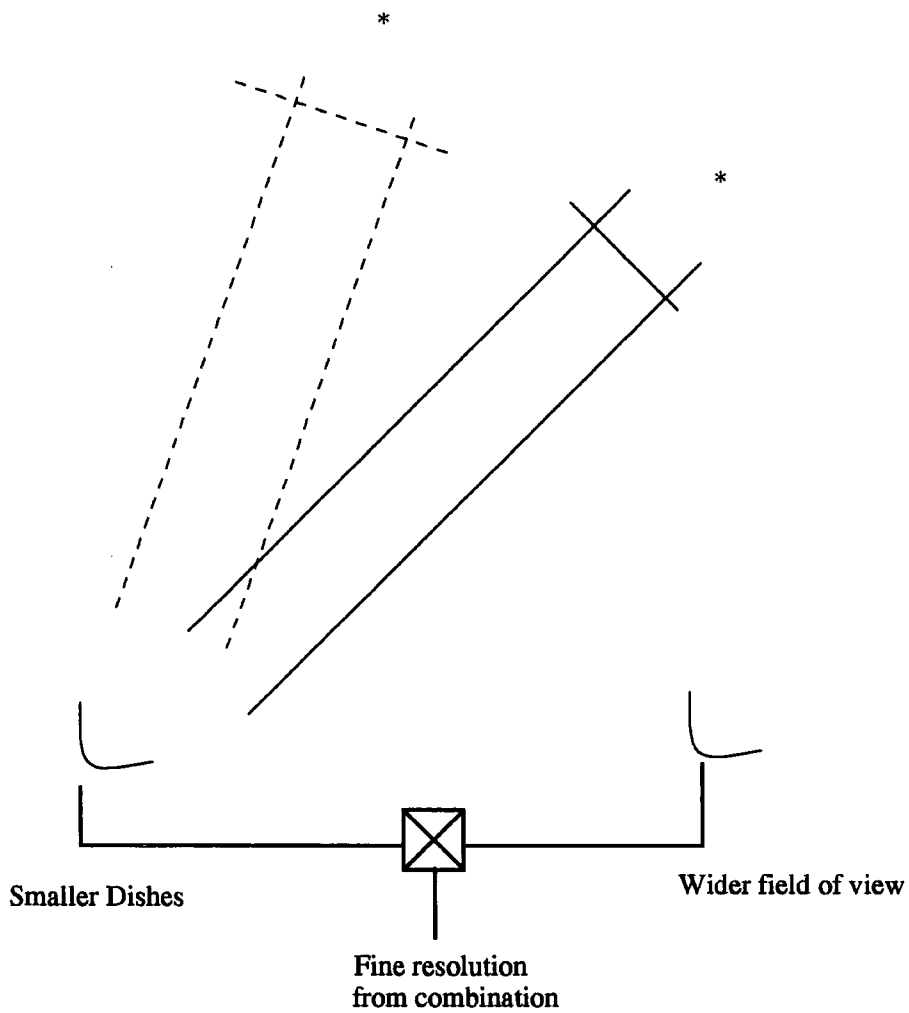


Figure 1.2: Radiation from two sources arriving at an interferometer baseline.

The installation of the receiver system, observations and the data analysis for synthesis imaging were carried out under his supervision.

1.3.1 The Telescope

Specifications

The MRT specifications are as follows:

- Location: Bras d'Eau, N E Mauritius. Latitude: 20.7°S. Longitude: 57.7° E.
- Instrument Zenith Declination: -40°.
- Centre frequency: 151.5MHz
- Instantaneous collecting area: 4352 m²
- Primary beam response: ~ 50°
- Final resolution at Zenith: 4' × 4'.2
- Instantaneous RF bandwidth: 0.75/1.5/3 MHz.
- Sensitivity: ~ 150mJy.

Configuration

The MRT is a 2km × 1km T-shaped aperture synthesis array, and is fully described in Chapter 2. The 2km EW arm has 1024 fixed 2m helical antennae. The 1km NS arm has 64 antennae on 16 movable trolleys. In the EW and NS arms the signals from 4 adjacent elements are phase equalised and combined. In turn, in the E-W arm after filtering and amplification, 8 such outputs are phase equalised and combined to produce a single section output. There are 32 of these sections. Because of the non-uniformity of the terrain the EW sections are at a number of different levels. After further processing these 32 channels and the 16 NS channels are correlated using a modified 1024 channel correlator receiver from the former Clark Lake array. Bandwidth decorrelation limits the sky coverage to ~ 10°. To cover the complete beam of 60° there is need to introduce delays. To this end a recirculator system is used which stores the astronomical data and reprocesses it through the correlators each time with a different delay. The Data Acquisition System interfaces the correlator to a PC. Its storage data format is compatible for transferring data to a SUN workstation for further processing, which is covered in Chapter 3.

1.3.2 Scientific Objectives

The telescope has mapped the southern sky at a higher resolution than has so far been achieved at its relatively low frequency of 151.5 MHz, and the final resolution is still to be reached. Its location on Mauritius means that it is relatively isolated from man-made radio interference and is in a zone where ionospheric effects are less harmful than elsewhere. Its geographical latitude is such that the centre of the Galaxy transits near to the Zenith.

The objectives are:

- to map the Galactic plane,
- to produce images and a point source catalogue for the Declination range from -10° to -70° ,
- to study pulsars.

The full map of the sky is still some way off, as the images need to be corrected for the sidelobes produced as an effect of the limited physical extent of the instrument, in a process called CLEAN. The CLEAN process is an approach to deconvolution by iterative subtraction of the known (or presumed) point spread function (PSF). However where the mapped object is resolved there are no sidelobes from the object² to be removed. Therefore Supernova Remnants (SNR) were picked as the best objects to study at this stage, and the class of SNRs with pulsars associated was the most interesting of these. The study of pulsar-SNR associations is an ideal one for the MRT, as it is an instrument with completely filled uv coverage, low frequency and a southern hemisphere location. The first gives it high surface brightness sensitivity, the second enhances the nonthermal sensitivity with respect to thermal sources and the third gives a view of the inner part of the Galaxy where the majority of these associations are to be found.

Identifying associations are the lode stone in astronomy; if one can tie two sources together the number of free parameters is massively reduced. The pulsar can limit the age of the SNR, and the SNR displays the energy loss mechanisms of the pulsar. In many cases studied in this thesis the big interferometric arrays, with high resolution and frequency, filter out the emission from the smooth features of the SNR, either as the non-thermal brightness is less at their operating frequency or because the spatial coverage of the instrument does not include the scales of the source. A lesson is here for the builders of the proposed square kilometre telescope; do not abandon the low to medium spatial frequencies!

²sidelobes from other objects might exist

1.4 Structure of the thesis

In building, developing and refining an instrument many things have to be tried. It is not possible, or interesting, to describe still-born ideas nor those that lasted longer, yet were shown later to be incorrect. We start by describing the hardware of MRT, and then the software developed to take the output of the back end and to check, then image the data. After this a selection of maps are shown, with discussion of how the calibrating and correcting terms were derived and applied. This is the MRT work and has taken our team over five years to produce. The final section, and gallingly, the most interesting, was derived over the last year. We look at the associations of pulsars and of SNRs, and these results are calculated from archived ROSAT, and published radio maps. Using these sources and some MRT information we can show that four of the most certain associations are classed as likely by these methods. Extension over all association strengths is left for future work.

1.5 Some Interferometric Theory

Two elements separated by some distance measured in wavelengths, \vec{u} , will receive radiation from a source in the (unknown) direction \vec{l} , and produce fringes. These fringes have a phase difference due to the geometric delay which is $2\pi\vec{l}\cdot\vec{u}$, shown in the figure 1.5. Knowing \vec{u} one can easily derive \vec{l} (to the resolution of the instrument). However it will also receive radiation from all sources within its field of view (set by λ/D , as before, but now D is much smaller. A subsection of the previous single unit). The case for point sources, just described, is easy to visualise. The transformation of the emission from an extended source has a limited extent, called coherence length. In simplistic terms this means that a baseline much longer than the coherence length will receive signals at opposite ends that are decorrelated.

From a set of baselines for which the relative radiation is measured one can invert the expression, within the limits set by the number and coverage of these baselines. As \vec{u} and \vec{l} are a transform pair, the accuracy to which one can constrain \vec{l} depends on the longest \vec{u} , and the broadest feature depends on the shortest \vec{u} . In principle one needs a matching number of observed and deduced features. Implicit in this definition is the two dimensional coverage of \vec{u} as, obviously, a two dimensional positioning of \vec{l} is required. At its simplest the relationship between \vec{u} and \vec{l} can be thought of as a two dimensional Fourier transform pair of the spatial frequencies (separations) measured on the ground, and the brightness distribution of the sky. However as we will see these constraints can be relaxed in the light of other constraints

that apply to the sky.

To state this explicitly, say that $B(\vec{l})$ was the distribution of light across the sky, normally called the brightness distribution. Then the visibility, $I(\vec{u})$, received is the intensity as a function of the antenna separation;

$$I(\vec{u}) = \int B(\vec{l})e^{-i2\pi\vec{u}\cdot\vec{l}}d\vec{l} \quad (1.1)$$

where \vec{l} is the cosine direction on the sky, i.e. the cosine of the angle from zenith measured away from the EW line and NS lines, \vec{u} is the distance between the two antennas, on the reciprocal axes.

This visibility is only measured at discrete points on the ground, and thus the transform of I is the brightness convolved with the sampling transform, i.e.

$$B(\vec{l}) * P(\vec{l}) = \int I(\vec{u})S(u)e^{i2\pi\vec{u}\cdot\vec{l}}du \quad (1.2)$$

where $P(\vec{l})$ is the point spread function.

So the brightness B is not the true distribution of emission on the sky. The introduction of a sampling function, which implicitly contains the response function of the antenna, means the produced map are convolved with a point spread function (PSF) which needs to be removed. The deconvolution of our maps is not tackled in this thesis, but in that of Golap's, "Synthesis Imaging at 151.5 MHz using the MRT" (Golap, 1997).

A further complication on this simple sample is that of the non-monochromatic light being used. This introduces a coherence time as well as the length that we have all covered. The signal will not correlate with itself after increasing periods of time, because the different frequencies within the bandpass become slightly out of phase. In an instrument which has a small field of view this is not usually a problem as a single delay can be introduced to equalise the path time for the entire observed area, and so the bandwidth has a very small effect. In MRT the individual elements receive information from across 60° of the sky, and we therefore have correction for several field of view centres.

The first interferometer radio telescope built, the Mills cross, had a physical two dimensional extent. It was later realized that the same result could be achieved, given an increase in the computational cost, with a much simpler hardware configuration. This trick was to build a single baseline, perfectly aligned East to West. Then as the day passed, and the earth rolled under the sky, a set of concentric circles on a plane were traced out as shown in figure 1.3.

This is the first example of hardware simplifications being made possible by the increasing power and sophistication of software and computing. This

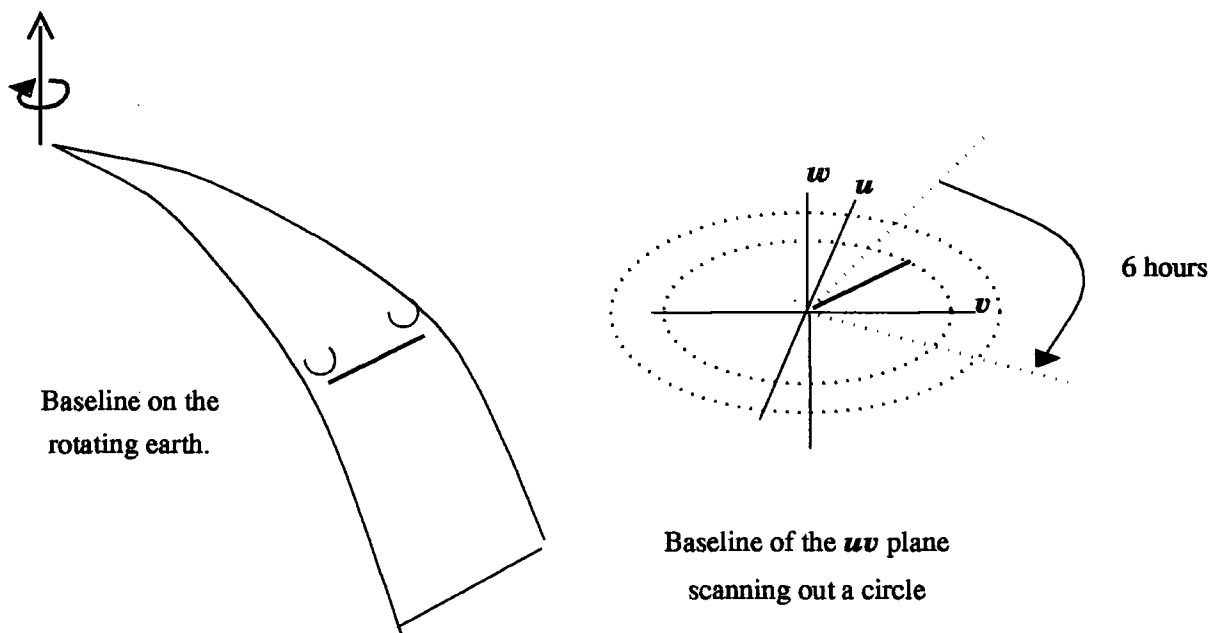


Figure 1.3: EW baseline rotating under the north pole to trace out circles on the uv plane.

remorseless transfer of the work load has continued to this day, and is amply demonstrated in the case of the MRT.

The East West rotational synthesis telescope has its natural coordinates defined towards the pole. As the earth on which the EW arm is laid out rotates during the day, one is recording the response of each antenna projected in a different line towards the sky. Thus after 6 hours the measured vector \vec{u} is 90° from the starting \vec{u} . Thus each pair draws out a circle over 24 hours on the uv plane. As one moves away from the pole the presented area to the source falls as $\cos(\delta)$. This is the reason why the same method cannot be used to observe the sky at lower latitudes or declinations. At all positions on the globe the presented area towards the equator is small, and for positions near the equator, the maximum coverage lies on or near the horizon, which is the worst direction for terrestrial interference pickup.

Therefore, when building a interferometer near the equator one is forced to revert to the two dimensional design. The modern saving over the cross is the realization that, as the sky is real, the visibility has rotational symmetry. Therefore only half of all possible baselines need to be measured, i.e. a T can be used instead of a cross. The baseline measured from North to East is equivalent to that measured from West to South as illustrated in figure 1.4.

At the MRT the chosen uv axes reflect the the operation the telescope. As it is used in the zenith transit mode, in which it looks upwards and lets the sky spin through its line of sight, it makes more sense to define the earth based axes as fixed, and the skybased axes as changing with time. This means that the time delay across a baseline \vec{u} from a point source at $\vec{l}(t)$ on the sky is τ_s where;

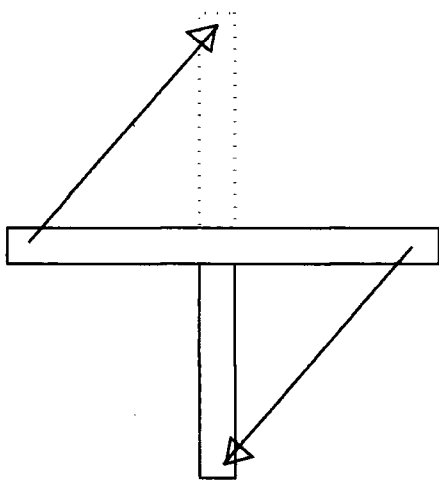
$$\tau_s = \frac{\lambda \vec{u} \cdot \vec{l}(t)}{c} \quad (1.3)$$

1.6 Digital Signals

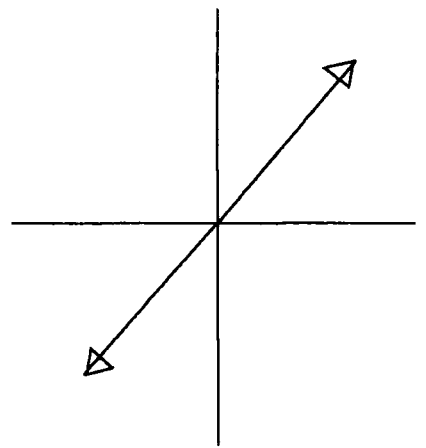
At the primary dish, or receiver, the signal is both the carrier frequency, ν and the geometric phase, τ_s . For two dishes, 1 and 2 which both have a gain G the voltage pattern as a function of time is;

$$V_1 = G \cos(2\pi[\nu t + \nu\tau_s/2]); V_2 = G \cos(2\pi[\nu t - \nu\tau_s/2]) \quad (1.4)$$

Here τ_s contains information from right across the sky, in the sense many sources combine to build up the wavefront that arrives at the telescope, but it is most easily visualised as the delay across the baseline of a wavefront from a single point source. Once the signal is picked up the signal is down



Equivalent baselines in
xy



and in
uv

Figure 1.4: T style array, with the un-necessary Mills Cross style extension shown dotted in. The vectors are 180° rotations around the centre and therefore are conjugate (for a real sky).

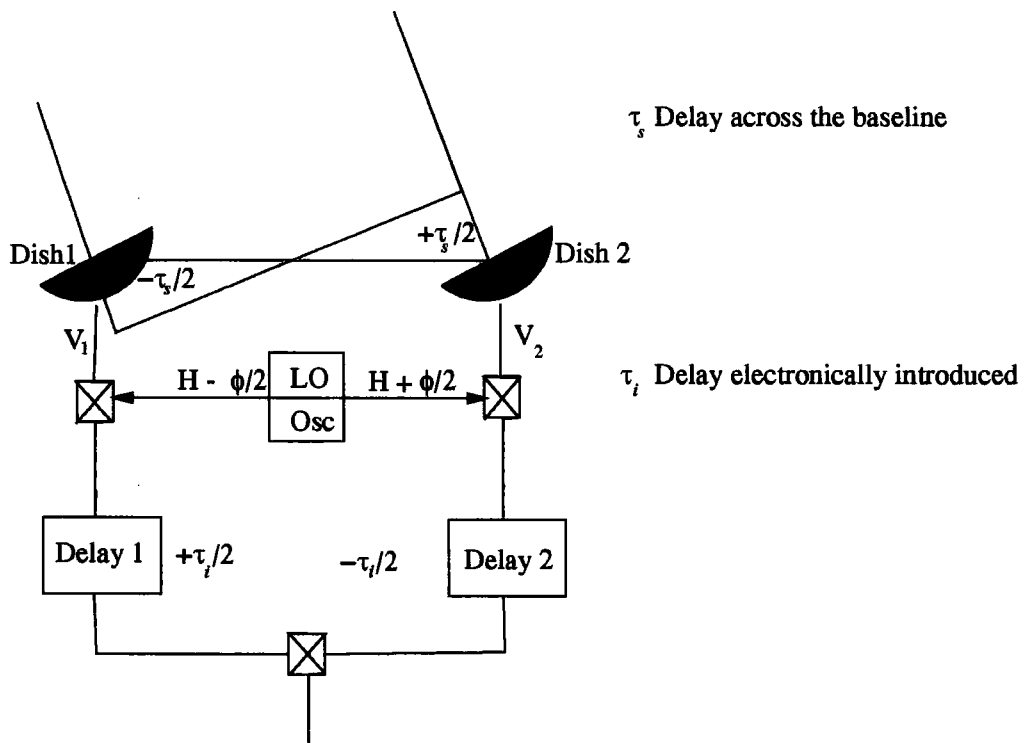


Figure 1.5: Delays along the signal path for a correlated baseline using an LO

converted by heterodyning with the Local Oscillator (LO) which is at a frequency H . The band centre of the instrument, also called the intermediate frequency, is ν less the local oscillator frequency, LO. The voltage patterns after heterodyning³ (and the unwanted contributions filtered out) are;

$$V_1 = G \cos[2\pi(IF.t + (LO + IF).\tau_s/2 - IF.\tau_i/2) - \Phi_1] \quad (1.5)$$

$$V_2 = G \cos[2\pi(IF.t - (LO + IF).\tau_s/2 + IF.\tau_i/2) - \Phi_2] \quad (1.6)$$

where Φ is the instrument phase, and the introduced delay is τ_i . In other words an extra term is introduced, i.e. $IF.\tau_i/2$, which is zero when no artificial delays are introduced. This is the case for the first dozen positions, after which the decorrelation becomes important.

A correlator instrument multiplies these two voltages and then takes the average over many cycles of the frequency.

$$\langle V_1 V_2 \rangle \propto \cos(2\pi[LO\tau_s - IF.(\tau_i - \tau_s)] - (\Phi_1 - \Phi_2)) \quad (1.7)$$

In an instrument like MRT not only is the cosine correlation taken, but with phase quadrature (adding 90° to the signal path) the full complex visibility, $I(u)$, can be recovered.

$$I(u) = G_{ij} \exp(2\pi[\nu\tau_s - IF.\tau_i] - \Phi_{ij}) \quad (1.8)$$

where Φ_{ij} is $\Phi_i - \Phi_j$.

1.7 What do we see, why do we look?

The question we were asked most often (after "could we/do we receive messages from aliens") was why; why in Mauritius, why 150MHz, and why a medium resolution instrument. The answer to the first question is that there are many excellent reasons for the siting a radio telescope in Mauritius, and a surprising number of them are scientific. The close historical and political links between India and Mauritius, and the existence of a university there are important. The islands southern latitude, isolation from radio interference present in the highly developed west, and India's continuing work in these low frequencies contributed. The answers to the wavelength and resolution are covered by this thesis; answers to the first two are yes and no (so far).

³heterodyning or mixing a signal is to combine two voltages in a nonlinear device (e.g. diode) where the second order terms are equivalent to multiplying the voltages

1.8 The Development of Supernova Remnants

In this thesis we will be looking at the subject of SNR and pulsar associations, therefore the basic theory of the development of a SNR is covered. We will not cover the preceding stages; those that go into the production of a supernova.

Baade and Zwicky first suggested in 1934 that supernova remnants come from supernovae. They also deduced that neutron stars and cosmic rays could be produced. The results depend on the mass of the progenitor star, and are very briefly summarised here;

| Mass, M_{\odot} | Produces | Called |
|--|----------------------------|---------|
| < 2 , standard pop. II stars (sol) | No Supernova | - |
| $> 2, \leq 6$, pop. II stars, or by accretion | Supernova only | Type I |
| $> 6, \leq 15$, younger pop. I stars (OB) | Supernova and pulsar | Type II |
| ≥ 15 , very young | Supernova and a Black Hole | Type II |

There will be no description of the lead up to a SN as this is another topic in its own right. They will be treated only as the source of a burst of energy dumped instantaneously into the interstellar medium (ISM). Types I and II seem to release roughly the same amount of energy in their explosion. We also deduce from equating the numbers of pulsars and their birthrates with the occurrences of SNe, that most SNe must produce a pulsar.

The evolutionary cycle of SNR's is typically described in four relatively distinct phases. The standard picture begins with a SN explosion releasing some 10^{50-51} ergs of energy into the ISM in the form of a rapidly expanding blast wave accompanied by slower moving ejecta. In this earliest free-expansion phase, the initial explosion energy is imparted in the form of kinetic energy to the ejected material. As the SNR evolves, the blast wave sweeps up ISM material forming a shell of $\sim 10^7$ K gas surrounding a tenuous, hotter interior; a reverse shock propagates into the slower-moving ejecta. The result is a shell of radio emission associated with magnetic field compression and particle acceleration behind the primary shock, accompanied by enhanced X-ray emission associated with the hot swept-up and ejecta components.

When the mass of the swept-up matter approaches that of the ejecta, the SNR enters an adiabatic expansion phase during which the energetics are dominated by the kinetic energy imparted to the swept-up ISM. During this phase the SNR properties are described by the well-known Sedov solutions (Sedov, 1959). Once the shock velocity falls below about 300 km s^{-1} , the energy loss becomes dominated by radiative channels which results in a reduced expansion rate as the main front progresses under its own momentum.

Complications associated with non-uniformities in the surrounding medium (e.g. pre-existing circumstellar cavities, or nearby molecular clouds) as well as instabilities at the shock front can play important roles in producing modifications to the expected morphological characteristics. However, both the radio and X-ray observations of SNRs have provided stunning confirmation of the standard picture described above, including detailed images of instability-driven clumping, temperature measurements consistent with the expected development, and spectral evidence for ejecta with non-solar abundances consistent with models for nucleosynthesis in SN explosions. We will start with the simplistic, but satisfactory, Sedov model, take this to through the flux to distance model, then briefly review the failures of the Sedov model when this distance measure will not work. We will list the indicators that should warn us when it is not appropriate.

1.8.1 The Sedov Description of SNRs

The theory is based on the Sedov analysis, and uses the assumption that the expansion follows a scalable form. That is the explosion can be reduced to a function of two (independent) parameters. When this is the case it falls into the class of self similar problems. These results can be applied to any “one dimensional unsteady motion of a gas”, including our case where we are looking at the behaviour of the interaction of the SN explosion with the surrounding ISM.

The equations of conservation of matter, momentum and energy across the shock front, and with reference to the shock front, are;

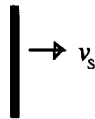
$$v_0\rho_0 = v_*\rho_*; P_0 + v_0^2\rho_0 = P_* + v_*^2\rho_*; 1/2v_0^2 + \frac{u_0 + P_0}{\rho_0} = 1/2v_*^2 + \frac{u_* + P_*}{\rho_*} \quad (1.9)$$

The subscript 0 refers to the original, pre shocked condition and * refers to that on the side of the SNe. v_* is the opposite of the shock velocity v_s , ρ is the ISM density, P is the pressure and u is the internal energy.

When dealing with shock waves it is usual to work with the equations of enthalpy, i.e. $H = U + PV$, (or dividing through by the volume to get the reduced equations, $h = u + P$). This is because enthalpy describes the behaviour of a system developing under a constant pressure. Enthalpy can be rewritten using expression for the internal energy, $U = VP/(\gamma - 1)$. Replacing this in the conservation of energy and eliminating the extra variables, (v_* and v_0), using the mass and momentum conservation gives;

$$\frac{\rho_*}{\rho_0} = \frac{(\gamma + 1)P_* + (\gamma - 1)P_0}{(\gamma - 1)P_* + (\gamma + 1)P_0} \quad (1.10)$$

Velocity of the shock through the ISM



Velocity of pre and post shocked ISM relative to the shock front

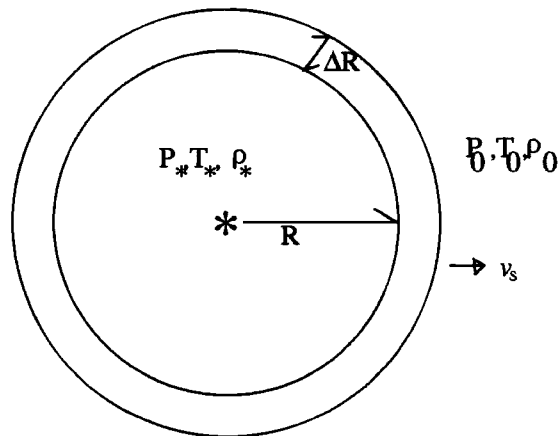
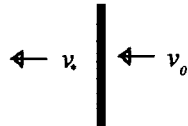


Figure 1.6: Shell formed from the supernova explosion

This equation gives the strong shock limits, called the junction conditions, when $P_* \gg P_0$;

$$\rho_* = \rho_0 \frac{\gamma + 1}{\gamma - 1}; P_* = \frac{2}{\gamma + 1} v_s^2 \rho_0; u_* = \frac{2v_s}{\gamma + 1} \quad (1.11)$$

Full treatment of the next step requires numerical analysis, but the essential result can be obtained by introducing an approximation; taking the pressure behind the shell, P_c , as some constant fraction, α , of the shock pressure gives

$$\frac{d}{dt}(Mu_0) = 4\pi R^2 P_c = 4\pi R^2 \alpha P_*$$

as the expression for the change in momentum (Mu_0) due to the pressure on the shock front, i.e. the area by the internal shell pressure. This simplifies to $d(R^3 \dot{R}) = 3\alpha R^2 \dot{R}^2$ and solves for the family of equations; $v_s = AR^{3(\alpha-1)}$. $v(R)$ can be integrated to give the radius with time. We can then substitute this into the energy conservation equation $\epsilon_0 = U_s + E_k = \frac{4\pi R^3}{3} \frac{P_c}{\gamma-1} + 1/2 M u_*^2$ to get the constants of integration. We replace the values for P_c , M and u_* in the equation to get;

$$\epsilon_0 = \frac{4\pi}{3} \rho_0 A^2 \left[\frac{2\alpha}{\gamma^2 - 1} + \frac{2}{(\gamma + 1)^2} \right] R^{6\alpha-3} \quad (1.12)$$

From the fact that the total energy must be constant it is obvious that α must equal 1/2, and therefore combining these gives;

$$R(t) \propto (\epsilon_0/\rho_0)^{1/5} t^{2/5}. \quad (1.13)$$

When we have an ideal gas $\gamma = 5/3$ this simplistic assumption gives a constant of proportionality of 1.06, a more rigorous analysis gives 1.17 (Bowers and Deeming, 1984).

1.8.2 The Four Phases of SNR development

Using these equations we can now examine the details of the development of the remnant. At time $t=0$ a mass M_* with velocity v_* and energy ϵ_0 is injected into a cold medium ρ_0 . The shock front that separates the expanding matter from its undisturbed surroundings has a radius R , the radiative loss with time is $(d\epsilon/dt)_{rad}$. The 4 stages are;

Phase I. $M_* \gg 4\pi/3 \rho_0 R^3$

In this phase the importance of the swept up matter is minor and everything depends on the details of the initial explosion. Without that knowledge not very much can be said, however it has a short lifetime.

Phase II. $M_* \ll 4\pi/3\rho_0 R^3$; $\int (d\epsilon/dt)_{rad} dt \ll \epsilon_0$

The remnant is dominated by swept up matter but the radiative losses are small and energy can be treated as conserved. This is the region in which the Sedov analysis applies. The dimensional analysis combined by similarity solution for a gas with a specific heat, $\gamma = 5/3$ (as derived above) gives;

$$R = 1.17 \left(\frac{\epsilon_0}{\rho_*} \right)^{1/5} t^{2/5} \quad (1.14)$$

this gives for the velocity

$$v_s = \frac{2}{5} \frac{R}{t} \quad (1.15)$$

As we have taken the medium in front of the shock as cold the density behind the shock, ρ_* , will reach the limiting value of $4\rho_0$ and P^* , pressure on the SN side of the shock will be equal to $(3/4)\rho_0 v_s^2$. Therefore in turn for the ideal gas, $P_* = \rho_* \frac{kT_*}{\bar{m}_*}$;

$$kT_* = 3/16 \bar{m}_* v_s^2. \quad (1.16)$$

We take the assumption of solar abundances (H 65% and He 35%) to fix a value for \bar{m} and use standard astronomical units (kms^{-1}) to give;

$$T_* = 11.3 v_s^2 \quad (1.17)$$

Now we estimate the losses due to radiation. The efficiency of radiation from hot gases is beyond the scope of this work but an approximation from (Woltjer, 1972) is that for $T > 5 \times 10^6 \text{K}$ the cooling is $\propto T^{1/2}$ and between $10^5 < T < 5 \times 10^6 \text{K}$ the rate is approximated (to a factor of two) by; $2.5 \times 10^{-16} T^{-1} n_*^2$ ergs/cm³/sec. Therefore, as the energy per unit mass is also $\propto T$, the cooling effects from the low temperature gas dominates. Using these assumptions with a shell swept up matter (at $4\rho_0$) in a volume $\pi/3 R^3$, and using our formula for the temperature as a function of radius we arrive at;

$$\dot{E} \propto n_0^2 R^3 T^{-1} \propto n_0^2 R t^2 \propto n_0^{9/5} \epsilon_0^{1/5} t^{12/5}.$$

The integrated energy loss is therefore;

$$\int_0^t \frac{d\epsilon}{dt} dt \propto n_0^{9/5} \epsilon_0^{1/5} t^{17/5}$$

The time to lose half the initial energy ($\epsilon_0/2$) from radiative losses, after putting in the constants and converting to useful units, is then;

$$t_{rad} = 3.5 \times 10^4 \epsilon_{51}^{4/17} n_0^{-9/17} \text{yr} \quad (1.18)$$

Phase III $t > t_{rad}$

By now the radiative cooling time has become short, and the matter behind the shock cools quickly. Therefore pressure forces are no longer important and the shell moves at a constant radial momentum. I.e. $(4\pi/3)R^3\rho_0v = \text{constant}$.

Phase IV

The interstellar gas has random motions of the order of 10 km s^{-1} and when the expansion velocity of the remnant reaches this level it will start to lose its identity and merge into the general ISM.

Table 1.1 lists the conditions at the cross over between the different phases for a model SNe ejecting a mass, M_* of $0.1 M_\odot$, at an initial velocity, v_* of 10^4 km s^{-1} , n_0 of 1 cm^{-3} and a ϵ_0 of 10^{50} ergs. This model SNR is from (Woltjer, 1972). Attention is drawn to the fact that the typical lifetimes of phase II is from about a century to 22 kyr, which we will take (fairly arbitrarily) as the end of the period when a SNR will be defined as young.

| | t(yr) | R(pc) | v(km/s) | M(\odot) |
|--------------|---------|-------|---------|--------------|
| Phase I-II | 90 | 0.9 | 10,000 | 0.2 |
| Phase II-III | 22,000 | 11 | 200 | 180 |
| Phase III-IV | 750,000 | 30 | 10 | 3600 |

Table 1.1: Fundamental parameters of a developing SNR

1.9 Types of Emission from Supernova Remnants

This thesis looks at the X-ray emission from hot fast thermal electrons, and radio emission from relativistic electrons. These two populations are usually related, the latter most probably seeded by the former. This is why studies of SNRs in both X-ray and radio can be very fruitful. When the regions of radio and X-ray emission are not the same an explanation has to be provided.

1.9.1 Radio

Although some thermal emission may be present in the radio spectrum the overwhelming contribution is that of synchrotron radiation, from relativistic electrons in the magnetic field of the remnant. The magnetic field is trapped in the swept up material, so the rim of the remnant should be brightest. Also the radio dominates the emission spectra and traditionally SNRs have all been identified from the lower (sub-Gigahertz) frequencies, although recently some SNRs have been discovered directly from the X-ray data from the

ROSAT satellite (Pfeffermann and Predehl, 1991). There is the interesting indication of radio quiet SNRs, possibly due to an absence of magnetic field or a low density (delaying the Sedov stage). These are of course both related to low density 'swept out' regions of the ISM.

Types of remnant are classed as shell, centre filled or plerionic, and composite. The filled centre is traditionally due to a pulsar embedded. The observed polarisation values tend to be between 5 and 15%, and the spectral index, the power law change in flux with frequency, ranges from -0.3 to -0.7, but tends towards -0.45.

1.9.2 Optical

The Crab, being very young, has synchrotron optical emission and is an exception, since generally SNRs are optically faint. Some wisps of optical emission in the shocked shells is one of the indicators that the source is an SNR. In particular forbidden transitions from collision excitation are found to be strong. The SII line is usually comparable to the H_{α} , whereas in planetary nebula it is rarely greater than 10%.

1.9.3 X-ray

X-ray and radio emission usually show good correlation. The population of relativistic electrons, radiating via synchrotron, tends to be associated with the thermal electrons radiating via thermal bremsstrahlung.

Some sources are centre filled rather than shell like, and this is symptomatic of a two component ISM, with the denser ionising at a slower rate than that of the lower. Alternatively (particularly if the SNR is centre filled at the radio wavelengths) the centre emission can be driven by the embedded pulsar as in the Crab. In these case the spectrum of the centre is best fitted by a power law spectrum. For most others the spectrum is due to thermal bremsstrahlung. These classes of X-ray type are easily separated into those which are pulsar driven, and those which are not (i.e. centrally filled and shell like remnants).

1.10 Some Emission Theory

1.10.1 Synchrotron

The details of the derivation of the spectrum of synchrotron radiation can be found in many references (Rybicki and Lightman, 1979) (Feymann et al., 1963). An extremely brief summary is given here.

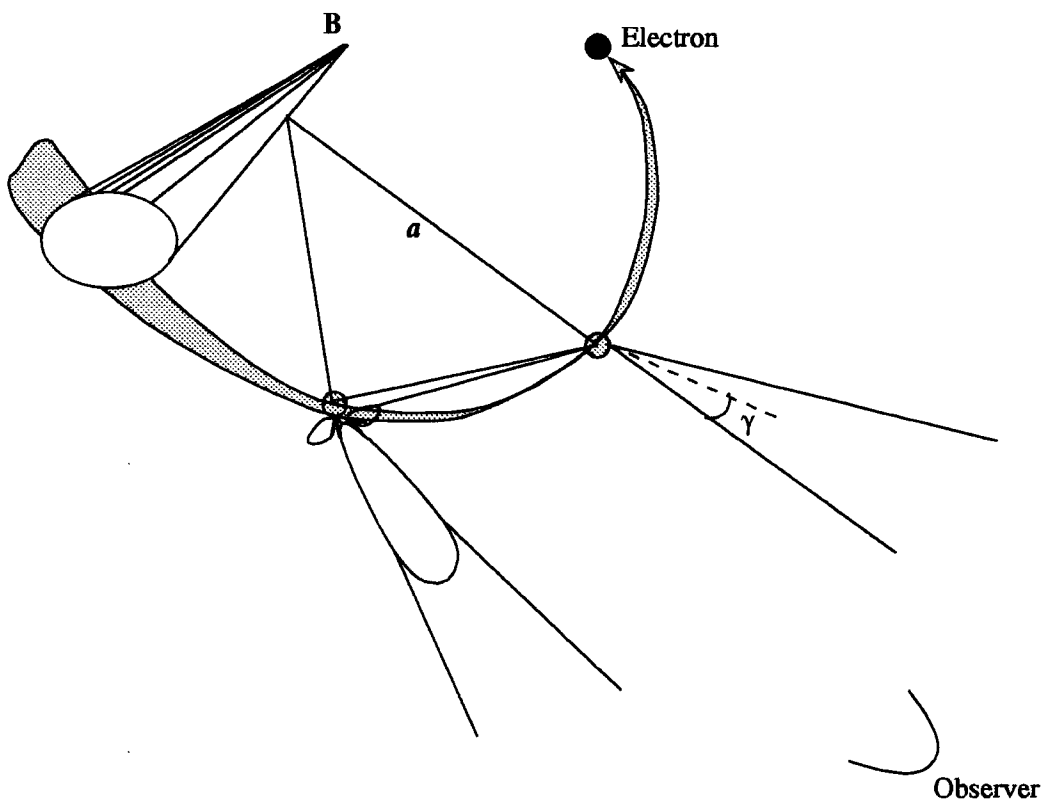


Figure 1.7: An electron travelling into the page and spiralling around the magnetic field lines

An electron travelling through a magnetic field, in a direction at some angle ϑ to the field, gyrates, and therefore radiates, following Maxwell's equations, where γ is the Lorentz factor;

$$\gamma m_e \dot{\mathbf{v}} = q/c \mathbf{v} \times \mathbf{B}$$

$$\dot{\mathbf{v}}_{\parallel} = 0; \dot{\mathbf{v}}_{\perp} = \frac{q}{\gamma m_e c} \mathbf{v}_{\perp} \times \mathbf{B}$$

There is no acceleration parallel to the field and the path of the electron is a helix around the field lines, with a rotation frequency of $\omega_B = \frac{qB}{\gamma m_e c}$. These relativistic electrons have their power pattern, normally that of a dipole, beamed forwards within a cone of $1/\gamma$, and an observer will then receive a pulse of emission for the time that it takes for this cone to sweep through the line of sight. The electron is spiralling with a radius \mathbf{a} , so the distance covered is $2\mathbf{a}/\gamma$, and \mathbf{a} is $v/\omega_B \sin(\vartheta)$. Finally the time over which this radiation is received is Doppler shifted, and at high energies this approximately $1/2\gamma^2$. The pulse lasts in the observer frame for $(\gamma^3 \omega_B \sin(\vartheta))^{-1}$. This will be related to some critical frequency, which we define as;

$$\omega_c = \frac{3\gamma^2 B \sin(\vartheta)}{2m_e c} \quad (1.19)$$

The power emitted with frequency (Rybicki and Lightman, 1979) is;

$$P(\omega) = \frac{\sqrt{3} q^3 B \sin(\vartheta)}{2\pi mc^2} F\left(\frac{\omega}{\omega_c}\right) d\omega \quad (1.20)$$

where $F(x)$ is a standard function; explicitly it is a modified Bessel function of the $1/3$ order for the parallel polarisation and of the $2/3$ for the perpendicular. This function is sharply peaked around 0.29 and the details need not bother us. The reason the power per unit frequency has been determined is to illustrate how the synchrotron radiation is a function of the energy distribution of the electrons. This distribution can be represented by $N(E)dE \propto E^{-p}dE$ where p is the energy spectral index. E can be directly replaced with γ and if we now integrate the power radiated a frequency $P(\omega)$ over all energies;

$$P_{total}(\omega) \propto \int_{\gamma_1}^{\gamma_2} P(\omega) \gamma^{-p} d\gamma \propto \int_{\gamma_1}^{\gamma_2} F\left(\frac{\omega}{\omega_c}\right) \gamma^{-p} d\gamma \quad (1.21)$$

Because ω_c is $\propto \gamma^2$ and F is a function of $x = \omega/\omega_c$ we can substitute to get;

$$P_{total}(\omega) \propto \omega^{-(p-1)/2} \int_{x_1}^{x_2} F(x) x^{(p-3)/2} dx \quad (1.22)$$

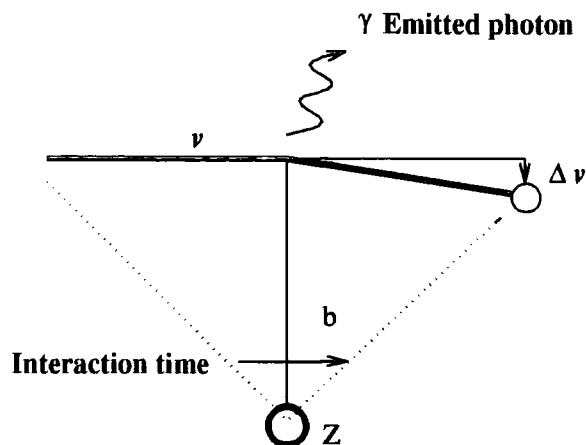


Figure 1.8: An electron travelling across the page

If x_1 and x_2 are widely spaced the integral is roughly constant. This requires that p is also constant over a large range, normally a justifiable assumption. Thus we have that the spectral index, α , is related to the power index of the radiating electrons.

As said the function $F(x)$ is different for the different polarisations so more is radiated by the perpendicular orientation than the parallel, therefore there is a residual polarisation $\Pi = \frac{p+1}{p+\frac{1}{3}}$.

1.10.2 Bremsstrahlung

Thermal bremsstrahlung emission is that due to the passage of one charged particle past another. The same standard references cover the derivation, but to summarise brutally again;

An electron passing an ion, at closest distance b , will be deflected from its straight path Δv , with an acceleration \dot{v} . The interaction time, τ , will be the order of b/v . The dipole radiation is;

$$d(\ddot{t}) = [-\omega^2 d(\omega)] = -e\dot{v}$$

The integral of the force on the electron as it passes is;

$$\Delta v = Ze^2/m_e \int_{-\infty}^{\infty} \frac{b dt}{(b^2 + v^2 t^2)^{3/2}} = 2Ze^2/m_e b v$$

The standard formula of $\frac{dW}{d\omega}$ (from the integral of the square of the radiation vector of over space) = $\frac{8\pi\omega^4}{3c^3} |\dot{d}(\omega)|^2$. The lower (non-quantum)

limits of b are at that distance where there would be a collision, the upper is where the interaction becomes insignificant. These limits define the gaunt factor. The element of emission per unit volume and and time then is;

$$\frac{dW}{d\omega dV dt} = \frac{16e^6}{3c^3 m_e^2 v} n_e n_i Z^2 \int_{b_{max}}^{b_{min}} db/b$$

$$\frac{dW}{d\omega dV dt} = \frac{16\pi e^6}{3\sqrt{3}c^3 m_e^2 v} n_e n_i Z^2 g_{ff}(v, \omega)$$

For a population N that is in thermal equilibrium $dN \propto \exp[-m_e v^2/2kT]d^3\mathbf{v}$, and using the fact that the lower emission limit is $h\nu \leq 1/2mv^2$ this can give;

$$\frac{dW}{dV dt d\nu} = \frac{2^5 \pi e^6}{3m_e c^3} \left(\frac{2\pi}{2km_e}\right)^{1/2} T^{-1/2} Z^2 n_e n_i e^{-h\nu/kT} \bar{g}_{ff} \quad (1.23)$$

This applies for bremsstrahlung radiation only and many detailed calculations are required to model the behaviour of astronomical source, taking into account of the likely composition of the ISM. For this thesis all such calculations have been done in the program **Xspec** (Jacoby and Barnes, 1996).

1.11 Criteria for the acceptance of Associations

So many assumptions and models go into characterising a pulsar and supernova pair that it is not surprising that there is a large amount of subjective judgment as to whether a pairing is correct. Examples of this are too numerous to mention. V. Kaspi (Kaspi, 1996) suggested a simple and straight forward framework for rating associations;

The points of test are;

- Do independent distance estimates agree?
This is obvious, but a secondary consideration is whether the estimates use the same kind of model. If both are kinematic estimates, the association will not be affected if the galactic radius is changed again.
- Do independent age estimates agree?
Ages of remnants are hard to estimate, but a new method is discussed in this thesis.
- Is the implied transverse velocity reasonable?
Traditionally the test was whether the pulsar was within the remnant, but for old remnants this test is not reasonable.

- Is there evidence for any interaction between them?
Still subjective but there are several cases where there is little question that some input is going from the pulsar to the SNR. Two of these are covered in this thesis.
- Does the proper motion vector of the pulsar point away from the centre?
Proper motions are the final brick in the structure, as they require long term observations of the pulsar.

A fail in each of these test counted as a “black mark” and the number of black marks is used to judge the goodness of fit. In this thesis a slight variant is used, for a pass +1 is given, a fail scores -1. This is so absent observations (such as proper motion) do not skew the result. This also allows half marks to be given when the results are border line.

This relatively simple structure might reduce the rancor in the field.

Chapter 2

Hardware

How many hardware engineers does it take to change a lightbulb?
None: "We'll fix it in software."

2.1 Design criteria

The array design was constrained by the following factors; the nature of the 6C survey (Baldwin et al., 1985), the Clark Lake (Erickson et al., 1982) correlator system, and the presence of man-made interference, the location and the terrain. The 6C survey, which one wished to match, had a resolution of $4.2'$ and sensitivity around 100mJy; the Clark Lake system came with a 32 by 16 complex digital correlator, and local terrestrial interference spectrum was dominated by a pager system nominally running at 149 MHz. The site is at a latitude of $-20^{\circ}.14$ on a rocky volcanic plane.

A T-shaped configuration was chosen partly for its simplicity, but also because at a latitude of -20° EW rotational synthesis is very inefficient. The parameters of the 6C survey required a 2 x 1 km baseline to match the resolution. Aperture synthesis, with fixed antennas in the EW arm and movable elements in the South arm, was chosen for to reduce the hardware required. The signals from the EW and NS antennas could then be fed into the two sides of the correlator matrix. Within a state forest where land was in the remit of the government an old abandoned railway line ran NS, and it was recognised that this would be convenient for the Southern arm. This arm slopes down smoothly at $0^{\circ}.5$ to the horizontal for about 700 m and then slopes up at $0^{\circ}.5$ for a further 200 meters, slightly short of the hoped for 1000m, but it was considered to be adequate. On this rail the trolleys cannot approach closer to the EW arm than 11 m. A 15 m North extension with a single trolley, which can approach the EW arm down to 2 m has been built and is used to measure the lowest spatial frequencies. Finally the

zeroth baseline, from the self correlation of a single group can be included, although it is not in the maps produced for this thesis. This ensures that the array responds to all structures on angular scales from 4' to 50°.

A disadvantage of the chosen site is that the terrain is rocky and very uneven along the EW arm with height differences of up to 35m (figure 2.4). Some effort was expended attempting to flatten this, but the volcanic rock was too tough. To minimise these problems of non-coplanarity it was decided to level the EW arm sufficiently so that the antennas in each group would be at the same height. The largest flat section that was achievable across the whole of the EW arm was 64 m (32λ at 150MHz), this was taken as the size of an EW group. This led to the requirement that the cosine channel side of the correlator matrix (with 32 channels) had to be used for the EW arm, so only 16 trolleys could be cross correlated at one time.

To match the sensitivity of the 6C survey, with this system, a 1MHz bandwidth was necessary. Thus the 149MHz pager system used on Mauritius forced us to move up from the design frequency (exactly 2 meters) and observe at 151.5 MHz. The expected RMS values of the background in the synthesised images arising from system noise with 1 MHz bandwidth and an integration time of 8 seconds (a half of the Half Power Beam Width (HPBW)) and from confusion (derived from the 6C figures) are expected to be around 60 mJy and 10 mJy respectively.

2.1.1 Description of MRT

The primary element of the array is a monofilar axially fed helix. The helical antenna has a collecting area of about λ^2 (4m^2 at 150 MHz) with a HPBW (Fig. 2.1) about $50^\circ \times 50^\circ$ (Kraus, 1988).

The helices are mounted with a tilt of 20° towards the South, to achieve a better coverage of the under mapped Southern sky (-15° to -65° dec) including the Southern-most part of the galactic plane.

There are 1024 helices in the EW arm, which are mounted on a 2 m wide ground plane with an inter-element spacing of 2m (1λ at 150 MHz, 1.01λ at 151.5). The resulting 2046 meters¹ is divided into 32 groups of 32 helices each. The HPBW of the Primary Beam of each of these EW group is $2^\circ \times 50^\circ$, thus a source will be within the HPBW for roughly $8 \times \sec(\delta)$ minutes of time.

Within each group every four helices are combined using hybrids and the output is preamplified in a low noise amplifier. Eight such outputs are further combined and amplified to form one group in the EW array (Fig. 2.2). Four helices are mounted on a trolley with a 2 m wide ground

¹Not 2048m, as we have a single missing helix within one group

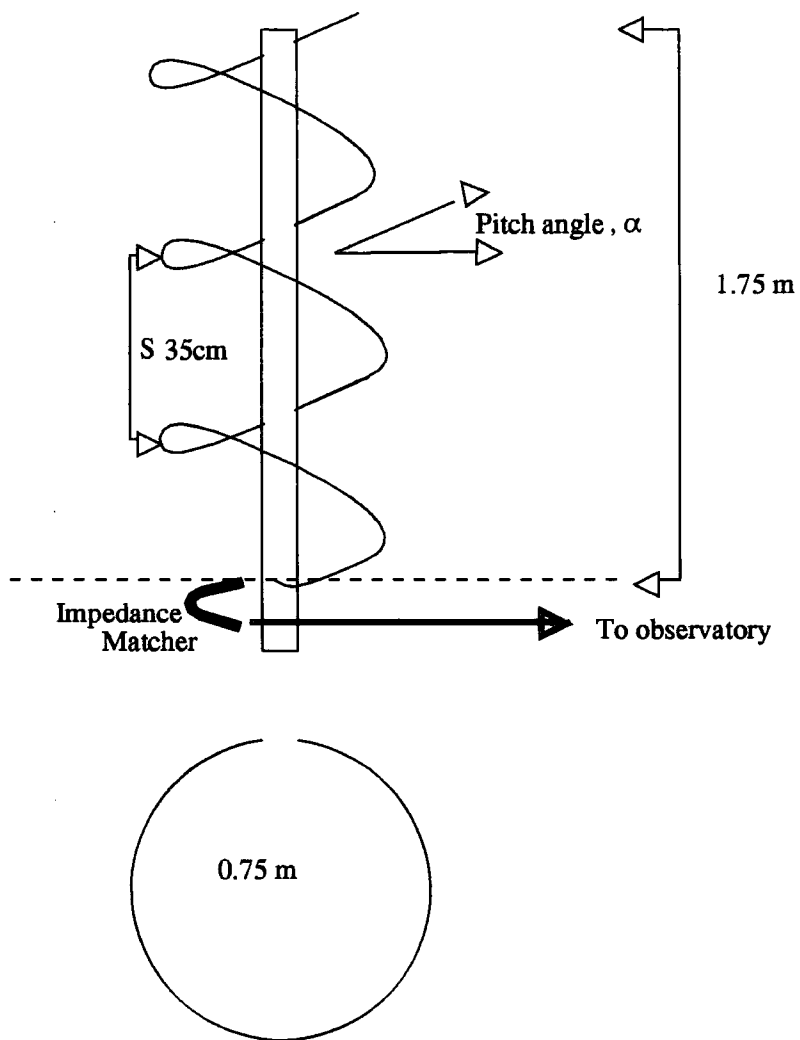


Figure 2.1: The basic helix element

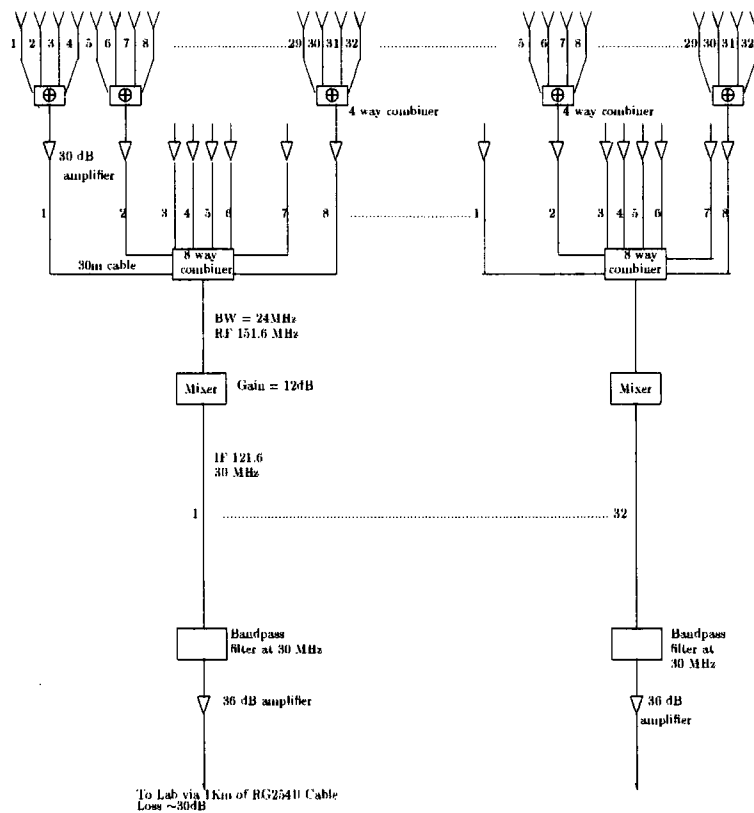


Figure 2.2: MRT Field signal path for EW groups

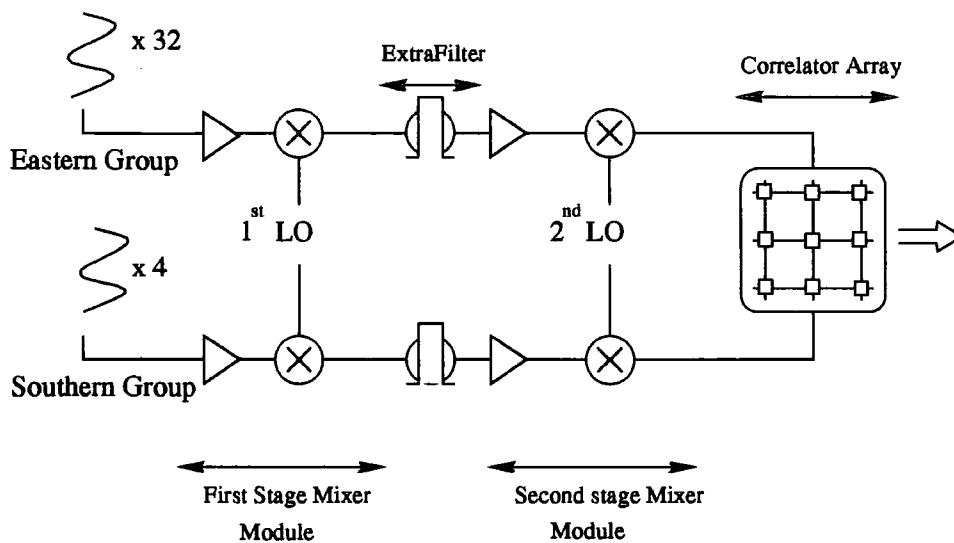


Figure 2.3: Schematic signal paths for both the EW and S groups to the correlator

plane, i.e the first stage of an EW group. This constitutes a group on the S array. The HPBW of the primary beam of each S group is $13^\circ \times 50^\circ$. Both EW and S group outputs are heterodyned to an intermediate frequency (IF) of 30 MHz, a frequency more appropriate for transmission (loss at 150 MHz per meter of RG274U is 0.1 dB/m and 0.03dB/m at 30 MHz). After further amplification the 32 EW and 16 S group outputs are carried using coaxial cables to the observatory situated close to the centre of the array. Approximately equal lengths of coaxial cables are used irrespective of the distance of the groups from the observatory to ensure that the interferometer outputs are not affected by changes in the ambient temperature. The signal paths along the EW and S arms are shown in figure 2.3.

Heliac cables running parallel to the East, West and South arms of the array are used to distribute LO signal required for heterodyning. This cable is superior to braided cable and is made up of solid copper corrugated outer conductor which results in low loss (0.024 dB/m at 121.6 MHz), and better EMI shielding. At each group the LO signal is obtained by using directional couplers. To maintain a constant power level of -5 dBm in all the groups, high power amplifiers are placed at several places along the heliac cable. These high power amplifiers are broadband and were found to amplify the spectral impurities of the signal generator, as well as the LO. The spectral

impurities around 30 MHz leak into the IF port through the mixers and cause large spurious correlation between nearby groups. (For groups further apart the impurities become decorrelated). These effects are rejected by using band elimination filters centred around 30 MHz at the output of the LO amplifiers. A bandpass filter attached to a directional coupler acts as band elimination filter and is described further in section 2.2.4.

In the observatory building the 48 group outputs are further amplified and down-converted to 10 MHz (second IF). Three IF bandwidths, ranging from 1.5 to 0.15 MHz are selectable on the CLO system. The outputs of the 32 EW and 16 S groups are fed into a 32×16 complex, 2 bit-3 level, digital correlator sampling at 12MHz (reduced to 10.625MHz in the recirculator). To check the repeatability of the data and also help in phase calibration, one of the EW arm outputs is also multiplied with the EW group outputs. This reduces the number of usable trolleys to 15.

The Correlation receiver measures 512 complex visibilities using 32 EW groups, 15 S trolleys and an E group. These are recorded with approximately one second of integration on the disk of a workstation. At the end of 24 hours of observing the trolleys are moved to a different position and new visibilities are recorded. The visibilities are sampled in the S direction at intervals of (almost²) $\lambda/2$ to ensure that there are no grating responses in the declination. This sampling needs a minimum of 60 days of observing to obtain the visibilities up to 880 m spacing. Experience so far shows that around 3 days of observing are required with one set of trolley positions to obtain repeatable and interference free data. This is further increased by breakdowns. However we are now in our second year of observations and are nearly finished. To prevent cross talk between the trolleys they were each separated by 6 meters. As there was 15 of trolleys this means that a block covering nearly 100 meters was done at one time, and for each observing day they were moved a single meter until each had covered 6 meters and the block was filled. The next block would then be started. A side effect of this is that any single day's map has a six fold repetition across it, from the sampling. Normally this is of no concern as one would only map blocks at a time, but fleeting events such as the transit of a satellite broadcasting on the 150MHz bandwidth, do retain this six fold structure.

The size of the EW groups was constrained by the uneven terrain. All the EW groups cannot be at the same height (Fig. 2.4) but it was possible to make sure that they were the same width, thus have identical primary beams.

The Fourier transform of the phase corrected visibilities obtained after

²The sampling supposed to be one meter. It was found that this was measured with a rule that was 3mm short. Combined with the 151.5MHz observing frequency the sampling becomes $.998/2 \lambda$

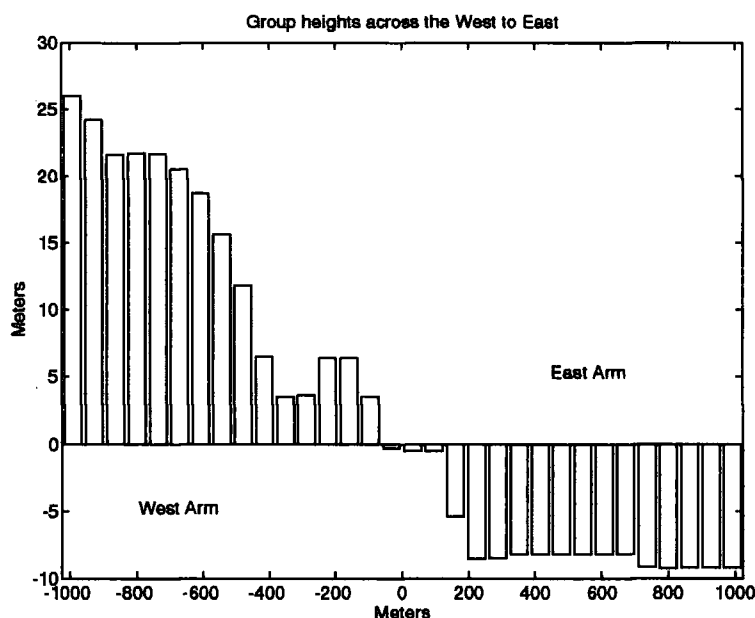


Figure 2.4: Heights of EW groups across the EW arm

the complete observing schedule (32×880 visibilities per second) produces a map of the area of the sky under observation with a synthesised beam width of $4' \times 4'.6 \sec(Z)$. The phase corrections mentioned above take into consideration the non-coplanarity of the baselines.

2.2 Hardware description and design

The following sections describes each of the individual modules which make up the system in detail.

2.2.1 The Helix

The primary element of the array is a peripherally fed monofilar axial mode helix (Fig. 2.1) of 3 turns with a diameter of 0.75 m and a height of 1.75 m, the pitch angle is 13° and the turn to turn separation, S , is 35cm. This is mounted above a stainless steel reflector mesh of grid size $5 \text{ cm} \times 5 \text{ cm}$. The helix is made of round aluminium tubing, 1.5 cm in diameter, supported with a central light weight, UV stabilised, PVC cylinder and radial PVC rods. The axial mode provides maximum radiation along the helix axis (i.e

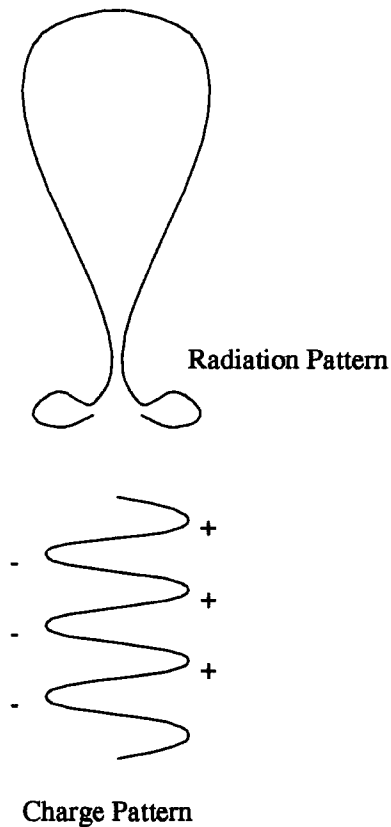


Figure 2.5: The R1 emission mode for a helix.

the R1 mode, with alternating polarity between turns along the axis). This is shown in figure 2.5.

The antennae respond to frequencies between 100 and 200 MHz with right circular polarisation. A quarter wave transformer used in the feed network optimizes the Voltage Standing Wave Ratio (VSWR) to ≤ 1.5 around 151 MHz. The VSWR is $\frac{1+\rho}{1-\rho}$ where ρ is the ratio of the voltage reflected back into free space to the voltage put into it. That is a VSWR of 1 shows perfect matching as all power is transmitted.

The characteristics of the antenna are as follows (Kraus, 1988):

- The centre frequency, which depends on the circumference ($\lambda_{central} =$ distance between 2 turns).
- The Half Power Beam Width (HPBW) and band width, which depend mainly on the number of turns, the pitch angle, diameter of the helix.

- The characteristic impedance, which depends on the circumference.

With the helix of the above dimensions, the

$$HPBW = \frac{52}{C_\lambda \sqrt{nS_\lambda}}$$

where C is the circumference of 1 turn in wavelengths, n is the number of turns and S is the separation between turns (as shown on Fig 2.1). In our case this gives a HPBW of 50° . The full equation for the power pattern is;

$$E = (\sin(90^\circ/n) \frac{\sin(n\phi/2)}{\sin(\phi/2)} \cos(\theta)) \quad (2.1)$$

$$\phi = 360^\circ [S_\lambda (1 - \cos(\theta)) + \frac{1}{2n}] \quad (2.2)$$

The intrinsic impedance from (Kraus, 1988) is;

$$Z_l = \frac{150}{\sqrt{C_\lambda}} \Omega.$$

Various direct methods for matching this antenna to the 50Ω RG-8U cables were tried. The simplest was to flatten the pitch angle as the tubing approached the mesh but it was found that this solution was very sensitive to the mesh distance in the the last $1/4$ turn before the feed. As the mesh tends to sag it was then very hard to repeat from helix to helix, and to maintain this over time. The best results were obtained by using a quarter wave transformer. Assuming the antenna has an impedance of Z_l and the transmission cable is Z_{out} and we use a wave guide to match the two, the impedance of the waveguide (Z_w) is given in (for a lossless case):

$$Z_{out} = Z_w \frac{Z_l + jZ_w \tan \beta x}{Z_w + jZ_l \tan \beta x}$$

where $\beta = 2\pi/\lambda$ and x is the length of the waveguide (see Fig 2.1)

If one uses a $\lambda/4$ transmission line between the load and the output one has:

$$Z_w = \sqrt{Z_{out} Z_l}$$

In this case that is 83Ω . A coaxial cable of 75Ω impedance was used and empirically we trimmed the length till a matching of ≈ 1.1 VSWR was achieved.

For checking the match of the 1024 East West and 64 Southern helices, the VSWR was measured groups of 4 helices combined together. A test signal was fed into the 4-way combined output and the return was measured. The contribution from each single antenna could be estimated by shorting the feed of each individual antenna. All of the helices have VSWR of less than 1.4 (with most having a VSWR of 1.2, those that are hard to reach were set at about 1.4). In practice the VSWR was tuned by a combination of moving the height of the last turn which was supported by a PVC bush, or by tapering slightly the last quarter turn (i.e. adjusting Z_l) as well as trimming the stub. A typical plot of return power versus frequency is shown

**WILTRON 6400 Series
RF Network Analyzer**

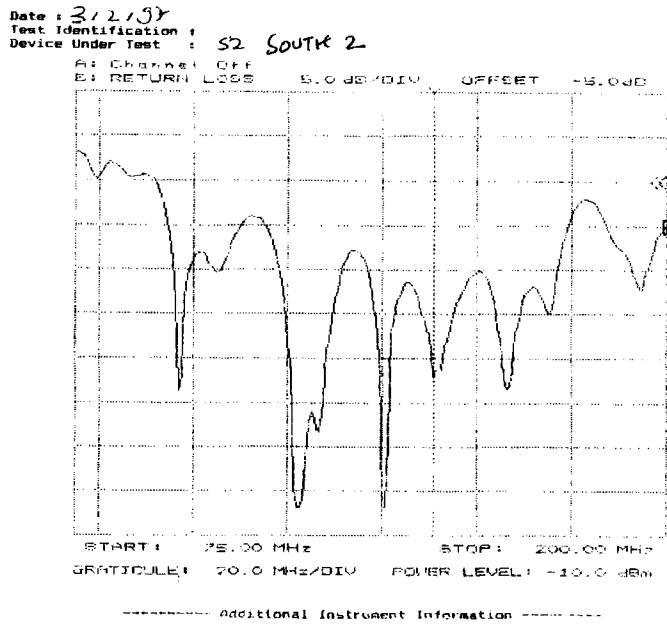


Figure 2.6: Voltage Standing Wave Ratio for a typical element.

in Fig. 2.6 for a group of 4 helices. Note the narrowness of the frequency band which is due to the quarter wave stub while one expects the helix to be quite broad in frequency response, note also with local minimum at 125 MHz, which will be discussed in appendix C.

2.2.2 Pre-Filter amplifier

Most of the RF electronics are designed from commercially available modules. The Pre-filter amplifier used (Fig. 2.7) consists of a 127 MHz High pass filter and a broad band amplifier of gain of 30 dB.

The amplifier has a gain of 30 dB for the frequency range of 0.5 to 500 MHz. Putting such an amplifier after a broad band antenna like the helix, there is a high risk of saturation by signals in the public communication band (0 to 10 MHz). Thus a high pass filter was put before even the first amplification to protect against saturation but at the cost of a signal loss of ≈ 0.5 dB (the typical insertion loss of the high band pass filter). This is

important as it is the signal to noise ratio (a.k.a. the noise figure) of the first stage that sets the lowest possible limit of the final signal to noise ratio.

The quoted typical noise figure of the amplifier is 2.8 dB. So the estimated noise temperature³ of the filter followed by the amplifier is 270K, adequate at these frequencies where the sky temperature is of that order. The measured noise figure at 150 MHz is 3 dB.

2.2.3 The 4-way and 8-way combiners

As can be seen from Figure 2.2 one amplifies the signals that comes from 4 helices combined. As the length of cable before 4 way combination is some 5 m, the loss at 150 MHz is 0.5 dB. The combination is done by using 4-way 0° power combiners. In the EW groups only, after the first amplification, 8 groups of 4 are combined in 8-way 0° power combiners therefore the length of cable carrying signals before combining is 30 m. The cable before combination are both length and phase equalised to within 5° (at 150MHz). The equalisation was done at two widely separated frequencies. This keeps the option of changing the operating frequency without having to modify the combining arrangement.

The insertion loss for both the power combiners are typically 0.8dB and the signal isolation between any 2 combining ports is 30 dB.

2.2.4 The Mixer Module

The mixer module (Fig 2.7) starts with a Low Pass filter ($F_c = 150\text{MHz}$) followed by a high pass filter ($F_c = 127\text{MHz}$) and, in its turn, followed by an active mixer. The IF produced after mixing with the LO of 121.6MHz is then filtered with a band pass filter at 30 MHz and amplified by a 14 dB amplifier.

The gain of the mixer is +7 to +8 dB for LO level of -10 dBm to +5 dBm. Its RF to IF feed-through is at -25 dB for 100 to 200 MHz. The LO to RF feed-through for 100 to 200 MHz is -33 dB. But the LO to IF feed through for the frequency range 100 to 200 MHz is -14 dB.

The LO power feed-through is quite high, unfortunately the signal generator was found to produce spurious frequencies some 60 dB below the level of the main signal it is programmed to produce. If one provides LO of the order of 0 dBm at the mixer port after amplification, the common noise due to LO spurious is still ≈ -60 dBm. The sky background power at this stage (assuming 1 MHz band and background temperature of 300 K) is of the ≈ -65 dBm. Hence the spurious signal is ≈ 3 times the uncorrelated noise. With a 1 MHz bandwidth and 1 second integration one should be

³NF=10 log((T+300)/300)

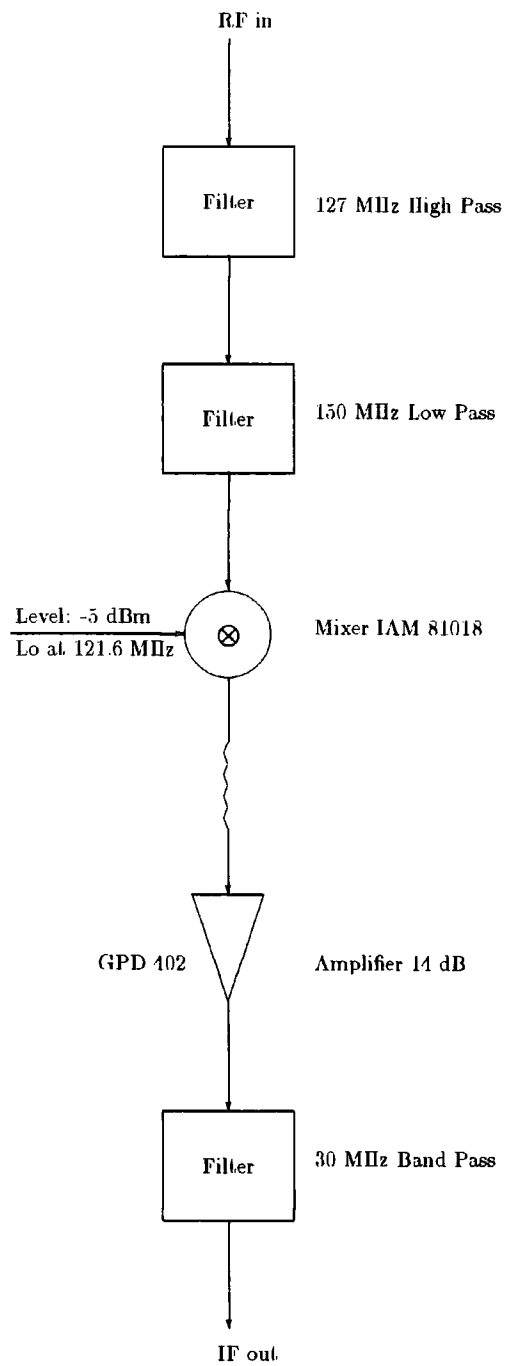


Figure 2.7: First Stage Mixer Module

able to detect a thousandth of the signal⁴. Hence the spurious signal from the LO can be as much as 3000 times over the detection level. The simplest way to avoid this problem is to have a very good band pass filter which will pass the LO frequency but cuts the other spurious frequencies by 50 to 60 dB. The disadvantage is that this arrangement is inflexible. The LO could not be changed if the need arises, more importantly one did not have the required filter available. It was decided to pinch out only the 30 MHz region of the spurious LO spectrum, as other bands will get suppressed off by the 30 MHz band passes that follow the mixers. This band rejection is achieved by the simple use of a band pass at 30 MHz and a 2-way combiner (see Fig 2.8), all available on site. The signal arriving at port IN1 is bounced out port IN2, from the output port, except for frequencies around 30MHz which are passed through, then terminated.

The net gain of the mixer module as measured was found to be between 12 dB to 14 dB.

2.2.5 Transmission of the signals to the receiver room

The amplifier used at IF stage has a gain of 36 dB. This amplifier is again broad band 1 to 250 MHz with a noise figure of 3.7 dB at 30 MHz. The average signal level is of the order of -45 dBm. The signals are sent to the lab via 1 km cables (RG8U) which have measured losses of 35-40 dB at 30 MHz, in line with specifications.

2.2.6 The RF back end

Since the incoming signal is to be mixed with a second LO of 40 MHz in the second mixer modules, and the the mixer image at 50MHz⁵ was not suppressed sufficiently by the previous filters in the path, a further filter centred at 30 MHz and bandwidth of ≈ 3 MHz on the IF path (insertion loss of 1 dB) was added. See figure 2.3.

2.2.7 The Second Mixer Modules

The 48 modules were provided by the Clarke Lake Radio Observatory (Erickson et al., 1982), they have been modified for MRT. The module (figure 2.9) starts with a 15 dB amplifier (with a noise figure < 12 dB). The signal is next mixed in a passive mixer which is fed with an LO of 40 MHz at +7 dBm with a typical conversion loss of 6dBm. This is followed by a current

$$^4 \frac{\Delta T}{T} = \frac{1}{\sqrt{\Delta f \tau}}$$

⁵The LO of 120 produces 50MHz with the 170 and the 70MHz signals which are picked up by the antenna. This 50 is insufficiently squelched by the 30MHz filter

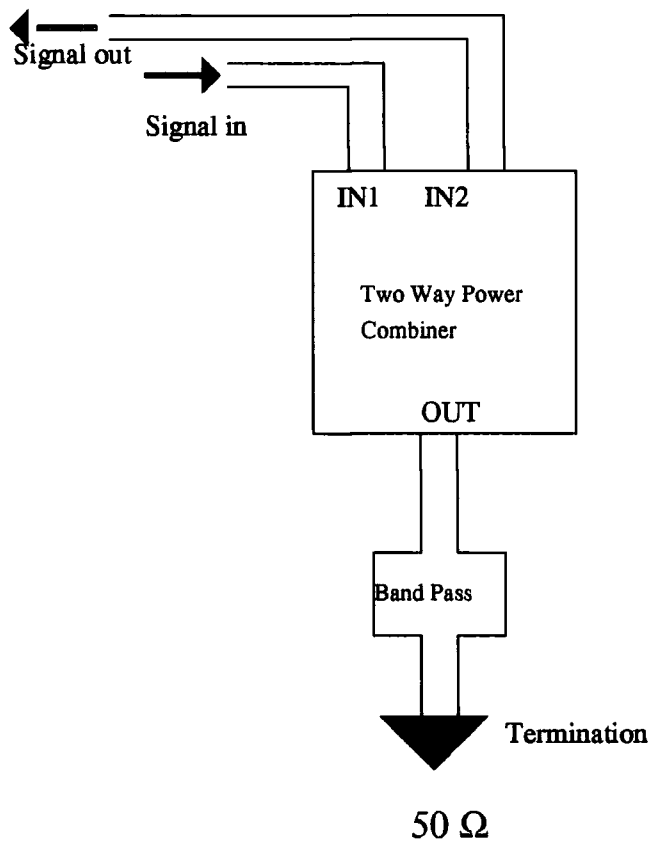


Figure 2.8: Band rejection with a power combiner.

buffer stage. The second IF is then filtered by a band pass at approximately 10 MHz with bandwidth of 3 MHz followed immediately by another one with a bandwidth of 1.5 MHz.

All filters available in the module are used in series to cut the band interference to a minimum.

Between filters there is a 34 dB voltage amplifier followed by a current buffer. There are three possible paths (diode switchable) for the IF which produces the final bandwidth of 1.5 MHz or 0.75 MHz or 0.15 MHz. After the filtering the signal goes through an auto-gain amplifier which can be set into a fix gain mode by switching the gain control to a current source. The automatic gain control, AGC, stage is followed by a current buffering stage along with a diode and RC power detector circuit at the output which drives the feedback circuit to the AGC. The feedback circuit is tuned so as to give a final 0 dBm output. The second mixer module has a dynamic range of 30 to 40 dB of the input power.

The AGC amplifier is needed in order to keep the digital correlators in their optimum working range for the best signal to noise ratio. This is addressed in the next section.

2.2.8 The 2-bits 3-levels samplers

The signal is digitised to 2 bits, i.e. coding only three levels; whether the $signal < -V_{th}$ or $-V_{th} < signal < V_{th}$ or if $signal > V_{th}$. The signal to noise degradation for a three level digitising scheme is some 12% at 6 times Nyquist sampling; i.e. the signal loss for a Gaussian noise correlation is only 12% less than an analogue system with a infinite level correlation.

As can be easily extracted from the standard literature on the topic (D'Addario et al., 1984; Kulkarni and Heiles, 1980; Bowers and Klinger, 1974). the optimal r.m.s. deviation (σ) of the signal is $V_{th}/0.6$. It should also be noted that the signal degrades by only 5% from this optimal value if power changes by up to 40% (see Fig. 2.10). Thus we have tuned our samplers so that all the V_{th} s are between 0.6 and 0.7 σ .

To avoid sensitivity to threshold asymmetry one of the input signals to any correlator is switched with orthogonal waves (Walsh Pattern switching in our case). The sampler asymmetry is thus averaged out. If threshold asymmetry is not taken care of, there will be a DC offset in the correlator output. The switching was introduced to solve this problem, it also removes spurious pickup from along the signal paths.

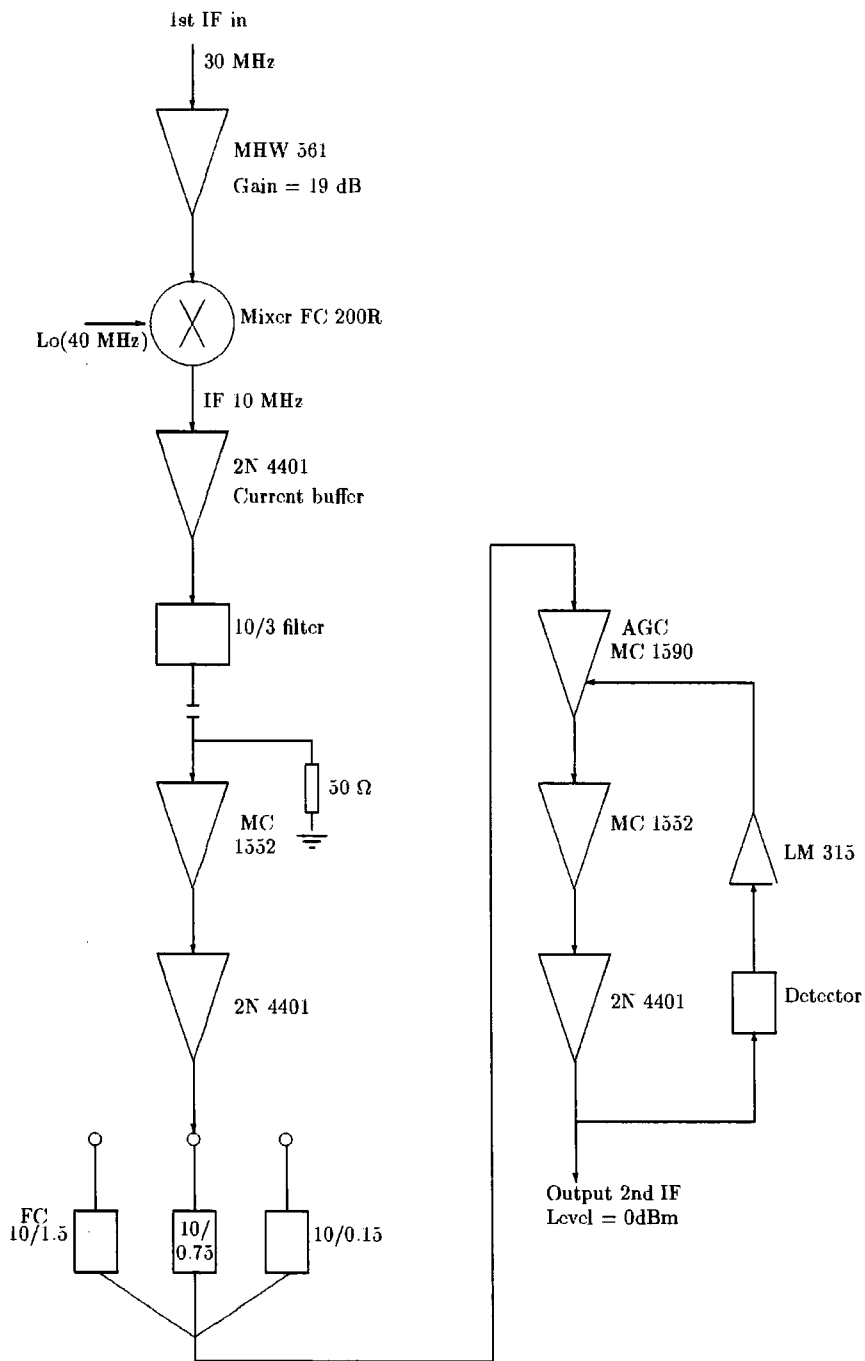


Figure 2.9: Second stage mixer module, adapted from the CLRO module

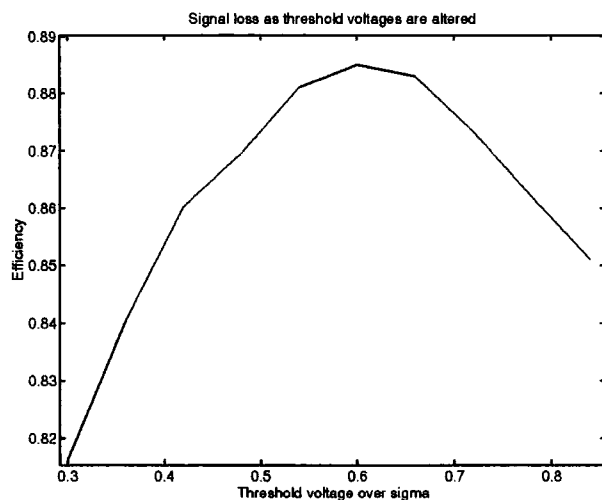


Figure 2.10: Change of signal recovery efficiency with V_{th} for a two bit three level correlator, From Bowers 1974

2.2.9 The 1088 channels correlator

The correlator has 512 complex correlators (1024) plus 64 self correlators. It is distributed in such a way that one can correlate 32 channels with 32 channels and monitor the self-correlation of each channel. The 16 channels on one side are quadratured before transmitting to the correlator. This gives one the complex correlations (see Fig 2.11). The basic correlator system and samplers were designed to work at 12 MHz. Data can be integrated within the correlator system in steps of 10.9 ms by 2^n . If the user decides to integrate only up to 10.9 ms then the 1088 channels (each 2 bytes wide) have to be read in that time, meaning a rate of 200 kbytes s^{-1} .

Before the digitised data is sent to the correlators they are sent to delay boards (whose delays can be programmed in) where appropriate delays are given to each of the 48 channels.

The correlators are distributed on 64 boards with the basic correlators being the custom made chips VLA1 and accumulators VLA2 (each board having 16 cross correlators and one self correlator). Each board is controlled by a microprocessor (the Rockwell 6505). The first 2^{13} clocks are integrated on the VLA1 and VLA2 combination and then the microprocessor continues the integration in its RAM for an integral number of times. It works on a double bank system, i.e while the microprocessor is integrating data from the VLA2's on one bank of RAM the other is made available for reading by

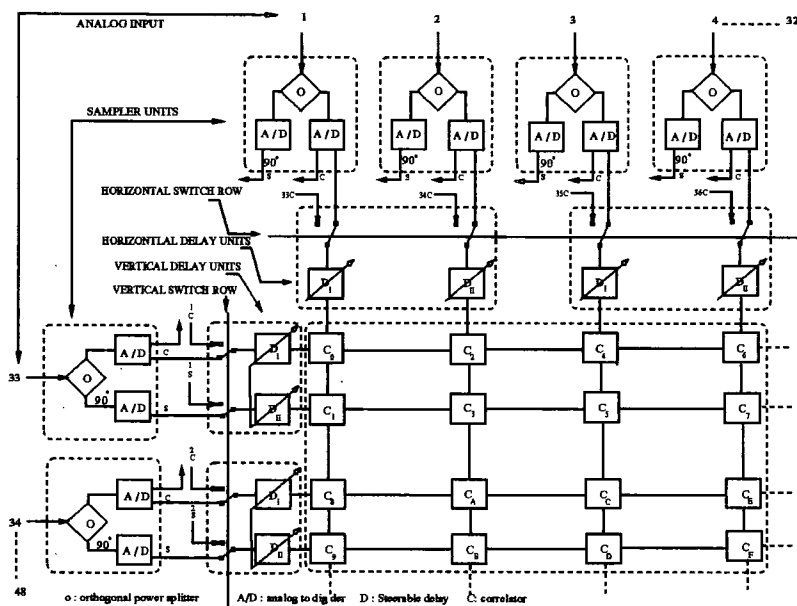


Figure 2.11: The MRT/CLRO correlator; a schematic matrix showing 32 real and 16 complex signals being feed into the correlator array.

the acquisition PC.

This machine can be configured to correlate the E with the EW (NS fan beam mode) or to correlate the NS with NS+W (EW fan beam mode) or to correlate the EW with NS (pencil beam mode). These can be selected by choosing which sets of signals goes to which side of the correlator matrix. The latter is the mode which is used for the MRT sky survey. But the first comprehensive data collection was done in the NS fan beam mode so as to make a 1D map of the sky.

Before any typical observation the correlator system has to be programmed (which is done by the acquiring PC) with the integration time of correlations in the machine, the delay settings on each channel and the mode of observation. These can be dynamically changed while observation is going on, even to the extent that each integration has a different configuration.

2.2.10 Data collection and storage

The limitation of integrating on the correlator boards RAMs is that each correlator only has enough memory for 16 bits of storage but with truncation it is equivalent to a 20 bit storage. One should not allow this to overflow, but this would only occur for highly correlated signals. If one operates at 12 MHz then one can integrate to a maximum of 43.6 ms (2^{19} clocks, plus one bit reserved for sign) the correlator system. Thus one has to read the data that are 1088×2 bytes in 43.6 ms which is 52 kbyte s^{-1} . To acquire this one needs a piece of hardware which collects it and integrates 25 times (to 1.095 s)⁶ before making it available to the computer for storage (Rughoobur, 1996). Again a double bank system is used, while data are being collected and integrated every 43.6 ms on one bank, the other bank is made available to the computer for file writing. The data are taken by the collecting PC and is sent via PC-NFS to the hard drive of a Unix station. There every 24 hours of data or so is transferred to 8-mm Exabyte high density tapes. Various programs are run on these data, now visible on the local network, for checking, analysis and processing.

2.2.11 The Walsh switching

The standard way to remove spurious common pickup on different channels is the Walsh switching technique. One of the signals to any correlator is switched at two different places between which cross talk or common noise

⁶these figures are for the system before introducing the recirculator, when the clock was changed to 10.625MHz and the number of acquisition PC integrations to 22 to give 1.089 secs.

pick up is occurring. The switching period has to be smaller than the integration time by at least a factor of two, making the common pickup signals to correlate half of the time positively and the other half negatively, which thus causes them to be averaged to zero. This works if the signals from both channels are switched with any orthogonal waveform. These Walsh functions are just such a set of orthogonal functions.

At MRT we have found that most of the pickup and/or crosstalk occurs after the making of the first IF. So it was decided to switch the LO signal itself which will produce a switched IF. The second switch is at the sampler after digitising. As mentioned earlier any spurious signal on the LO path will get switched twice before going through the correlators.

The LO is distributed separately to the three arms, where it is picked up serially. All the Eastern arm signals are left unswitched, the Western arm signals are switched by a square wave of 5.45 ms period and those of the Southern arm with a wave of 10.9 ms period. Figure 2.12 shows the fringe pattern on a 1km and a 2km baseline produced after switching was introduced. With this set up only cross correlation between different arms are free of pickup. However, for the map, one is only interested in the South arm crossed with the West and the East. The East to West and East to East correlations can be used to deriving closure values during the calibration, the East to East is not switched in this arrangement, and thus have poor signal quality. This is discussed in section 3.7.

2.2.12 The recirculator

We are using rather large primary beams as well as large bandwidths in the MRT telescope. This leads to signal de-correlation on longer baselines for signals away from the zenith. For a square bandpass of $\Delta\nu$ MHz the signal correlation between two paths falls as a sinc function with delay, Δt .

$$\text{Fractional signal loss} = \text{sinc}(\Delta t \Delta \nu) \quad (2.3)$$

The first null comes at $\text{sinc}(\Delta t \Delta \nu) = 0$; that is, at a delay of $1\mu\text{s}$ per MHz, we lose all signal. More importantly the signal fall off becomes significant well before this delay. There is a ten percent loss after only $0.24\mu\text{s}$, or only $\pm 8^\circ$ from zenith with a baseline of 500 meters and a 1MHz bandpass.

To cope with this problem it was decided to acquire the data in separate zones for these larger baselines. Each zone would have delay settings such that the correlation maximum was in a different point (in altitude) on the sky, and these pointings would cover the primary beam, with a maximum signal loss of 10% (Sachdev, 1997).

To avoid the problem of taking four times longer to run the observation a totally new acquisition system was built. The data sampling was cut by

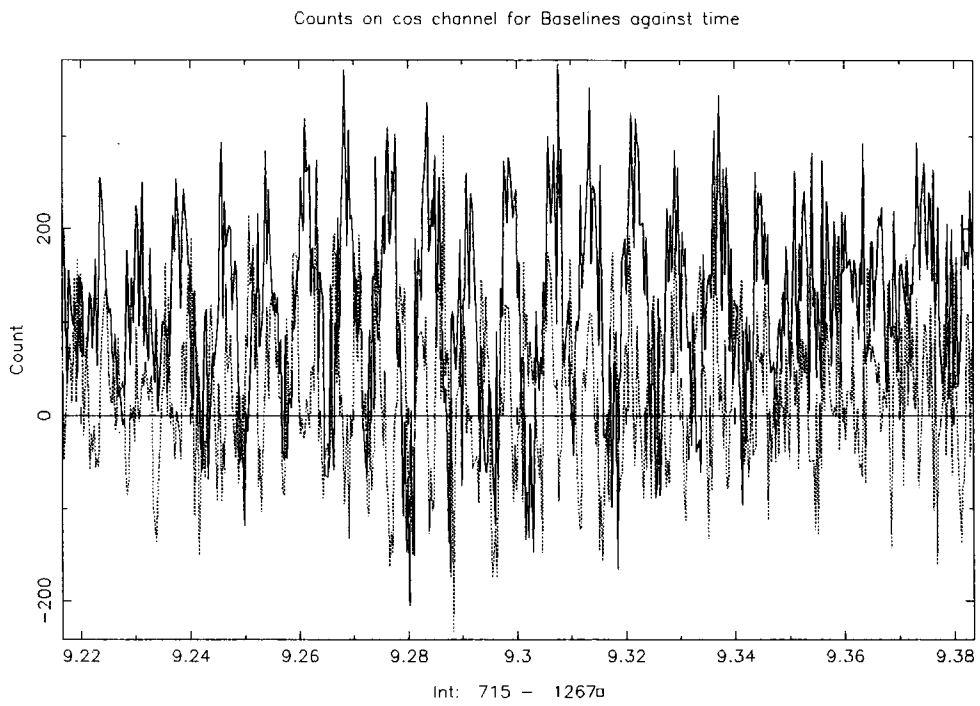


Figure 2.12: Fringes from the transit of Hydra A, with a 1km and 2km EW baseline

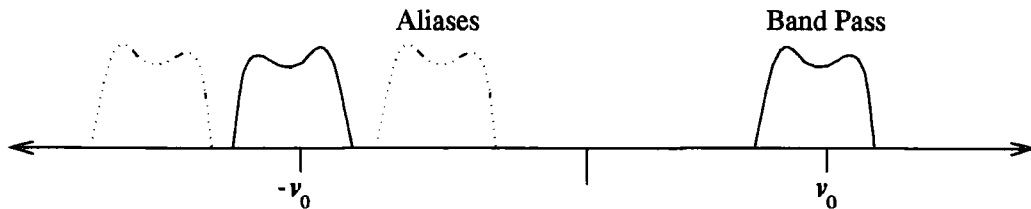


Figure 2.13: Signal recovery with the sampling lower than the carrier frequency.

a factor of four, and in each cycle four new delay setting were written to the correlator boards. These delays were such to position the phase centre in four widely separated positions on the sky. How is that we can get away with cutting the sampling frequency to below twice the highest frequency contained in the signal? For any signal of a certain maximum frequency ν_m there is no point in sampling over the Nyquist rate $2\nu_m$. We however are attempting to characterise a signal with a small band pass, on a high frequency carrier wave, with a sampling rate appropriate to the bandpass. To achieve this the sampling rate has to be carefully chosen so that non-zero multiples do not fall on any translate of the band or its reflection. This is represented in figure 2.13. This was done in MRT, both theoretically, and practically by checking the autocorrelation of the signal (done in the same correlator) to ensure that there was no aliasing and resultant signal loss. (A small aside: we do in fact lose signal to noise, but this is in the 2 bit 3 level sampling within the correlator. The signal lost in digital sampling is a function of the excess over Nyquist. In going from 6 times to 1.3 times over Nyquist we lose only 6% of signal. That is at 6 times Nyquist we have a 88% efficiency (compared to analogue) and at 1.3 times this has fallen to 82%. (D'Addario et al., 1984))

The recirculator resamples the data, or more accurately samples and holds the same sample for four ticks of the clock, so the same datum is shown to the correlator for all the zones. The original sampling frequency, before the recirculator, is 12MHz. The band width is 1MHz; therefore we can reduce the over sampling to 2MHz. We reduce the sampling by four times and reduce the clock speed to 10.625MHz, i.e. giving a sampling of slightly more 2.65 MHz.

The setup within the correlator therefore remains largely unchanged, the data is integrated as before then passed on the Data Acquisition System (DAS). A reduction of the acquisition data rate was imposed by the

upper limit of the rate for writing to the disk over the network by the DAS. The data size was reduced from 8 bytes to 4 bytes and the clock speed was brought down. The smaller data size was acceptable as we now only integrated the VLA2 values (2^{13} cycles, with the sign to make 2^{14} bits, and the two least significant two bits being discarded) in the processor on the correlator board for one fourth of the time used previously, i.e 2^4 cycles. This gives a 2^{16} maximum value, which is the byte size of a SHORT or INT*2 variable. This meant that we could use this variable size and only have integer overflow on self correlations counters for the group, as only they consistently give near maximum values⁷. However as we know the self correlation must be positive so we can use an unsigned integer for those particular values (and only those). Furthermore we discarded the final few bits on these as we know that the correction needed to convert a 2 bit 3 level value to the analogue equivalent is not terribly sensitive to the self correlation value.

The actual clock frequency had to be carefully chosen as with the clock-splitting (done within the DAS (Sachdev, 1997)) harmonics started showing up in the signal channel. We are forced to reduce rather than increase the clock frequency as the DAS could not cope with a greater speed, and the value settled upon was 10.625 MHz. The harmonics from this falls around the observing band centres.

The DA-PC integration was altered from 25 to 22 to bring us as near to the same acquisition rate as before as possible, but it we still find ourselves with two sampling rates. How this is dealt with is covered in the software section. It requires two regimes, each with the different sampling, in map making with the combination in the map domain after (Fourier) resampling.

Post digitisation each signal is stored in a memory and recirculated in the existing correlator to measure the correlation with four delay settings.

⁷The theoretical value for a self correlation in a 3 level 2 bit machine is 2/3 of the maximum.

Chapter 3

The MARMOSAT Suite: Programs for the Mauritius Radio Telescope

As soon as we started programming, we found to our surprise that it wasn't as easy to get programs right as we had thought. Debugging had to be discovered. I can remember the exact instant when I realized that a large part of my life from then on was going to be spent in finding mistakes in my own programs.
– Maurice Wilkes discovers debugging, 1949

3.1 Introduction

The principal aim of MARMOSAT, The MAuRitius Minimum Operating System for Array Telescopes, is to provide a link from the back end of the Clark Lake Correlator to the vast number of highly developed astronomy packages that are available. To this end we have collected together routines and methods from a variety of sources and maintained them as a separate set. These programs use the approaches that we have chosen as natural for our particular problems and strengths. Most of the documentation of the work is not appropriate for a thesis, and examples of usage are in the MARMOSAT documentation directory and also in the appendix A. The aim of this section is to provide a description of the concepts behind the MARMOSAT suite. Illustrations of the results are given in Chapter 4.

The Raman Institute's experience when designing the GEETEE telescope led to the realisation that the software needs to be developed in concurrence with the hardware. So it was that in 1991, even as the MRT correlator was being put through its first tests, the software was also begin-

ning to take shape. The original form can no longer be seen in the present setup, but it can be found deep in the code. Most of the development of the software was done during my three six-month placements at the telescope site in close collaboration with the hardware engineers, with whom forceful discussion was expected and fruitful.

Unlike most other packages, the MARMOSAT suite has the limited design intention to be no more than a front end to give access to the other larger (and better supported) suites, such as AIPS or IRAF. It is loosely organised, so that it is very easy for different operators to add new programs for their own particular interest (e.g. the pulsar observations being done at 150MHz), with many **#defines** used for those system variables that might be altered. MARMOSAT consists of separate programs which communicate via standard data files, rather than having all possible operations integrated into one huge program or kernel. This is the approach successfully taken by Unix. It has some disadvantages in that tasks often require a script to chain together several programs, i.e. it is difficult to run the programs 'blind'. On the other hand whether this is truly a disadvantage, in that it is a good idea to be able to use programs without knowing what one is doing, is debatable. The reason that this approach is becoming more common in many applications because of its increased flexibility and ease of maintenance.

3.2 Tasks that MARMOSAT has to accomplish

3.2.1 Documentation

There is no point in doing work if no-one uses it, and no-one will use it if they do not understand it. Thus the documentation is at least as important as the program. We have tried very hard to make sure that every program has copious comments at the start (in the source code) documenting all the changes and discussing the usage. The discussion tends to focus on the changes from version to version, rather than the grand plan but ensured the user was kept up to date with the system development. The task of this chapter is to provide that overview. Also minimal, but sufficient, comments are returned when run with the **-help** flag. Having the documentation built in forces the software and documentation to stay in step.

3.2.2 Data Management

The MARMOSAT suite must provide routines to convert the output of the correlator into the maps, and the first stage of this is to check the huge stream of data that is being received continuously. We need to detect gross errors quickly as the original approach of a daily visual inspection of the

output of the previous night's data led to the loss of too much observing time. These errors were usually malfunctioning components and therefore were easy to look for, either a loss of signal or too much signal. Two programs exist to tackle these problems, **online** and **health**. **Online** follows a few baselines in detail, **health** gives the scatter of all baselines from the mean, and as the data are stored on a distributed network disk both can monitor the signals as they are acquired. Details of their precise operation can be found in the relevant documentation.

3.2.3 Data Storage

As it became obvious that there was going to be several different machine architectures between the telescope site, Durham and RRI, we had to choose a standard data style. The (IBM clone) PC doing the data collection has an architecture called little-endian; i.e. the Last or Least Significant Byte in a number is High, (LSBH), as do the Digital Alpha's. The Sun Microsystem's Sparc used the opposite (MSBH)¹. The Linux O/S machines on which it was planned to do almost all our on-site data reduction are based on the IBM machines. Thus, to minimise the byte swapping on the smaller machines, the stored binary data files are kept as little-endian, and converted on the fly when working on the Sun machines. Most programs do, however, have a **-swap** and or **-bswap** option to override the default.

It was decided that the best way to keep track of the data files was to keep an ASCII header for each as a separate file. As much information as possible was put in these small universally readable files. Examples are the calibration files and interference files. To maintain a simple tracking system all names are standardised, and the software, knowing that name, can work out the date and the positions observed.

The header information could easily be added to the raw data file when it was time to pass to another stage, e.g. the output from the program transform gives the map file and a FITS (Payne and Hayes, 1995) style header. These can be concatenated² to pass to programs which read FITS files, such as AIPS.

The raw data, the calibrated visibilities and image file formats are binary, and use the C unformatted style. There are two reasons for this:

- Text files and files containing records are substantially larger and consequently take more time to read from disc even if the decoding is relatively cheap and space is not a consideration.

¹Most Significant Byte High

²% dd if=our-map.map bs=2880 conv=sync >> our-map.hdr

- It is not difficult to write software to convert freely between language and architecture formats.

3.2.4 Calibration of the signals

There is no independent calibration in MRT, so these results have to be derived from the observations. The major stages are;

- A approximate estimate of the (complex) gain on each baseline, after subtraction of the expected geometric phase.
- An improved estimate of the instrument gain by reducing each baseline gain to its two antenna based components.
- Corrections to the baseline positions by the comparison of the phases from different sources spread across the sky.
- Derivation of the effective band centres for each baseline from the phase differences as delays to prevent the decorrelation are introduced.

This cycle has to be repeated several times, and is covered in detail in later sections. Once done we can apply the gains to our collected data.

3.2.5 Generation of the Images

Once the instrument phases are known it is a trivial process to collate all the different files together then transform the calculated visibilities and produce the map. The relevant programs are **apply_cal** and **transform**.

3.2.6 Others

Various utility programs are needed, mainly to reformat files for other packages. All these are fully described in the MARMOSAT documentation called **marmosat**, reproduced in appendix A.

3.3 Recognising Spurious Data

With the MRT's extended observing periods problems are to be expected from terrestrial interference. The more modern instruments deal with these difficulties by rejecting those sub-bands that contain the source of interference. MRT is a broad band machine where the interference can only be detected from the correlation of the complete observed spectrum, and it is not possible to reject subsections of a band post-collection; the entire baseline has to be rejected. Furthermore there is the suspicion that if one baseline has detectable interference all the others may also have been affected.

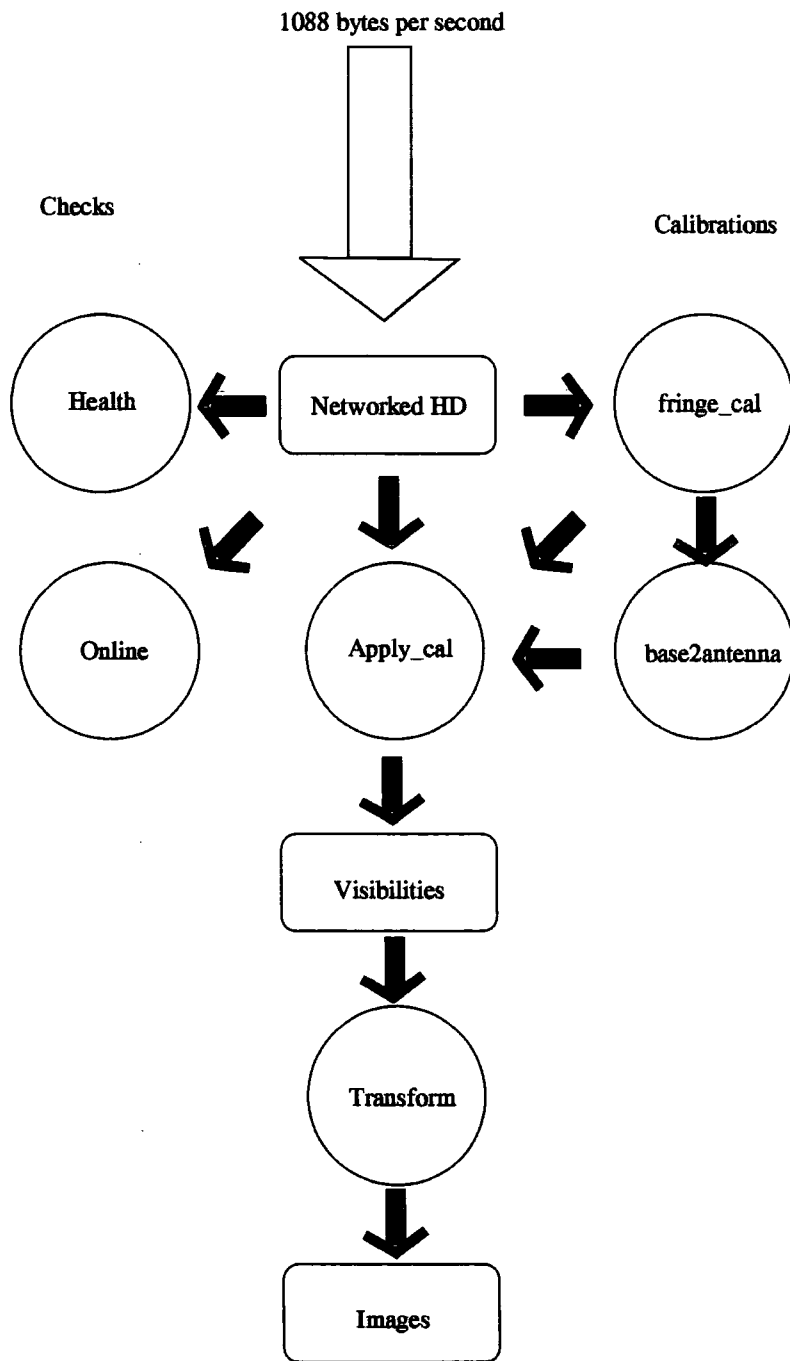


Figure 3.1: Flow Diagram for MARMOSAT

To ensure this is detected, the magnitude of all baselines are summed then transformed, i.e. we transform the total power of the transit instrument³. The reason for working on the total power is that the fringe frequencies due to the extent of the baselines are lost, and the only changes to be expected should be due to the passage of the source through the primary beam, which takes about $8/\cos(\delta)$ minutes between the half power points, i.e. a very slow change. Therefore if there is any sign of high power in high frequencies, i.e. a fast change in received power, we can be sure that it is not from the sky. The lower frequencies are blanked out, and the data is back transformed to identify the bad integration. Having back transformed only the fast changing integrations remain (convolved with the transform of the blanking function), and can be identified. The worst interference points are then removed from the original data and the process repeated until all bad sections are excised. The relevant regions producing this high signal are noted in a file, which all subsequent programs can access. This work was largely done by S. Sachdev (Sachdev and Udaya Shankar, 1995).

3.4 Coordinates

A list of the actual positions of the trolleys during the observations is recorded in the position file which is always named thus **pos*.xyz**. The coordinate axes chosen define its contents, and must be carried through into all subsequent stages. The units are assumed to be in metres along the different axes.

There has been a great deal of discussion, sometimes heated, over the most appropriate coordinate axial system. The compromise reached was to allow every possibility that anyone wanted in the software. While democratic, this has been one of the most common sources of error, where one stage of the calculations has been done assuming one convention, and the next using a different one. It is highly desirable to record the convention used within the file headers, and it is planned to do this in the future. The two sets are derived from the physical properties of the telescope and are shown in figure 3.2.

Note that in what follows 'arm' is taken along the telescope (as in 'NS arm') and 'line' refers to the line on the imaginary latitude and longitude grid, as in 'NS line'. "Zenith" is defined relative to the cross product of the NS arm and the EW line.

The properties of MRT are;

³This is not the same total power one would get if one was using a additively combined instrument, but the sum of the cross terms only. I.e. it does not include the self correlations that are naturally included in a *true* total power instrument.

- It operates as a transit instrument, and does not track the sky.
- The trolleys are regularly sampled along a track running NS. This is not quite horizontal, dropping at about half a degree for the first 700m then rising by half a degree for the remaining distance.
- The EW arm is nearly normal to the NS direction, but with the helices at elevations different by as much as 30m vertically, as shown in figure 2.4.

Given these constraints a very natural set suggests itself. Firstly the fixed coordinates are the earth based ones, i.e. these are unchanging with time and it is the sky that moves. The type I coordinate system is then;

- u along the EW horizontal line and normal to the NS arm.
- v along the NS arm and normal to the EW line.
- w the vertical, normal to the EW line, but not the NS arm.

Alternatively, a similar but not identical orthonormal set was used pre-1995, and called type II;

- u along the EW horizontal line and normal to the NS arm.
- v along the NS arm and normal to the EW line.
- w the normal to the NS arm and the EW line; ie a direction 0.5° to the vertical.

The advantages are;

- For type I. The baseline w coordinate is independent of v for the trolley positions.
- For type II. The axes represent the natural right angle coordinate system, which is more familiar for calculating transforms. Its main advantage is that is the usual coordinate system used by astronomers, even though it does not aligned with the sampling of the uv plane at MRT.

Because of disagreement on which of these two possibilities is the better it was decided to allow both. They are selected in the making of these positional files by the program **map**, the default is to use Type II, i.e. the w is defined as the normal to the plane, but if the flag **-tilt** is given type I is used.

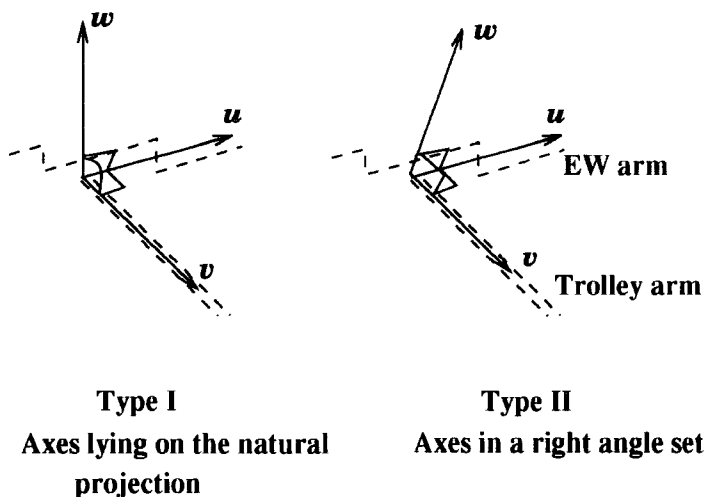


Figure 3.2: Two types of coordinate system in the MARMOSAT software. The tilt of the NS arm is exaggerated.

Type I is usually to be preferred as the user is rarely bothered with the method of transforming of the coordinates when there is a program that (semi) invisibly does it all; but it is possible to see occasions when the user might choose type II.

A consequence of the telescope coordinates being fixed is that the sky coordinates are treated as changing. It is trivial to show that the cosine directions, \vec{l} , are;

$$\vec{l} = \begin{pmatrix} \cos(\delta) \sin(\text{HA}) \\ \cos(\text{HA}) \cos(\delta) \sin(\delta_L) - \sin(\delta) \cos(\delta_L) \\ \cos(\text{HA}) \cos(\delta) \cos(\delta_L) + \sin(\delta) \sin(\delta_L) \end{pmatrix}. \quad (3.1)$$

where HA is the hour angle, δ the declination and δ_L the latitude.

3.5 Further remarks on transforms and the coordinate system

The telescope is sited in very rough terrain, and this has lead to the alignment of the arms being far from perfect. Many, if not most, of the difficulties which have had to been solved would not have occurred if a better site had been available. The feeling of the time, that the problems could be solved

post-factum, has been born out although all now accept that this would not be the way we would do it if we had our time over again. The relevance of the construction to the sampling is that the visibilities are taken along the axes of a non-orthonormal cube; the question that the software had to address is how best to correct for this, or even if it is necessary.

One of the few advantages for MRT over most telescopes is that the visibilities are taken on a regular rectangular grid, not quasi-randomly as for large arrays such as the VLBA or GMRT, nor regularly on great circles facing the pole, as for rotational synthesis instruments such as the CLFST. These instruments require the measured visibilities to be resampled onto a regular array, and this operation introduces yet another sampling function to the conversion of the visibilities to the image (equation 1.2). The corrections due to the irregular weighting (from the different numbers of samples near different grid points) and those of the relative contributions based on the distance these samples are from the grid point centre (Perley, 1989, Chapter 6 p123) are not required in our case. This vastly simplifies the deconvolutions of the images, which are the largest and slowest part of the software.

For a point in the sky in orthonormal coordinates the phase term is;

$$2\pi\vec{l}\cdot\vec{u} = 2\pi(lu + mv + nw) \quad (3.2)$$

where

$$n = \sqrt{1 - l^2 - m^2}$$

(after Thompson et al. (1986, Chapter 4))

For the same point in the sky in non-orthonormal coordinates the phase term is;

$$2\pi\vec{l}\cdot\vec{u} = 2\pi(lu + mv + nw \cos(\text{SOUTH_ARM_ANGLE})) \quad (3.3)$$

where the SOUTH_ARM_ANGLE is the tilt of the trolley arm from the orthonormal plane.

The uv coverage of MRT can be thought of as a pleated sheet, extended in both u and v , with discrete steps in w as we move from one EW group to the next. Furthermore as we are doing extremely wide field imaging of a degree very rare in other instruments (an instantaneous 60° field) the approximate approach often used is invalid. In this approximation the phase term due to the heights is assumed to be a constant as the n term in ($\vec{l} = [l, m, n]$) in equation 3.2 is very small (i.e. one is looking at sources near the center of the field). Thus for MRT a 3D imaging method was required, with all the attendant difficulties therein (Perley, 1989, Chapter 14). The major problem is that of relating a three dimensional visibility, $I(\vec{u}(u, v, w))$ to a two dimensional sky brightness $B(\vec{l}(l, m))$. The only way of reducing this

artificial three dimensional brightness (introduced as the reciprocal of the 3D visibilities) is to treat it as a *surface* (defined as where $n = \sqrt{1 - l^2 - m^2}$) in a 3D image *volume*. Three dimensional imaging can be thought of as attempting to force the surface in 3D onto a 2D plane. For small sections this is straight forward as the errors are small, but for wide fields these errors become very significant. What is done at MRT is to do a FFT along the regularly sampled v axis, apply a DFT to the w axis and finally sum along u - giving the zeroth Fourier term on this axis. A DFT on w is required as the sampling is not uniform so the fast Fourier technique can not be applied and a discrete FT is the only option. The discrete transform corrects every term along the m axis for the height of that group, phasing the terms to a common (and artificial) 2D plane. These comments obviously apply to all styles of axes.

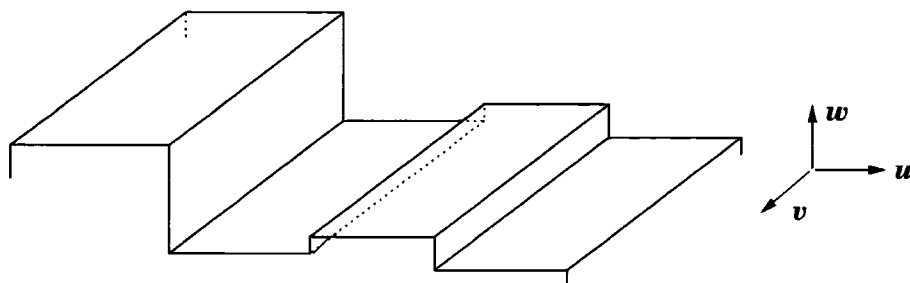


Figure 3.3: A representation of the uvw coverage at MRT

Therefore, as we were prepared to go to some lengths to avoid regridding, we looked at ways of using the sampling grid that we had inherited from the constructors. Consultation with the mathematical texts showed that this approach was common, and indeed standard in all those fields using reciprocal space.

A simple calculation count shows that the least intensive way to apply the correction is to apply it once to the constant in the calculation, i.e. the baseline, and use that in the phase shifting stage⁴.

Mathematically it does not matter how one calculates the correction, which is why type I and type II axes give the same answer. However there is no need to abandon our *actual* sampling axes to convert to an equivalent one, for which one has to assume that one knows apriori the SOUTH_ARM_ANGLE. By maintaining the files in the sampled domain one does not need to convert the files as the parameters are refined. Finally, it is planned to attempt to make deeper images of interesting regions of the map by imaging off axis (giving a possible reduction of $\sqrt{32}$ in the T_{sys}).

⁴This is the equivalent of course of using orthonormal baselines axes where an identical correction would have been applied to the axes from the first instant

While these ideas are speculative at this point in time it is likely that when the full three dimensional treatment is undertaken that this 'true' coordinate system will be even more useful.

3.6 Calculating the instrument phase

The baseline signal path described in section 1.5 and figure 1.5 shows how the instrumental delay, Φ , is introduced.

After the mixer has combined the voltages from the two different groups, and the correlator has integrated over many cycles the signal in equation 1.8 can be rewritten thus;

$$I_{ij} = G_{ij} \int B(\vec{l}) \exp[\Phi_{ij} - 2\pi\vec{l}\cdot\vec{u}_{ij} + 2\pi IF\cdot\tau_i] d\vec{l} \quad (3.4)$$

Where $2\pi\vec{l}\cdot\vec{u}$ has replaced $\nu\tau_s$, the delay from one direction on the sky. As before the instrument absolute gain is G_{ij} and the phase is Φ_{ij} . The delay phase is $IF\cdot\tau_i$, and the sky brightness distribution is $B(l)$, to give the observed visibility, for the baseline ij of I_{ij} .

The first approximate values for Φ (which includes $IF\cdot\tau_i$ at this stage) are obtained by the simplistic approach of assuming the sky is dominated by a single point source of known position. That is $\int B(\vec{l})d\vec{l}$ can be taken as an integral over a delta function at the source position \vec{l}_0 . From this we need to separate the free parameters, i.e source position (two parameters; RA and declination), baseline orientation (three parameters; u, v and w), and baseline gain (two parameters; phase and magnitude). The first program written, **phase_cal**, attempted to minimise all parameters together, but it was found that the signal to noise level was too low to do this with such highly correlated parameters. Nowadays all variables other than the gain are found from comparison of the gain from different sources.

The phase estimation is done after subtraction of the expected geometric phase. Assuming that the received visibility, I_{ij} , in equation 3.4 is of a single source at a position as a function of time, $l(t)$, in the sky then the observed phase of the signal is $\Phi_{observed}(t) = \Phi_{ij} - 2\pi\vec{l}(t)\cdot\vec{u}$. As \vec{l} and \vec{u} are known the instrument phase can be recovered. When the found Φ_{ij} is integrated over the primary beam it is insensitive to short term interference and other fringe frequencies (for example DC) if they are sufficiently well spaced in the frequency domain, because these contributions cycle in phase and when integrated sum to zero. This is because, normally, there is a 360 degrees rotation (in the geometric phase terms) of all baselines over the time that the source moves through the primary beam. This in turn means that the short baselines, in which this condition is not met, cannot reject other fringe

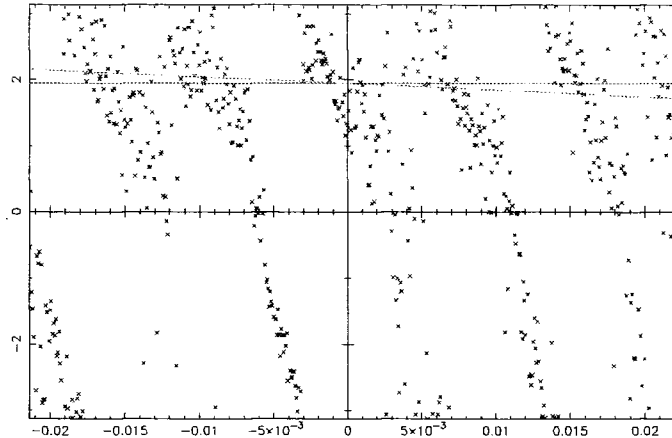


Figure 3.4: Rejection of confusing fringe frequencies in the `fringe.cal` program. Instrument phase is plotted against hour angle in radians

frequencies. How this is dealt with is covered later. DC is rejected by this procedure because the number of cycles over the time the source is in the beam is exactly the number of groups separating the two ends of the baseline (as the size of one group defines the time within the beam) The action of rejecting can clearly be seen for the E1 to E15 baselines to E16 which are measured to give closure phases for the short baselines. E to E16 are on the same LO arm so are not switched, and have high DC pickups. Figure 3.4 shows the instrument phase as Hydra transits the primary beam when the DC levels are high for TJD 10001. The baseline is E12 to E16 so the DC is cycled 3 times over the primary beam.

3.7 Improving the calculated calibration

Baselines gains, G_{ij} , are really combinations of antenna gains, G_i , plus an individual baseline offset.

$$G_{ij} = G_i \times G_j^\dagger + O_{ij}; \Phi_{ij} = \Phi_i - \Phi_j + \Theta_{ij} \quad (3.5)$$

Obviously if we can reduce the number of unknowns, for a fixed amount of information, the standard error will be reduced. More importantly the gain for the short baselines cannot be resolved because of confusion between sources; they are too short to allow discrimination between the fringes from

our calibrators and the rest of the sky. Thus a large effort was put into removing contributions to the calibration which are derived from the baseline, after which we can get the individual antenna gains, and recover all baseline gains including the short ones. The offsets were mainly the DC levels due to cross talk between cables as they are delivered to the observatory building. These were removed with Walsh switching and have been shown to be zero by removing the sky contribution while keeping all the electronics live (Golap, 1996). The baseline dependent contribution is that due to the $IF\tau_i$ term in equation 3.4. As covered in section 2.2.12 the acquisition is run with four zones, each with a different delay, to compensate for the bandpass decorrelation. Each zone steps the delay by an extra clock cycle. Each bandpass, one per group, imposes its filter characteristics, i.e. phase and magnitude for each, onto the transmitted signal, these characteristics cannot be reduced to a single number. Thus the correlated cross product of each band pass is individual to the baseline, that is, when the delays are introduced each baseline acquires an error which cannot be reduced to an effect due to the antennas. Fortunately the bandpass values are well determined as they are stable over many days, so we can integrate to reduce the errors. The differences from one zone to the next are not a function of any of the other unknowns, as the two measurements are made at the same time and position of the same sky. Therefore the corrections to the errors in the bandpass centres are tractable.

The program **base2antenna** solves for the above equation, in terms of the baseline gains, to reduce them to antenna gains. Weiringa discussed the recovery of gain magnitudes in *The use of redundancy interferometry - A comparison of redundancy and selfcal* (George, 1991), however there was no discussion of phases. This (presumably) is because the phase case is more complicated. If one has some degree of redundancy in the observations as shown in figure 3.5, and one assumes that the sky is dominated by a single source⁵ the gains of the short EW baselines can be reconstructed from the longer ones, and where there are several measures of the same phases the errors on the estimates can be reduced.

A simple least squares fitting of unknown parameters to a system with a greater number of equations, or observations, can be done a number of ways. We chose to use Single Value Decomposition (SVD) (Press et al., 1992).

In principle there are a number of equally valid methods to extract the least squares solutions for an overdetermined system of equations. The advantage of SVD is that the eigenmatrix⁶ of solutions is constructed with the magnitude of each eigenvalue representing the confidence with which one

⁵equivalent to the closure phase being zero, but I do not want to get into that

⁶Strictly the eigenmatrix is only the description of the square, just determined, system. I have stretched the language to cover all shapes of matrices

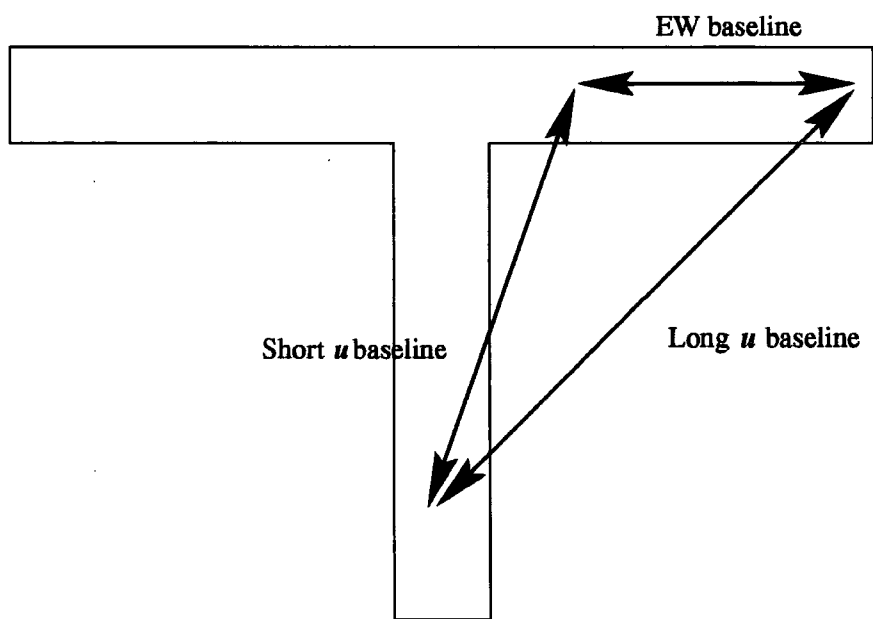


Figure 3.5: Closure baselines on MRT, allowing the gains of the short EW baselines to be covered

can separate this parameter from the others. If one has infinite precision this ratio, of the largest to the smallest value, is immaterial; when working within machine limited precision it is the most common source of error. If, say, one wanted to separate the parameters from a combination of two numbers and the ratio of the second to the first was less than the machine accuracy then one could not recover it. No method can overcome this, but looking at the ratio of the largest eigenvalue to the smallest gives an estimate of the problem. The program where this is of issue, **base2antenna**, checks this ratio and, if out of range, identifies the dubious baseline; then stops.

For the gain magnitudes it is straightforward. The logs of the power combine additively.

$$\log(|G_{ij}|) = \log(|G_i|) + \log(|G_j|)$$

while

$$\Phi_{ij} = \Phi_i - \Phi_j$$

which becomes for many baselines;

$$\Phi_{ij} = \bar{A}_{ij} \bar{\Phi}_i \text{ where } \bar{A}_{ij} \text{ is;}$$

$$\bar{A} = \begin{pmatrix} 1 & \cdots & 0 & -1 \\ \vdots & \vdots & -1 & 0 \end{pmatrix}$$

We invert \bar{A} , and multiply this with $\bar{\Phi}_{ij}$ to obtain $\bar{\Phi}_i$.

The phase case is not strictly linear as $\Phi_1 + \Phi_2 \neq$ measured Φ_{1+2} if $|\Phi_{1+2}|$ is greater than 2π . Therefore we need to make a rough estimation of the phases and then, with these values subtracted out do the least squares fit on the residuals. Assuming the maximum difference between the rough estimate and the final values in any of the phases is less than $\pm\pi/2$, we do not need to worry about the cycling over 2π .

The individual baseline effects need to be removed before this calculation can be done. Given that the Walsh switching removes all the baseline pickups from the cables and the correlator we only have to be concerned with the phases from the delays. The introduced phase is $IF\tau_i$, so it is easy to compare one zone to the next, each of which has one extra clock cycle of delay added to the signal path for the NS trolleys. Thus this phase difference can be subtracted from the baseline phase before solving for antenna phases, then added back afterwards. It was found that the errors introduced by not doing this are minimal, all within 5° .

3.8 Further improvement of the calibration values

As previously pointed out the calibration routines could not discriminate between some of the variables that contribute to the geometric component

of the instrumental phase. This is because the terms for errors in position and errors in direction to the source are highly correlated. Therefore we have to use different sources to differentiate.

These variables are separated by comparing different sources for each trolley positions. As the day to day variation of the phase on one source are small we can assume the phase remains the same for fractions of the day. Using the catalogued source positions means that the difference of the phases from two different (widely spaced in declination (δ) or zenith (Z)) sources are directly related to the errors in the trolley positions.

The errors are the differential (between source 1 and 2) of the phase terms in equations 1.3, 1.8 and 3.1 i.e.;

$$\Delta\Phi = \frac{2\pi}{\lambda}[(\cos(Z_1)-\cos(Z_2))*\Delta w+(\sin(Z_1)-\sin(Z_2))*\Delta v+(\cos(\delta_1)-\cos(\delta_2))*\Delta t u] \quad (3.6)$$

The sources available for these calculations were limited as the only strong point sources (to our resolution) in our field of view (-10° to -70°) were PKS1932-46, PKS2152-69, Hydra (PKS0915-11) and PKS2211-17. The source PKS2152-69 began to resolve when we reached baselines of the order of 200 meters. It was only useful for confirming the errors in the shorter trolley baselines and the timing. In this area the source Cygnus A also appears in the observed visibilities, and could be used. PKS2211-17 also resolved, and this left only Hydra and PKS1932-46 as truly ideal sources. However these two have nearly equal and opposite zenith angles, so we could not extract the w component. Thus a combination of sources were used, each to identify one type of problem.

The first correction necessary was that to our clock at MRT. Due to an unfortunate oversight for much of the observing period the program that converted the local time to Sidereal time assumed that our position was some 12 miles out to sea, equivalent to a 54.1 second error. The option to make a time correction was therefore introduced to all programs (**-dt [n secs]**). This error was found by studying the phases across the EW arm, as the phase difference is a function of u and is easily spotted as shown in figure 3.6.

Further study of the EW arm forced us to conclude that it was not straight. The plot of $\Delta\Phi$ with sin of zenith angle showed that the western end of the array had a twist. These values were most clearly shown by the first few trolley positions, where other sources of error were not significant. Here also Cygnus A could be used as a source as it was not washed out by the bandwidth decorrelation. It was found that the EW arm curved round to the south at the western end. Our attempts to repeat and improve the

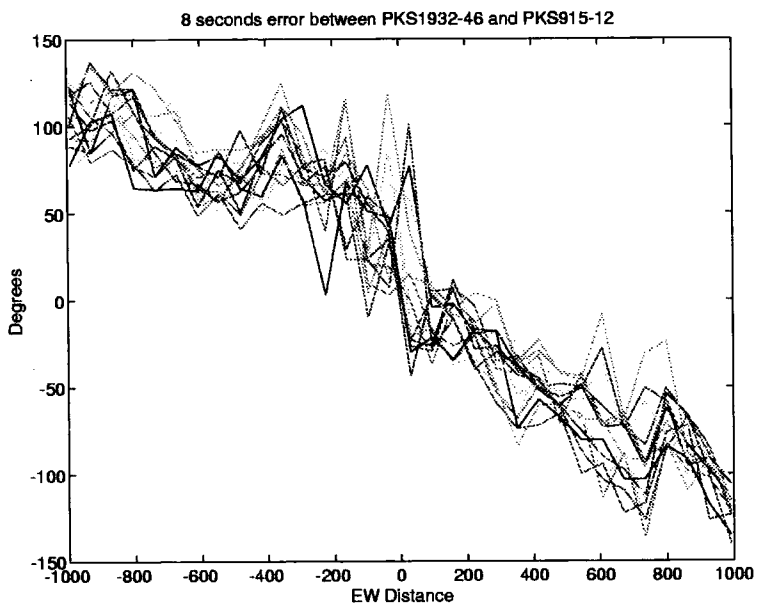


Figure 3.6: A typical 8.5 second time error showing up as a phase error along the EW arm

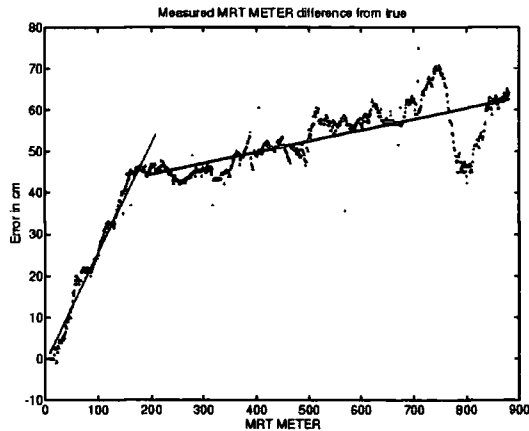


Figure 3.7: The MRT_METER measured directly

surveying were equally inaccurate. With a theodolite accuracy of about 0.1° it is not possible to get better than $\lambda/20$ on any baseline longer than 60m.

We also found that for the first 200 meters the separation of the trolley positions was not a meter but 99.7 cm. This separation, defined as the MRT_METER, was included in the software as a variable. After 200 meters the MRT_METER was found to change to 99.9 cm. This observation was deduced from the source to source phase differences, and has been confirmed by direct measurements. See figure 3.7. This means that the sampling in these two domains is different and thus each has to be mapped separately then resampled to a matching $\Delta \sin(\delta)$. This is trivially done with the program **resample**.

The tilt of the trolley arm, SOUTH_ARM_ANGLE, has to be derived and this also comes from source phase differences. However this method is limited to those regions where there are other sources apart from Hydra and PKS1932-46. These two have virtually the same value of $\cos(\text{zenith angle})$, and the phase due to height errors is multiplied by the difference of this value (see equation 3.6). At the price of an increase in the signal to noise the partially resolved source PKS2152-69 can be used. Firstly the phase remnant of PKS2152-69 is compared to either Hydra or PKS1932-46 with the current best guess for the trolley positions. We assume that anything that is non-uniform is due to the intrinsic source phase variation, and that the average is due to the extra z component from the SOUTH_ARM_ANGLE. This is now measured directly using the column height of water in the telescope's garden hose.

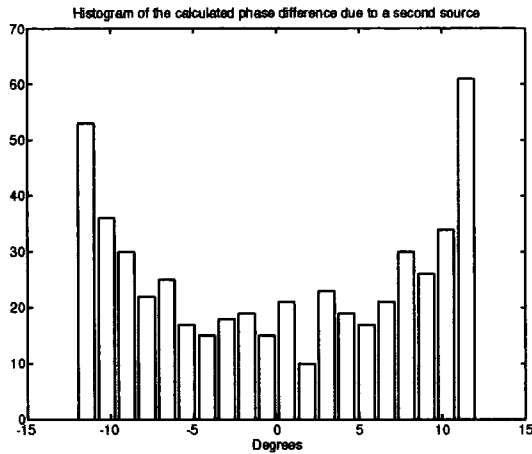


Figure 3.8: The theoretical phase difference when PKS1929-45 is a quarter of the strength of PKS1936-46

It was found that there is another source very near to PKS1932-46, therefore the programs were adapted to calculate the phase due to two or more extra sources in the same primary beam of known relative strength. In our case we do not a priori know what this ratio is, but by extrapolation from other frequencies we would expect it to be about a 10^{th} of that of PKS1932-46. Investigation showed that the phase error due to the second source would always be small, and that it would therefore be insensitive to the actual ratio. We plot in figure 3.8 the phase errors associated with a modelled second source a quarter of the brightness of the first, at a very similar declination and slightly in front. The positional values are from the source that cause us to consider this problem, PKS1929-45, separated from PKS1936-46 by only $44''$ in declination.

We were very conscious of the dangers of confusing the contributions from the different sources of the errors. Luckily the three bright sources, Cygnus, PKS1936-42 and Hydra span the declinations of the sky well and where observations of all 3 can be used we can be quite confident of the corrections. The distances down the S arm where there are large decorrelations to the Cygnus source are not so well determined, and we trust that there is not a radical change in the sources of error.

The position refinement was joint work with K. Golap.

3.9 Applying the calculated calibration

The program **apply_cal** takes the precalculated gains and applies them to the raw data. It unravels the raw numbers in the data files and produces visibilities organised into u and v . There is one file for each u position, i.e. each EW group. This file has the correlations with the trolley Φ s organised by the v index. Thus the corrections for height (associated with each EW group or u value) are kept as further correction for a later stage, in **transform**. It works with one data file after another in a linear fashion, building up the v coverage. Thus it needs the position file associated with each data file. Data flagged as bad is replaced with equivalent good data (where available) at this stage.

3.10 Transforming from visibilities

The previous stage produces the uv visibilities from the raw correlator data. These need to be transformed into the map. The corrections for the non-coplanarity are most easily included at this point. **Transform** accepts the height separated files from **apply_cal**, transform each strip, then phase-shifts each set to a common declination plane before co-adding to get the transit response. This is equivalent to a 3D transform in the sense that the final stage is producing only the zeroth Fourier term; the sum of the components.

The most crucial part of transform is the height correction. This can be equally well be done with a 3D transform with non-orthogonal axes - or a 2D transform with geometric corrections. These are equivalent, and seem to the equally robust to rounding errors. The program has the option of following either route for this. I feel that the more symbolic way of looking at u, v, w will make it easier if we try to do any real 3D transforms. In any case it makes no difference to the program.

The virtual plane to which all strips are shifted is along the trolley ground planes, parallel to the rails. After the separate strips (in u) have been corrected they are added together with the weight given in the **map2height** produced height list. This is now the raw map.

Chapter 4

Our Maps

4.1 Introduction

This chapter presents the 24 hours map constructed by Golap (Golap, 1997), and limited sections from the maps made at Durham. The software discussed in the previous chapter was used to produce these, except for one difference for the 24 hour map. As this map is limited to a 15' beam size only the central EW groups were used. These have a larger HPBW so the integration could be longer. Thus this map does not suffer from sections of missing data as did the map produced in Durham (with a beam size 4' by 10'), nor did it have the difficulty of having two sampling regimes.

The Durham maps made use of data collected between TJD9550 (July 1994) and TJD10055 (December 1995), covering trolley positions at a minimum of 2m from the EW arm to 350m from it, giving sensitivity to angular scales from 4' to 50° in RA and 10' to 25° in declination.

The broadscale maps, as they are in the natural coordinates (RA and sin of zenith) will show the errors most clearly. These faults are the interference lines that score across the sky at one RA, the sweeping multiple images of the Sun which occur around the equinoxes, and the conventional sidelobes. Discussion of the treatment of these problems will come in the conclusions.

4.2 Phase stability

The first tracer of our data is the comparison of the instrument phases derived from our stronger sources. These sources are Hydra A, PKS1932-46, PKS2152-69, and PKS2211-17. For the short baselines where decorrelation is not a problem Cygnus A is also useful.

4.2.1 Day to Day Phase Differences

The phase from day to day (for the same source) was found to be very stable; figure 4.1 shows typical values for the phase of PKS1932-46 between TJD 00199 and 00198. The RMS phase difference is 10° .

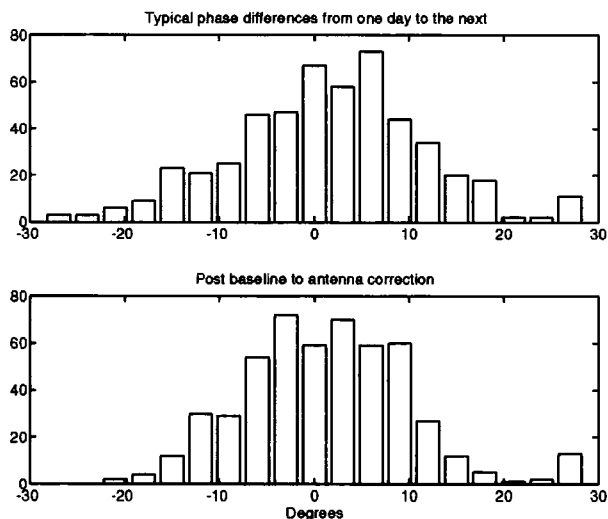


Figure 4.1: Phase differences for the calibrator source PKS1932-46, both before and after passing through **base2antenna**

4.2.2 Source to Source Phase Differences

The phase stability on the sources means that we can assume that the instrument phase is unchanged over the day. Therefore the phase difference between sources observed on the same day can be used to determine the positional errors.

Timing Errors

Equation 3.6 has a dependence of $2\pi[\cos(\delta_1) - \cos(\delta_2)] * \Delta t u$. When the phases of two sources with different declinations are compared an error in the clock at the telescope results in a phase gradient across the EW arm. Thus it was simple to separate this error from those due to errors in v and w . A typical error of 8.5 seconds was shown in figure 3.6, and timing errors for all observing days are shown in figure 4.2.

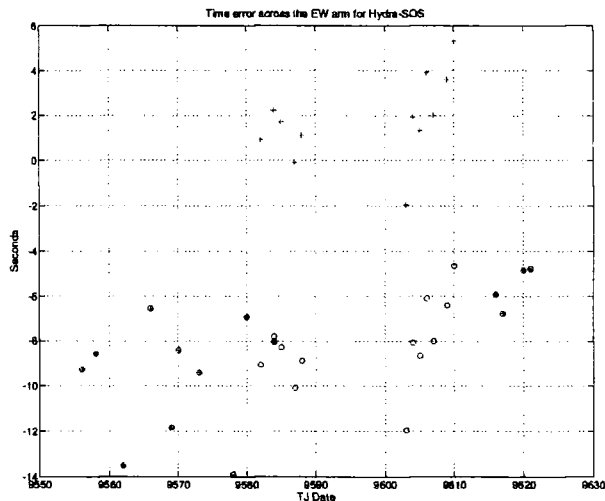


Figure 4.2: Time errors found for the first 100 days of observation

Positional Errors

Once the timing errors have been removed the relative positions of the groups can be found. The errors were from two main sources; there are fixed errors such as the curve of the EW arm and the height of the trolleys and there are cumulative errors, such as the SOUTH_ARM_ANGLE and the MRT_METER. Both of these need to be separated on the basis of the dependence of Zenith angle. The w errors will be a function of the difference of the cosine of the zenith angle, and the v errors a function of the sin. As MRT is a transit instrument errors in the sampling along u are hard to detect, but equally they have little effect.

The final positional errors are all less than 10 cm, with 95% less than 5cm.

4.2.3 Zone to Zone Phase Differences

Finally the introduced delay when recirculating ($IF\tau_i$) is found by comparing the measured phase from sets of data from adjoining zones, as in figure 4.3. Comparison of the phase differences over many days shows that this is very stable, but it will change when the filters themselves are swapped. Therefore the same values are used as long as there is no sign of changes, after which the new set of values is derived and used.

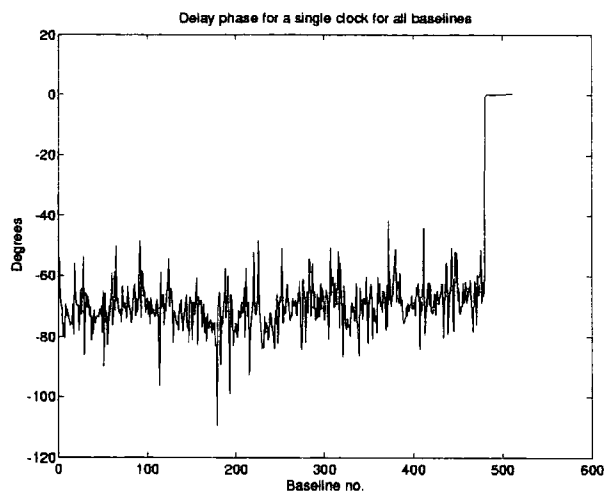


Figure 4.3: Delay phases for zone 1 to zone 2, for Hydra on TJD10022

4.2.4 Improvement of phases by Base to Antenna reduction

Having removed all the baseline dependent contributors to the phases we can reduce the baseline phase to the antenna based phase (section 3.7) and recover the short baselines and improve the signal to noise on the others.

4.3 Other unexpected errors

When the maps were first made we found peculiar features in some of them, using data collected around the equinox. The significance did not strike us at first.

The extraneous features looked like satellite tracks in the sense that they had the six fold repetition across declination which is typical of an event that lasted only a day, owing to the sampling. Yet over several days the same source was to be found in different, but nearby, positions in the sky and could not be understood in term of any likely source of emission. The source took nearly an hour to transverse the primary beam and this implies a declination of 80° . We eventually solved the problem when we realised that, at the equinox, the Sun would set exactly on the Eastern horizon, where the sampling response for a separation of 1.01λ (forced by the paging system introduced after construction) gives a broad lobe above the horizon. The effects are shown in figure 4.4.

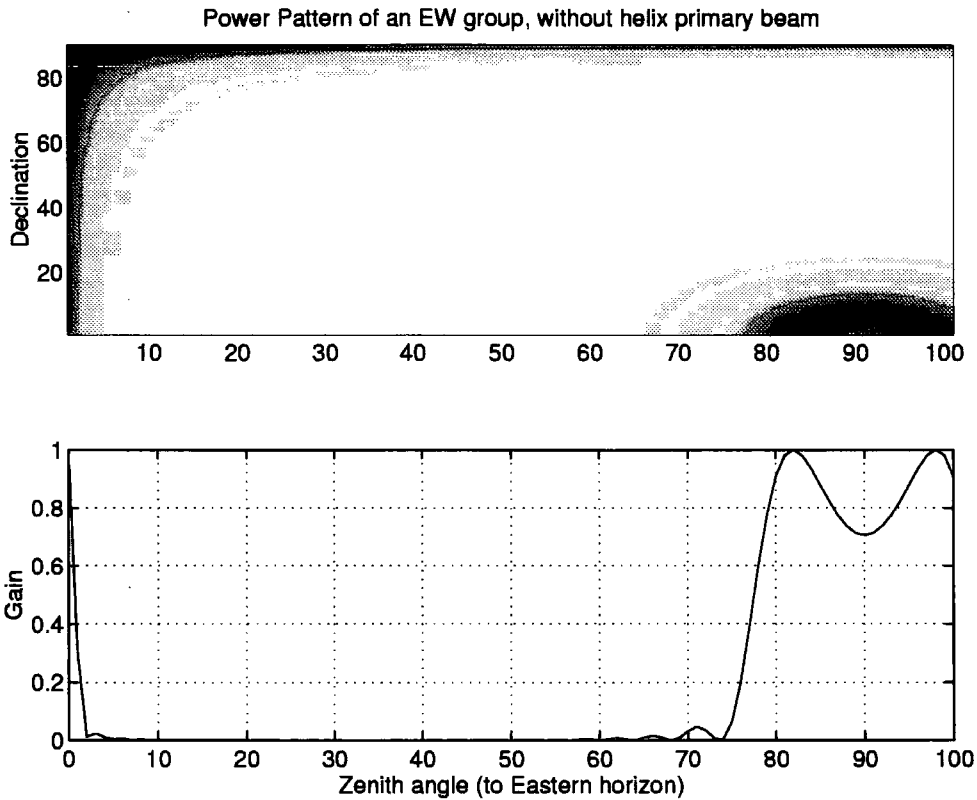


Figure 4.4: The array response for a single EW group (32 helices) at 151.5MHz

$$E = \sin(n\Phi/2)/(n\sin(\Phi/2)) \quad (4.1)$$

and

$$\Phi = 2\pi\vec{l}\cdot\vec{u} \quad (4.2)$$

The sun tracks through this lobe around each equinox. For a reason not yet understood the combined array was responding to the emission, despite the individual helical elements having an attenuation of around 30 dB. We played with the idea of recovering the data by blanking the spatial frequencies associated with the sun. We never succeeded in excluding these without distorting the map in other ways so we are having to reobserve these hours. Also fortunately none of our stronger sources fall on this lobe (roughly +10 to -10 degrees). On completion a careful search of the map for

repetitions of such sources, elongated and at $\pm 87^\circ$ in RA from their actual position, will have to be made.

4.4 Maps of the 150 MHz sky from Mauritius

4.4.1 Flux scale at the instrument Zenith

Sources near the instrument zenith have been selected and their expected 150 MHz flux calculated. Only those near the zenith were selected as at the time to the characterisation of the helical antenna's primary beam had not been finished. This has now been done (Katwaroo, 1997) and has been shown to match that expected from the standard formula (Kraus, 1988). The sources near the instrument zenith, between -57° and -43° declination, are plotted in figure 4.5 with their predicted strengths from the latest Parkes catalogue (Wright and Otrupcek, 1990) against the peak flux after critical smoothing. If smoothed to the beam size (at this declination) the peak height should be equivalent to the integrated flux under the beam area. The fit result is $S_{PKS} = S_{MRT} \times 10.08 - 0.8$. The non-zero intercept is due to the RMS noise levels in the MRT map, which also gives us the limiting flux; $3\sigma/\sqrt{2}$ (as the two maps are combined) gives 1.7 Jy. The scale for both the low resolution map (1λ to 100λ) and the high resolution map (101λ to 180λ) is taken from the fit to the high resolution, the low resolution fit is almost the same, but has a higher intercept because of the broadscale contributions. Fuller analysis is required, and this should be considered as a interim result.

4.4.2 The whole sky and the galactic plane

The map of the whole sky (figure 4.6) is in our natural coordinates, RA against $\sin(\text{zenith angle})$. The resolution is $15' \times 15'$ at the zenith, rising with the secant of the angle. This raw map is presented largely to illustrate the typical challenges in our observing method.

Firstly the sinusoidal wave in declination at 210-220 degrees (14 to 15 hours) is due to DC pick up in one particular day of observation. The relevant file has been identified. Secondly the tracks due to the sun passing through the grating lobe on the horizon can be seen, and also the distressing length of time that this effects. The Sun is the blob at, e.g. 155° and a $\sin(\text{Zenith angle})$ of 0.15, about a declination of -10 when it would be moving out of the grating lobe. This can be seen backwards in every effect data file producing a six fold strip with the sun at a declination that is a little higher, until it passes out the Northern edge of the lobe. These are the files that have to be replaced.

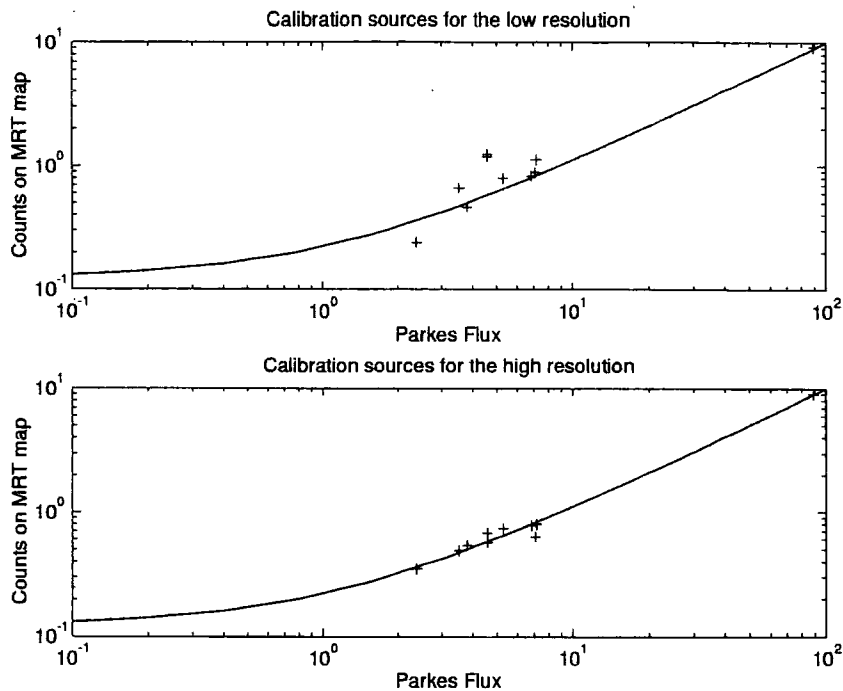


Figure 4.5: Parkes flux values against the flux from MRT maps

Figure 4.7 shows a section along the galactic plane, including the centre so that the potential of these maps can be judged. The resolution is as before, so is a function of latitude.

4.4.3 Higher resolution map of sections the 150 MHz sky

Because of the different MRT_METER for the pre-recirculated and post-recirculated data we have to resample one map to match the other, and then combine the two. This has not been done yet for the whole sky, but only for selected regions. The maps made are resampled to the coordinate system of the galactic plane, and the different sections combined to produce a single map. This is ideal for sources on, or close to, the galactic plane but not so suitable for extra galactic sources. Both the maps from which the sections are taken were smoothed to the beam size, but not CLEANed or corrected for primary beam attenuation nor has the decorrelation attenuation been done fully. Both these effects are believed to follow the theoretic-

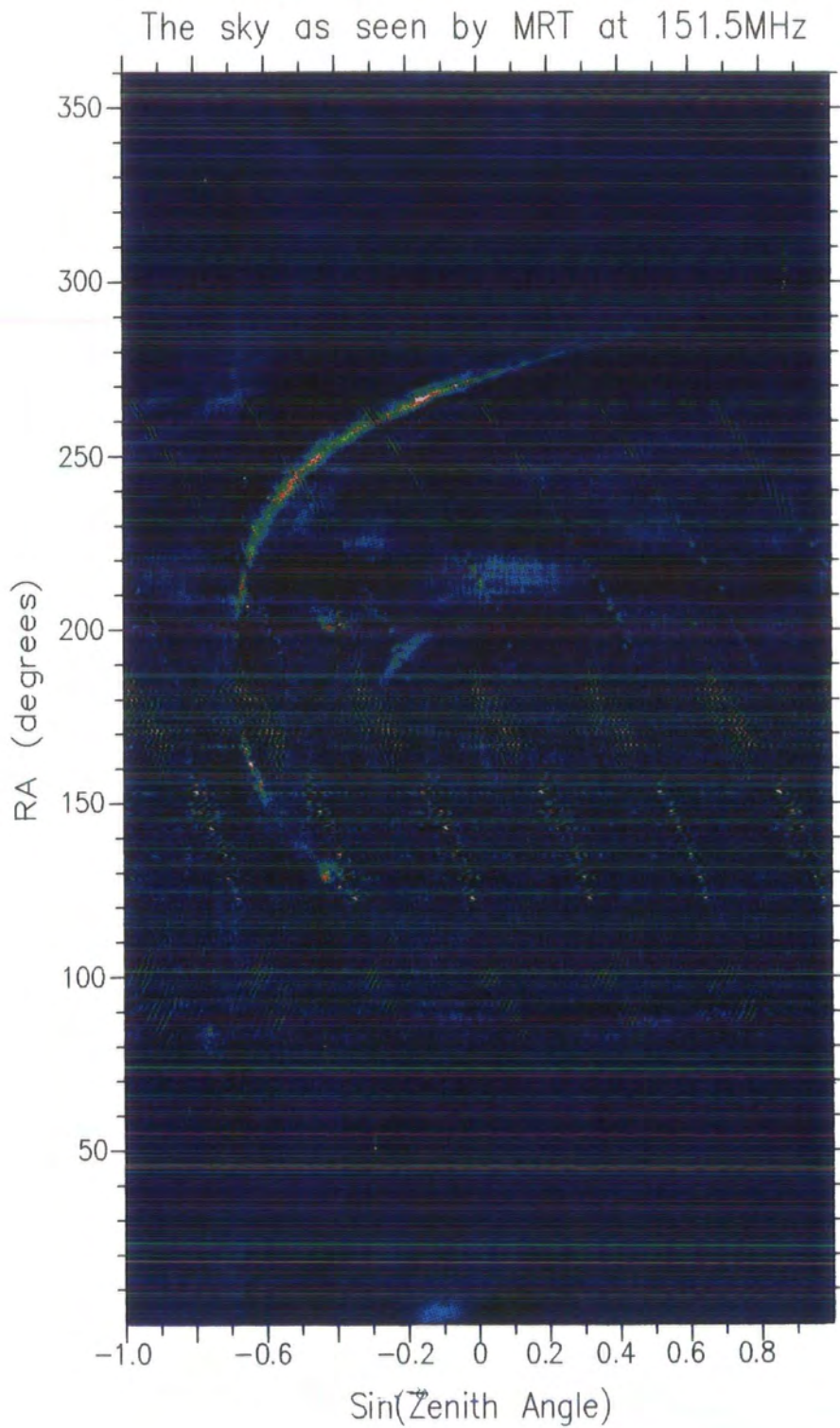


Figure 4.6: the MRT 15' map of the whole sky

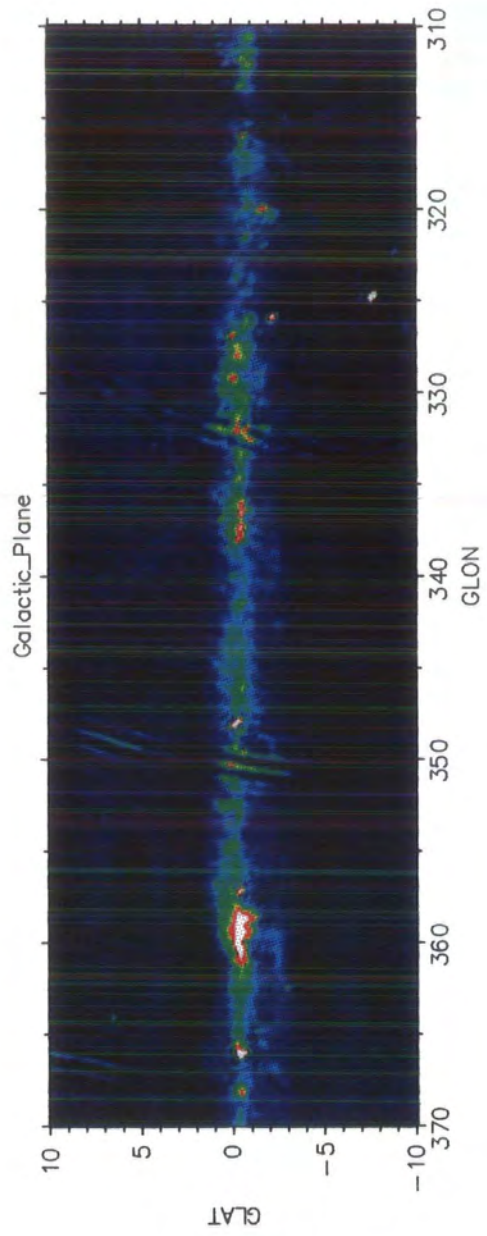


Figure 4.7: the MRT 15' map of the galactic plane

cal curves (equations 2.1 and 2.3), but large scale flux calibrations will be needed to confirm these results, and these have not yet been done. Until they are completed, these maps cannot be CLEANed and until they are CLEANed only limited conclusions can be drawn from them. Fortunately one of these conclusions is the extent of the broadscale emission, which is what we need to know to study the SNRs. As the calibrator used throughout in the generation of the maps is PKS1932-46 the corrections are zero around this declination. For the regions mapped away from this declination, other point sources were used to confirm the predicted signal loss. The two maps were then scaled and added together. This is not very satisfactory, as it leads to variations in the weight given to each baseline, but as these are no more than 10% it is an acceptable solution for these early stages of map making.

G5.4-1.2

Our observations of this source, shown in figure 4.8, have a peak at $\ell = 5.4$, $b = -1.1$, and second peak at $\ell = 5.45$, $b = -1.0$ and a broader component that tails away from the plane to lower b and ℓ . The apparent splitting of the peak could be related to the nebula G5.27-0.9, but is too far within the edge of the shell for this to seem likely. The unrelated HII cloud at $\ell = 6.0$, $b = -1.2$ is also clearly visible. The high resolution maps of, for example Frail et al. (Frail et al., 1994b), show much greater detail of the same features and are to be found in figure 6.2.

The primary beam attenuation is 7% and the beam shape is $4' \times 9.7'$ at -60° to b . The integrated flux is 36 Jy over 0.4 of a square degree, significantly less than would be expected from the values in Greens catalogue, which is 51 Jy.

G8.7-0.1

This very bright source is clearly delineated at these frequencies, as compared with the unsuccessful surveys of Braun et al. (Braun et al., 1989) at around 1.5GHz, and yet is not absorbed, as in the survey of Ödegård taken at 57.5 MHz (figure 6.5). Our map, figure 4.9, is (not surprisingly) similar to that of Frail et al. (Frail et al., 1994b) at 327MHz (figure 6.4). We also see the low surface brightness extensions that run along the plane towards lower ℓ .

The primary beam attenuation is 10% and the beam shape is $4' \times 9.6'$ at -60° to b . The integrated flux is 245 Jy over a square degree, in line with the Greens catalogue value of 206 Jy.

G315.4-2.3

This source, figure 4.10, is not believed to contain a pulsar and is only mapped as the source has to be discussed in section 6.5 on G320.4-1.2. It shows the classic double peaked ring shape of many SNRs, which are often called barrel SNRs. The MRT maps indicate greater emission from the centre than that seen by MOST (figure 6.8), but still well below that from the two peaks.

The primary beam attenuation is 15% and the beam shape is $4' \times 13'$ at about -20° to b . The integrated flux is 50 Jy over 0.7 square degrees, although this is another for which the background is hard to judge as the sharp features lead to significant sidelobes, significantly less than would be expected from the values in Green's catalogue which would give 153 Jy.

G320.4-1.2

The MRT map (figure 4.11) shows up the intense bright peak associated with RCW89 and the weaker broadscale emission is lost. The secondary, resolving, peak below it is a twisting trail of weaker emission, as can be seen on the MOST map shown in figure 6.10.

The primary beam attenuation is 10% and the beam shape is $4' \times 12'$ at about -30° to b . The integrated flux is 157 Jy over 0.8 square degrees, in line with the Greens catalogue value of 128 Jy.

G343.1-2.3

Two maps of this SNR (figures 4.12 and 4.13) are presented as the low resolution map shows the broadscale features more clearly. The first uses only the measurements made up to 100λ , the second is filled up to 180λ . The second set of data is contaminated with low level ripples from the sun image which is picked up at the equinox as described in section 4.3. New data for this region has been collected, but not yet reduced.

The primary beam attenuation is 0.5%, and the beam shape is $4' \times 10.4'$ at about -50° to b . The integrated flux is hard to determine as the background is hard to define, but over the one square degree is between 60 and 100 Jy, much more than would be expected from the values in Greens catalogue, which give 21 Jy. However using the single dish flux measurements of the SNR (MSH17-14 (85MHz) 25 ± 4 Jy, KOM43 (408MHz) 45 Jy, CTB36 (960MHz) 30Jy and MHR59 (1,440 MHz) 15 ± 7 Jy) we can see that its clear that the Green flux value, like the MOST and VLA values, is an underestimate. If the 85MHz value is not in error the spectral index has turned over between 408 and 85 and not much can be deduced. If that value is in error

the expected flux is 60 Jy (spectral index from 1.44 GHz to 408 MHz) or 100 Jy (960MHz to 408 MHz).

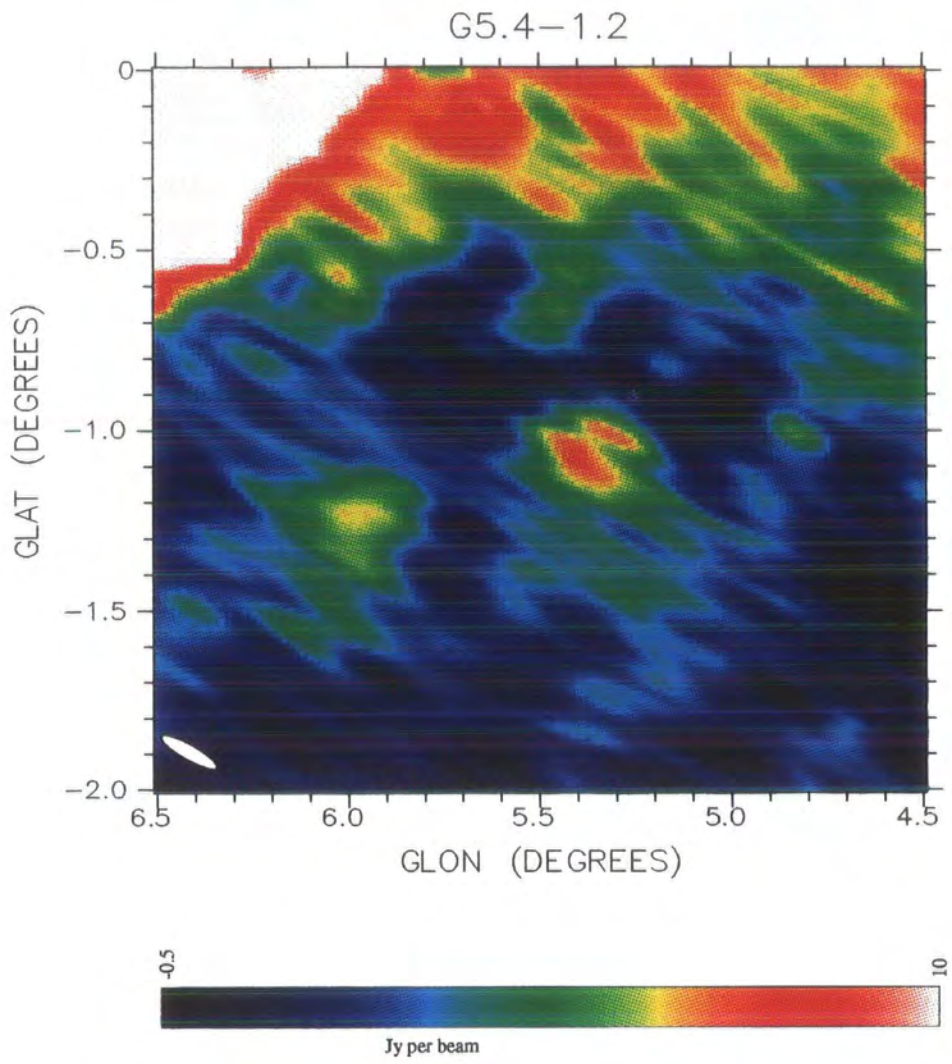


Figure 4.8: The MRT map of G5.4-1.2, the Duck

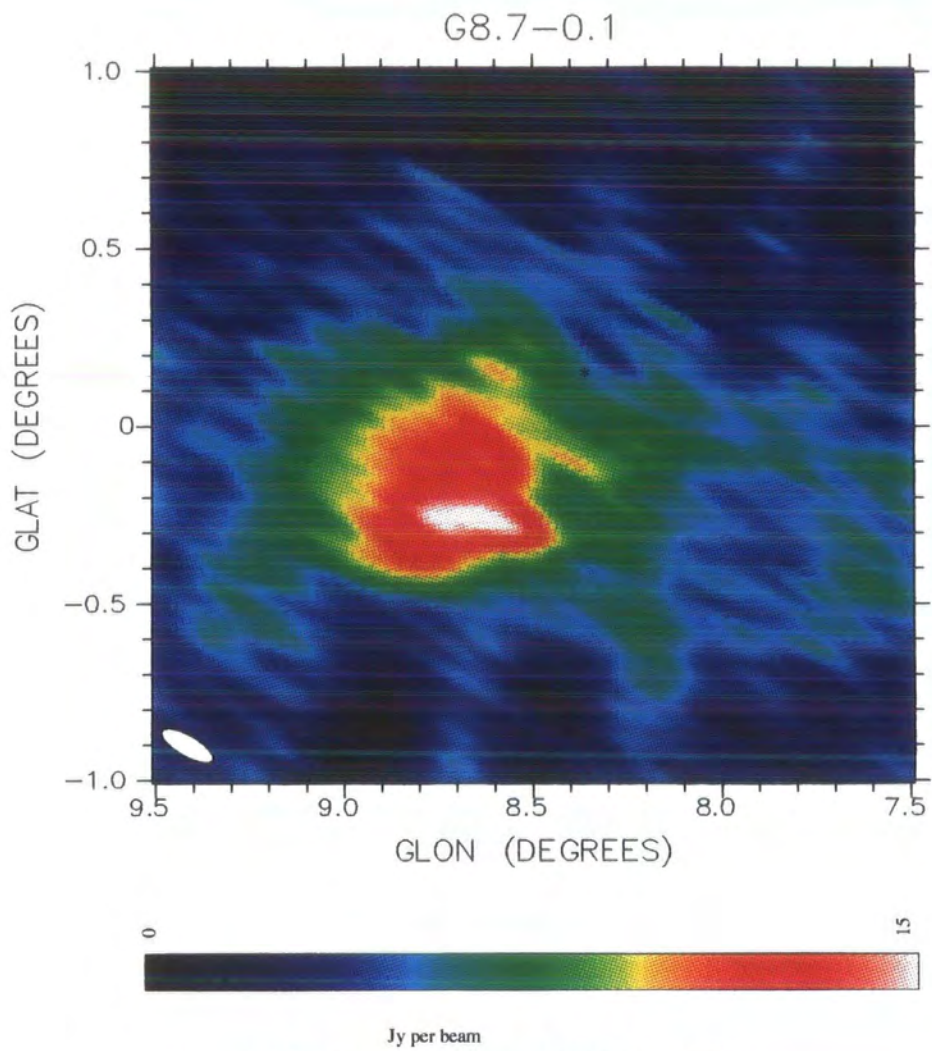


Figure 4.9: The MRT map of G8.7-0.1, W30

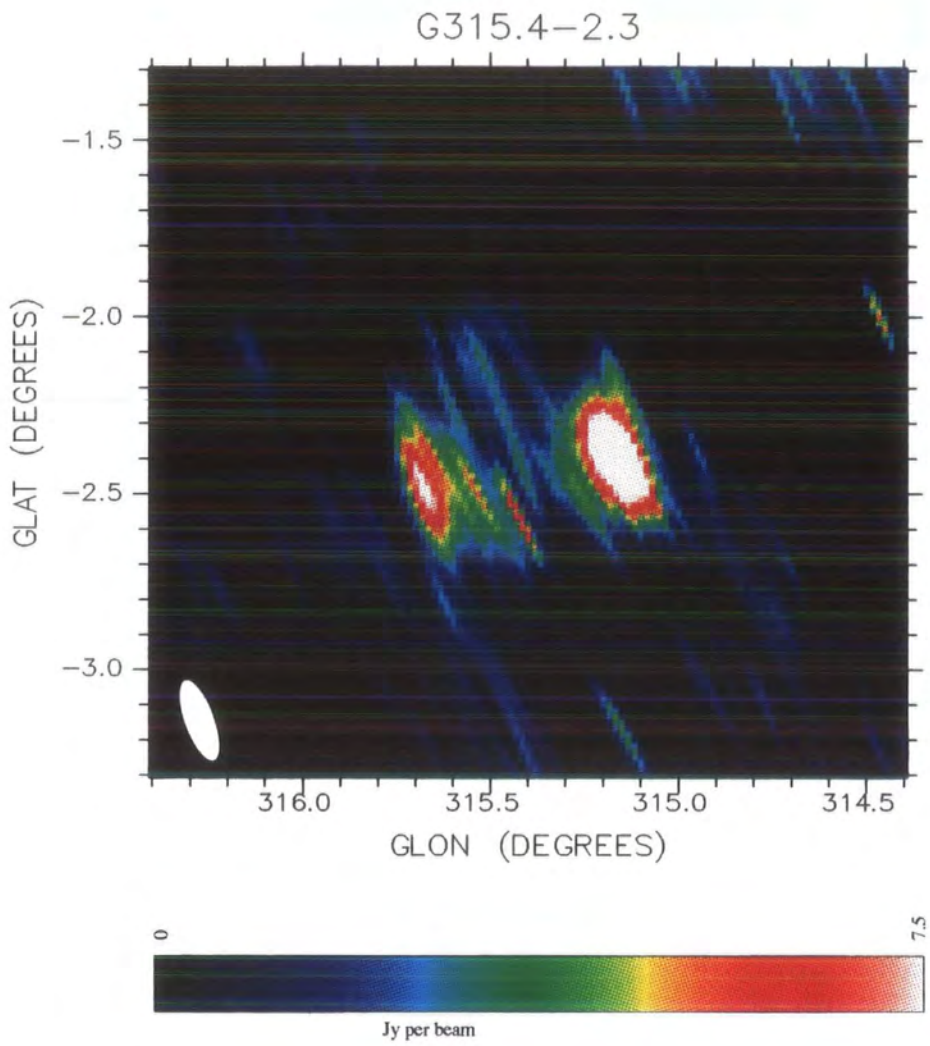


Figure 4.10: The MRT map of G315.4-2.3, possible site of SN185

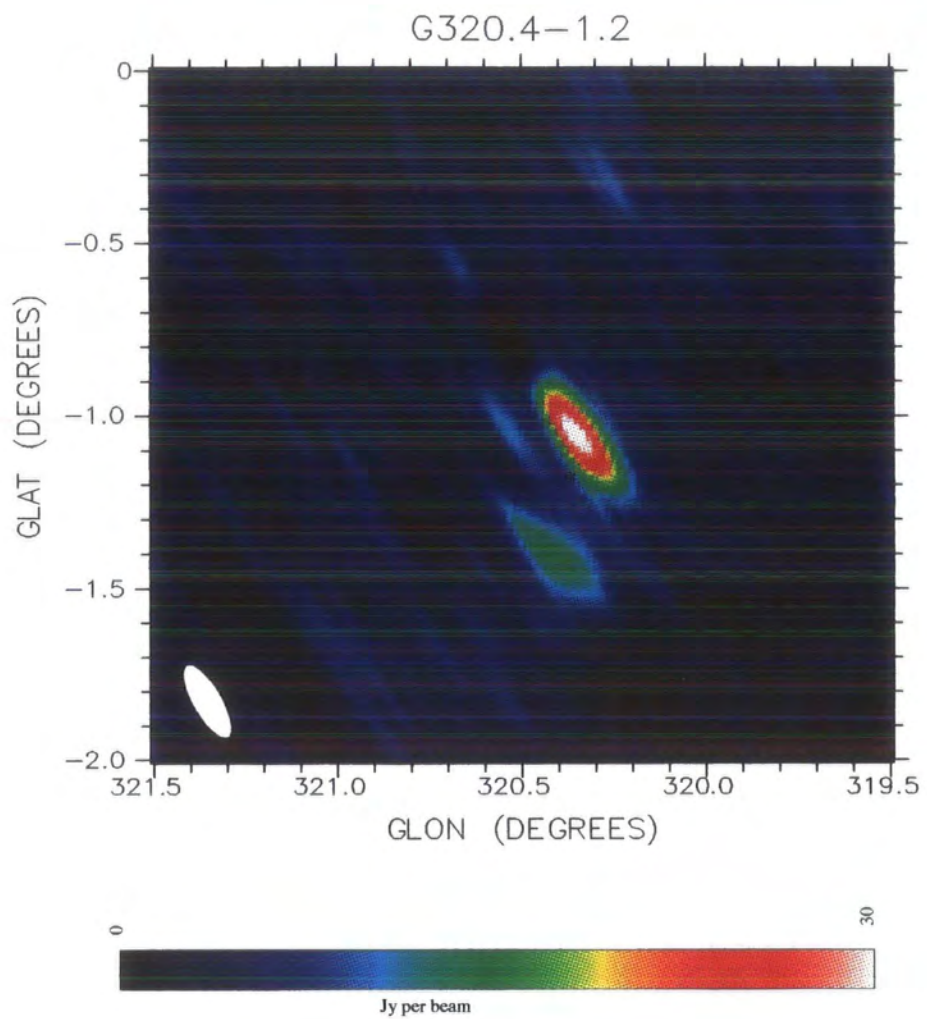


Figure 4.11: The MRT map of G320.4-1.2, MSH15-52 and possible site of SN185

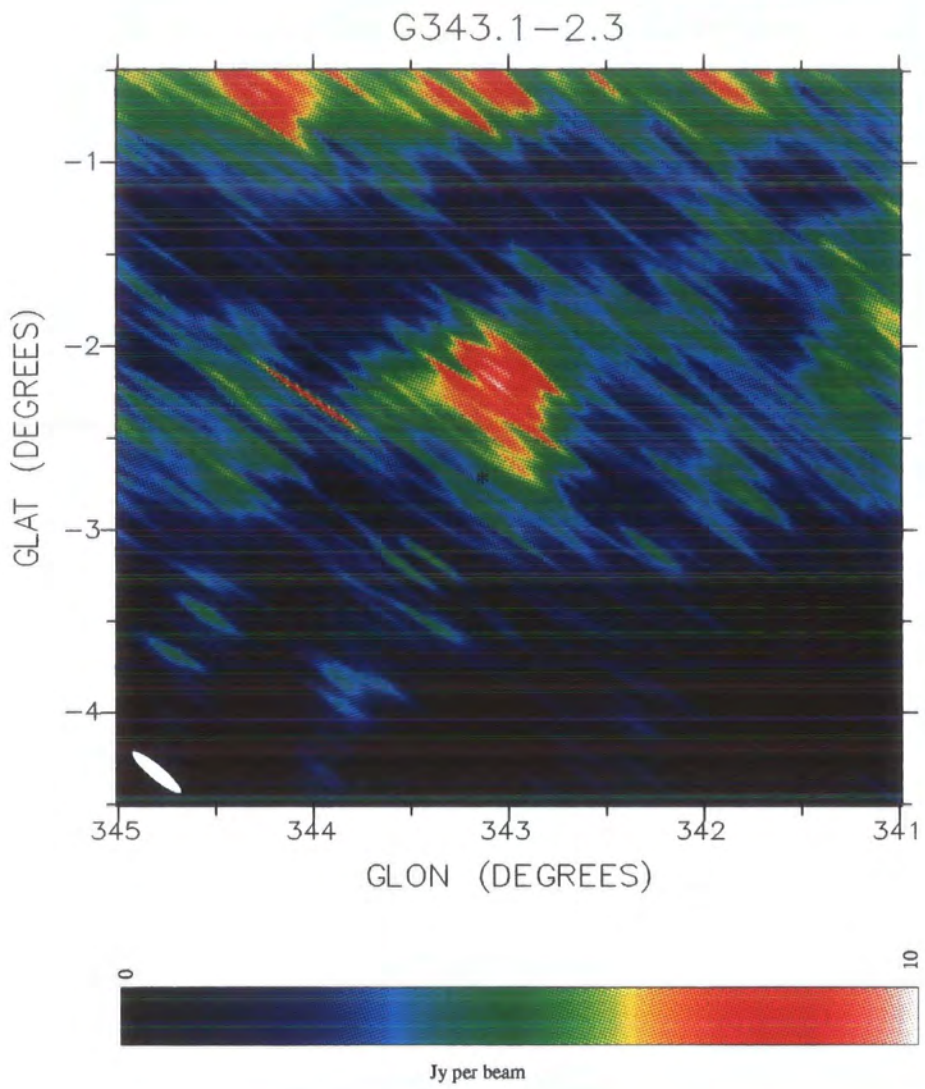


Figure 4.12: Lower resolution map of G343.1-2.3

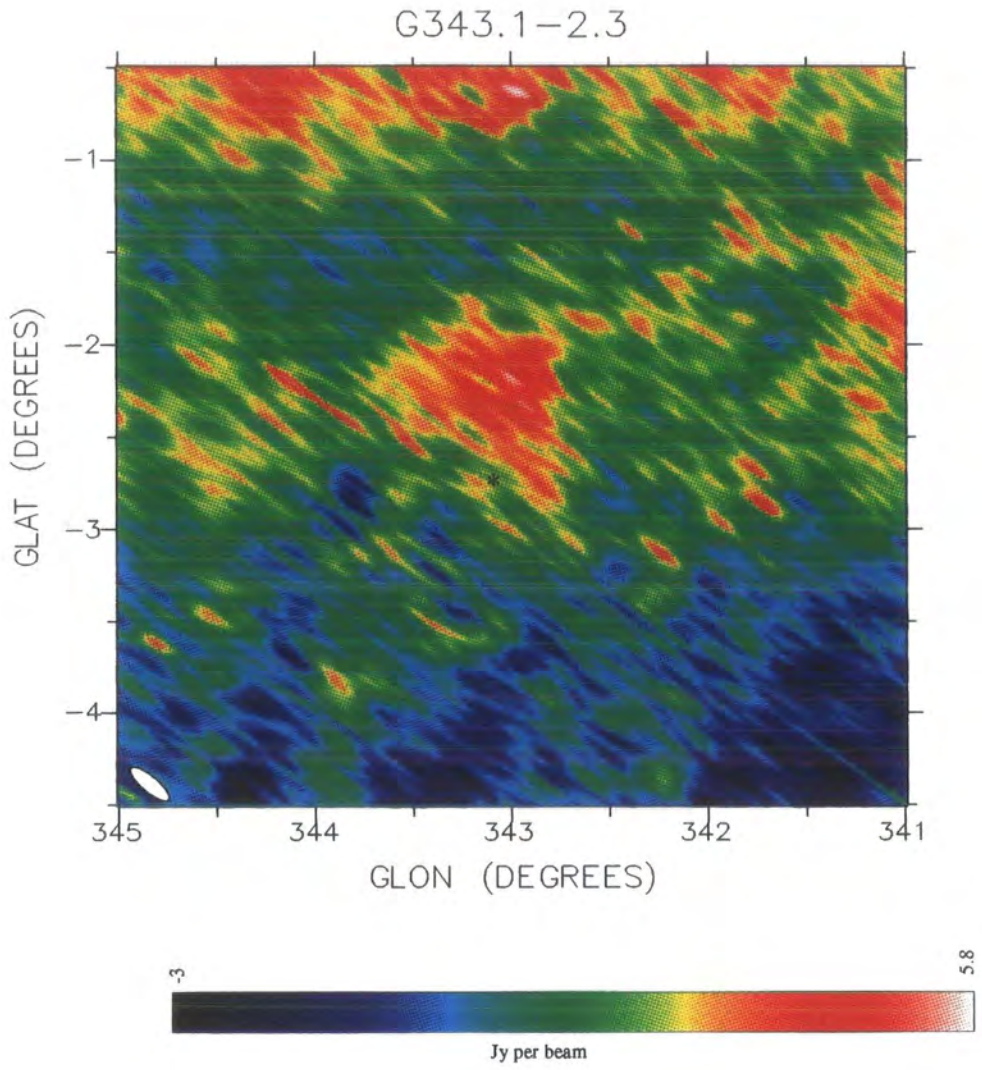


Figure 4.13: Higher resolution map of G343.1-2.3

Chapter 5

Methods

5.1 Introduction

The fundamental problem in attempting to investigate the association of pulsar and supernova remnant is the usual astronomical one; the objects exist in three dimensional space but we can only observe a two dimensional projection.

Two model based methods can be used for both pulsar and SNR distance estimations. These are the kinematic methods, based on the rotation curve of the galaxy, and column density methods, based on estimates of the variation of column density (of either N_H or N_e) with line of sight.

The latter, the Taylor and Cordes model (Taylor and Cordes, 1993) of variation of electron density, n_e , within the galaxy has been widely used for the distance to the pulsar, D_{pulsar} , estimation. However this model, which uses few parameters to describe the complexities of all the features of the arms of the galaxy, will always estimate individual distances with limited accuracy. Likewise the model based on the correlation for integrated surface brightness, Σ , to distance (or Σ to age) provides such poor constraints that it is virtually useless as a primary distance estimator.

In this chapter I will review the methods used in this thesis;
The pulsar distance estimation;

- The Dispersion Measure, the change of delay with frequency, can be used to convert the traversed electron column density to a distance using the Taylor and Cordes model.
- Parallax; for close objects one can use the change of apparent position with season to deduce the distance, the pulsar period can give accurate timing positions and be used in the same way.

- Absorption; Material (such as neutral hydrogen, HI, and H₂CO) between the object and ourselves absorbs. If this is line absorption the relative velocity of the absorber can be deduced. This velocity can be placed at a distance using the Galactic rotation curve.
- Proper motion from timing and direct measurement. Proper motion with velocity gives the distance.
- Scintillation and pulsar wind velocity.

Estimation of SNR distances;

- Historical records of astronomical events which can be associated with SNR.
- Phenomenological Σ - D relationship.
- H II emission from energised particles.
- Neutral hydrogen, HI, and H₂CO absorption, as in the pulsar case.
- X-ray thermal plasma measurements from the Sedov theory of blast wave expansion.
- Velocities of filaments in the SNR shock front.

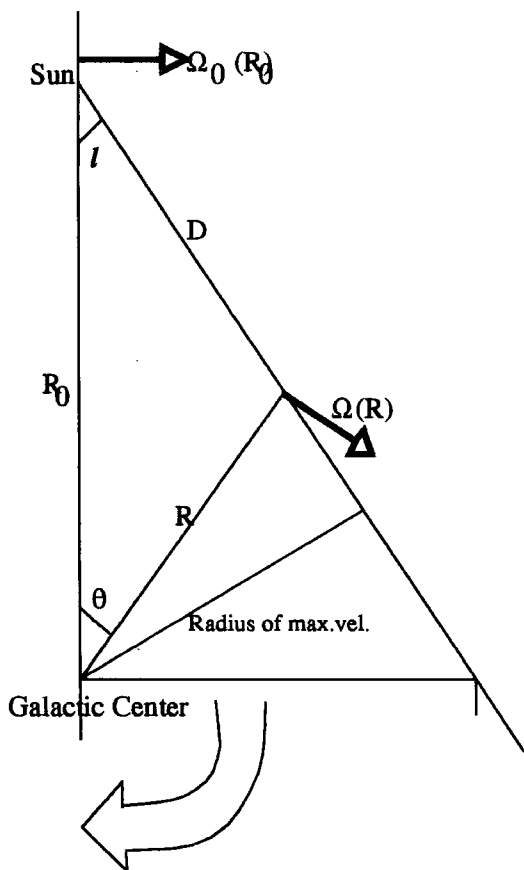
5.2 Distance indicators for both pulsars and SNR's

5.2.1 Kinematic methods

Theory

Kinematic methods can be applied using HI, OH and H₂CO absorption as well as HII emission, although HI is preferred, as neutral hydrogen is the only tracer evenly distributed throughout the galaxy. All the others tend to be clumped, so can only give an approximate limits for the distance. From a molecular (or magnetic) line, in absorption or emission the change in the "at rest" frequency ($\nu = \nu_L(1 - \frac{v}{c})$) gives the velocity at which the object is receding (or approaching) and from this velocity the distance can be deduced.

The galactic rotation speed is taken as a function of radius only, $\Omega(R)$, i.e. local motion towards galactic arms and random dispersion are ignored. Then the velocity, v , (compared to our local standard of rest) with distance along the line of sight at an angle l is illustrated by Figure 5.1. D is the



R , galactic radius of the source

R_0 , galactic radius of the sun

D , distance to the source from the sun

l , angle from galactic centre to the source

θ , angle from the sun to the source.

Ω , Rotation velocity

Figure 5.1: Conversion of galactic rotation to line of sight velocity, after Galactic Radio Astronomy 1988

distance to the source, Ω_0 and R_0 are the rotation speed and the galactic radius of the sun. (Verschuur and Kellermann, 1988).

From figure 5.1;

$$\begin{aligned} v &= \Omega(R) \cos(90^\circ - l - \theta) - \Omega_0(R_0) \cos(90^\circ - l) \\ &= \sin(l + \theta)\Omega(R) - \Omega_0(R_0)\sin(l) \end{aligned} \quad (5.1)$$

To estimate $\Omega(R)$ we use the measurements of Clemens (Clemens, 1985) shown in figure 5.2. They fitted a polynomial of the following form to the rotation curve with the coefficients shown in Table 5.1.

$$\Omega(R) = \begin{cases} \sum A_i R^i, & \text{where } R < 0.09R_0 \\ \sum B_i R^i, & 0.09R_0 < R < 0.45R_0 \\ \sum C_i R^i, & 0.45R_0 < R < 1.6R_0 \\ D_0, & R > 1.6R_0 \end{cases} \quad (5.2)$$

Several previous rotation models existed, some based on the older IAU standards which placed the sun at 10 kpc from the galactic centre distance. All velocity to distance conversions used in this thesis have been converted to the present IAU standard of 8.5 kpc distance and $\Omega_0 = 220\text{kms}^{-1}$. This method cannot be used when the lines of sight are towards the galactic centre or anti-centre where, for the circular motion, the line of sight velocity is zero for all distances. For the 1st and 4th quadrants a single speed can be due to two different distances. Normally this is not a serious constraint as other indicators can be used to select between the two options; for example $\Sigma - D$ is one such indicator for SNR's, and the dispersion measure for pulsars.

The rotation model of the galaxy is global, and suffers from the usual limitations therein. The errors of the model are about $\pm 7\text{kms}^{-1}$. These errors are assumed to be due to local turbulence in the galactic velocity stream, and have been reduced by some workers by the introduction of further parameters.¹

Therefore we have two sources of uncertainty in the kinematic approach to distances. One is due to the non-uniform sampling of velocity space by the absorber, i.e. the clumpiness of the clouds, making it hard to place the object exactly on the velocity curve. This does not effect the cases when emission measured, but these are rarer. Secondly the velocity cannot be converted to a distance accurately. Thus distances derived from absorption tend to be (and should be) quoted as a pair of bracketing distances each

¹A more recent paper(Fich et al., 1989) claims a better fit (in the sense of fewer parameters) with a straight line through $\Theta_0 = 220\text{kms}^{-1}/s$, i.e. a constant rotation field, for galactic radii more than $R_0/5$ and less than $2R_0$, but with velocity residuals which are about doubled.

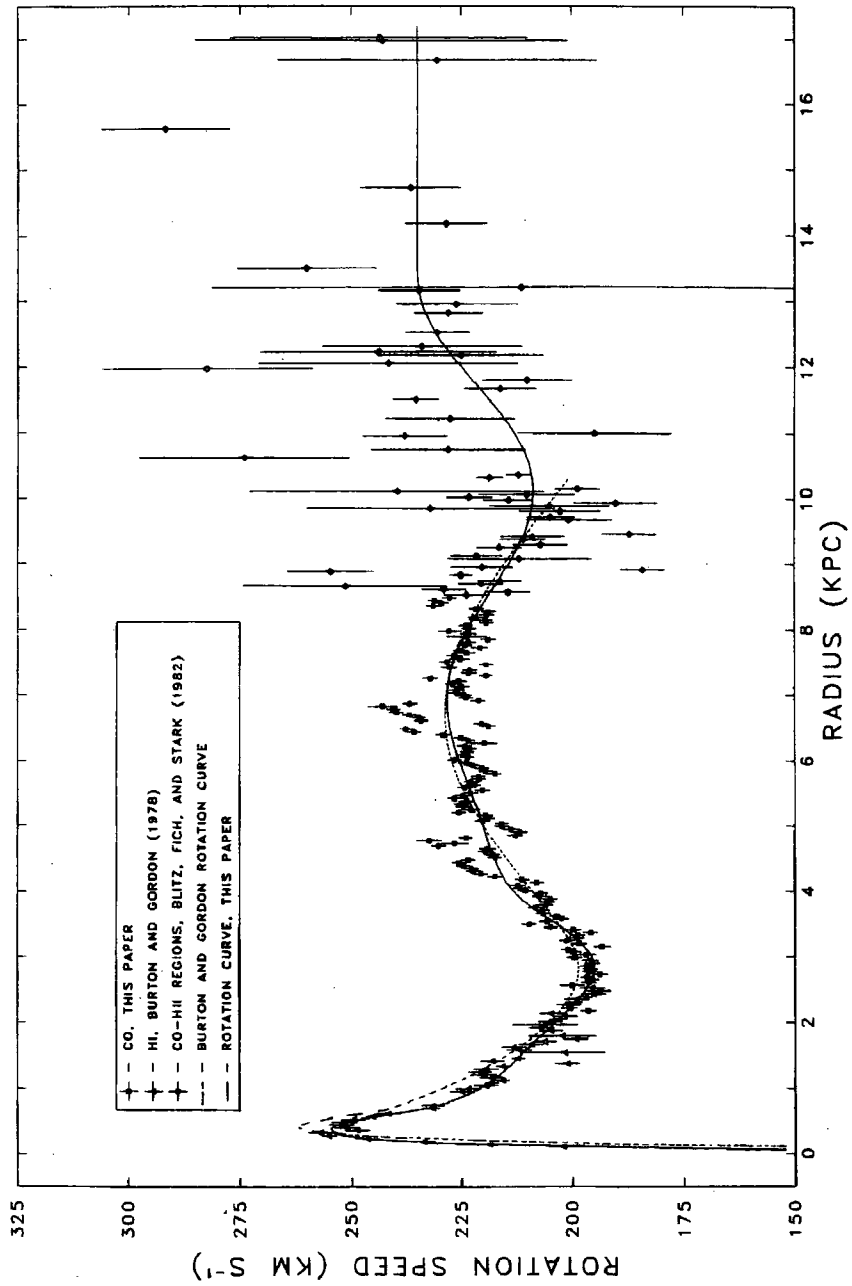


Figure 5.2: Plots of the rotation speed, Ω , versus galacto-centric radius (Taken from Clemens, 1985). The solid line correspond to the polynomials in equation 5.2.

| Coefficient | $R < 0.09R_0$ |
|-------------------------|---------------|
| A_0 | 0.00 |
| A_1 | +3069.81 |
| A_2 | -15809.80 |
| A_3 | +43980.10 |
| A_4 | -68287.30 |
| A_5 | +54904.00 |
| A_6 | -17731.00 |
| $0.09R_0 < R < 0.45R_0$ | |
| B_0 | +325.0912 |
| B_1 | -248.1467 |
| B_2 | +231.8701 |
| B_3 | -110.7353 |
| B_4 | +25.0730 |
| B_5 | -2.1106 |
| $0.45R_0 < R < 1.6R_0$ | |
| C_0 | -2342.6564 |
| C_1 | +2507.6039 |
| C_2 | -1024.06876 |
| C_3 | +224.562732 |
| C_4 | -28.4080026 |
| C_5 | +2.0697271 |
| C_6 | -0.08050808 |
| C_7 | +0.00129348 |
| $R > 1.6R_0$ | |
| D_0 | 234.88 |

Table 5.1: Coefficients of the Rotation Curves

with errors, e.g. for the example shown in figure 5.3 of PSR1706-44, the distance velocities found are -18.2 kms^{-1} to -29.7 kms^{-1} giving a distance between 2.6 ± 0.6 and 3.2 ± 0.4 kpc (Koribalski et al., 1995).

The pulsar is much simpler to handle as one automatically receives the spectrum from the pulsar (when it is in the on state) and the total galactic emission (when it is in the off state). The ratio of the two is independent of all the features that are behind the pulsar. This is shown in the central frame in Figure 5.3.

Measurements

With the SNR's the absorption lines are only explicitly useful for particularly bright sources which most shells are not. Also one has to assume a constant emission spectrum across the SNR, therefore it is difficult to be confident about the absence or otherwise of spectral features. However when one can associate other features with the shell these can then be used for the velocity measurement. For example Kassim and Weiler (Kassim and Weiler, 1990) were able to identify HII clouds in front and behind a SNR (from absorption at 57MHz), then convert their line velocities to get bracketing distances. Other such features include molecular clouds, OB associations and pulsars.

The HI lines are more commonly observed but H_2CO or H II spectra have also been used. The lower distance limit is always identifiable, as the absorption has to be due to clouds in between the observer and the source. If a cloud can be identified that shows no sign of absorption its distance provides an upper limit. The great advantage of observations on pulsars over those on SNR is that for the latter, one has to assume that two nearby portions of the source are emitting in a similar fashion, for the former all that is needed is the ratio of the on absorption against the off emission. The on absorption gives the velocity (and distance) to material in front of the pulsar and if an emission feature can be identified this gives the velocity (and distance) to material behind the pulsar. It can be expected if the absorption is strong, then the lower limit is likely to be a reliable estimate of the actual distance (Radhakrishnan et al., 1972).

Optical astronomy can also assist here as the H_α lines can be measured in the optical filaments associated with the shock edge. These lines tend to be confused with earth bound contaminants (such as the H_α and OH lines) which require the observed lines to be fitted by several different Gaussian components. The velocity separation between the contaminants and the desired lines is usually large (the OH line is equivalent to a velocity of 220 kms^{-1}) but the intrinsic width of the lines due to shock broadening, up to 100 kms^{-1} , can make accurate identification difficult.

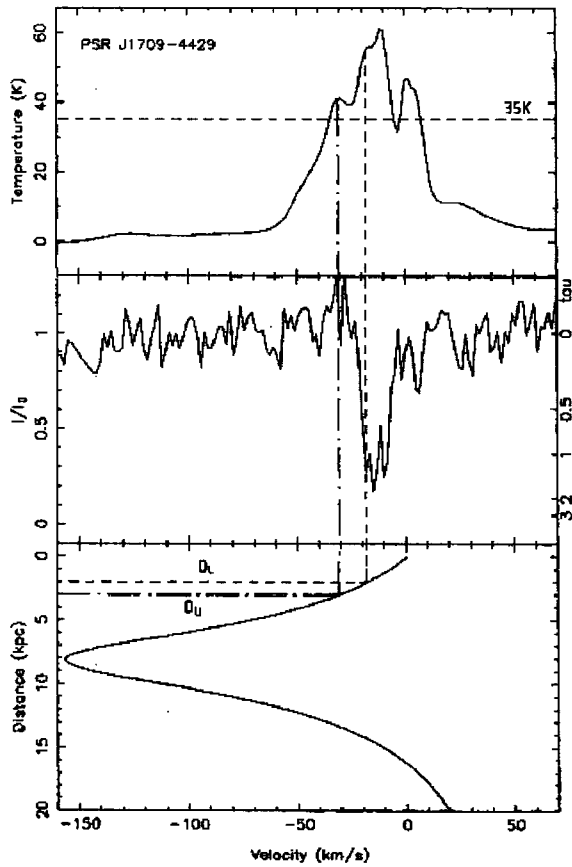


Figure 5.3: Velocity to distance conversion for pulsar PSR1706-44, from HI measurements of Radio Pulsars, Koribalski et al. 1995. The picture is of a) The total sky brightness with velocity, b) the ratio of the brightness with pulsar on over that with the pulsar off, and c) the rotation curve

5.2.2 Column density methods

A similar method is based on the neutral hydrogen column density, N_H . Obviously column densities have to increase monotonically along the line of sight. Distance estimates are not always necessary to make an association, since it is likely that if there is a similar measure of N_H for both the pulsar and the SNR they are probably associated. However it is still advantageous to convert the value into an estimate of distance. The simplest approach is to assume that the distribution of absorber is roughly constant across most of the galaxy. Such a crude approach can obviously be improved, but it is arguable whether more elaborate models give answers that are much improved in reliability. The column density of N_H used for both pulsars and SNRs is modelled as either about 1 cm^{-3} , or $3 \times 10^{18} \text{ cm}^{-2} \text{ pc}$, the usual galactic figures. The uncertainties of the local density, usually much lower as it has been swept out by the pre-SN wind, play little role in this estimation. The Durham Parkes HI survey provides an undersampled survey for all points on the southern galactic plane of the column density with velocity. The integral of the curve to the given density gives a velocity. However the undersampling of this survey, as well as the intrinsic inaccuracies of the model and measurements, reduces its usefulness.

5.3 Supernova Remnant Distance indicators

5.3.1 Historical Methods

The expected frequency of Supernova occurrence is about one every hundred years, there are however only a few remnants which can be confidently associated with documented observations of supernovas. The definitive work on this is Clark and Stephenson (1977). If one knows the absolute maximum light, from a given type, one can derive the SN distance. And hence the distance to any associated SNR also can be derived. The problem with historical records is in their association with a given SNR.

The light extinction of a SN (or any other optical phenomenon) with distance is;

$$5 \text{Log}(D/10) = M_v(\text{max}) - m_v(\text{max}) + A_v$$

where D is the distance to the SNe in pc; M_v is the absolute magnitude, m_v the apparent magnitude and A_v the extinction.

Type I and II SNe show little scatter in the absolute magnitude; -18.9 ± 0.5 for type I and for type II -16.3 ± 2 . Therefore from observations of the m_v for the SN and measurements of A_v from a variety of sources the distance can be obtained, providing one knows the type. The falloff in the

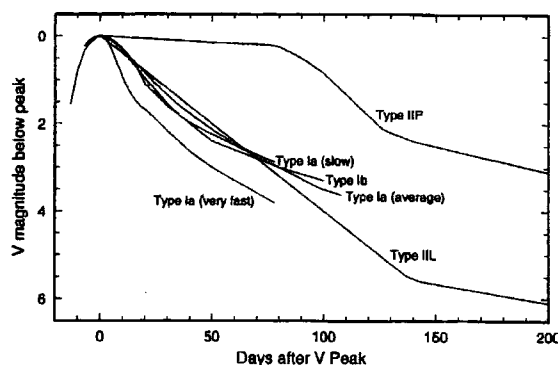


Figure 5.4: Light Curves of type 1 and 2 SNe. From Schaefer 1996

luminosity for any SN is known as it depends on the half life of the various isotopes produced. Therefore the recorded rate of decay can be used to give the type, and hence the distance for a given SN. Clark and Stephenson (Clark and Stephenson, 1977) used the detailed observations of Kepler and of Tycho Brahe on the SNe that bear their names. Both recorded the relative brightness (and position) to other stars and planets over the lifetime of the SNe. Clark and Stephenson used these values to match the decay times of the types and confirmed that both were type I. The distances they found for these SNe are 5.4 and 5.2 kpc respectively. Unfortunately for the other historical SNe there is not sufficient detail to assign types confidently but some reasonable results can be obtained, and will be for the SN185.

The other unknown is the extinction, A_v ; methods for estimating that have been based on the reported colours of the SNe (using the definition $A=3.1xE(B-V)$ where E is the excess of blue over visual, or the colour), or on recent N_H measurements, assumed to be associated with the dust and related by;

$$A_v = \frac{N_H}{1.9 \times 10^{21}} \quad (5.3)$$

Historically Recorded Supernovae

| SN year | SNR | High Confidence | Observed by, or recorded in |
|---------|--------------------------|-----------------|-----------------------------|
| 185 | G315.4-2.3 or G320.4-1.2 | No | Hou-han-shu |
| 386 | G11.2-0.3 | No | Sung-shu |
| 1006 | G327.6+14.6 | Yes | Sung-shih |
| 1054 | Crab | Yes | Sung-shih (and others) |
| 1181 | G130.7+3.1 | Yes | Sung-shih |
| 1572 | Tycho's SNR | Yes | Tycho |
| 1604 | Kepler SNR | Yes | Kepler |

One can also use the age, τ (in years), to put an upper limit on the distance using the simple canonical initial velocity (\bar{v}), 10,000 kms⁻¹, and the angular extent, θ in arc minutes, to limit the distance, in kpc;

$$D < 1.8 \times 10^{-3} \frac{\bar{v}\tau}{\theta}$$

5.3.2 Σ - D relationship.

Following an SN explosion the ejecta will sweep into interstellar medium. It is obvious that a shock front will develop and energy will be lost. As the SNR expands the integrated brightness will decrease. Observations of Cas A, the nearby and young SNR, shows that as the radius and age increases the surface brightness (flux per steradian) Σ decreases. Therefore it seems reasonable to look for an association between the surface brightness and the radius, and thus through the angular size, to the distance. Such a relationship of size to brightness has been constructed, using the SNRs for which there is an independent distance measure. This indicates a possible correlation, $\Sigma \propto D^{-n}$, where n is some power to be derived. While the early work seemed to confirm this relationship, and the scatter in values was assumed to be due to uncertainties in the distance, improved distance measures have not reduced the scatter on the Σ axes, and in some cases they have increased. The correlation has turned out to be largely due to the algebraic relationship of distance (and thus size) with brightness, rather than luminosity. For any object at a distance d with a flux S and angular diameter θ , the luminosity $L \propto Sd^2$, and $\Sigma \propto S/\theta^2$, so $\Sigma \propto L/(\theta d)^2$, or L/D^2 . Figure 5.5 plots the latest (Green, 1996; Green, 1991) Σ - D and L - D plots. While there does seem to be a general correlation in the Σ - D plot, the evidence is much less clear in the L - D plot. As indicated in this figure the average luminosity of SNR can be used for canonical discussions, but it is too widely scattered to be used usefully in the study of individual SNRs. This has been confirmed with samples from external galaxies where there is no confusion of widely different (and possibly incorrect) distances. The scatter is probably due to the variation of environment into which the

SNe was born. Some attempts were made to correct for this by including a dependence on the height above the galactic plane into the Σ -D relationship, as the mean density falls off with the height. However these corrections have not been particularly successful.

A survey of the M82 galaxy has just been finished using the VLA, (Huang et al., 1994). In this it is claimed that there is a Σ -D relationship with $n=3.6$. This fit is to measurements of SNR radii taken over nearly 5 decades, including the very small shells of several recent SNe at several epochs in their development, the M82 shells and those SNR in our own galaxy. However while the range is improved, the scatter for individual points around the fit in the range of 10 to 100 pc is not very different from that of previous studies. Further analysis is beyond the scope of this thesis.

5.3.3 Filament Velocities

The optical filaments usually seen at the shock front of an SNR contain the usual components of the ISM. The classic image of this is the Crab nebula where the strands of molecular emission are obvious.

Measurements on the filaments provide information on the shock front. In this thesis we are concentration on distances, so only those filament properties which can contribute to estimates of these are described.

Figure 5.6 shows a typical shell. The line width due to emission from the far side and from the front of the SNR (v_{radial}) can be observed in those filaments that are near the centre of the SNR. These can be combined with the observed proper motion of the edges. The distance can be calculated by equating the measured v_{radial} with the transverse velocity (v_{tr}) giving the observed proper motion using equation 5.16.

Alternatively filament velocities can give a kinematic velocity. The same filaments that can be used in proper motion studies (i.e. those on the rim of the SNR) are assumed, due to their expansion, to have no line of sight motion. Therefore they can be examined for their line of sight velocities due to their motion from differential galactic rotation. These observations are usually done on the $H\alpha$ lines. The measured line widths are large and are associated with their internal dynamic processes. Since we are only interested in the mean velocities, these line widths will not considered. Special care needs to be taken as the emission is usually found to be contaminated by earth bound features at nearby frequencies. For the $H\alpha$ line (at $\lambda = 6562.7\text{\AA}$) these are the OH "glow" at 6568\AA (giving an apparent velocity of 200kms^{-1}) and the earth bound $H\alpha$ component, which contaminates the near zero velocity. Therefore the velocity profile is fitted by a number of Gaussians, and comparisons with empty fields allows the terms which confuse to be rejected.

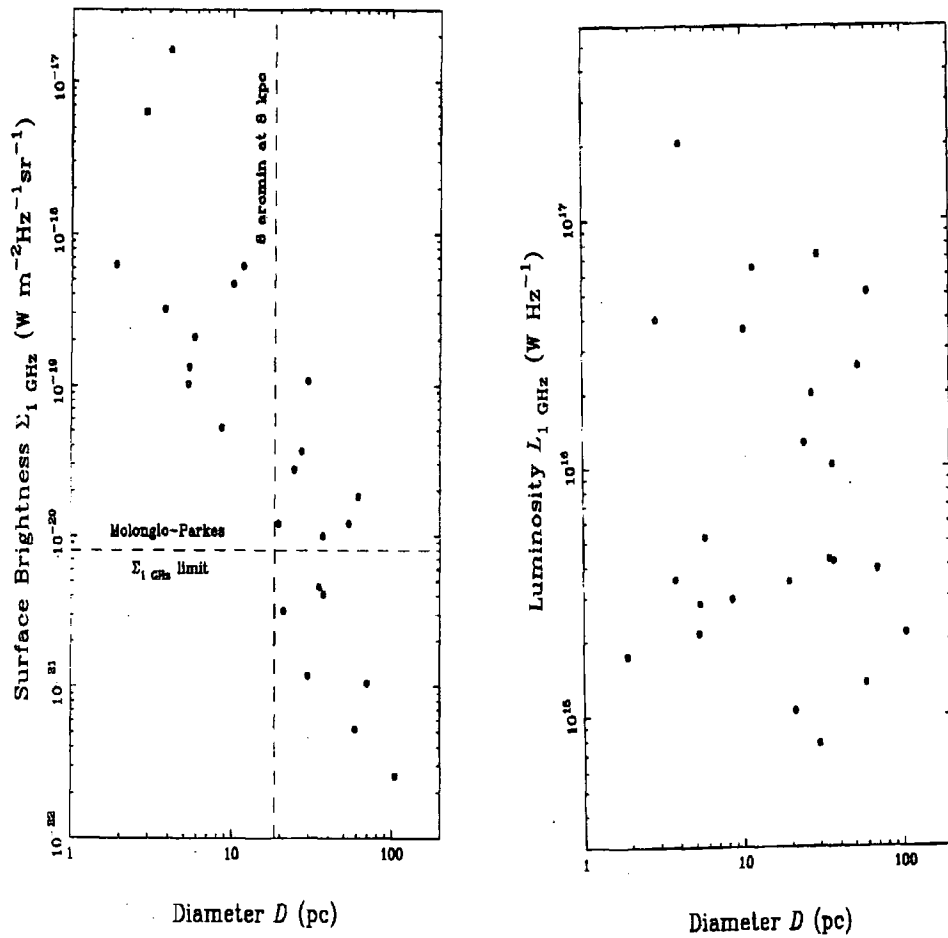


Figure 5.5: Surface brightness and Luminosity with Diameter, from Green 1991

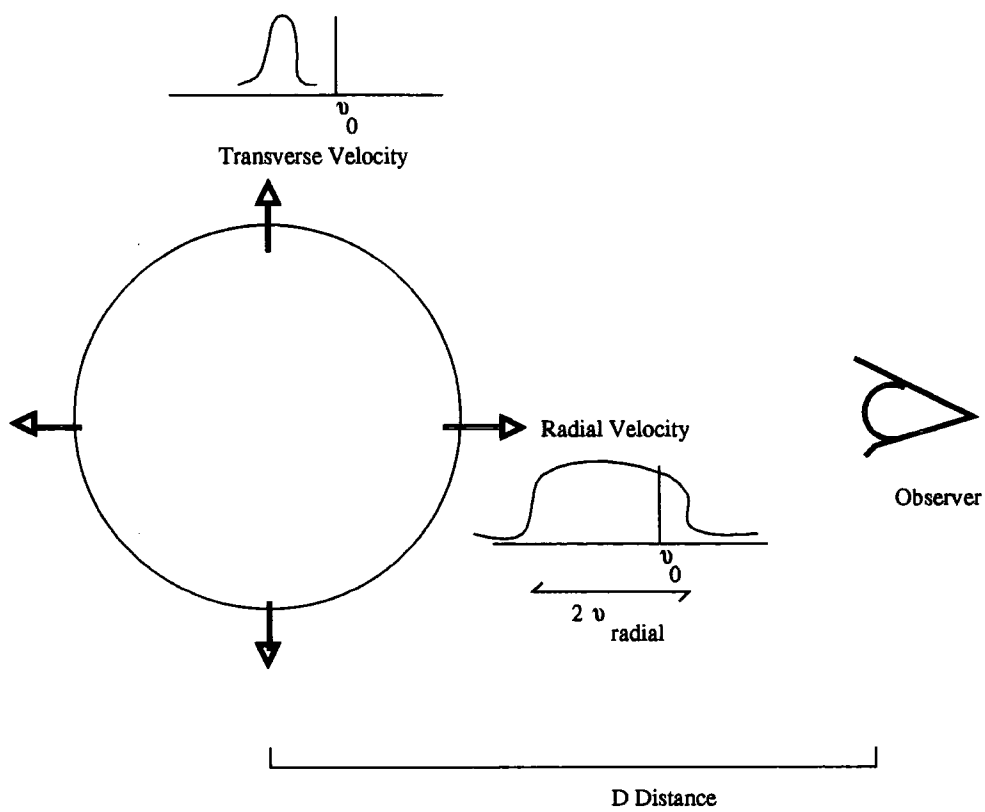


Figure 5.6: Distance from the filament proper motions and line velocities

5.3.4 Derivation of the distance from X ray emission

Winkler and Clark (Winkler and Clark, 1974) drew attention to the fact that by assuming thermal X-ray emission from SNRs (reasonable if in the adiabatic expansion regime and there is no pulsar driven emission) their distance can be estimated. From Sedov's analysis (as covered in the introduction), the relationship between the radius (R in parsecs), the energy released (ϵ_0 , in units of 10^{51} ergs) and the local density (n_0 in atoms per cc) is;

$$R \sim 14 \left(\frac{\epsilon_0}{n_0} \right)^{1/5} t_4^{2/5}$$

also the shock velocity, v_s kms^{-1} , in terms of the age, t_4 , in units of 10,000 years is;

$$v_s \sim 39R/t_4$$

Assuming that the material behind the shock is thermalised (as would be expected for a Sedov stage SNR) we get the temperature, T_* in Kelvin, as;

$$T_* \sim 11v_s^2$$

The mass swept up, the spherical volume and the ISM density is $M_{su} = 0.1n_0R^3$ and the luminosity in X-rays is $L_x = 3 \times 10^{56} R^3 n_0^2 P(\Delta E, T)$ and also $L_x = 1.2 \times 10^{44} D^2 F_x$.

These can be combined to give the Sedov distance, D_s ;

$$D_s = 8.7 \times 10^6 \epsilon^{0.4} P(\Delta E, T)^{0.2} \theta^{-0.6} F_{x0}^{-0.2} T^{-0.4}$$

or

$$D_s = 7.58 \times 10^6 \epsilon^{0.4} \epsilon^{0.2} \theta^{-0.6} F_{x0}^{-0.2} T^{-0.4} \quad (5.4)$$

We calculated ϵ in the program **Xspec** (Jacoby and Barnes, 1996) which gives the efficiency² per atom rather than per gram, $P(\Delta E, T)$. As the mean mass of a proton and an electron is half that of a proton, ϵ is a factor $2^{1/5}$ less than $P(\Delta E, T)$.

We often find that the published information is not quoted in this form, but as luminosity. Therefore it is useful to have the same expression in terms of luminosity rather than the unabsorbed flux.

$$D_s = 1.45 \times 10^{26} \left(\frac{\epsilon_0}{T} \right)^{2/3} \theta^{-1} \left(\frac{\epsilon}{L} \right)^{1/3} \quad (5.5)$$

²The ratio of the flux to the normalisation.

This formula was derived in the 1970's, but until ROSAT data were available there were few cases where it could be applied reliably. Kassim et al (Kassim et al., 1993; Kassim et al., 1994) showed that for the cases in which there is an independent distance estimate, the relationship is tight; D_{sedov} is found to be 1.1 ± 0.3 of $D_{independent}$. For this they assumed a standard SNe energy, ϵ_0 , of 10^{51} ergs. This represents a huge improvement in accuracy.

This technique has not been widely applied. Apart from the Kassim papers, only a single analysis based on this method has been performed (Finley and Ogelman, 1994), that on the G8.7-1.2 SNR. In this thesis this analysis has been conducted, where possible, on all the examples of southern SNR-pulsar associations we study, and we will demonstrate the predictive power and the limitations of this X-ray plasma model.

5.4 Pulsar Distances

5.4.1 Models of Electron Density

One of the observables for pulsars is the dispersion measure (DM), the change in pulse arrival time with frequency. The extra delay comes from the traversed ISM.

The dielectric constant ϵ , for zero magnetic field, is $1 - \omega_p^2/\omega^2$.

The group velocity for frequencies below the plasma frequency is;

$$v_g = c \left[1 - \frac{n_e r_0 \lambda^2}{2\pi} \right]$$

where r_0 is the classical electron radius $e^2/m_e c^2$, and λ is the wavelength.

The delay, t , on the pulse with frequency after travelling a distance L is therefore;

$$t = \frac{n_e r_0 c}{2\pi \nu^2} L$$

$$t = 1.345 \times 10^{-3} \nu^{-2} n_e L \text{ seconds or}$$

$$t = 4.15 \times 10^3 \text{ DM } \nu_{MHz}^{-2}$$

I.e. DM is $n_e L$ in units of pc cm^{-3} . Most pulsar distances are still derived from models of the free electron density (n_e) within the galaxy, i.e.

$$\frac{\int_0^D n_e(l) dl}{\int_0^D dl} = \frac{\text{DM}}{D}$$

This method, while better than most, does not and cannot, deal with variation of n_e on scales smaller than the model parameters.

A number of models were constructed over the years, the most successful for many years was that of Manchester and Taylor (Manchester and Taylor, 1981). However, as alternative distance measures were refined and improved, it was found to be an overestimate by factors of 1.5 to 2 for most directions. When one considers that the model took no account of the known parameters of the galaxy, such as the spiral arm structure, but was based on a smooth two component layer of dispersant material its limitations are not surprising.

5.4.2 Taylor and Cordes Model of electron density in our galaxy

The only model used nowadays is that of Taylor and Cordes (Taylor and Cordes, 1993). Its components are the two cylindrically symmetric components of Manchester and Taylor, and the spiral arms, determined from HII velocity observations. The Gum Nebula is also included, but is less significant. Its extent and density are reasonably well established, and are included in the model as constants.

The arm positions were experimentally determined more than twenty years ago, by Georgelin and Georgelin (Georgelin and Georgelin, 1976), and can be defined by the set of points in table 5.2 and interpolated using cubic splines.

| Arm 1 | | Arm 2 | | Arm 3 | | Arm 4 | |
|----------|-------|----------|-------|----------|-------|----------|-------|
| θ | r/kpc | θ | r/kpc | θ | r/kpc | θ | r/kpc |
| 164 | 3.53 | 63 | 3.76 | 52 | 4.90 | 20 | 5.92 |
| 200 | 3.76 | 120 | 4.56 | 120 | 6.27 | 70 | 7.06 |
| 240 | 4.44 | 160 | 4.79 | 170 | 6.49 | 100 | 7.86 |
| 280 | 5.24 | 200 | 5.70 | 180 | 6.95 | 160 | 9.86 |
| 290 | 5.36 | 220 | 6.49 | 200 | 8.20 | 180 | 10.37 |
| 315 | 5.81 | 250 | 7.29 | 220 | 8.89 | 200 | 11.39 |
| 330 | 5.81 | 288 | 8.20 | 252 | 9.57 | 223 | 12.08 |

Table 5.2: Coordinates of Fiducial points defining shapes of the model spiral arms, from Taylor and Cordes 1993.

The Gum Nebula is centred at $l = 260^\circ, b = 0^\circ$ and has an angular size of $\approx 40^\circ$ and a distance $d \approx 0.5$ kpc. It is modelled by a constant density of $n_e = 0.25 \text{cm}^{-3}$ for a radius of 130pc and then falls as a Gaussian with a 50 pc scale length. The parameters defining the Gum Nebula are poorly constrained by the data, thus they are fixed and not optimised.

The two remaining (and more important) components are axisymmetric sech functions, each with different scale lengths and electron densities for both radius and height. The total electron density (n_e) is then estimated by the combination of all these. Measuring x, y and z from the galactic centre;

$$n_e(x, y, z) = n_1 g_1(r) \text{sech}^2(z/h_1) + n_2 g_2(r) \text{sech}^2(z/h_2) + n_a \text{sech}^2(z/h_a) \sum_{j=1}^4 f_j g_a(r, s_j) + n_G g_G(u) \quad (5.6)$$

The first two components are the smooth parameters similar to the previous models and;

$$r = (x^2 + y^2)^{1/2} \quad (5.7)$$

$$g_1(r) = \text{sech}^2(r/A_1) / \text{sech}(8.5/A_1) \quad (5.8)$$

$$g_2(r) = \exp(-[(r - A_2)/1.8]^2) \quad (5.9)$$

$$(5.10)$$

The Gum Nebula component, g_G , is modelled by;

$$g_G(u) = \begin{cases} \exp(-[(u - 0.13)/0.05]^2), & u > 0.13 \text{kpc} \\ 1.0, & u \leq 0.13 \text{kpc} \end{cases} \quad (5.11)$$

and $u = [(x + 0.492)^2 + (y - 8.587)^2 + z^2]^{1/2}$ is the distance from the centre of the Gum Nebula.

Finally the arms are represented by the components, g_a and the weight f_j , where $j = 1$ to 4. The scale factors, f , for each arm are;

$$f_1 = f_4 = 1, \quad (5.12)$$

$$f_2 = \begin{cases} 1, & \theta < 215^\circ \\ 1 + (\theta - 215^\circ)/20^\circ, & 215^\circ < \theta < 235^\circ \\ 2, & \theta < 235^\circ \end{cases} \quad (5.13)$$

$$f_3 = \begin{cases} (3 + \cos[2\pi(\theta - 120^\circ)/40^\circ])/4, & 120^\circ < \theta < 160^\circ \\ 1, & \text{elsewhere} \end{cases} \quad (5.14)$$

$$g_a(r, s_j) = \begin{cases} \exp(-[s_j/w_a]^2) \text{sech}^2[(r - A_a)/2], & r > A_a \\ \exp(-[s_j/w_a]^2), & r \leq A_a \end{cases} \quad (5.15)$$

Here s_j is the distance to the nearest arm, j , i.e. $[(x - x_0)^2 + (y - y_0)^2]^{1/2}$, where $[x_0, y_0, 0]$ is closest point on the arm.

| Parameter | Adopted Value |
|---------------------------------|---------------|
| $n_1(\text{cm}^{-3}\text{kpc})$ | 0.01875 |
| $h_1(\text{kpc})$ | 0.88 |
| $A_1(\text{kpc})$ | 20 |
| $n_2(\text{cm}^{-3}\text{kpc})$ | 0.1 |
| $h_2(\text{kpc})$ | 0.15 |
| $A_2(\text{kpc})$ | 3.5 |
| $n_a(\text{cm}^{-3}\text{kpc})$ | 0.08 |
| $h_a(\text{kpc})$ | 0.3 |
| $w_a(\text{kpc})$ | 0.3 |
| $A_a(\text{kpc})$ | 8.5 |

Table 5.3: Parameters for electron density model, $n_e(x, y, z)$, from Taylor and Cordes 1993

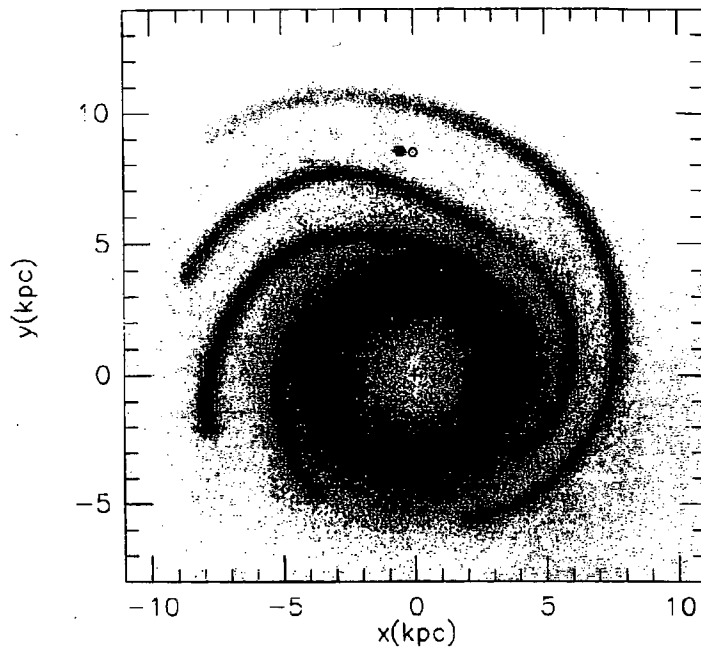


Figure 5.7: The electron density in our galaxy from the model of Taylor and Cordes 1993.

The fitted components are listed in table 5.3.

The model is used widely, almost excessively, to convert the dispersion measures to distances. However it is unable to deal with features smaller than those included, and there is also the risk of incorrectly scaled pulsars affecting the fit. The independent distance measurements which are used in the model are crucial, they are derived from parallax, limited to distances close to the earth; associations, which are dubious since this is usually what we are trying to establish (i.e. in our sample PSR1509 is defined as associated with RCW86); and finally kinematic methods, covered already.

All these details are easily available electronically, and the model is contained with subroutines which are easily obtained from, and even directly callable from the web, presently at <http://pulsar.princeton.edu/>.

5.4.3 Parallax Observations of Pulsars

Parallax measurements can in principle determine distances up to kiloparsecs. Radio telescopes can use transcontinental baselines and, with satellites coming on line, beyond. This allows the possibility to measure positions beyond thousandths of arc seconds. However, at present only three non-zero measurements have been made by Lyne et al. and Gwinn et al. (Gwinn et al., 1986) (Harrison et al., 1993). The limitations to the theoretical range are the instrument sensitivity to these very weak signals, the removal of the large systematic effects of the earth's motion around its axis and the changes in the signal delay paths due to the earth's atmosphere (Gwinn et al., 1986). Therefore all the published distances are less than a kpc.

| Pulsar | Parallax | Distance |
|------------|-------------------|----------------------|
| PSR0823+26 | 2.8 ± 0.6 mas | 357^{+97}_{-63} pc |
| PSR0950+08 | 7.9 ± 0.8 mas | 127 ± 13 pc |
| PSR1929+10 | 22 ± 8 mas | 45^{+24}_{-14} pc |

5.4.4 Associations with pulsars

Associations present the same basic limitations as the direct measurements of pulsar distances, in fact these are usually considered the more reliable since their strobing nature allows much better removal of systematic effects. The exception to this is the distance measurements to globular clusters where, because of the number of binary systems, there are many pulsars. The colours of the horizontal branch in the HR diagram and the models of stellar evolution allows the determination of the distances to these clusters, and thus, to a good fractional accuracy, these pulsars. Unfortunately this class is normally produced by being spun up from an aged pulsar in a low mass X-ray binary, and is therefore unlikely to have an associated SNR.

A few examples are to be found in the Magellanic clouds, but these are at distances which make observing SNRs very difficult. Therefore in those cases when associations are reliable, they are not useful.

5.5 Related techniques

There are a number of techniques which in combination can assist the distance estimation. For example there are several ways of measuring the pulsar transverse velocity. Then if the site of the original SN or the age of the pulsar is known the other can be derived, or more usually when the centre of the SNR and the pulsar age are known the velocity can confirm the birth of the pulsar was at the SNR centre.

5.5.1 Proper Motion of the Pulsar

Proper motion studies can also be done using very long baseline interferometry and tracking them over a long period. The pulsar velocity is then related by;

$$v_{pm} = 4.74\mu D \text{ kms}^{-1} \quad (5.16)$$

where μ is the proper motion in milliarc seconds per year, and D is the pulsar distance in kpc.

As milliarc seconds are resolvable for the best radio instruments the theoretical limits are of the order of 20 kms^{-1} in one year for distances of about 5 kpc away. Pulsars, with their very high transverse velocities have always been prime candidates for these studies. Most pulsars are in the process of being measured this way, but the results can take many years to become available. The proper motions of pulsars, as they increases with time, are much easier to measure than the parallax. If one has not got the instrumental precision one can increase the observing time. However this cannot in itself give the distance without a transverse velocity as well.

5.5.2 Scintillation velocity

Scintillation velocities which track the wave front of the pulsar signal through the interstellar medium are also useful, but require assumptions about the character and (mean) position of the ISM through which the signal has travelled. Their advantage is that, unlike the positional based methods, they do not require long observation times.

Scintillation methods (Lyne and Graham-Smith, 1990; Gupta et al., 1994; Cordes, 1986) use a model in which a thin screen of electrons between the observer and the pulsar causes an interference pattern as the rays

from the pulsar recombine after taking different paths through the screen. This pattern of the radiation alters with frequency and time as the line of sight moves across the ISM. The contributors to this movement are the pulsar itself, the screen and the earth. Fortunately the pulsar contribution dominates that of the earth and that of the screen as it is so much larger. Furthermore if several measurements are taken over a year, the component due to the Earth's motion changes and can be removed, and some estimate of the pulsar direction be made. The speed of the diffraction pattern transverse to the line of sight is $v_{ISS} = S_I/\tau_{ISS}$ where S_I is the spatial scale of the diffraction pattern, and τ_{ISS} is the time scale of the pattern. τ can be measured directly from the autocorrelation of the pulsar signal with time, but S_I will much greater than that reachable with earth bound baselines. The drift velocity is of the order of 100 kms^{-1} and with a lifetime of around ten minutes that leads to a requirement of a 60000 km baseline to measure the decorrelation. Fortunately S_I can be estimated from the bandwidth of the autocorrelation of the signal ($\Delta\nu$), with frequency (ν). S_I is $\propto (cD\Delta\nu_{ISS})^{1/2}/\nu$ (Rickett, 1977). Thus the estimate for the velocity becomes;

$$v_{ISS} = A_{ISS}(D\Delta\nu_{ISS})^{1/2}(\nu\tau_{ISS})^{-1} \quad (5.17)$$

The constant A_{ISS} is model dependent. Using simplistic scaling considerations Lyne and Smith (Lyne and Smith, 1982) found $A_{ISS} = 2 \times 10^4 \text{ km}^{1/2}\text{s}^{-1/2}$. Cordes derived a value by assuming a Kolmogorov spectrum of the ISM turbulence to give $A_{ISS} = 1.27 \times 10^4 \text{ km}^{1/2}\text{s}^{-1/2}$ (Cordes, 1986). In this thesis the value from Gupta (Gupta et al., 1994) of $3.85 \times 10^4 \text{ km}^{1/2}\text{s}^{-1/2}$, also derived for a Kolmogorov spectrum, is used. The difference between the values of Cordes and Gupta et al. could possibly be in the detail of the definition of $\Delta\nu_{ISS}$ or τ_{ISS} . Insufficient details are given in Cordes' paper. Gupta et al. point out the difference, but are unable to explain the Cordes derivation. The fit of the Gupta et al. version of the model to the data is clearly the best, as it requires the smallest secondary correction. This 'lever arm' term is to correct for pulsars above the plane, where the fall off the galactic electron density (with distance above the plane) shifts the centre of the diffraction screen towards the observer. With an A_{ISS} of $3.85 \times 10^4 \text{ km}^{1/2}\text{s}^{-1/2}$ the scale height is now a more physically reasonable 1 kpc rather than 50 pc needed to correct the Cordes version. It should be noted that the reasonable v_{ISS} to v_{pm} fits based on the Cordes model used the earlier estimates for the pulsar distances. These were recalculated using the new Taylor and Cordes galactic n_e model in Gupta et al., where no other estimates were available. For the proper motion measures the v_{pm} scales linearly with distance, but for v_{ISS} it is a function of the square root.

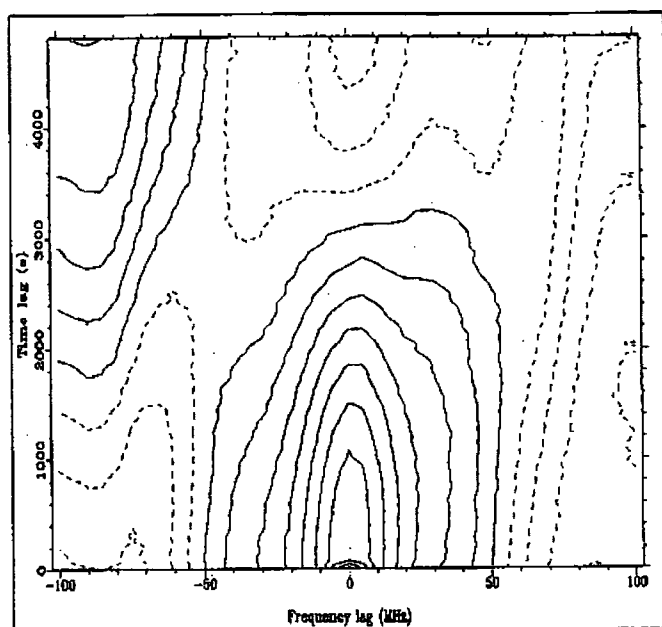


Figure 5.8: Autocorrelation of the pulsar signal with frequency and time. Figure 1 from Evidence against the PSR1706 association, Nicastro et al. 1996

Therefore the ratio of v_{pm} to v_{ISS} is sensitive to errors in the pulsar distance.

The autocorrelation of the signal with time and frequency gives us values for both $\Delta\nu_{ISS}$ and τ_{ISS} , τ is defined as the point where the correlation falls to $1/e$ of the maximum and $\Delta\nu_{ISS}$ is where the correlation is $1/2$ the maximum.

5.5.3 Pulsar velocity from the Pulsar Wind Nebula

Just as the SN will develop a shell, a pulsar moving through the ISM ejecting particles will generate a pulsar wind nebula, PWN (Frail and Scharringhausen, 1997). These are created in two ways. One is from a basically static pulsar which is losing energy via radiation and particle losses. This sets up a shock front described by the same equations that govern the development of the SNR but with the energy being steadily provided by the pulsar energy loss. This has been observed in the Crab nebula, although further analysis on this has failed to nail down all the details (Rees and Gunn, 1974). For

most cases the rate of energy loss is too small to produce an observable PWN this way. The static shock radius, R_s , in pc is;

$$R_s = \left(\frac{\dot{E}}{4\pi\rho_0}\right)^{1/5} t^{3/5} \approx 2.1 \dot{E}_{34}^{1/5} t_5^{3/5} n_0^{-1/5} \quad (5.18)$$

where \dot{E}_{34} is the rate of the energy loss of the pulsar in units of 10^{34} ergs/sec, t_5 is the age in 10^5 years, and n_0 the number density.

There is also a nebula produced by the ram pressure of the pulsar as it moves through the static ISM, with the outflow pressure balanced by the external ISM pressure. This will be more important than the static when the pulsar velocity is greater than the expansion velocity of the static shock PWN. The bow wave radius, R_w , of these type of nebulae falls where the pulsar ram pressure, $P = \rho v_{pulsar}^2$ balances the radiation pressure or the Poynting flux ($\dot{E}/4\pi cR^2$). An archetypal example be seen in figure 6.2;

$$R_w = \left(\frac{\dot{E}}{4\pi c\rho v_{PSR}^2}\right)^{1/2} \approx 0.475 \dot{E}_{34}^{1/2} n_0^{-1/2} v_{150}^{-1} D_{kpc}^{-1} \text{arc seconds} \quad (5.19)$$

This becomes the more significant when the pulsar velocity (v_{PSR}) is greater than that of the expansion of the static shock³, $\dot{R}_s = 3/5 \left(\frac{\dot{E}}{4\pi\rho_0}\right)^{1/5} t^{-2/5}$. Given that the R_w will be smaller than R_s , the related nebula would also be expected to be brighter.

By observing the size of this nebula we can make certain deductions about the pulsar, in particular its speed. We should also see a comet-like trail in the bow wave from which the radiation life time, t_{rad} , and the direction of motion of the pulsar can be derived. This kind of nebulosity has been observed, as will be discussed in the description of the PSR1757-24, i.e. section 6.2. However a recent paper which gave the results of a large scale survey for PWN (Frail and Scharringhausen, 1997) reported that *none* of the targeted sources showed signs of a PWN. The upper limits to the efficiency of energy transfer from the spin down of the pulsar to the PWN was found to be less than about 2×10^{-4} % for nearly all the 21 examples, and those showing a significantly higher efficiency were due to the lower \dot{E} of these pulsars and the limiting instrument sensitivity. Of course the experimental arrangement to observe these was not ideal. The observations were done with the VLA with missing small spacings which leads to loss of broad scale structure. However their sensitive scales were $0.8''$ to $20''$, and one would expect that this range would be perfectly adequate for the predicted PWN scales.

³In (Frail and Scharringhausen, 1997) the authors lose the factor of 4π , which further reduces the range where the static shock is important. (Frail, 1997)

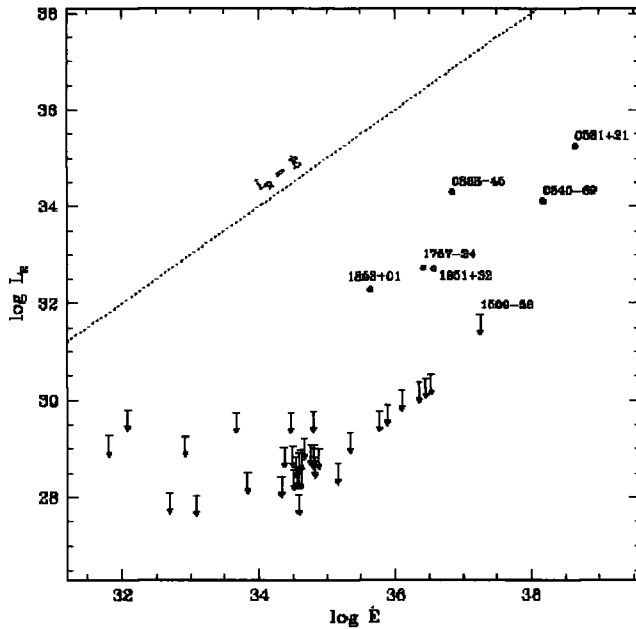


Figure 5.9: Efficiency of PWN generation, with rate of energy loss, from the survey of Frail 1997. The dotted line represents 100% efficiency. All new results from that paper are upper limits. Labelled PSR are from other works.

The absence of expected PWN has been used in the literature to rule out associations, using the absence of a nebula to provide a upper limit to the pulsar velocity (Frail et al., 1994a). In the light of the wide spread failure to find these nebulae it would seem premature to use this relationship until there is fuller understanding of the requirements for their production.

5.5.4 The Pulsar Age, τ_c

The age of the pulsar is the easiest parameter to derive. The major assumption used for pulsar dating is that the braking index is that due to the magnetic dipole. The rate of change of the moment of such a dipole spinning with angular momentum Ω is;

$$d(I\Omega^2/2)/dt = I\Omega\dot{\Omega}$$

For example for a magnetic dipole, of perpendicular magnetic field M_{\perp} , the rotational energy loss would be (Lyne and Graham-Smith, 1990);

$$I\Omega\dot{\Omega} = -2/3M_{\perp}^2\Omega^4c^{-3}$$

The loss moment in this case follows a cubic power law. When there is outflowing of particles these can stretch the magnetic field lines in the radial direction and reduce the rate of falloff of the field, thus the rotational energy loss is less. Alternatively there could be another parameter which changes with time, such as the alignment of the magnetic and spin axes (Blandford and Romani, 1988). Therefore we assume, whatever the loss mechanism, that the pulsar starts off with the a high angular velocity and decays following a power law, which is to be determined;

$$\dot{\Omega} = -k\Omega^n \quad (5.20)$$

The integration leads to (if $n \neq 1$)

$$t = -\frac{\Omega}{(n-1)\dot{\Omega}} \left[1 - \frac{\Omega_i^{n-1}}{\Omega^{n-1}} \right]$$

where Ω_i is the starting angular velocity, assumed to be much greater than Ω , the observed angular velocity. That means that the characteristic age, τ ;

$$\tau = -\frac{1}{n-1} \frac{\Omega}{\dot{\Omega}} = \frac{1}{n-1} \frac{P}{\dot{P}} \quad (5.21)$$

Taking $n = 3$, i.e. the pure magnetic braking, we therefore have $\tau = \frac{1}{2} \frac{P}{\dot{P}}$, called the characteristic age. For a limited number of cases the very small \dot{P} has been measured; the braking index has been found always to be smaller than three.

| Pulsar and braking index | |
|--------------------------|-------------------|
| B0531+21 | 2.51 ± 0.01 |
| B0833-45 | 1.4 ± 0.2 |
| B1509-58 | 2.837 ± 0.001 |
| B0540-69 | 2.24 ± 0.04 |

Using the characteristic age would therefore have underestimated the actual age. Furthermore young pulsars might be expected to be still near the initial spin period and this also leads to an underestimate. We cannot correct for these without knowledge of the braking index and the starting period. This can be done only on those pulsars for which we have both the actual age (from an observed SN) and the second derivative of the period. This is why the possible identification of B1509-58 with SN185 is of such importance, and will be discussed in a later section.

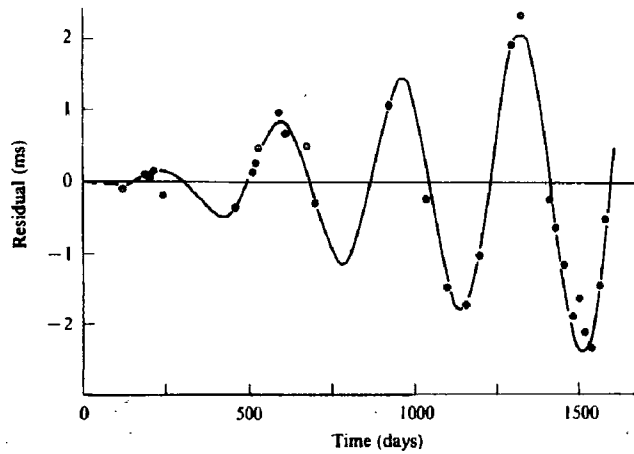


Figure 5.10: Fitting timing residuals to get a proper motions, from Pulsar Astronomy, 1990

Also related to the accuracy of the timing information is the ability to place the pulsar very accurately on the sky. The barycentric correction, which has to be applied to the pulsar signal arrival times, is a function of the pulsar position. A slight error (or movement) in the pulsar position gives a shift in the residual time delay over and above that due to P as shown in figure 5.10.

Unfortunately the effect of timing noise can completely mask this effect. Given that timing noise is particularly associated with the younger pulsars the method is inappropriate for our selected sources. No example could be found where time positions have been used to measure parallax, although it has been used for the proper motions of pulsars and has sufficient (theoretical) accuracy to give these results.

5.5.5 Morphology

It is hard to turn the 'hand waving' description of the morphology of a SNR into a tool of objective analysis. Given the "one shot" nature of astronomy it is far from easy to link the features across the image; however several things are clear.

If the expansion is into a uniform ISM, and spherically symmetric, the velocity will be equal in all directions and a circular remnant will result. If one has such a circular remnant its centre would be the site of the SN. This is not a reliable assumption as it is easy to construct cases where a

circular SNR can be offcentred from the site of the SN. A simple model with a gradient in the SNR can be found in Frail et al. (Frail et al., 1994b).

The angle between the SNR centre and the pulsar can be thought of as parameterising the pulsar age (Gaensler and Johnston, 1995a) (Gaensler and Johnston, 1995b). The pulsar velocity, from its birth time kick, is a constant and the order of hundreds of kilometres per second. The shock front velocity starts at thousands of kilometres per second, but decreases steadily. The ratio, β , of the angle from the centre to the pulsar over the angular diameter of the remnant is monotonically increasing with time. Gaensler and Johnston modelled a random distribution of the SNRs and pulsars based on the known birthrate and lifetime parameters. They found that a large number of coincidental associations were made if the allowable alignment was $\beta > 1$. They argue that this parameter can be used with the age to comment on the likelihood of association, and in particular that any young association in which $\beta > 1$ is unlikely. Without denigrating its use, an estimation for each individual association would seem to be more sensible; in particular this method ignores matches in distance estimates, and misshapen SNRs.

The SNR synchrotron emission will be more polarised than that of the general background as the trapped magnetic field in the shell will be tangentially aligned, indeed polarisation is one of the tests for a SNR. From the change of polarisation with frequency one get the rotation measure (RM). The right, or left, handed polarisation of the radiation is retarded, or advanced, travelling through the ISM.

The ϵ when a magnetic field is present is;

$$\epsilon = 1 - \frac{\omega_p^2/\omega^2}{1 \pm \omega_c/\omega}$$

Where $\omega_c = e\mathbf{B}/m_e c$. Its sign depends on the hand of the rotation. The effect of ϵ was covered in section 5.4.1.

The dispersion measure records the column density of the ISM travelled, and the rotation measure gives the mean magnetic field. However for our studies of SNRs we are interested in only the local (to the SNR) magnetic field, so the galactic contribution is assumed to be constant and removed, after being calculated from the RM. This means that the variation across the source lies in the variation in the starting synchrotron polarisation, which is due to the magnetic field of the SNR shell. If the magnetic field traces the tangent to the shell, we know that we are looking at a wave front of swept up material (as the magnetic field is basically pinned to the ISM). We can use this observation to associate different parts of the shell.

5.6 Conclusions

We have reviewed all the common methods of estimating distances for both pulsars and SNRs. Particular emphasis is placed on the relatively unused X-ray plasma method, and the problems with the inconsistent results from the pulsar wind nebula method.

Chapter 6

Description of some selected SNRs

“You know my methods, apply them.” Holmes, S; Study in Scarlet.

6.1 Introduction

A group of known SNR which are possibly associated with pulsars were selected as one of the most interesting studies which we could do with the MRT.

SNR have a short lifetime¹ of the order of 60 kyr, while pulsars have a lifetime approximately 100 times longer. SNe are either the type I, which are not expected to produce a pulsar, or type II which usually do, see section 1.8. Hence a significant fraction of SNRs should have an associated pulsar, and all young pulsars are expected to have an associated SNR. However it is not always possible to observe any association, and even when candidates are found it is hard to prove that they are resultant of the same SN. Pulsars may not be beaming in our direction and the evolution of SNRs is dependent on both initial conditions and environs, which are hard to determine. Associations have been postulated for all the young pulsars observed (Frail et al., 1994a), but now many of these are being questioned (Kaspi, 1996)

The MRT, an instrument with completely filled uv coverage, low frequency and a southern declination is ideally suited to investigate these. The filled uv coverage gives it much higher large scale surface brightness sensitivity, the lower frequency results in higher non-thermal sensitivity and the southern declination is an ideal positional placement for observing the

¹in comparison with the time it takes to write a thesis

galactic centre where the majority of these associations are to be found. Furthermore the wide beam allows us, in fact forces us, to survey the sky much further from the galactic plane than most other studies.

The discussion will cover the following SNRs selected from the literature (Green, 1996);

- G5.4-1.2 with PSR 1758-23
- G8.7-0.1 with PSR 1800-21
- G315.4-2.3 with SN 185
- G320.4-1.2 with PSR 1509-58
- G343.1-2.3 with PSR 1706-44

Table 6.1 lists the instruments from which the best maps available were obtained. The problems and conclusions reached from analysis of these are summarised. While some of these are old conclusions, and are indicated as such, others use new data or new methods.

| Instrument | Wavelength(cm) | Resolution |
|----------------------|----------------|-------------|
| TPT | 520 | 10' |
| MRT | 198 | 4' |
| MOST | 36 | 43'' |
| VLA, A Configuration | 21/4 | 1.4''/0.2'' |
| VLA, D Configuration | 21/4 | 50''/9'' |

Table 6.1: Radio Telescopes, their frequency and resolution

In this chapter all the selected associations are shown to be tenable; they will be classed according to Kaspi's method of rating (Kaspi, 1996) covered in the introduction 1.11. For the sources, G5.4-1.2 and G8.7-0.1, no new results are introduced, but the analytical methods are evaluated. The evidence for and against is weighed up, and the difficulties in confirming associations explained. Both G315.4-2.3 and G320.4-1.2 have been proposed as remnants of a possible SN in AD185 (Clark and Stephenson, 1977; Thorsett, 1992), but recently they have been discounted; (Schaefer, 1993b; Strom, 1994; Chin and Huang, 1994; Schaefer, 1995; Schaefer, 1996). In the section on the source G315.4-2.3 the Chinese records of this SN are discussed. For both this source and for G320.4-1.2 we show that the objections to the interpretations of the records are not sustainable. For the last two SNRs, G320.4-1.2 and G343.1-2.3, the X-ray thermal plasma model is used to good effect to derive distances to the shell, thereby clearly linking the pulsar and the SNR. Potential problems that others have raised are reviewed,

and dismissed. Finally the association between G343.1-2.3 and PSR1706-44 (McAdam et al., 1993) is reexamined in detail, and shown to be convincing. The objections to this unpopular postulate (Frail et al., 1994a; Nicastro et al., 1996) are shown to be incorrect.

6.2 The SNR G5.4-1.2

The source is often called the Duck or the Swan, and the various portions are called, or have been called Milne 56, G5.3-1, G5.4-1.2, G5.27-0.9, PSR1758-24 and PSR1757-24. The assumed centre of the continuum source is no longer the brightest point, and a separate nebula has been resolved to the west. The position of the pulsar, originally placed at a RA of 17^h58^m has been refined to a RA of $17^h57^m55^s$. The question to be addressed is whether this is a SNR accidentally aligned with a remarkable degree of coincidence with the pulsar, or that they are associated and interacting. The association has compelling evidence both for and against. If distance measures for the remnant and the the pulsar roughly agree, and there is clear evidence for the pulsar interacting with the SNR shell one would expect to make the association. However since the pulsar is outside the shell of the SNR its velocity must be much greater than the norm (Lyne and Lorimer, 1995).

6.2.1 First Observations of the Shell and the Pulsar

The SNR was first observed by Clark et al. (Clark et al., 1975) using the original Molonglo telescope at 408 MHz. The emission was non-thermal, but it was not obviously a remnant. Its peculiar “v” morphology (which gives it its common name) led Becker and Helfand (Becker and Helfand, 1985; Helfand and Becker, 1985) to propose that it was a new kind of radio source. However a new high resolution observation by MOST, at 843MHz, revealed a lower surface brightness extension to the West (Caswell et al., 1987). The slightly extended compact source at the edge of the bright region, G5.27-0.9, which was within the error box of the known PSR B1757-24 also was observed. This PSR, at first called 1758-24, was discovered by Manchester et al. in a survey for short period pulsars (Manchester et al., 1985). The pulsar age deduced from the period and the period derivative is 16,000 years, but the braking index from the second derivative is 38 ± 3 (as in equation 5.20). This is obviously in error, and probably due to a glitch between observing runs. Giant glitches have been observed in the periodicity of PSR1757-24, as expected for such a young pulsar (Lyne et al., 1996).

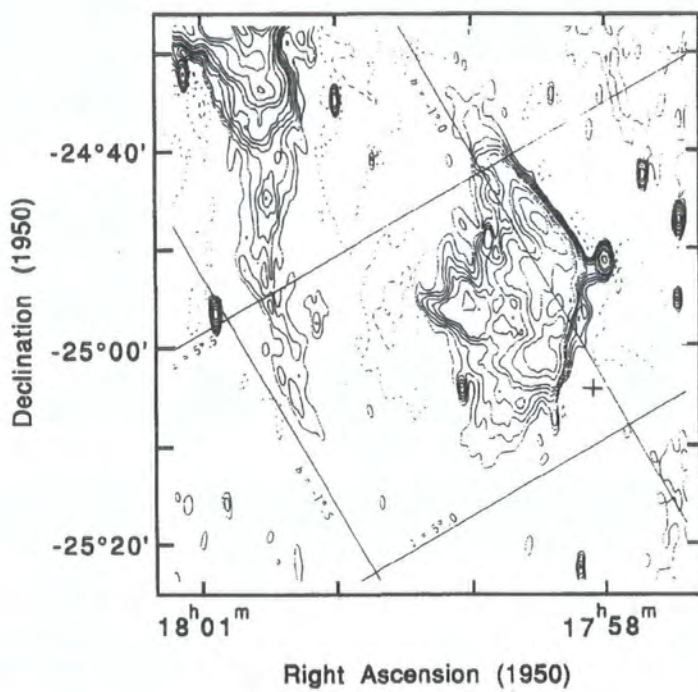


Figure 6.1: The MOST image of G5.4-1.2 that first showed the far side of the remnant, Caswell et al. 1987

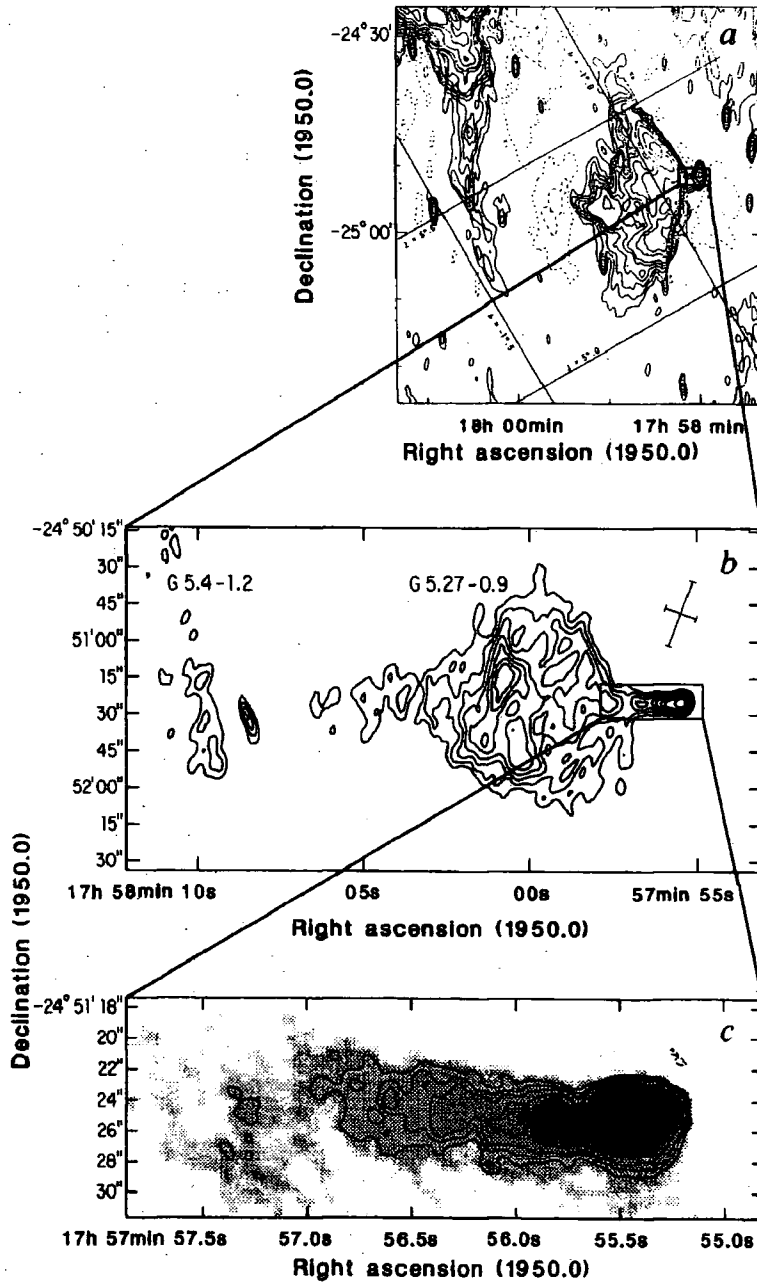


Figure 6.2: The progression of images of the PSR nebula. The Caswell et al image from MOST (a) with a beam size of $110'' \times 42''$. Expanded from the marked region is the second image (b) from Becker and Helfand ($7'' \times 4''$), and expanded from that is the highest resolution image of Frail et al (c) $2'' \times 1.3''$

6.2.2 Emission driven by the pulsar

Figure 6.1 shows the high resolution MOST image of G5.4-1.2, and figure 6.2, that of Frail and Kulkarni (Frail and Kulkarni, 1991), shows a progression of observations resolving the pulsar position. The lower two are both from VLA, at 20 cm in the lower resolution, central, image. The final, highest resolution, image is at 6cm. As we see the G5.27-0.9 is not the site of the PSR, which is in the westward projection. Here we see an archetypal example of a pulsar wind nebula (PWN) (section 5.5.3). It is hard to explain how a young pulsar could be outside the shell of its progenitor (Gaensler and Johnston, 1995b) as the required pulsar velocity has to be greater than that of the shock front; here either very low shock or high pulsar velocity would be required. This difficulty remains irrespective of distance. However there seems to be a bridge of emission between the western edge of the shell, G5.27-0.9 and the PWN around PSR1757-24.

6.2.3 Interaction of the pulsar with the SNR shell as a whole

The spectral index of the shell, going away from the pulsar, provides some evidence of interaction. Frail et al. (Frail et al., 1994b) made measurements of this with respect to the angle around the shell. The zero angle is defined as towards the pulsar and $\alpha_{0.33}^{1.4}$, the spectral index from 0.33 to 1.4 GHz, changes from -0.04 nearest the pulsar to -0.6 when the angle is 60° . The flatter spectral index is usually a sign of the injection of energetic particles from the pulsar. While this could be caused by an increase in the ISM density as one approaches the galactic plane it is more likely that this is further confirmation of the association.

6.2.4 Estimates of the Pulsar Velocity

We have no good distance estimates for the G5.4-1.2 shell. The X-ray method is not possible as there is a very strong source, GX5-1, which dominates all ROSAT images of the area. The HI method is not very accurate as the line of sight is very close to the galactic centre. However, despite these difficulties, Frail et al (Frail et al., 1994b) succeeded in measuring the HI absorption to G5.4-1.2, G5.27-0.9 and the PSR1757-24. There are no bright sources which can be identified beyond the association, so only a lower limit to the distance can be made. While the errors are large, the values indicate a distance greater than 4.3 kpc. This must be considered as ill-constrained. The DM is $298 \pm 1 \text{ pc cm}^{-3}$ which gives a pulsar distance 4.6 kpc, using the Taylor and Cordes model. The model errors are usually taken as 20%, i.e. 1 kpc. This is the best estimate available, and probably cannot be improved upon.

The centre of the remnant (in 1950 coordinates) is $17^h59^m00^s$, $-24^\circ55'$, and the pulsar position is at $17^h57^m55^s$, $-24^\circ51'24''$, giving an angular separation of $16'$. This requires a proper motion of 60 milliarcsec per year (equation 5.16) and if the distance is 4.6 kpc a velocity of 1300 kms^{-1} . Assuming the more usual distance of 6 kpc gives a velocity of 1700 kms^{-1} . No VLBI observation of the proper motion have been published yet, although have been reported as being underway (Frail and Kulkarni, 1991). There are no scintillation measures, and since the PSR glitches (Lyne et al., 1996) timing positions are not possible. The paucity of observations is due to it being a very weak PSR of 1 mJy at 1.4 GHz.

To make the association the velocity required to move the pulsar from the centre of the shell to its present position is at the higher, or highest, end of the velocity distribution as shown in figure 6.3 (Lyne and Lorimer, 1995). The best available figures based on the proper motions and the latest distance estimates for *young* pulsars (where the fastest one have not had a time to leave the galactic plane) give a mean and r.m.s. v_t of about 300 kms^{-1} and 499 kms^{-1} . The distribution is not Gaussian, but the probability of a 1300 kms^{-1} in a randomly selected pulsar is of the order of 3%, and even less for a v_t of 1700 kms^{-1} .

The predicted size of the PWN for a distance of 6 kpc, from equation 5.19, is $R_w = 0.11'' / (n_0^{1/2} v_{1700})$. As the PWN has a radius of $2''$ we require either the velocity to be 95 kms^{-1} , or the density to be about $3 \times 10^{-3} \text{ atoms cm}^{-3}$. At the DM distance of 4.6 kpc, the velocity required is 124 kms^{-1} . As mentioned previously, the PWN method has consistently failed to meet expectations, so its failure to reproduce the required pulsar velocity may not be of significance. Also it would seem that previously, when the pulsar was passing through the area of G5.27-0.9, the pulsar wind nebula was even bigger, which would require a even lower density (assuming the pulsar speed is not increasing). Conceivably there might have been a sudden change in the rate of energy loss, but there are no theories to explain how this might happen.

6.2.5 Other Observations

Our MRT maps (figure 4.8) are not yet at a resolution to add much to the detailed discussion of the remnant, except to show that the body of the remnant, between the wings of the Duck and the eastern ridge, shows more complete signs of emission than the previous higher frequency surveys. This confirms that these ridges are related and from the same object.

There is a reported optical detection (Zealey et al., 1979), but this is of a wisp which is not near any part of the observed SNR radio shell, being nearly a degree to the west of the pulsar and the excited shock front, at

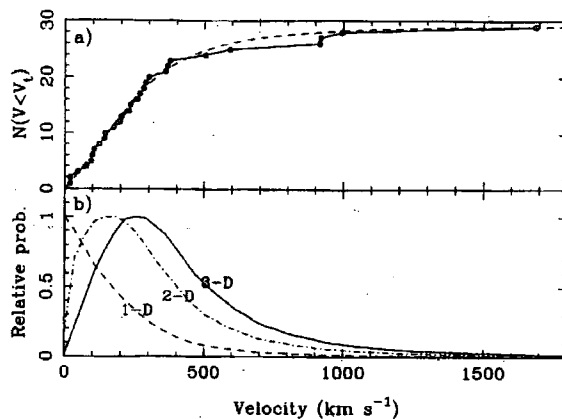


Figure 6.3: The cumulative distribution of pulsar velocities, and the derived velocity distributions in one, two and three dimensions; from Lyne and Lorimer JApA 1995

$17^h57^m00^s - 24^\circ30'$. It is almost certainly not related, although if it were the required PSR speed would become much more reasonable as it would now be near the centre of the remnant.

6.2.6 Conclusions

In summary there is strong evidence that at least some of the radio emission is being driven by the pulsar. Furthermore the absorption of the PSR, and the various parts of the SNR all have the same relative velocity to us. This places them at the same kinematic distance, although the model is weakly constrained, being close to the galactic centre. The kinematic distance matches the dispersion measure distance. The association would be unquestionable if the required velocity was not so high. Such a high velocity generates a PWN. The observed PWN has a derived velocity a tenth of the expected. One solution would be to take the centre of the SN not the geometrical centre, but displaced towards the pulsar (Frail et al., 1994b). In fact the unexpected high velocity of the association could be used to argue against the simplistic placing of the SN at the geometric centre as is normally assumed. Largely because of the pulsar nebula this appears to be one of the strongest associations in the southern sky.

6.3 G8.7-0.1

This SNR is part of the W30 galactic complex which has both thermal and nonthermal components. It has been mapped at frequencies from 57.5 MHz to 10 GHz, as reviewed in Kassim and Weiler(1990). The MRT map in Figure 4.9 shows a similar distribution of emission to the VLA map at 330 MHz. Detailed comparison with that and the 57.5 MHz map, where the edge of the complex along $b = -0.4^\circ$ appears in absorption, help to distinguish the thermal and nonthermal components. The young ($\sim 16,000$ yr) pulsar B1800-21 is possibly physically associated with the SNR as the evidence is that they are both at a distance of ~ 4.5 kpc. If, however, the pulsar was born near the present geometric centre of the SNR a very high transverse velocity is implied.

6.3.1 Previous Observations of the Shell

W30 has been comprehensively studied at 57.5 MHz with the Clark Lake telescope, TPT, at 330 MHz and 1.5GHz at VLA, plus the X-ray frequencies, and now by MRT map at 151MHz. The complex is a mishmash of non-thermal and thermal emission and absorption. This is a perfect example of the complications that bedevil the mapping SNRs expanding into complex media. The TPT map was complicated by absorption, VLA at 1465, 1508 and 1665MHz, even in the C/D configuration (that is, including the lowest spatial frequencies) failed to observe it (Braun et al., 1989). The Parkes 6 and 11 cm single dish surveys picked it up, but saw more of the HII regions which border it. However the VLA 327MHz survey mapped the remnant completely (Kassim and Weiler, 1990), as do the MRT maps.

The supernova remnant itself was first mapped in detail at 57.5 MHz at Clark Lake (using the correlator now at MRT) by Ödegard (Ödegard, 1986). He realized that there would be a large amount of absorption on the southern edge. A VLA image of the region around the pulsar was made by Braun et al. (Braun et al., 1989) using the D array at several frequencies around 1500 MHz. This resulted in an improved position for the pulsar but they saw no evidence for a SNR in the immediate vicinity of the pulsar. Later observations at roughly the same frequency, by Kassim and Weiler (Kassim and Weiler, 1990), also saw only patchy nebulosity. However, they attribute the emission seen on their maps to part of the SNR, as they also had evidence from a low frequency image made at the same time.

The lower frequency VLA images of the region at 327 MHz were produced, firstly by Kassim and Weiler (Kassim and Weiler, 1990) and then, as the problems of this new VLA observing frequency were solved, by Frail, Kassim and Weiler (Frail et al., 1994b). From these observations it was pro-

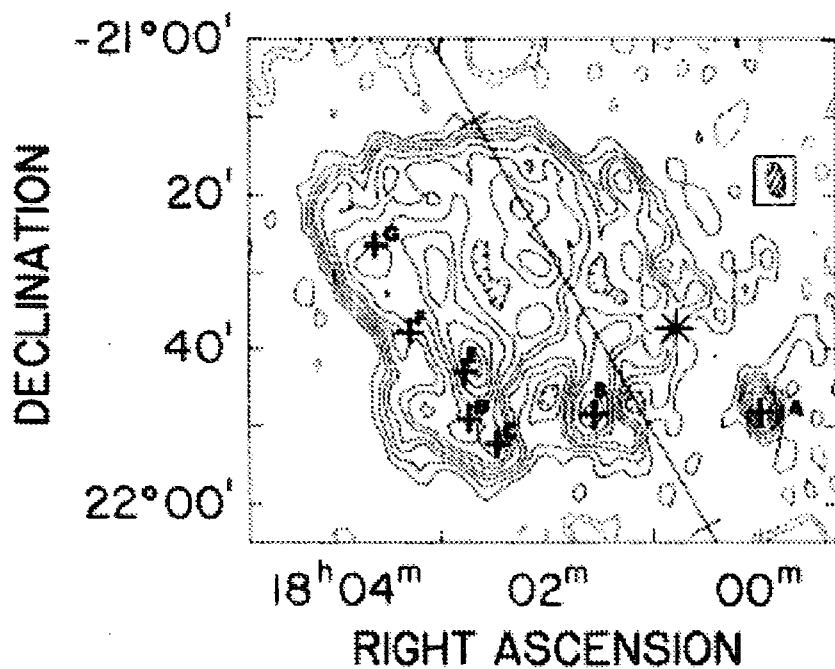


Figure 6.4: The VLA 327 MHz map from Kassim and Weiler (1990), that first showed the full extent of W30. The HII regions that were all that was seen at high frequencies and absorbed at low frequencies are labelled with the letters A through to G. The pulsar position is marked with a star.

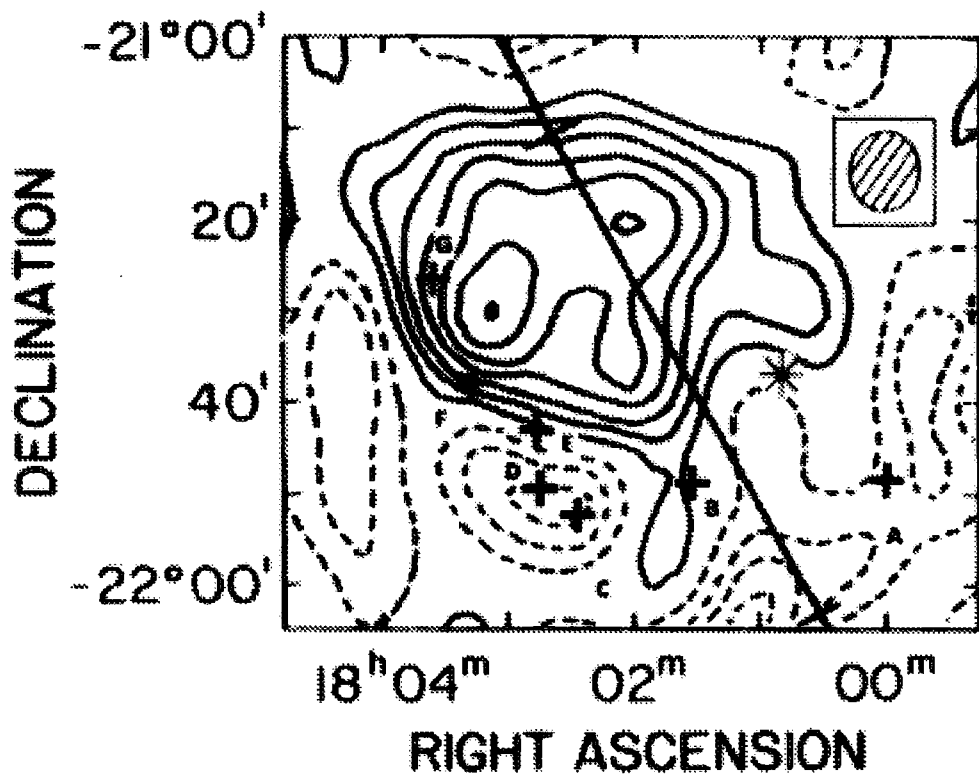


Figure 6.5: The TPT 57.5 MHz map by Ödegard, from Kassim and Weiler (1990)

posed that W 30 and PSR B1800-21 were associated. They found that the remnant itself was larger than that seen by Ödegard (Odegard, 1986) (figure 6.5) and the improved position of the pulsar was consistent with it being in the outer regions of the SNR. In figure 6.4 taken from the Kassim and Weiler paper, the HII regions are labelled A through G. At the high frequency of the Duncan map these HII clouds clearly stand out over the SNR emission. On the TPT maps most, but not all, of these clouds are in absorption. The assumption is that those clouds not absorbing the SNR emission are behind it; those absorbing are of course in front. Once the distances to these clouds are known the SNR is bracketed between them. Clouds C and D are definitely in the foreground as they absorb, E is an extended background object and therefore would be expected to absorb if positioned in front. Sources B,F and G are classified as unknown by Kassim and Weiler. They are very compact therefore would not produce a large absorption on the TPT map because of the beam size at that frequency. Kassim and Weiler then used H110 α and H76 α recombination line measurements to the HII clouds to derive distances for regions B-G of 6 ± 1 kpc. All of these have a velocity of 40 ± 5 kms $^{-1}$. Finally the velocity of region A is much less, at 22 kms $^{-1}$ with an equivalent distance of about 3.5 kpc, and being further from the body of the complex it is assumed to be unrelated.

In the analysis of the HI absorption of the pulsar spectrum performed by Frail et al. (Frail et al., 1991), they gave a lower limit of 24 kms $^{-1}$ but were only able to give a weak upper limit, settling on a value of 40 kms $^{-1}$. In Frail and Kassim (Kassim and Weiler, 1990), when they were arguing against the association, they returned to the lower limit. Therefore the HI absorption measurement to the pulsar will be taken as ill-constrained, with a velocity between 24 and 40 kms $^{-1}$.

More recent models of the galactic rotation give a closer distance for this velocity. Finley and Ögelman (Finley and Ogelman, 1994) recalculated this to the reduced value of 4.8 kpc, based on the mean of all the HII sources. Taking the values from only those sources involved in the distance bracketing (C to E), gives 4.6 kpc. The formal errors on this value are only ± 0.1 but model uncertainties gives an total error of ± 0.4 kpc. They also used the X-ray thermal plasma method to calculate a SNR distance of between 3.2 kpc and 4.3 kpc. The same method gives an age range of 15 to 28 kyr, with the closer distance yielding the younger age. The velocity limits on the pulsar (between 24 and 40 kms $^{-1}$) give distances between 3.6 and 4.8 kpc with the new rotation model.

X-ray results of Finley and Ögelman

| | |
|-----------------------------|-----------|
| T_6 (10^6 keV) | 4-8 |
| v_s (kms^{-1}) | 530-750 |
| d (kpc) | 3.2-4.3 |
| t_4 (10^4 yr) | 1.5-2.8 |
| n_0 (cm^{-3}) | 0.02-0.04 |
| M_s (M_\odot) | 80-160 |

The original, kinematic, distance that Kassim and Weiler calculated was compatible with the DM derived distance in the model of Manchester and Taylor (Manchester and Taylor, 1981). The estimated ages of the two objects were roughly similar at ~ 15 kyr, although the SNR size and age were based on the Σ relationships. Frail and Kassim (Frail et al., 1994b) in their later work ruled out the possibility of the association because they believed the distances were no longer compatible. Our latest calculations now suggest that in fact the kinematic and dispersion distances are in agreement, and thus the association is likely.

6.3.2 The Pulsar, and the required Velocity

The pulsar was discovered in the high frequency survey of Clifton and Lyne (Clifton and Lyne, 1986). It has a period of 0.133607 secs and a period derivative of $1.343 \times 10^{-13} \text{ s s}^{-1}$, which gives a characteristic age of 15.8 kyr. The flux at 1GHz is 16.5 mJy. Its position (in 1950 coordinates) is $18^{\text{h}}00^{\text{m}}51^{\text{s}}$, $-21^{\circ}37'17''$ so it is offset from the SNR centre by $14.1'$. Using the characteristic age, and the best kinematic distance the required velocity is 1200 kms^{-1} . This is again very high; the only measured velocity from a sample of 59 which exceeds this is that of PSR 2224+65 (Gupta, 1995; Harrison et al., 1993).

This is the main problem with the association, acknowledged by Kassim and Weiler (Kassim, 1992) at the time. In the later paper (Frail et al., 1994b) they point out that a pulsar moving at 1700 kms^{-1} (their preferred speed, the same applies for 1200 kms^{-1}) should produce a bow shock when the pulsar wind runs into the ISM as does PSR1757-24. The pulsar energy loss rate is $2 \times 10^{36} \text{ ergs/s}$. The absence leads them to believe that the pulsar is not a high velocity object and therefore not associated with W 30. Alternatively the authors suggest that the remnant may be even further extended and/or constrained in some way and that the centre of the explosion could be nearer the pulsar than supposed. Given the general failure of the PWN model (section 5.5.3) to behave as expected we favour the second alternative. With the MRT we find no sign of further extension, in fact our map traces that of the VLA at 327 MHz very closely. Therefore we investigated the evidence for variations in the ISM that could cause a misshapen SNR.

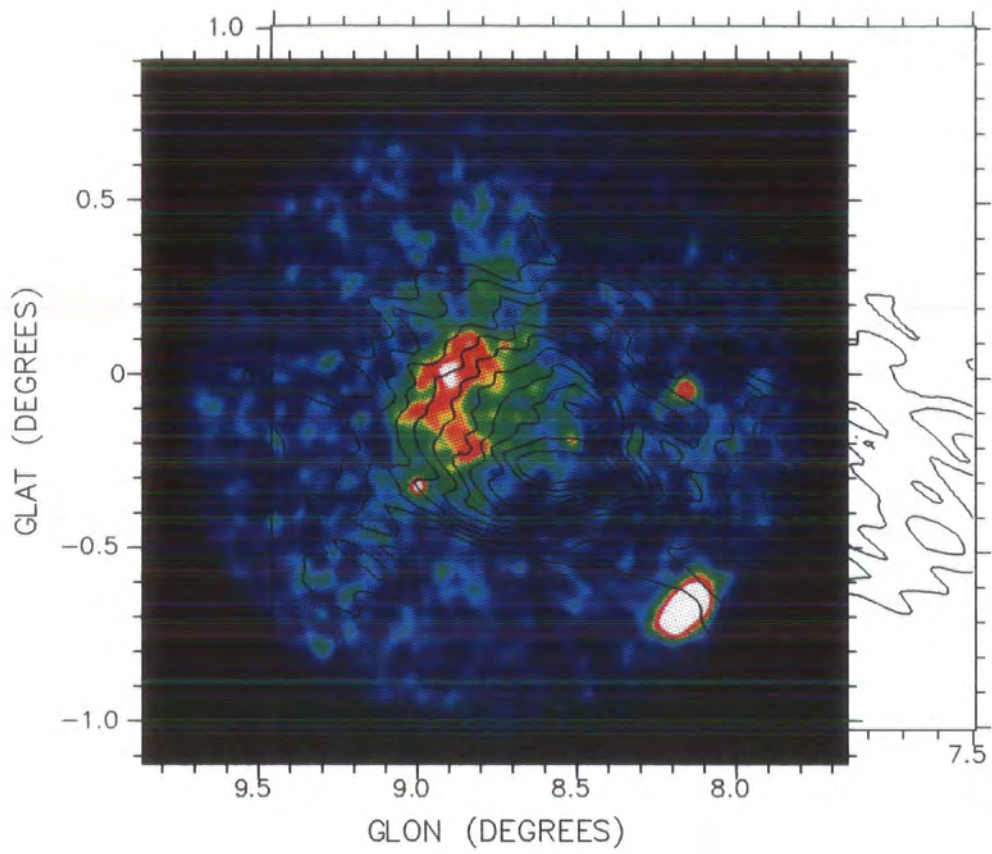


Figure 6.6: Overlay of the ROSAT emission with the MRT brightness contours.

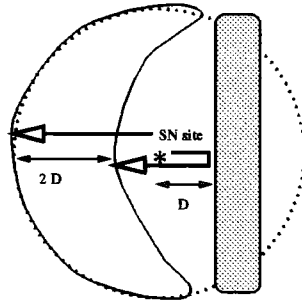


Figure 6.7: The geometry of a reflection such as might be occurring in W30.

6.3.3 Evidence for a reflection of the Shock Front

The MRT image 4.9 is able to confirm the existence of the plumes described by the Frail and Kassim (Frail et al., 1994b). These extend down to the south from the body of the SNR. We assume that these features are due to the 'break out' of ejecta through a high density region (Frail et al., 1994b; Finley and Ogelman, 1994). An overlay of the ROSAT and our radio images (figure 6.6) shows that the X-ray shell does not match the radio shell². Finley and Ögelman have suggested that this is because the Western edge has been reflected. They proposed a region of high density to the West, which has sent the shock front back across the main body of the SNR, sweeping the hot (X-ray emitting) gas in front of it. There is a lot of additional evidence to support the existence of a molecular cloud where it would reflect and distort the shape of the SNR in this fashion. The IRAS maps at $60 \mu\text{m}$ and $100 \mu\text{m}$ show a knotted thread of HII regions to the south and the west of the pulsar. There are indications of these in the CO surveys (Sanders et al., 1986) as well. Parts of this string are the clouds marked in figure 6.4, and named B through to G. As stated previously HII measurements have shown that these are at the correct distance.

These clouds describe a loop of material surrounding one side of the SNR. Taking this as the reflection site, we can then model an expansion. We assume a very simple model of a wall at the site of thermal material. We assume that the SN centre was near the pulsar position based likely velocities and the absence of a 'motion' nebula. Therefore we expect the width of the X-ray emission to be approximately twice the distance of the pulsar from our assumed wall. This is so. Now we consider how the normal application of the Sedov relationships would be in error if the SNR is not a

²More heat than light (Shakespeare, 1603)

sphere.

6.3.4 Effect of a misshapen shell on the X-ray plasma model

Let us assume that instead of a perfect sphere our SNR is distorted; both the volume and hence the luminosity are reduced by of a factor, ζ , which is between zero and one. The angular size would also be reduced, by a similar factor ζ' . In the case of W30, as the reflected shock has not yet caught up the far edge, the temperature fit will still give the velocity of the undisturbed shock front and will not need to be corrected in equation 5.4. Assuming that ζ and ζ' are equal as they would be if, say, the presumed sphere was actually a hemisphere with the normal to the face perpendicular to the line of sight this distortion would cause an error of $\zeta^{-2/5}$ in the distance and $\zeta^{3/2}$ in the age. To illustrate the effect, in this particular geometric case ζ is a half. That would increase the distance by 30% and reduce the age by 70%, i.e. for G8.7-0.1, the new age and distances would be 5 to 9 kyr and 4.2 to 5.6 kpc. This exercise can only raise doubts over the age derivation, and show that the distance formula is less sensitive.

6.3.5 Conclusions and Difficulties

In summary, there is no sign of the pulsar contributing to the brightness of the SNR, despite it having one of highest energy loss rates observed, and an expected speed of 1200 kms^{-1} . However it is possible that the site of the SN was not the geometric centre of the SNR if the shape is now distorted, and could have been much nearer to the pulsar. This would allow it to have a much lower velocity. There are indications that there may be such a reflection of the shock at the Western edge. The X-ray plasma method of estimating the distances is shown to be robust to misshapen SNRs, but the age estimates are not.

Many of the associations postulated are questioned on the grounds that the velocity required for the pulsar to travel from the geometric centre of the SNR to its observed position is much higher than that observed for the field pulsars. However the positioning always rests on the assumption of spherical expansion which may be doubtful. Of course this is often the only useful assumption possible, and it would be very hard to make estimates of the centre position without it. However just because it is difficult to do does not mean that the possibility should be ignored.

Finally, we note the VLA's weakness at its normal frequencies in detecting extended emission, and that the absorption at the frequencies used by TPT lead both surveys to be incomplete. Work at the lower frequencies by VLA, ourselves and eventually the Giant Meterwave Radio Telescope, will

find and fill many of these unsuspected and exciting gaps in our knowledge.

6.4 G315.4-2.3

This SNR is commonly associated with the SN described in the Chinese records of AD185, although the identification is far from certain (or even that there was a SN in AD185). It is also commonly referred to as MSH 14-63, or RCW 86. It does not quite fit into the parameters of the chosen sources for this thesis, but as it will be referred to in my discussion of G320.4-1.2 it is included. The Chinese records may apply to either of these sources; they are discussed here and will be referred to in section 6.5.

The SNR shell G315.4-2.3 is clearly spherical with a circular ridge. The centre of the remnant falls at $14^{\text{h}}39^{\text{m}}00^{\text{s}}$ $-62^{\circ}17'$ in 1950 coordinates. The MOST map is figure 6.8. There have been many X-ray observations of this SNR, all attempting to characterise it (Kaastra et al., 1992; Nugent et al., 1984). It has the classic SNR morphology in both radio and X-ray with a ring of emission at the shock front. The *ROSAT* map is shown in figure 6.9.

6.4.1 The Chinese Records

The earliest postulated observations of this source are found in a single Chinese text of AD185 recording a “guest star within the southern gate” (Yushan., 1955). The record, translated by Stephenson (Clark and Stephenson, 1977), is as follows;

On the *kuei-hai* day in the tenth month of the second year of the Chung-Phing reign period a guest star appeared within (*chung*) the southern gate *Nan-Mên*. Its size was as large as half a mat, while its five colours were fluctuating. It became smaller and went out of sight during the sixth month of the following year (*hou-nien*). *Hou Han-shu*, Dec 7th 185

The size of half a mat is estimated to be about 5° across, and sources that scintillate, i.e. are not resolved, are usually described as fluctuating. The *Hou Han-shu* was compiled during the first half of the fifth century and contains astronomical observations taken from the original records from the Hou Han period (AD25-220)

Dating the records

The planetary events recorded in *Hou Han-shu* can be self calibrated against the records of known conjunctions. Examples of these are the entry of



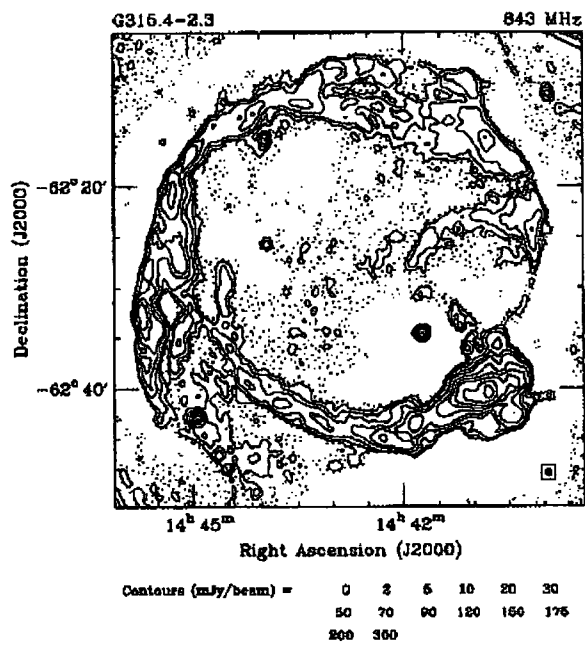


Figure 6.8: MOST image of G315.4-2.3.

Mars, Venus or Jupiter into various constellations, or of these planets coming together. From these calculations it was possible to derive error limits for the information.

The detailed analysis of Clark and Stephenson (Clark and Stephenson, 1977) showed systematic errors in some of the dates, possibly introduced in the recompilation of the records. They were able to show that a precise date, given to the day, was always correct, but an approximate date giving only the month tended to be out by one month in either direction. Allowing for this they were able to show that the other astronomical records in the same treatise were accurate and not corrupted by any astrological "requirements". While not all possible events are recorded, all those that can be verified prove to be genuine.

Identifying the *Nan-Mên*; the "southern gate"

Clark and Stephenson identified the two stars involved by using all the available Chinese star maps and taking the average angles between constellations. The most likely pair are α and β Cen. (β and ϵ Cen has been proposed, but this pair is unlikely as the direction is wrong and the records imply that the stars are approximately equal in brightness.)

| Magnitudes for candidate stars | | |
|--------------------------------|---------|------------|
| α | β | ϵ |
| -0.3 | 0.6 | 2.3 |

Identifying the correct dates

Allowing for the uncertainty about monthly dates, we can assume that the star appeared on December 7th 185, but it may have disappeared in either May, June or July. The guest star was recorded from the capital, Lo-yang, which is located at 34.75°N, 112.47°E and at a height of 200m. This constrains the times at which it could have been observed. *Nan-Mên* was visible in December 185, being on the horizon just before dawn, but by June it would have only risen during the hours of daylight (sun set is in the NW, *Nan-Mên* is on the southern horizon). The sky around *Nan-Mên* starts to brighten considerably after May 15th.

There is also some doubt whether the word "*hou-nien*" refers to the year after next or the more modern translation of "next year". The shorter time scale gives a reasonable lifetime for a "guest star" whether it be a comet, a nova, or possible a SN. The required peak brightness for a SN which vanishes after 20 months is unreasonably large so we have the probable date of disappearance as after 150 days and before 240 days.

Identifying the guest star

Is it a nova? The record is of an event that lasted from early December to sometime near the middle of the year. A nova is too short lived to be solely responsible for this.

Is it a comet? A lifetime of about 200 days makes it possible for the guest star to be a comet, but not a nova. This was proposed by (Chin and Huang, 1994) who pointed out that the apparent size would be consistent with a comet. However the size would be distorted by the position low in the sky, and it is clearly described as scintillating which is very unlikely. Also a comet that was visibly for 150+ days would be one of the longest lasting (pre telescope) comets of all time. Schaefer (Schaefer, 1995) suggests that the observation could be the combination of two events, a nova and the Swift-Tuttle comet, but this can be discounted as the same comet is reported elsewhere in the records, and is not close to either α or β Cen.

Is it a SN? Therefore the translation points to a SN between α and β Cen, eighteen hundred years ago. The initial brightness must have been great enough to only vanish about 200 days later. Clark and Stephenson searched for known SNRs in the area and that search has been repeated using Green's catalogue; there are no significant new sources in the area of interest. There are four SNRs to be found between α and β Cen. These are G316.3-0.0, G315.4-0.3, G311.5-0.3 and G315.4-2.3. G311.5-0.3, G315.4-0.3 and G316.3-0.0 can be rejected on the bases of their distances, leaving G315.4-2.3. Outside *Nan-Mén*, yet still suggested as possibly produced in the SN, is the pulsar PSR1509-58 (Thorsett, 1992), as its age is in very close agreement to that of the record. Both of these will be discussed in this section.

Visibility

To match the records we need the site to have been visible at the time of the explosion and to have been visible when it is recorded as vanishing. The proposed site is low in the sky on the date of appearance, and hidden by the sun on the recorded date of vanishing. Allowing the consistent errors of one month in the dates recorded it was proposed (Clark and Stephenson, 1977) that the date of vanishing was a month earlier, when the setting times of the sun and rising time of the southern gate were more widely spaced and the source would be visible after the sun had set.

Questions have arisen based on the extinction of a source so low in the sky. As the sun moves across the sky sources will become obscured, and

this is obviously a function of the brightness of the source. Therefore the last observed date can be used to calculate the brightness at that time. The column of air is taken into account, and Schaefer³ has built up a database of dust extinction from many sites and altitudes. This method has been tested against the Chinese records for the rising and setting of Canopus, with magnitude -0.72, and was found to be accurate to an R.M.S. of 5 days (Stephenson, 1997). The actual magnitude at which any source around the constellation would vanish to astronomers in the capital could be calculated from Schaefer's values

Schaefer (Schaefer, 1993b; Schaefer, 1996) has calculated the required absolute magnitude from the heliacal rise and setting times for both the positions of G513.4-2.3 and the PSR1509-58.

When we examined the relative positions of the Sun and the constellation *Nan-Mén*, it was clear that in the sixth and seventh month both the precessed positions of PSR1509-58 (and therefore G320.4-1.2) and G315.4-2.3 ($13.17^h - 50.4^\circ$ and $12.72^h - 52.41^\circ$), both of which clip the southern horizon, are rising before sunset. However in the fifth month the Sun has been set for several hours by the time these positions reach their maximum. That is for G320.4-1.2, 4.8 degrees above the horizon, and for G315.4-2.3 about 3 degrees above (on the 9th of May 186⁴). Calculations of the extinction at these angles gives the extinction (for dust scattering only; the dominant factor) $k = 0.1066 e^{-(H/8.2)}$, and $\Delta m = k X$, where X is the air mass. Air mass follows $X = [\cos(Z) + 0.025 e^{-11\cos(Z)}]^{-1}$ (Schaefer, 1993a), therefore at $Z=85$ and 87 , $X = 10.3$ and 15.1 . As Lo-yang is at a height of 200 m the extinction is $\Delta m_{87} = 1.65$, $\Delta m_{85} = 1.12$. These are the lower limits as the extinction due to aerosols or ozone has not been included. These are much less than that due to the scattering, but both will increase the loss of intensity. Schaefer's formulae give the sky brightness of this point in the sky as about 350 nanolamberts, roughly the surface brightness of an average night sky. I.e. on these dates there is no loss of clarity for these sources, therefore we can take the normal limiting source brightness as the vanishing magnitude. However if one was to wait for another month, into June, the sky brightness levels would be 100 times greater (i.e. sources would have to be 5 magnitudes brighter to be seen).

Ionisation ratios from X-ray observations of (Kaastra et al., 1992) using *Ginga* point to the SN that produced 315.4-2.3 was a type II which would have a slower decay time, but unfortunately cannot say which class of type II it was. All their other conclusions are from the assumed distance of the SNR based on its identification with SN185.

³the only person publishing results based on this method

⁴May 9th is on the new moon near the apogee of heliacal track for PSR1509-58.

As can be seen in figure 5.4, the fall from peak brightness of a SN over 160 days would be the order of 5 magnitudes for the type I and type III varieties, but as little as 2 for the type IIP's. To confirm that these sources are not contradictory with the Chinese records, we now use results from elsewhere; i.e. the A_v , from the *ROSAT* column density, and the distance from kinematic studies.

6.4.2 The optical data on G315.4-2.3

On the edges of the SNR there are optical wisps (RCW86) which have been studied to extract the line velocities as described previously. These have been studied by Rosado et al. (1996). They find a component with a central velocity of $-33 \pm 4 \text{ kms}^{-1}$, equivalent to a distance of $2.8 \pm 0.4 \text{ kpc}$. This matches the distance to the OB stellar association (2.5 kpc) that (Westerlund, 1969) had claimed was physically associated.

6.4.3 The *ROSAT* data on G315.4-2.3

ROSAT data for the source has been publicly available, but I can find no publication using it. The data used, request ID rp500078a02, was collected in late august 1993. The pointing was to the northern half of the SNR; in galactic coordinates, $\ell = 315.5$ $b = -2.2$. From the observing run 4659 seconds was considered acceptable. Simple interpretation is difficult, the most complete studies, done with *Ginga* (Kaastra et al., 1992) and *Einstein* (Nugent et al., 1984) describe the source as a non-equilibrium shocked plasma. Two temperatures are required to fit it. The high temperature, at 5keV, would be poorly determined by the *ROSAT* data. However, only the the column density is used in our discussion, usually best found from the low energy *ROSAT* data. The column density gives the optical extinction.

The interpretation of the data, using the program **Xspec**, again fails to find a simple temperature or power law model, with absorption. Nor does the inclusion of second temperature or power term improve the situation much. Some success was obtained separating the SNR into regions and performing independent fits on these. The selected regions are shown in figure 6.9. It is essential to maintain a significant number of photons in each part. Fortunately this is a very bright source, and with nearly 5000 seconds of observing time in the file there was no problem with photon statistics. I therefore did not include the number of older and shorter files that are available.

The sections taken were each of the bright filaments, plus the centre;

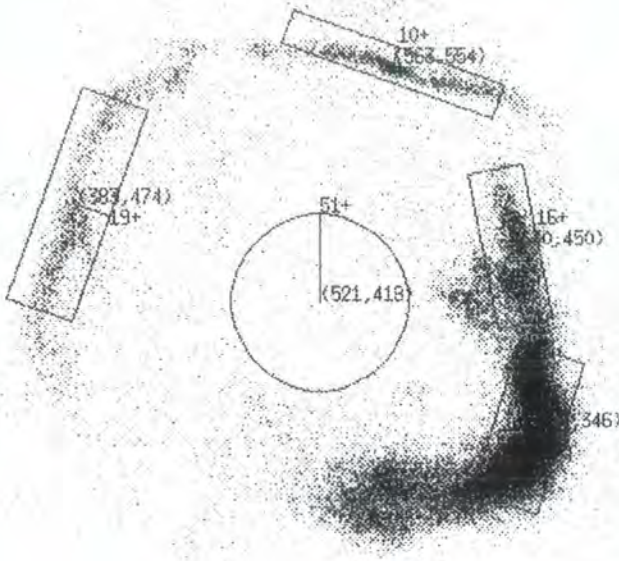


Figure 6.9: *ROSAT* image of G315.4-2.3, showing the subsections selected for individual analysis.

| | N edge | NE edge | NW edge | SW edge | Centre |
|---|--------|---------|---------|---------|--------|
| Counts/s | 0.72 | 0.92 | 1.3 | 4.4 | 0.22 |
| Area (sq degrees) | 0.011 | 0.021 | 0.012 | 0.015 | 0.11 |
| Reduced χ^2 for power law fit | 4.0 | 8.0 | 5.2 | 28.0 | 1.7 |
| Reduced χ^2 for thermal model fit | 3.4 | 11.6 | 1.7 | 11.3 | 2.1 |
| $N_H 10^{22} \text{cm}^{-2}$ | 0.65 | 0.87 | 0.64 | 0.65 | 0.05 |
| T_{keV} | 0.16 | 0.16 | 0.16 | 0.18 | 5.3 |
| Spectral Index | 8.5 | 10 | 10 | 10 | 1.9 |

Firstly it is clear that the source is not going to be fit by a single component or even several components so the results deduced from *Ginga* and *Einstein* satellites are unlikely to be correct.

The results for each region are different, but there are several sections that are best fitted by a thermal model with roughly the same column density and temperature. The centre has a reasonable spectral index but such a low column density that the emission is probably not part of the remnant and is due to something in the foreground. I therefore use the average temperature and flux from the edges, weighted by their χ^2 . This

gives a measure of 0.16 keV, or 1.8×10^6 K, for the temperature of the plasma, and $6.6 \times 10^{21} \text{ cm}^{-2}$ for the column density. Unfortunately since the fits are to only part of the image we can no longer assume that the luminosity from a spherical volume can be matched with the unabsorbed flux. However, assuming a reasonable ISM density of 1 cm^{-3} gives a distance of 2.2 kpc. This is in rough agreement with the values from the kinematic distance, and this is the distance will be used from here i.e. 2.8 kpc. It is not in agreement with the values used by Strom in arguing for association of G315.4-2.3 with the SN185 (Strom, 1994). The values he uses are from a fit across the whole remnant.

As the remnant is $\sim 40'$ across, this leads to the radius being the order of 16 ± 2 pc. With the canonical values of ϵ (10^{51}) and n_0 (1 cm^{-3}) the age is then about 14 ± 5 kyr. This is far too old to be associated with the SN185 without assuming a particularly high energy ($\epsilon = 2 \times 10^{52}$) or low density region ($n_0 = 0.03$).

6.4.4 The association; conclusion

Our reinterpretation of the data leads to the conclusions that the source G315.4-2.3 is associated with an OB cluster near to RCW86, first postulated in 1969 (Westerlund, 1969).

With regard to the SN185, given the Chinese records and their fallibilities, we can either accept the evidence and assume that there was an event, or reject the records on the grounds of internal inconsistencies. Contrary to previous analysis we find that objects in the constellation would have been visible, and the absolute brightness of the type II SN need only be the order of -15^{th} magnitude, as shown in table 6.2. This is only a lower limit because as the moon rises the limiting sky brightness would get lower. The postulated source G135.4-2.3 could be resultant from SN185, but it is not likely. This is because we find, from three independent methods, that the distance is around 2.5 kpc. The age, which cannot be derived accurately, can be made to match an event 1800 years ago, but requires unlikely conditions.

This SNR in particular deserves more investigation, mainly as if it could confidently be rejected as the source from SN185, the claim for the more interesting association of G320.4-1.2 with SN185 would be strengthened.

6.5 G320.4-1.2

The SNR, also known as MSH15-52 and containing RCW89, has the pulsar PSR1509-58 on its edge; this physical proximity led to the association being postulated. Furthermore the age and position of the pulsar is consistent with the SN event being SN185 (Thorsett, 1992); its characteristic age is

| | G315.4-2.3 | G320.4-1.2 |
|---------------------------------------|------------|------------|
| limiting magnitude, m_v | 5 | 5 |
| elevation, degrees | 3 | 5 |
| air column extinction | 1.6 | 1.1 |
| fading of type IIL after 155 days | 5.5 | 5.5 |
| fading of type IIP after 155 days | 3.5 | 3.5 |
| A_v from X-ray column density | 3.4 | 3.1 |
| Brightness loss from assumed distance | 12.0 | 13.3 |
| Deduced absolute magnitude for IIL | -17.5 | -18.0 |
| Deduced absolute magnitude for IIP | -15.5 | -16.0 |

Table 6.2: Estimates for the Absolute Magnitudes for the two candidates for SN185

1550 years and when the measured braking index is included the age found is 1700 years (Kaspi et al., 1994). The third derivative is consistent with an unchanging braking index (i.e. $n = \Omega\ddot{\Omega}/\dot{\Omega}^2$ and $\ddot{\ddot{\Omega}} = n(2n - 1)\ddot{\Omega}^3/\Omega^2$ implying that the braking index is constant. The formal errors on the age are minute, assuming the model is correct (equation 5.21). The measured braking index of 2.837 ± 0.001 gives an error of less than a single year. If the initial spin period was slow (with respect to the present) the age would be less. Therefore, within the constraints of model, the ages do not exactly match, the difference is within the probable deficiencies in the model.

6.5.1 The Chinese Records

Questions about the interpretation of Chinese astrological records is a quagmire for even the most experienced sinologists. However the coincidence of a possible record of an SN and the discovery of a pulsar of the correct age less than 5° from our best attempts to interpret these records is an event too tempting for anyone⁵ to pass by. Of course if the interpretation was simple it would have been done. We have argued in the section on G315.4-2.3 that the records are still consistent with a SN. However the traditional source attributed (G315.4-2.3) might not be responsible as all the indications are that it is too old. Therefore we looked at the possibility that the PSR1509-58 could fit the Chinese constraints, see section 6.4.1. Estimates of the absolute magnitude are shown in table 6.2. They are seen to be sensible. We estimate the magnitude of vanishing for May the 9th is 5^{th} , therefore the peak magnitude would have been either 0.5 (for a type IIP) or -2.5 (for type IIL). The expected A_v , based on the column density of the best fit of the X-ray observations (Tamura et al., 1996) ($N_H = 5.9 \times 10^{21}$) and from equation 5.3 gives 3.1 magnitudes, and the distance from the association with RCW89 is

⁵possessing a romantic soul

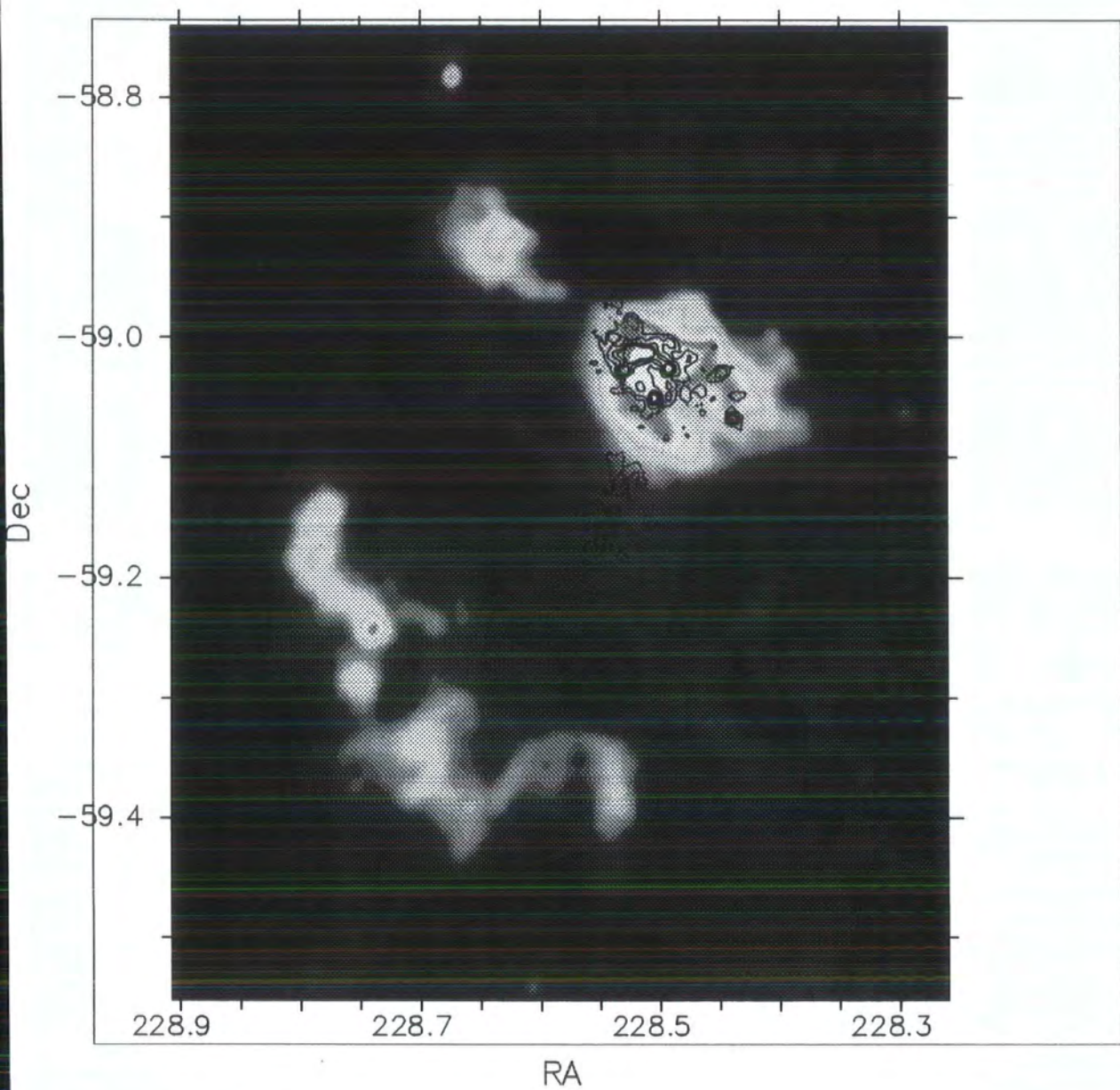


Figure 6.10: High Resolution X-ray contours overlaid on the MOST image of G320.4-1.2, after Brazier and Becker 1997

4.5kpc. Thus the peak absolute magnitude would have to be greater than -16, less than the mean for type II SNe. We therefore find no difficulty in associating the PSR with Chinese records.

However, whether this is the SNR recorded in the Chinese records or not, does not affect the association, which will be examined only on the basis of the distance estimations.

6.5.2 Previous distance measurements

H_α (Rosado et al., 1996) and HI absorption measures (Caswell and Murray, 1975) have been done on RCW89, and these give a maximum velocity of about -54 and -65kms⁻¹ respectively. The H_α line for the SNR is weak and the measurements are also heavily contaminated by confusing sources thus the error range given by Rasardo et al. is large ± 10 kms⁻¹. Caswell gives no discussion of the errors at all, these will be assumed as typical for the rotation model, ± 7 kms⁻¹. The distances derived from these are $3.7^{+0.8}_{-0.6}$ kpc for the H_α and the HI gives a lower bound of 4.5 ± 0.5 kpc. The original Caswell paper used the old IAU standard of 10kpc for the galactocentric radius, giving the oft quoted distance of 4.2 kpc. The correction used the rotation curves given previously in section 5.2.1.

The pulsar DM (253.2 pc cm⁻³) gives a distance of 5.8 kpc. This is odd since it is used in the Taylor and Cordes model (Taylor and Cordes, 1993) as a defined distance, based on its association with RCW89! Therefore we would be using a circular argument if we claimed the distances matched. What a circle that fails to close represents is open to discussion.

6.5.3 Radio and X-ray observations

The source G320.4-1.2 has been mapped at all frequencies from sub-GHz in the radio to the X-rays and these have been reviewed in a paper by Du Plessis et al. (Du Plessis et al., 1995). However neat conclusions cannot be drawn as the source is complex. There is the pulsar nebula, that is clearer in the X-ray than the radio, but still visible in both. To the north is the RCW89 optical nebula, which consists of a dense tangle of H_α filaments. To the south east there is an area of low surface brightness emission, also seen in X-ray and radio, although it is clearer in the higher frequency radio observations. MRT does not record this. I shall follow the naming convention of Trussoni (Trussoni et al., 1996) which names these regions as SE nebula (SEN, the low surface brightness region to the SE), Northern nebula (NN, the RCW89 to the N), S nebula (SN, containing the pulsar) and central diffuse nebula (CDN, containing everything else). These are marked on the *ROSAT* image, figure 6.11.

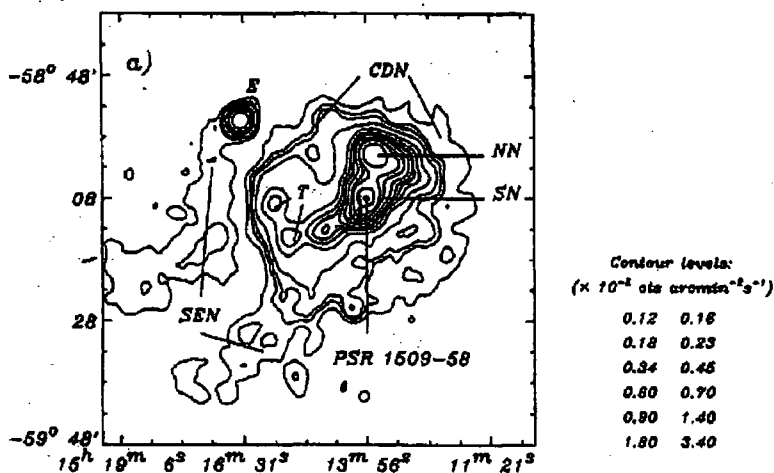


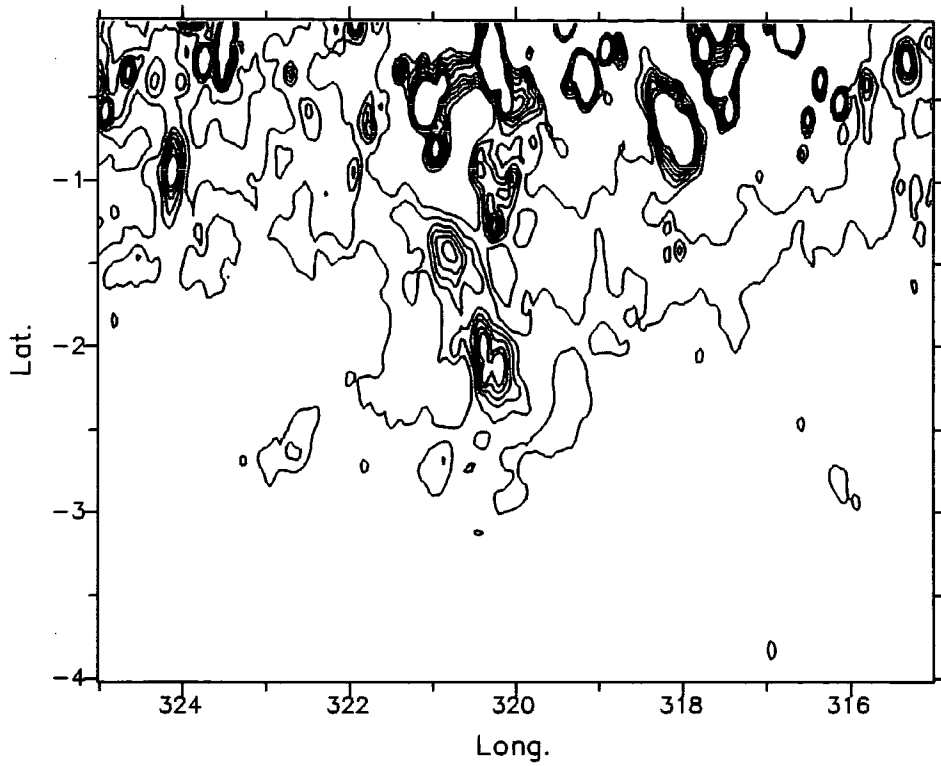
Figure 6.11: Supernova remnant G320.4-1.2 as seen by ROSAT. From Trussoni et al 1996.

Comparison of the IRAS image and the Duncan map (figure 6.12) shows that the low surface brightness ridge, corresponding to the SEN in X-ray, is in both, although the peaks are anti-correlated (centred on $\ell = 320.5$ $b = -2$); compare this to the G315.4-2.3 SNR (at $\ell = 315.5$ $b = -2.5$) which is not seen in the IRAS map. This, combined with its absence in the MOST and MRT maps, would suggest that it is thermal, and not a SNR feature. It is puzzling that the polarisation angle (Milne et al., 1993) across the two portions seem to be related and the spectral index (from 4.8 to 8.4GHz) is *steeper* than that of the brighter section. The IRAS ridge, most likely being a molecular cloud, should be visible in velocity space. The CO velocity survey (Dame et al., 1987) shows a very clear peak for the lower end of the ridge at with a speed of -43.5 kms^{-1} , and a distance of 2.9 kpc. The NE end seems to have two components, the stronger at the same -43.5 kms^{-1} , the second at -60 kms^{-1} . This may therefore be connected to the the G320.4-1.2 source.

There was a proposal that the two ridges are the pulsar jets (Danziger and Gorenstien, 1982), but this fell into disfavour on the grounds that it did not account for the lower surface brightness to the south west of these. However the same structure has been proposed again, based on the X-ray observations of Brazier and Becker (Brazier and Becker, 1997).

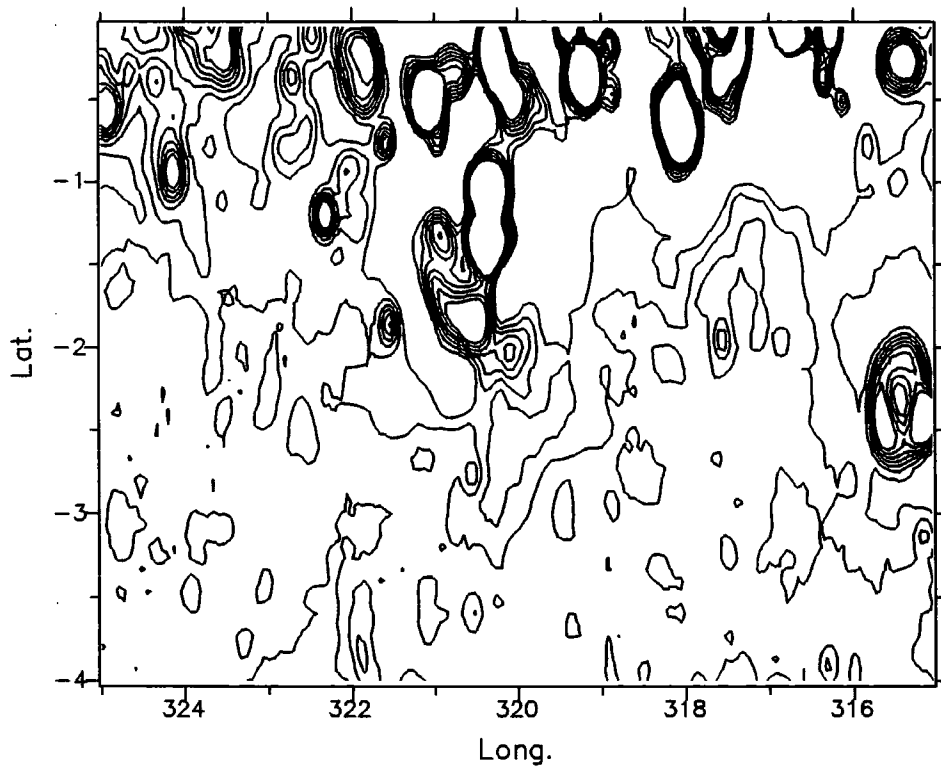
The subsections which can be identified in the *ROSAT* observations are

IR around G320



- Contour heights
in MJ/SR
- 1 : -300
 - 2 : -100
 - 3 : 100
 - 4 : 300
 - 5 : 500
 - 6 : 750
 - 7 : 1000

12 cm around 320,-2



- Contour heights
in mJy
- 1 : -300
 - 2 : -100
 - 3 : 100
 - 4 : 300
 - 5 : 500
 - 6 : 750
 - 7 : 1000

Figure 6.12: IRAS and 2.4GHz contour maps. IRAS has been smooth to the radio resolution, and a 1 degree smoothed version has been subtracted

| | S nebula | N nebula | CDN | SEN |
|------------------------------|----------|----------|------|------|
| Counts/s | 0.51 | 1.24 | 1.14 | 0.67 |
| Spec Index | -1.9 | - | - | - |
| T_{keV} | - | 0.35 | 0.5 | 0.35 |
| $N_H 10^{22} \text{cm}^{-2}$ | 0.92 | 1.37 | 1.45 | 0.95 |
| $L_X 10^{36} \text{erg}$ | 0.16 | 2.1 | 1.1 | 0.55 |

Table 6.3: Results from ROSAT observations on MSH15-52, Trussoni et al. 1996

not very well correlated with the radio, but the peak of the radio coincides with a peak in X-ray, and the highest peak in X-ray coincides with the pulsar. Both have a low surface brightness extension to the south-west.

The most detailed work on the X-ray source is that of Trussoni et al. (Trussoni et al., 1996), where nearly 10,000 seconds of *ROSAT* data was used to study the spectrum of the five identifiable regions, the Northern Nebula (NN), the southern nebula (SN) containing the pulsar; the south eastern nebula (SEN) and the central diffuse nebula (CDN). There is also an eastern source, but this is identified with a known optical source in the foreground. I have not repeated the analysis of the *ROSAT* data in detail, only confirming that similar results were obtainable. The details of the bounding region selected and the background used are not published, therefore we would not expect to get identical values.

The X-ray spectral fits to the observations give each nebula a different spectrum and column density. The southern nebula, surrounding but excluding the pulsar, is best fitted by a power law, but the other three regions are matched by thermal spectra. In the past these sections have been fitted with a two temperature thermal model (Seward et al., 1984), none of which have been well constrained. The *ROSAT* does not have the spectral resolution or range to refine an accurate temperature, and the other instruments do not have the spatial resolution to look at individual parts of the complex.

It is disturbing that these sections do not have the same column density. The problem is that if the thermal smooth X-ray emission cannot be separated from that of the nebulae and jet terminations the standard model cannot be applied. Therefore we must identify and removed these regions. This is exactly what has been done recently with the *ASCA* satellite (Tamura et al., 1996). The synchrotron nebula is modelled based on the *ROSAT* observations and removed from the *ASCA* spectrum. *ASCA*'s better spectral resolution allows the accurate identification of the ionisation lines such as the Ne K_α and Mg K_α . For the first time, we can get confident limits on the temperature of the Southern and Northern nebulae.

Non-thermal in both North and South nebula from *ASCA*
Spec Index -1.99 ± 0.08

Thermal in N nebula
 T_{keV} 0.35
 $N_H 10^{22} \text{cm}^{-2}$ 0.59 ± 0.06

The indications of a second temperature component have now been absorbed into the non-thermal model. A clear indication of the power of the high resolution *ASCA* SIS instrument is in its mapping of this source. Its spectral resolution allows maps of good spatial resolution to be made from just the Mg K_α excess, to give the thermal component, and the temperature > 2.2 keV, produced by the the non-thermal component only (Tamura et al. (1996) figure 3 reproduced here in figure 6.13). The Mg K_α excess is the strength of this line over the energy continuum either side of it. Using maps made this way the Southern and Northern nebulae can be separated, spatially, solely on the basis of their spectrum. The southern nebula extends up to where the Mg peaks. This clearly suggests that the two populations of photons are due to the transfer of energy from one emission process to another, occurring at the centre of the northern nebula. Brazier et al. (Brazier and Becker, 1997) have studied the details of the northern nebula structure using *ROSAT*, and while it is hard to extract spectral variations the geometric structure is compelling. The proposed model of Manchester et al. (Danziger and Gorenstien, 1982), with the pulsar beaming toward us and the polar jets striking the ISM and radiating with a thermal plasma, fits both the HRI X-ray and the MOST morphology (Figure 6.14).

This shows that the spectrum of these nebulae is a combination of a single temperature thermal spectrum and a power law contribution at a column density of $0.59 \times 10^{22} \text{cm}^{-2}$. This does not match the best fit in the lower surface brightness component only seen by the fine spatial resolution of *ROSAT*.

The CDN and SEN, the candidates for the remnant from the original blast-wave, are not seen by the *ASCA* satellite, therefore we have to use the results from *ROSAT*. We fit the X-ray plasma model to the results quoted above in table 6.3.

There are two possibilities to consider, there is either a single object with reduced surface brightness in the SE, or there are two objects one larger and dimmer and offset to the SE. Many people have suggested that the two are separate, however the polarisation angles across the complex are smoothly varying, (Milne et al., 1993) which would argue for association. These postulated two sections are the SEN and CDN. We can assign the values from that paper, calculate the respective age and distances for these. The confusing nebula NN and SN have been removed from these. If they

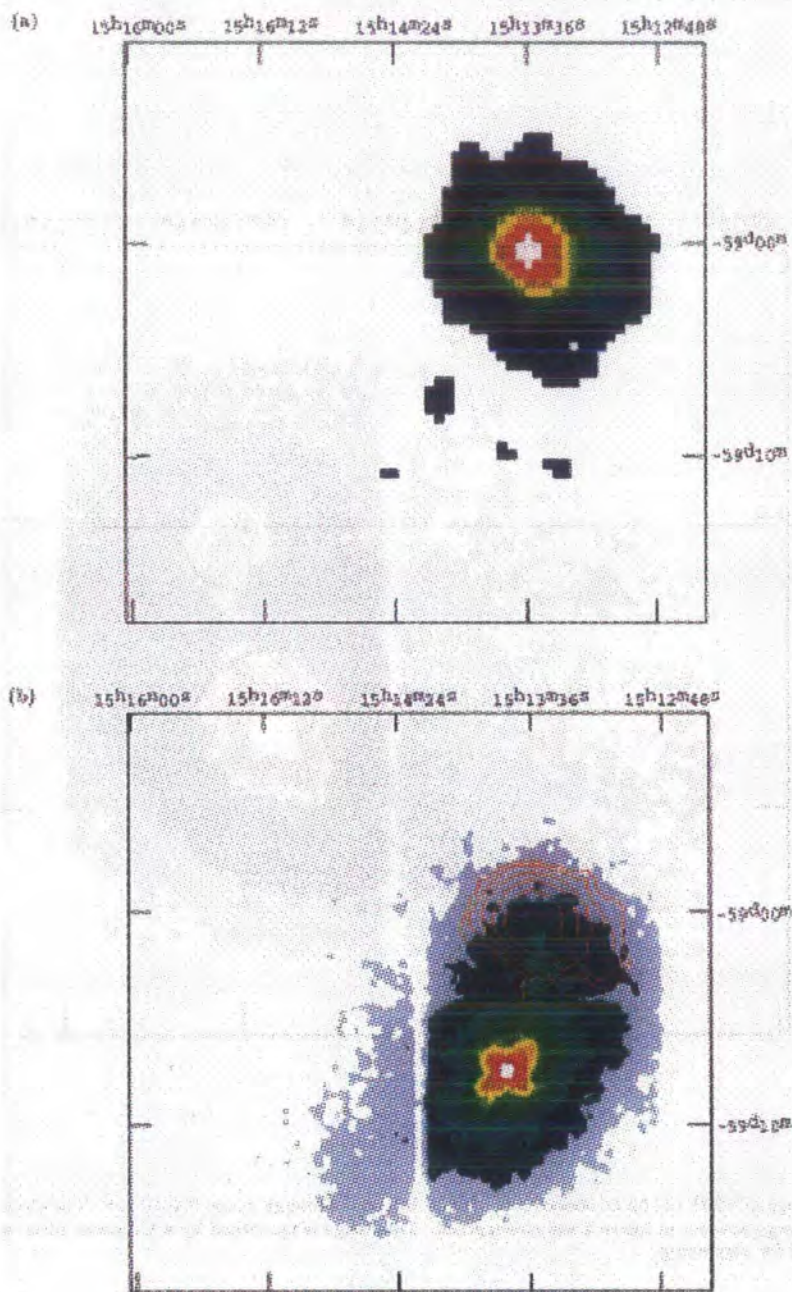


Figure 6.13: *ASCA* image of centre of G320.4-1.2 from Tamura et al. a) is mapped in the Mg K_{α} excess b) is with the highest (and therefore non-thermal) energies ($E > 2.2$ keV), and also has the contours from a) in red.

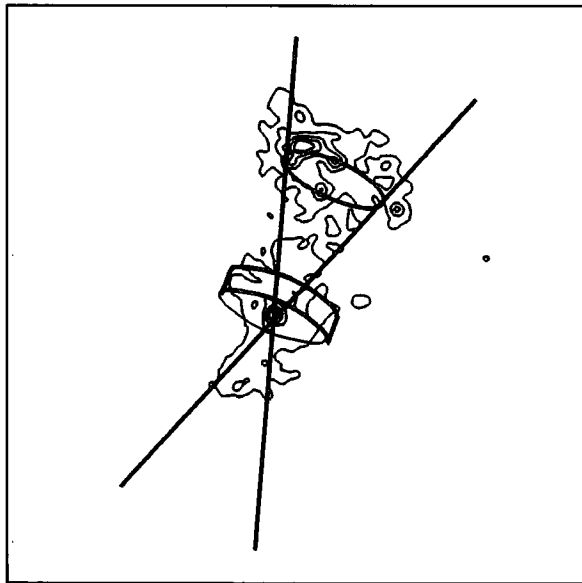


Figure 6.14: Proposed model and track of the PSR jet scoring an ellipse on RCW89. Taken from Brazier and Becker 1997.

are due to jets from the pulsar they will not fit our model.

The distance calculations, using the values in table 6.3 and the formulae 5.4, for the two diffuse nebulae are as follows;

| | S E nebula | C D nebula |
|---|--------------|---------------|
| T_{keV} | 0.5 | 0.35 |
| $L_X 10^{36} \text{ergs}$ | 1.1 | 0.55 |
| Efficiency, $\epsilon, 10^{-23} \text{ erg cm}^{-3} \text{ s}^{-1}$ | 2.8 | 3.2 |
| Size, θ , arc minutes | 60 | 30 |
| Distance, kpc | 10.9 ± 1 | 4.7 ± 0.5 |
| Radius, pc | 98 | 21 |
| n_0, cm^{-3} | 0.013 | 0.17 |
| Sedov Age, kyr | 147 | 11 |
| Swept up mass, M_\odot | 1,224 | 157 |
| Radiative time scale, t_{rad} , kyr | 350 | 89 |

While it is gratifying that the distance for the CDN is so close to the kinematic distance, we must be cautious, as the inaccuracies in the *ROSAT* modelling do not allow a high level of confidence. Also the age does not match that of the pulsar. However we can be confident that the ratio of the distances to the two sources is roughly two to one. This is not very sensitive to the temperature, and thus will not change with the model. Certainly if the SEN is at 10kpc we could expect a much greater column density. In the discussion of the *ROSAT* spectral fit Trussoni et al. note that the range of fitting values tends towards a higher column density. They rejected the fit on the grounds that the implied flux was then very high. At the best fit N_H was $1.27 \times 10^{22} \text{ cm}^{-2}$ and the temperature is 0.17 keV; The X-ray plasma model would place this (if an SNR) at a distance of less than a kiloparsec.

Therefore it is clear that this source requires a much longer observation to be characterised and it is probably not a SNR.

The age estimate from the model goes totally against the association of the SNR with the pulsar, being 6.5 times greater. It is hard to understand how this could be made to match. Either the X-ray plasma model is wrong, in which all the other results are mere coincidences, or this one result is in error. The age is nearly linearly dependent on the temperature, but that could not be six times greater. One explanation of this could be that the ISM density could be increasing with distance from the centre of the SNR, but confirmatory evidence will be hard to obtain. A collusion of effects is required to explain this, and must remain as a cautionary example of the limitations of this method.

6.5.4 The Optical observations

Van den Bergh and Kamper observed the proper motion of the optical wisps in RCW89 (Van Den Bergh and Kamper, 1984) to calculate the age. They

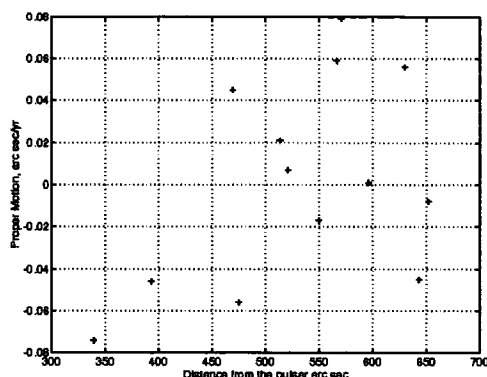


Figure 6.15: Proper motion of wisps (with reference to the PSR1509-58) against distance from the pulsar.

claimed that the very small proper motions mean that the age has to be much greater than 5,000 years. However we have seen that RCW89 is caused by the pulsar jet (Brazier and Becker, 1997; Tamura et al., 1996). Using this model we would not expect the wisps to be moving away from the pulsar but to trace the expansion of the termination nebula of the jet. The data show that the proper motion is centred on the RCW89 with the expansion greatest at the edge as shown in figure 6.15. The data do not contain enough information to say if there is radial expansion around the centre of RCW89, as only the proper motion along the radial vector from the pulsar is recorded. Fitting a straight line through the points allows us to make some realistic estimate of the mean velocity out from the centre of the nebula. The expansion velocity obtained, 700 kms^{-1} , matches that from the X-ray plasma temperature of 600 kms^{-1} . Using the Sedov expansion this would imply an age of 8000 years. However the *ROSAT* HRI image strongly indicates that a precessing beam from the pulsar is exciting RCW89 (Brazier and Becker, 1997). If this is the case the expansion velocity from the wisps cannot be simply 'wound back' to a centre to give the age; their starting point and deceleration, both unknown, would have to be included.

6.5.5 The Association with SN185

The birth of PSR 1509-58 could have been seen by the Chinese astronomers, and therefore it could have been produced in SN185. However the Chinese observation were made one hundred years earlier than the upper limit on the age of PSR1509-58. It is hard to see how this could be pushed back but

it is of course not impossible.

The *ROSAT* data, gives a distance of 4.7 kpc to the central diffuse nebula. This matches the distance to RCW89, which is seen by *ASCA* to interact with the pulsar nebula. Furthermore the pulsar lies only $3' \pm 3$ from the centre of this circular feature. The large errors on this measurement are due to the poor definition of the edge of this diffuse nebula. At 4.5 kpc and an age of 1700 years, that would give a required velocity of $2300 \pm 2300 \text{ kms}^{-1}$.

The South Eastern nebula, has IR emission so does not look like a SNR. Its distance, obtained from the X-ray plasma model, does not match the pulsar and RCW89 distance. It also has a lower column density, yet the model would place it at nearly 11 kpc. Therefore despite its circular shape, polarisation and non-thermal spectral index in part of the GHz range we do not believe it to be related to G320.4-1.2.

The Sedov age of the SNR is the only barrier remaining to confirming the association. The age, unlike the distance, is very sensitive to distortions and other errors in the underlying assumptions of the model, however it is hard to generate a 6 fold error.

Still the most likely conclusion is that G320.4-1.2 and PSR1509-58 are in a SNR/pulsar association, as there is strong evidence that the pulsar is interacting with the SNR. The age from the pulsar is 1700 years. The distance from the X-ray plasma model is 4.7 ± 0.5 kpc, from H_α 3.7 ± 0.6 kpc, and from the HI measurements of RCW89, 4.5 kpc with no quoted errors but taken as ± 0.5 kpc, giving a weighted mean of 4.3 kpc.

6.6 G343.1-2.3

PSR1706-44 is one of only seven pulsars that have been observed in pulsation at all wavelengths from gamma rays to the radio. Its period of 0.10245s, and \dot{P} of 9.304×10^{-14} give a characteristic age of 17.4 kyr, making it young, as would be expected for an extremely energetic pulsar. The association is hotly contested, which is surprising as there is no compelling evidence against it.

6.6.1 First Observations

The discovery of a new gamma ray source by *COS B* first drew attention to this area, and perusal of various older radio maps indicated that there was radio emission at the site of the gamma ray source. These indications were followed up by a MOST survey at 843 MHz which showed a very clear shell like ridge which passed through the pulsar position (McAdam et al., 1993).

The young radio pulsar PSR1706-44 was found in a high frequency targeted search for young short period pulsars (Johnston et al., 1992). The

period was folded back into the gamma ray data, and it has been found that the pulsation covers the range from 1500 MHz to GeV. Therefore we have a young, high energy, pulsar and in that case we would expect the SNR to still survive.

In the association proposal (McAdam et al., 1993) the pulsar distance was taken from the DM by the canonical electron density. This gives 2.5 kpc, rather than 1.8 kpc from the Taylor and Cordes model. The reason for preferring this value over any of the detailed n_e models was that the position of the proposed association was on the far side of the Sagittarius arm. At this distance a small variation of n_e along the line of sight will give a large range of distances. The Σ -D relationship gave a value of 3kpc, but more usefully the edge of the SNR was identified with a ridge of dust in the IRAS survey, and this ridge was also noticeable in the Durham-Parkes HI survey. This gives us a distance of 3.5 kpc which matches the pulsar distance, admittedly only if the feature is associated with the SNR.

However the association has been dogged by doubts. Originally the only radio map which could resolve the source was that of the MOST survey, as shown in figure 6.16. They saw a ridge of emission, which they assumed was defining the Eastern edge, but they also found that the integrated flux was only 3.2Jy, much less than the single dish observations found for the unresolved source. The MOST instrument has a large gap in its uv coverage and this was the explanation given for the shortfall in emission from that seen in the broad scale surveys, which imply an expected flux of about 30Jy at 843MHz. This was followed up by a VLA survey at 330MHz (Frail et al., 1994a). The authors disagreed with the association on the grounds that the DM measure for the pulsar gave a distance much closer than the SNR position.

Since this pulsar is visible in gamma rays it is an obvious candidate for other high energies. *ROSAT* observations were done at the end of September 1992 (Becker et al., 1995). The conclusion from these observations was that there was emission from the pulsar, but no sign of a nebula and there was no sign of emission from G343.1-2.3. However the region was dominated by a very bright and hard source, LMXB 4U 1705-44. It seemed worthwhile to reexamine this data for the possibility of deriving a SNR distance to test the association, for which an X-ray temperature is needed.

As mentioned earlier pulsars can be observed via their neutral hydrogen absorption features. This has been studied by Koribalski et al. (Koribalski et al., 1995) and a good distance measure was obtained. There are two strong components in the spectrum, one seen in absorption, the other not. The last strong feature in the absorption has an edge at -18.2 kms^{-1} , while the first feature expected but not seen gives a minimum velocity of -29.7 kms^{-1} . This sets an upper and lower limit for the distances of 3.2 ± 0.4

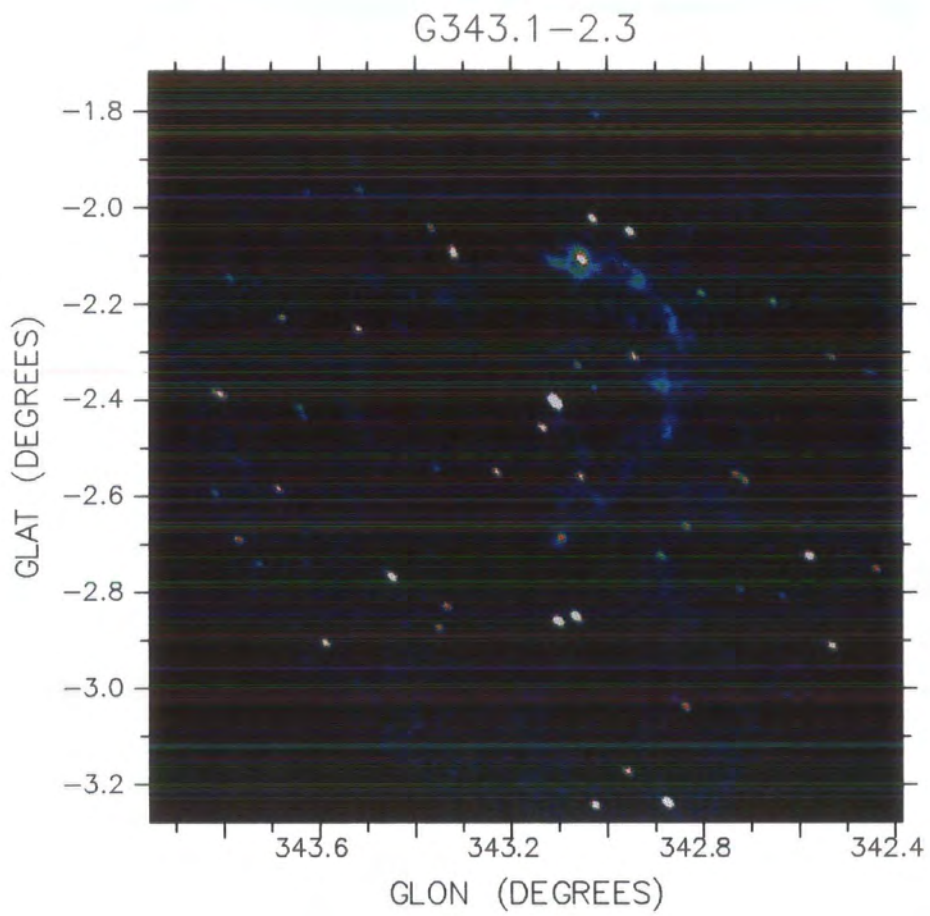


Figure 6.16: The MOST image from McAdam et al. 1993 of G343.1-2.3

and 2.4 ± 0.6 kpc. See figure 5.3. It is interesting to note that this distance for the pulsar makes it one of the most efficient gamma ray objects in the sky converting about 12% of its spin down energy into gamma rays, similar to Vela. We can also use the spin and brightness temperatures to calculate the hydrogen column density. The value given by this method is 3.7×10^{21} cm^{-2} . The original distance measure, using the identification of the ridge with the SNR, gave a very similar value to this. The same ridge can be seen in the HI velocity plot at -32 kms^{-1} . One would expect a ridge, if due to the SNR expansion to be on the side of the shell. It could therefore be that the pulsar is to the front of the bisecting plane of the SNR. Alternatively it may not be associated with the SNR at all.

Yet another problem was the required velocity to make the association. Assuming that the apparent centre of the SNR was the site of the SN and taking the distance of the remnant as 2.8 kpc, as deduced for the pulsar, the pulsar is at a distance from the centre of 14 pc. Using the spin-down age gives a transverse velocity of around 900 kms^{-1} . The proper motion has not yet been measured (but is being undertaken) and the timing velocity probably cannot, as the pulsar is young and has timing glitches. However the scintillation velocity has been measured by Nicastro et al. (Nicastro et al., 1996). The measured correlation width in time, Δt_{ISS} , is 2287 s and in frequency, $\Delta \nu_{ISS}$, is 15MHz at 20cm (1520MHz). Therefore using the formula derived by Cordes (Cordes, 1986) (which we will argue is outdated) they arrived at a velocity of less than 50 kms^{-1} (27 kms^{-1} plus (possibly) 17 kms^{-1} of the earth's own velocity). This is nearly twenty times less than that required to associate the centre of the MOST ring and the PSR1706-44.

The existence of a pulsar wind nebula for the pulsar has been claimed (Frail et al., 1994a). The angular size of this proposed nebula is $4'$, and might have a tail pointing due East, or alternatively it could be part of the shell seen by MOST. The resultant speed from the standard equations (section 5.5.3, equation 5.19) at distance of 2.8 kpc is about $2/n_0^{1/2} \text{ kms}^{-1}$. It will be argued that this method is invalid.

6.6.2 Refinement of the conclusions based on the MRT results

In the MRT map the remnant visible in our filled uv images as a hemisphere stretching from $17^h 06^m$ to $17^h 10^m$ and $-43^\circ 48'$ to $-44^\circ 48'$. The extent is much greater than that found in the maps of the VLA and MOST. The centre now moves from $\ell = 343.1$ $b = -2.3$ to $\ell = 343.17$ $b = -2.42$. Assuming a simplistic expansion into a uniform medium, i.e. that the geometric centre is the site of the SN, and the age is correct, we would require the PSR to be travelling at $0.06''$ per year, rather than the original $0.08''$ per year. Taking

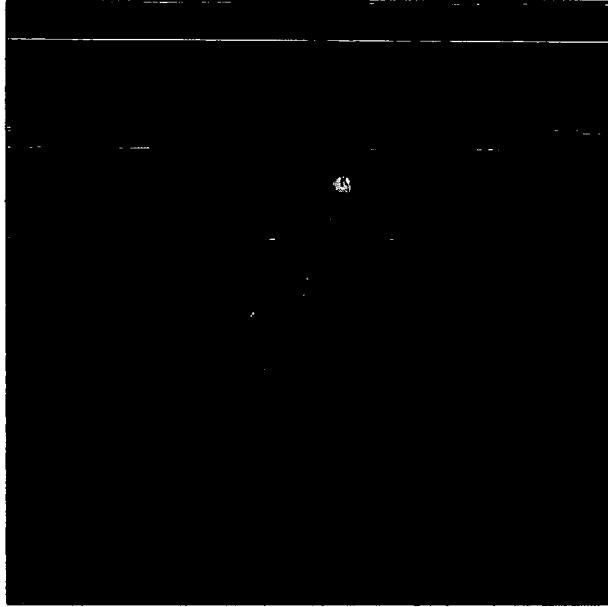


Figure 6.17: Supernova Remnant G343.1-2.3 in X-rays

a distance of 2.8 kpc that would require a transverse velocity of 750kms^{-1} . The scintillation velocity of PSR1706-44 has been measured by Nicastro et al. (Nicastro et al., 1996). However they have used the scintillation model of Cordes discussed in section 5.5.2. This has been improved upon by Gupta et al. (Gupta, 1995; Gupta et al., 1994) to give a much better fit to the known pulsar velocities. If we use this new formula we get a velocity of less than 100kms^{-1} . The ratio of the scintillation velocity to that required for an association with the SNR is still very high. It is, however, within the range of ratios of scintillation velocity to proper motion velocity for those pulsars for which both have been measured. The largest velocity ratio listed in the 59 pulsars used in (Gupta, 1995) is 7.5 for PSR1706-16. Furthermore scintillation widths vary considerably with time (Gupta et al., 1994), changing by as much as $\pm 50\%$ from day to day, and therefore these observations need to be confirmed.

6.6.3 Results from the *ROSAT* data

As the MRT map is showing emission from a larger area than that of the MOST map, we can split the central region of the PSPC data symmetrically through the LMXB 4U 1705-44 and the pulsar (in the centre of the image).

Figure 6.17 shows the regions selected. This allows a good background subtraction, very important when searching for a weak source hidden by a bright one. All the obvious bright sources (RX1709.9-4429, RX1710.7-4433 and PSR1706-44) were blanked out and almost equal detector areas were taken. Even at the early stage we find that there was about 10%, or 7.5σ , more emission from the region including the G343.1-2.3. Using the offside as the background (ensuring good matching of instrument PSF and the energy array response function (ARF)) the residual emission from this side was found. Obviously these data are borderline, and certainly there was no way that we could attempt to correlate the X ray photons with the SNR features, but within these constraints we attempted to assign a temperature to the emission.

Bad data channels were ignored and it was found that the fit errors, for all models, were dominated by errors in one channel, channel no 13 at an energy of around 0.4 keV. Therefore we ignored the bottom channels, between 0.0 keV and 0.4 keV, when doing all the subsequent fitting. The fit results were poor but for the Mekal model⁶ (the preferred thermal model) the best fit was;

$$\begin{array}{ll} T_{keV} & 1.5 \pm 7.5 \\ N_H (10^{22} \text{ cm}^{-2}) & 1.7 \pm 5 \\ \text{Efficiency } \varepsilon & 1.78 \times 10^{-23} \end{array}$$

χ^2 is 20.1, and a reduced χ^2 of 1.4, for 17 degrees of freedom. Figure 6.18 shows the spectral fit.

The Raymond-Smith and the Mekal thermal models gave the best fit. A power law fit returned parameters of;

$$\begin{array}{ll} \text{Photon Index} & -0.7 \pm 4.4 \\ N_H (10^{22} \text{ cm}^{-2}) & 0.4 \pm 1.5 \end{array}$$

with a marginally higher χ^2 of 20.51, or a reduced χ^2 of 1.5.

There was a vague indication of two peaks in the spectrum, therefore we attempted a two component spectral fit; Mekal, i.e. a temperature and a column density and added to this a power law spectrum. The χ^2 for this two parameter fit has more or less the same value as that of a single fit. The only justification is that the spectrum "looks" better in a cosmetic sense. The values for this fit were;

| | Component 1 | Component 2 |
|---------------------------------|-----------------------|-------------------------------------|
| T_{keV} | 1.1 | photon index 3.7 |
| $N_H (10^{22} \text{ cm}^{-2})$ | 0.85 | $N_H (10^{22} \text{ cm}^{-2})$ 4.8 |
| Efficiency ε | 6.9×10^{-23} | photons/keV/cm ² /s 0.09 |

with a reduced χ^2 of 1.3.

⁶The thermal plasma model of Mewe and Kaastra with the L band Fe lines by Liedahl

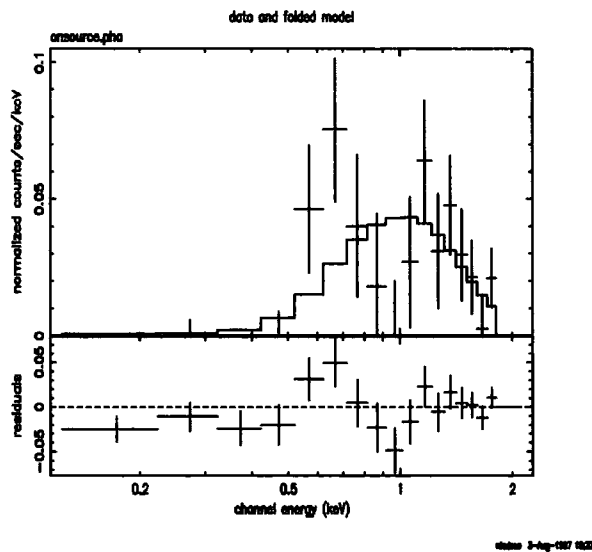


Figure 6.18: Xspec fit to the counts from the assumed SNR, the model is the solid line and the crosses are the *ROSAT* data

6.6.4 Discussion of the *ROSAT* fit

The counts that we are assigning to this source are of poor quality and offer very few constraints. There is little to choose between the two kinds of models, and it is of note that the column density for the power law fit is very close to what has been found for the pulsar. However we continued on the grounds that *if* the SNR is the source of the photons, the spectrum would be expected to be thermal. The pulsar nebula, where we would expect a power law spectrum, is blanked out.

The χ^2 contour plot (fig 6.19) shows that the data offers poor constraints against N_H and T_{keV} . Almost any value of N_H between 5×10^{21} and 3×10^{22} is allowable given temperatures of T_{keV} .

We attempted to use other information about the region to improve the fit. The bright source, 4U 1705-44, is the most likely cause of error. It is outside our field of view, but both the poor PSF of the *ROSAT* PSPC and the likelihood of a dust scattering halo around it makes it likely that there is some spectral contamination. This source is best fitted by a power law spectrum, as would be expected for a low mass X-ray binary, and has a T_{keV} of 1.3, and a column density, $N_H = 2.7 \times 10^{22} \text{ cm}^{-2}$. This N_H is much greater than that found for other parts of the SNR, and the accepted

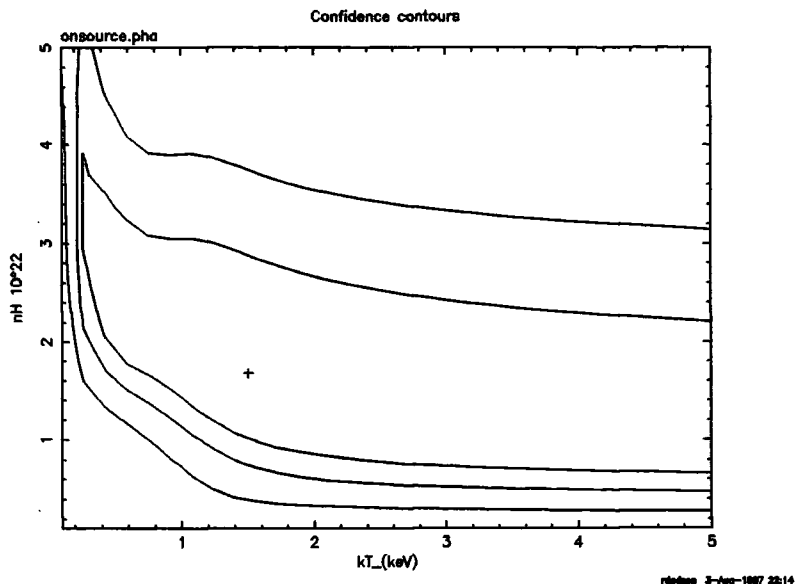


Figure 6.19: **Xspec** confidence with Temperature and Column density on the ROSAT data

distance to 4U 1705-44 is about 7kpc. It is safe to say that it is not part of the SNR. We searched for residual emission from this source in the counts assumed to be from G343.1-2.3. The counts were fitted for a single thermal source and then a second source with the N_H and T_{keV} of 4U 1705-44 was added. The normalisation constant for this component was started at zero, then fitted. The proportion of the spectrum that could be due to the second component is less than one twentieth of the main source. Therefore we conclude that the spectrum is not directly contaminated by 4U 1705-44. The dust halo contamination is more complex, as the spectrum gets softer as we look at the photons scattered through a higher angle, i.e. those on the edge. This was the justification for looking at the two component spectrum in the previous section. The component with the lower column density is more likely to be that of the SNR, and the other due to the binary system. Alternatively the thermal plasma within the SNR has not yet reached equilibrium (Shull, 1982). In non-ionisation equilibria the short life time of the SNR means that the heavier elements are not yet in thermal balance with the plasma and need to be fitted with a separate line temperature. This would generate misplaced peaks in the spectrum, but it is clear that the data are not sufficiently accurate to confirm or deny such

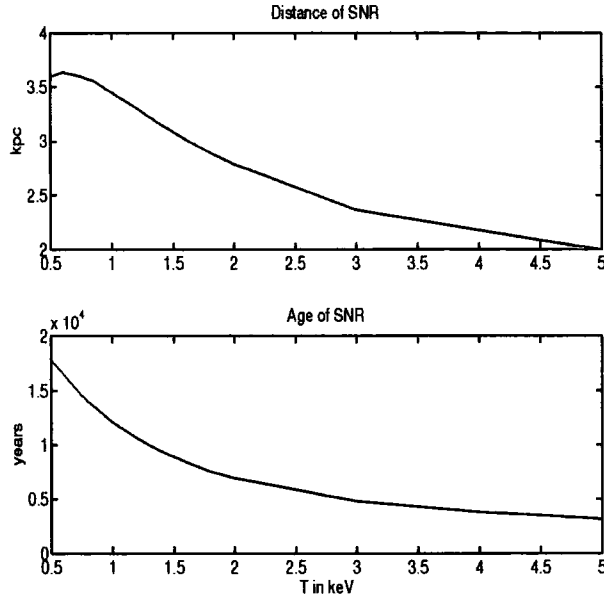


Figure 6.20: Derived distances and ages for SNR G343.1-2.3

an effect.

All this would seem to lead to extremely poor values for the distance and age of the SNR, but the *distance* parameter is not very sensitive to the temperature or column density. As one falls the other rises and ϵ is more or less static, leading to a higher luminosity and therefore larger extent). Figure 6.20 shows the distance derived for all value of T_{keV} and all other parameters fitted to give the minimum χ^2 . It shows that the distance is always constrained between 3 and 3.6 kpc for all the likely values of T .

The pulsar is quoted having a N_H density between 2 and $6 \times 10^{21} \text{ cm}^{-2}$ from (Becker et al., 1995), depending on the emission model. These values match the values that can be derived from the data in Koribalski et al. (Koribalski et al., 1995). From the relationship (Lang, 1978);

$$N_H = 1.8 \times 10^{18} \int_0^D T_s \ln\left(\frac{1}{1 - T_b V / T_s}\right) dV$$

we get N_H from the integration across the T_b as $3.7 \times 10^{21} \text{ cm}^{-2}$. This matches the PSR value from the rotation model (as well as the rather doubtful values found previously in section 6.6.3. This value of N_H is incompatible with the values from our Mekal model fits to G343.1-2.3. Using this value of N_H and minimising to get a T_{keV} we find a value of 100 keV, which

is physically impossible. The most likely cause of this will be 4U 1705-44 distorting the spectrum.

We can apply the X-ray plasma model to the SNR for the best single component fit to arrive at the following parameters;

| | | |
|--|------------|-----------------------|
| Flux received (absorbed), ergs s ⁻¹ | F_x | 2.3×10^{-12} |
| Calculated Flux (unabsorbed), ergs s ⁻¹ | F_{x0} | 2.3×10^{-11} |
| Emissivity, per atom cm ⁻³ | ϵ | 1.6×10^{-23} |
| Distance | D_{kpc} | 3.1 |
| Radius | R_{pc} | 28 |
| Age, in 1,000 years | t_3 | 8.9 |
| ISM density, using the pulsar age | n_0 | 0.09 |
| ISM density, using the Sedov age | n_0 | 0.02 |
| Swept up mass (pulsar age/Sedov age) | M_\odot | 198/53 |
| Radiative time scale, kyrs | t_{rad} | 125/280 |

The acceptable range of the fit results gives parameters in the range of 3-3.6 kpc for distance and 9,000 to 18,000 years for age, the latter well under the expected radiative timescale.

For the two component fit using the lower values we get a fit of;

| | | |
|-----------------|------------|------------------------|
| Absorbed Flux | F_x | 7.87×10^{-13} |
| Unabsorbed Flux | F_{x0} | 3.7×10^{-12} |
| Emissivity | ϵ | 1.78×10^{-23} |
| Distance | D_{kpc} | 5.2 |
| Age | t_3 | 17 |

As stated before the interpretation of PWN is very unreliable. Using the observed nebula around the pulsar (with a radius of 2'), and the formula for the static shock from the pulsar energy losses (equation 5.18) we predict a value for the radius of $R_s = 6' \pm 1$ which, while not in agreement with the observed, is more in line.

6.6.5 Conclusion

We have shown that while the thermal spectrum is poorly defined the range of the results only allows distances of between 3 kpc and 3.5 kpc. These are all consistent with the PSR distance range. The derived ages do not match unless the spectrum column density is very high, and it is more than possible that the spectrum is not thermal but is really due to a power index. There are not enough data to distinguish between these choices.

The scintillation results, using a combination of the re-centring of the remnant and a recalculation of the velocities, are not conclusive; but they move from the impossible to the feasible.

We expect an SNR to be associated with the PSR1706-44. The association was rejected in the past, and we have shown that the grounds for the rejection are not nearly as compelling as previously believed. These questions could be resolved by reobserving the scintillation velocity measurements at a different season to give a different earth to pulsar velocities, and possibly by reobserving the *ROSAT* field. Any improvement in the accuracy of the X-ray data would be worthwhile as this is the crucial measurement in investigating the association, and the photon statistics with this data are poor. The most definitive answer would be given by an interferometric measurement of the proper motion of the pulsar.

6.7 Summary for our selected Associations

We now summarise the parameters for each SNR and pulsar association, scoring them as discussed in section 1.11.

For G5.4-1.2 and PSR1758-23 we have no age estimate for the SNR, but the distances match, the transverse speed is high but observed so we allow a half point and there is interaction between the shell and the pulsar.

For G8.7-0.1 and PSR1800-21 the age is just about compatible, as are the distances. The required velocity is high, and there is no sign of interaction. Therefore we give three half points, less one.

For G320.4-1.2 and PSR1509-58 the age is incompatible, but the distances are in agreement, and there is sign of interaction. The age is too small to estimate (in a meaningful way) the velocity.

For G343.4-2.3 and PSR1706-44 the age is just about compatible and the distances match. The transverse velocity is reasonable, but there is no interaction.

| SNR | PSR | Age kyr | Distance kpc | velocity kms ⁻¹ | Interaction | Score |
|------------|------------|------------|-----------------|-------------------------------|-------------|-------|
| G5.4-1.2 | PSR1758-23 | -/16 | 4.3/4.6 | 1300 | Y | 2.5 |
| G8.7-0.1 | PSR1800-21 | 21±6/16 | 4.6/3.8 | 1200 | N | 0.5 |
| G320.4-1.2 | PSR1509-58 | 11/0.17 | 4.3/4.6 | - | Y | 1 |
| G343.4-2.3 | PSR1706-44 | 13±4/17 | 3.1/2.8 | 750 | N | 1.5 |

Chapter 7

Conclusions

Slave! I have set my life upon a cast
R-III v.v.ix

7.1 The Present Status of the Telescope

The data collected using MRT has been analysed to give a low resolution survey of the southern sky (Golap, 1997) and to map a few SNR associated with the pulsars, in this thesis. We are in the final stages of collecting the raw data, the data analysis in this thesis are with data that is two years old. The latest data are being analysed at RRI and seem to be fine. The second round of observing with the telescope to obtain interference free data and also to reobserve with those baselines corrupted by the Sun during meridian transit and also its transit in the grating lobes, began in Jan 1997. This schedule is expected to be completed in April 1998. The data so obtained will be used to fill in and complete the maps.

The software, like all software, continues to develop. However now it is sufficiently stable to be run by inexperienced users, without any support from the author.

Inevitably there are a number of problems which have either been left untackled or have only been solved for the shortest baselines.

Number one amongst these is the CLEAN question. Considering CLEAN in its widest possible sense includes calibration improvement, and self calibration. Golap (Golap, 1997) is working hard on this issue and has reported some considerable success. However he is looking at the 15' map, in which the band pass scatter, and the changing MRT_METER and effective zenith are not a problem. Considerable work is required to extend his methods to the whole map. This is why no correction has been attempted in this

thesis¹. Nor have the details of the combination of the zones with correct delay weightings been fully worked through. However the requirements are straight forward.

The other big question is the final solving of the treatment of the band pass centres. The software has been prepared for inclusion of band pass corrections, although in the data sets used here it was not used (as the corrections were much less than the RMS errors). However more important will be the question of how the longest baselines are going to be treated. Because the band passes have a scatter (0.1 MHz in 150MHz) when we reach baselines where the $\Delta\vec{u}\cdot\vec{l}$ approaches unity (i.e. when v is no longer much less than 1000λ) we should be regridding the visibilities. As we measure only to 500λ along the south, numerical modelling of the effects is required to decide whether to alter completely the mapping process for these last few sections. In all likelihood it will best handled by a numerical adjustment in the declination rephasing section of the program **transform**.

7.2 Results on Pulsar SNR Associations

7.2.1 G5.4-1.2

There is undeniable evidence of interaction between the SNR, the smaller nebula (G5.27-0.9) and the pulsar. The distance estimates are reasonable, but there is no good estimate for the SNR age. This could be derived from the X-ray observations if the very strong source GX5-1 could be blanked out, however this will require a new generation of instruments as the spatial resolution of present spectral instruments is insufficient. Unfortunately the required velocity for the pulsar is extremely high. The model for pulsar wind nebulae, one of which is seen for this pulsar, implies a much lower velocity. It is the model which is more likely to be at fault as it has consistently failed to perform as expected. On the modified Kaspi's test scale the association scores 2.5, stressing its strength.

7.2.2 G8.7-0.1

This source was discussed, on the basis of published works of others. The distance concerns of Frail and Kassim (Frail et al., 1994b) were answered, and the possibility of the SNR being deformed by known HII and CO clouds was discussed. The consequences of this deformation on the X-ray distance and age estimates was calculated. This could be the reason that the age estimate of the SNR is so much greater than that of the pulsar. The distance estimates approximately match and the required transverse velocity is high.

¹Deformed, unfinished, sent before my time

All these give a half point on the Kaspi scale, but one is lost as there is no sign of an interaction. The low cumulative score, 0.5, shows that the association is only just about sustainable. However the low score could be arising from a reflection on the Western edge.

7.2.3 G315.4-2.3

The position of G315.4-2.3, the favoured SNR for association with SN185, was shown still to be consistent with the reports on the SN, despite recent objections based on a rigorous translation of the date of the heliacal setting, which was always known to be inaccurate. The X-ray emission is not fitted well by any simple function, which raises the faintest possibility of an embedded pulsar in the Western edge of the SNR, which is not beaming towards us. As there is no visible pulsar the score does not apply.

7.2.4 G320.4-1.2

The central diffuse nebula, clearly identified only in the X-ray band, has been shown to be at a distance of 4.7 ± 0.5 kpc, based on the model of Kassim et al. (Kassim et al., 1993; Kassim et al., 1994). The ages however are in very poor agreement and we have no explanation for this. It is noted that the predicted age in the X-ray thermal plasma model is sensitive to poorly defined parameters. The model of Manchester et al. and Brazier et al. (Danziger and Gorenstien, 1982; Brazier and Becker, 1997) is used to describe the northern and southern nebulae, in which case the RCW89 nebula and the pulsar are directly associated and at a distance of 4.5 ± 0.5 kpc from the HI absorption to RCW89. The model is that of a pulsar jet slamming into the ISM. These nebulae are seen brightly in the lower frequency maps, dominating the MRT maps. Identification of a low surface brightness remnant in the same area will require good dynamic range, and is for future investigation. The distances to the pulsar and the SNR match.

The identification of the central diffuse nebula, as described by Trussoni in X-ray, as the shock front from the original SN explosion was made. We also rejected the association of what Trussoni has called the SEN, and is catalogued as G320.6-1.6 by MOST, with this remnant.

Using the Kaspi score, the age not matching loses one mark, but there is apparent interaction between the pulsar and the remnant, and the distances match. Therefore the overall score is +1, making it a likely association.

It is also noted that the Chinese records of SN185 are quite consistent with it being the parent of both the PSR1509-58 and G315.4-2.3 if the positional accuracy of the original records is relaxed. These accuracy limits are consistent with the other records in the same catalogue. Interestingly, if

this is so it seems that the understanding of pulsar spin down does not yet include all that needs to be known, as the age is greater than the theoretical upper limit (starting with a zero period).

7.2.5 G343.1-2.3

The PSR1706-44 is found, on the basis of the MRT observations, to be rather nearer the geometric centre than previously believed. The implied transverse velocity, 750 kms^{-1} , is reasonable but the measured v_{ISS} is much less, at a maximum of 100 kms^{-1} . The proposed pulsar wind nebula around the pulsar does not fit with the model, as that implies a speed of around 13 kms^{-1} . However, the ratio of 7.5 is not impossible, being at the 3σ level of the v_{ISS}/v_{pm} distribution. The SNR, or something at the site of the SNR, is detected by *ROSAT*. Assuming that it is the SNR and it is a thermal plasma source (as would be expected), we derive a distance to SNR which matches the pulsar distance. Unfortunately the number of photons from the SNR is much too low to resolve this question, and a (much) longer observation will be required with an imaging detector that discriminates well against contamination from bright unrelated X-ray sources nearby. The age is borderline, and there is no sign of an interaction. Otherwise all other indicators are positive, the score is therefore 1.5, and the association is likely.

7.2.6 Conclusions on Association

| SNR | PSR | Age (kyr) SNR/PSR | Distance (kpc) SNR/PSR | velocity v_t | Interaction | Score |
|------------|------------|----------------------|---------------------------|----------------|-------------|-------|
| G5.4-1.2 | PSR1758-23 | -/16 | 4.3/4.6 | 1300 | Y | 2.5 |
| G8.7-0.1 | PSR1800-21 | $21 \pm 6/16$ | 4.6/3.8 | 1200 | N | 0.5 |
| G320.4-1.2 | PSR1509-58 | 11/0.17 | 4.3/4.6 | - | Y | 1 |
| G343.4-2.3 | PSR1706-44 | $13 \pm 4/17$ | 3.1/2.8 | 750 | N | 1.5 |

We have seen that most of our sources can be associated, or the proposed association can be maintained. As a review of methods we have shown that the method of using the Sedov relationship as a distance indicator shows great promise, but there are cases to which it is not applicable. These are when the assumptions about the nature of the ISM are incorrect, explicitly that the ISM is not a single phase, and the second cooler component evaporates into the warm ISM to alter the thermal emission of the remnant in X-rays. This case can be recognised by the different topology of the remnant, that it is centre filled rather than a ring. The emission is tracing the density of the swept up matter, in the latter case picked and carried with

the shock front. When there is evaporation of a cooler phase the density distribution of ionised matter across the remnant is a function of the time scale of evaporation. Where the evaporation time scale less than but not much less than the age of the SNR the remnant will be centre filled. This fortunately allows one to recognise when the model is applicable. Much caution is need in cases like that of G343.4-2.3 where the morphology of the X-ray emission is not known. Until sufficient resolution of both spectrum and position (in particular the rejection of confusing sources) is available the conclusions drawn should be treated as no more than indications towards coincident distances for both the pulsar and the SNR.

7.3 Methods

7.3.1 The X-ray plasma model

It has been shown that for all but one the SNRs in our selection the X-ray spectrum from ROSAT can be used to estimate the distance of the SNR, and these data are easily available. In the case of G343.1-2.3 and G5.4-1.2 other bright sources in the X-ray sky, combined with poor point source function of the *ROSAT* PSPC, pollutes the information that can be extracted. For the case of G5.4-1.2 no result could be extracted, for G343.1-2.3 we *may* have seen the SNR emission, and derived a distance from this. Where the SNR was clearly seen, two cases required or require information from the better (spectral) resolution *ASCA* satellite. The G315.4-2.3 SNR needs further work before we can fully understand the sources that are radiating in the X-rays.

For G8.7-0.1 and G320.4-1.2 we get a clear result for the distance, which matches closely the pulsar distances we get from a number of other references. This success supports our assumptions in the model (that the energy released is 10^{51} ergs, and that the SNR is in the Sedov stage), and the robustness of the equation to deviations from these assumptions.

All the sources are in the Sedov stage, as would be expected, have swept up more mass than would have initially have been ejected yet not radiated away as much as half of the initial energy.

Care is needed of course when the model does not represent the reality, in particular those cases where the pulsar is driving emission within the SNR, such as the case for G320.4-1.2. If the integrated X-ray flux was used from this source the resulting distance would be wildly inaccurate. In the case of young SNRs it is known that often the environs around the shell has been swept out by the pre-SN wind. The n_0 will then not be a constant but will rise with distance from the site of the SN. This is hard to model, and can only be tackled in the clearest of cases.

7.3.2 The pulsar wind nebula model

The model was already thrown into doubt by the results of the large scale survey of Frail et al. (Frail and Scharringhausen, 1997) which found no evidence for PWN in a large scale targeted search. Here, while all the pulsars had sufficient rate of energy loss and velocities, no new nebulae were found. We also find no supporting evidence of the model. Where PWNs are seen they do not match the predictions, and in other cases where one would expect one to be seen they are not.

7.4 Pulsars and SNRs

There is no theoretical explanation of how a pulsar could be produced without a SNR. However accidental geometric associations are to be expected, Gaensler and Johnston (Gaensler and Johnston, 1995a) used a simple model (the greatest weakness of which is the assumption of uniform expansion) to look at the development of the SNRs using the current estimates for birth rates. They pointed out that the distance independent ratio of the pulsar to centre distance to shell edge to centre distance, β is a good descriptor of the associations, and in particular its behaviour with age (Gaensler and Johnston, 1995b). They estimated 10% of pulsars with an age of $\tau < 10^6$ years would be aligned with an unrelated SNR if "associations" with β less than two are allowed. When β is constrained to be less than one (i.e. the pulsar is within the shell) only 2% of associations are accidental. Therefore their results can be summarised as that associations with a young pulsar outside the shell should be considered a geometrical alignment.

We found the present fashion for rejecting the proposed associations is becoming unreasonable, with some of the arguments against them being disingenuous. While more work needs to be done to increase the number of SNRs covered, particularly as the sample here has been selected from the more likely, it seems clear that the situation is not as grim as has recently been painted.

The X-ray derived results in chapter 6 are largely complete; the results on G320.4-1.2 (MSH15-52) are interesting, but uncontroversial. The link between RCW89 and PSR1509-58 was made by Brazier et al. (Brazier and Becker, 1997), and the *ROSAT* observations of the region were made by Trussoni et al. (Trussoni et al., 1996), and just reinterpreted here. The observations on the Chinese records are repetitions of previous points, but point out an incorrect assumption that removes the problems with the SN position calculated by Schaefer's very detailed heliacal setting model.

The results derived from the *ROSAT* observations of G343.4-2.3 are completely new but suffer from poor signal to noise. A proposal to reobserve for

longer should be considered.

7.5 Further work on the MRT maps

The description of the instrument (Golap et al., 1995b; Golap et al., 1995c) and calibration (Golap et al., 1995a) has been given before, but the maps produced so far, although having been published in this preliminary form (Udaya Shankar et al., 1997) in order to demonstrate the potential of MRT, are not of the quality required for definitive publication. This is a summary of what I feel is still to be done.

The most important repair to be done is to identify the files that are producing problems (either containing those satellite tracks missed in the interference exclusion or pickup from the sun) and replace them with the new data acquired at a different point on the annual cycle. These data are collected, but will require a dedicated effort to implement. Once the new data has been included in the map making process the CLEANing stage can be begun.

Appendix A

Appendix: MARMOSAT

A.1 Definition of Marmosat

MARMOSAT, the MAuRitius Minimum Operating System for Array Telescopes, is designed to carry us from the raw data to a stage when we can transfer to AIPS (Astronomical Image Processing System). A marmoset is a small monkey, distantly related to the ape.

Most, if not all, of the programs are written in ANSI C, with a large number of the subroutines in FORTRAN, often taken from Numerical Recipes. This course of action was followed because C was considered the 'new' and therefore better language. Experience has shown that this simplistic belief was naive, FORTRAN can be quicker (and thus better) in big number-crunching jobs. This is due to the fact that all C language's mathematical functions are calculated in double precision. However FORTRAN's lack of good memory management ¹ and difficult string parsing has lead to all the top levels of software being in C, and the FORTRAN subroutines called from C when needed. This has allowed us to use the same setup across the different operating systems that always seem to find a way into a single project.

A.1.1 Where to find the Marmosat

In the forests of central America. Also to be found in a set of sub-directories from the user **marmosat**. The code for the four byte (not using the recirculator) and the two byte mode is separate, but soft linked to maintain an apparent separation (for the compilation) yet ensure that the code for each mode does not diverge.

¹The SUN FORTRAN 77 does have the ability to dynamically allocate memory, but this is non-standard FORTRAN so hard to port to other machines

A.1.2 Compatibility with other libraries

No banana recipes. Should we try mangos? The eventual output of MARMOSAT is a FITS file, this is of course portable to AIPS, IRAF, etc.

A.1.3 Allied libraries used in the MARMOSAT

Numerical Recipes, PGPLOT, CCP4's fft library and maybe in the future the Mechach mathematical libraries.

A.2 Introduction to MRT

Worked examples of all programs are to be found in the **Doc** directory. Here a general outline of the steps in the usage is given.

A.2.1 online

Online uses the most common functions in marmosat to present a uncalibrated view of the data. It is designed to read a few baselines from the data file, rather than all baselines (i.e. it is more efficient for a few rather than many), but it can do that.

It starts by attempting to auto detect the type of time stamp. If this fails it will be necessary to use the '-new' flag. After the baseline selection it offers 13 functions. All can be selected at once, then all functions will be run on the same stretch of data. These functions are;

1. Phase
2. Magnitude
3. Closure
4. Cos
5. Sin
6. Both (ie Cos and Sin)
7. FFT
8. Gray scale of magnitude
9. Gray scale of cos or sin
10. Fixed limits

11. Self Correlation corrections
12. Change File
13. Change plotting device

A.2.2 fringe_cal

The point of **fringe_cal** is to derive the phase and magnitude, but either one or the other can be calculated individually. If we are running in phase only mode, the subroutine **find_dec()** is skipped, otherwise this large subroutine Fourier transforms every baseline and finds the fringe peak height. A Fourier transform is a least squares fit of sinusoids to the data. In principle this alone could give both the phase and magnitude of the complex gain for each baseline, as the information from the sky is well approximated as sinusoids. The motion of the source in the sky as it crosses the transit deviates from a sinusoid by a maximum of 0.02%. In practice, as the fit is only for complete fringes (i.e. multiples of $2\pi l.u$) one finds that the errors are significantly larger than those from a full and careful fringe fitting. However the peak magnitude at the relevant frequency is taken as the fringe power, that is a multiple of the gain magnitude. It is also where the fringe filter can be applied. The fringe filter allows one to select only a subset of the fringe frequencies to fit. It is now considered redundant as contributions from other frequencies are expected to be filtered out naturally in the calibration. Problems in the phase calibration are common; and the program gives detailed graphical output, which is the easiest way to detect problems.

The instrument phase returned is the transit phase for the source declination, so needs shifting to the chosen declination. The minimisation subroutine also fits a best straight line through the phase, looking for small offsets in the source position (shown by the green line in the display). The intercept of this and the mean should be the same (particularly if both sides of the primary beam are taken for calibration), this gradient is used to calculate the equivalent observed phase. It is not a very accurate method, as the signal to noise is poor, but it should be within a degree or so for all except the shortest baselines. Also it assumes a southern declination so can be massively wrong if, say Cygnus, is used. The 'other method' uses a different approximation which is true for both northern and southern sources. The found complex gains, baselines, the best fit gradient and chi squared are saved to the calibration file.

A.2.3 base2antenna

The matrix representing the good calibrations, i.e. those not contaminated by other sources, is inverted to allow the recovery these bad calibrations. The program searches for the required closing baseline, can having found it checks that the matrix is invertible. It informs the user the ratio of the smallest to the largest eigenvalue, this representing the errors introduced by the limited machine accuracy. Roughly speaking the log of the ratio gives the number of significant figures lost.

A.2.4 1D and track

These two virtually identical programs differ only in that one gives the integrated signal received by the telescope for a requested zenith angle, and the other rephases the signal from a single point on the sky and integrates that. The uses of both are obvious. **Track** originally written to monitor Jupiter for radio bursts from the Levy-Suchmarker impacts (none seen) and was last used for looking for gamma ray bursts (none seen), it did however manage to provide the first pulsar signals before the Australian pulsar machine arrived.

1D gives a signal from the phased array as the sky, normally a calibrator of interest, rolls across the instrument.

A.2.5 apply_cal

Apply_cal collates the data, calibrating it, combining good values and replacing bad values. It works on a single data file at a time, making it slow when adding to a very large set. Therefore it is possible to **combine** partial sets. The calibration files can be a single one, or a list. If a list is given the data time stamp is used to calculate an interpolated calibration value between the two current in the list. When the time of the second file is passed the third is used in the same way. As **apply_cal** reads the raw data file the correct type needs to be used (four byte or two byte), its output is common to both, being float values.

A.2.6 transform

This is the MRT version of a three dimensional Fourier transform.

A.3 Utility programs

There are also many utility programs such as ones for converting formats (**cb2fb** C style binary to FORTRAN style, **byte_swap**), precessing coordi-

nates (**pre**), reading all kinds of data file (**read**) and resampling data files (**regrid**).

health It became clear as we worked that a program that could quickly check a few basic qualities of data and notify the users (audibly in need be) if there was any problem was highly desirable. The program **health** fills this role. Like **online** it is designed to run concurrent to the collection, or post-factum. Unlike **online** it is aimed at checking the distribution of noise on many baselines at once. Its default mode is to check for continuous time stamps (i.e. there has been no stall in collection) and for single baselines which have either a very low or very high RMS (typical signs of signal loss or amplifier oscillation) compared with all the other baselines. It also checks for loss of sky noise (the sky temperature represented by the fringes) with respect to the system temperature. Loss of the LO signal can produce this. This alone has probably doubled the amount of sleep we get at the telescope.

pre The program **pre** is a stand alone version of the subroutine **pre()** which returns the precessed RA and declination from the current RA and declination.

regrid allows the resampling of the maps to give matching between the two sampling regimes. As stated in the recirculator mode the clock was changed, thus the number of samples per hour was changed from 3287 to 3307. **regrid** uses the Fourier library from the CCP4 which allows the radix base to be any prime number below and including 17, and bases 4 and 8. This mean that normally all file sizes can be transformed, or at least nearby sizes. Either the fast or the slow axis can be transformed, but the default is the slow one. The fast axis is usually the declination axis which needs resampling when the MRT_METER changes.

cb2fb allows the conversion of C style binaries to the FORTRAN record style binaries. It is normally used with the data arrays that the mapping section produces. This is for use with the ADAM and the AIPS suites, which cannot cope with C style binaries. The record size is a free parameter, but by default the same as the fast axis of the array.

read We have a program to convert binaries to ASCII characters. Handles floats, single and double; and integers short and long; and characters. It can swap these on the fly, in either the natural mode for the size of data (eight, four or two) or in forced four byte style.

map This small program creates the position file, given the spacing of the trolleys and the position of the first one. Various options can be selected when running it (i.e. type I or type II as described in section 3.4)

map2height This strips out the values from the files made by **map** to give the EW group heights. The default height of the S and N plane (defined by the height of the arm) is automatically included.

combine Given two sets of output from **apply_cal** this produces a third which is the combination of the two.

Appendix B

Appendix: Library routines

A subroutine listing of the MARMOSAT library, with copious comments.

void fft(float *data,int n,isdigit) Lifted straight from NRP and converted to c. The array data must be 2n long where n is 2^m . isdigit must be +1 or -1, -1 for the transform +1 for the inverse multiplied by N (i.e. you need to divide by N).

void fourn(float *data,int *inn,ndim,isdigit) The same as the above; the NRP fourn routine. A n-dimensional FFT.

void fftt(float *data,unsigned *bitrev,n,int isdigit) An adaption of fft(). Instead of calculating the bit reversal for every call to the routine, it calls bit_reversal once only, to speed things up. Also uses bit shifts instead of by 2 division.

unsigned *bit_reversal(unsigned number) See above.

void fftt(float *data,unsigned *bitrev,n,int isdigit) A further adaption of fftt(). Uses a cos/sin look up table.

float ** read_base(FILE *file) Reads the file pointer to the map file and returns the baselines (first index) in wavelengths (0,1,2), the (EW, NS) i & j equivalent to ij (3,4) and the size of the groups (5,6). The variable SOUTH_ANGLE is used in converting the map file style, where either the south angle is included explicitly (style "given") or implicitly (default). Called by a lot of programs.

double * time_to_angle(double time_ang,dec_ang) Returns the direction cosines for a time and declination (in radians)

double * time2angle(double time,err) Old one of the above, instead of dec one gives the difference from the global DEC. Dropped in all supported programs.

char * Self_Map() A list of the mapping for the self correlations in the data file and the EW-NS numbers.

float swapped(char *in) Byte_swap the (DATA_TYPE) data values to floats. Needed to keep everything equivalent for the SUN and Linux.

float swapped_self(char *in) Same as above, but for the unsigned self correlations.

cs2pm(phasemag pm,int n)

pm2cs(phasemag pm,int n)

cs2pm2(complex pm,int n)

pm2cs2(complex pm,int n) real and imaginary (cos and sin) to phase and magnitude, and vice versa, for the structures phasemag and complex.

data2true(phasemag PhaseMag,FILE *fin,float **self, int no_sec,n_ew,n_ns)

Returns the phase and magnitude of the next data section read from fin. Integrates the self correlations for SELF_INT (100) seconds, to reduce S/N. Use with care as it is very out of date (w.r.t. single_data2true), also the S/N gain from this is minute ($\approx .1\%$).

float * Self(FILE *fin, int ant_num,no_sec) Returns the integrated self correlations for data2true.

float bit2true(float r,self) Given the 2 bit 3 level correlation the true correlation is returned. N.B. r is corr counts / tot_num counts NOT corr counts / r(0). All formulae are from Kulcani's 1980 paper (Ast J. 85 10 Oct 1980) Corrections for two different correlators from D'Arrario et al Rad.Sci.19-3 May1984. Note that the cubic approximation is used, not the sin, as this approximation breakdowns when ever the sign for the two correlations are not the same.

double ierf(double Iact) The inverse error function, uses a look up table. Calls my_erf to set it up.

double my_erf(double x) An approximation to the error function, rather than the slower maths library one.

double inverf(double x) Less accurate than `ierf()`, but faster.

float addario(float self1, float self2, float corvalue) Applies the addario correction to the data value. The addario correction is fully discussed in Addario et al 1984. To summarize, for a two byte three level digital correlator the true value is the inverse error function of all four thresholds (upper and lower of each digitizer for the baseline). The selfcorrelator values give an average for the upper and lower threshold

float addario2(float self1, float self2, float corvalue) The above but for two_byte data.

double sidtime3(char *)

double sidtime2(char *)

double sidtime(char *) The incredible ever changing time stamp.

float single_int_data2true(FILE *fptr, int no_ew, no_ns, char * use, phasemag * pm) Returns the phase and magnitude of the a single integration of the next data section read from `fptr`. Correction of the 2 byte 3 level correlation to the equivalent true correlation is done.

float precess(char *str) Calculates the precession (only) for the given RA string.

float find_max(phasemag *data, four_vec *time_ptr, float *max, int period, base)

Finds the maximum of absolute value of the data stream.

float read_cal(char * file, complex **cal, **offset)

float ** read_full_cal(char * file, int nlines, nitems) Reads a standard cal file. The first returns just the complex gains recorded in the cal file. The second returns all the values in the calibration file.

complex *complex_dif(c_1, c_2, n) returns the complex difference between the vectors, of length `n`, `c_2` and `c_1` (note order) i.e. `c2-c1`

int Time_to_int(str, t0, t1, num) Turns a string into an integration number.

float find_dec(phase_mag y, four_vec bases, int t_cent, tot_base, no_sec)

Find_dec is now a separate routine outside libmarmosat, as it calls the pgplot and X libraries. Finds the maximum fringe frequency from the transform of a time stream of data (weighted with the primary beam). The DC is removed by default, but can be prevented by setting the flag DC_remove to zero. This is usually done the command line argument -DC. It reports the position of the maximum peak, the value at the point corresponding to the expected fringe frequency, and the phase (an approximation to the instrument phase). If the filter window is set, it calls filter to remove non-source fringes, and re-transform.

void filter(pm, data, lower, upper, num, cent, M, bitrev) In many of the calibration approaches discussed we considered filtering the data after transforming to get the signal magnitude. This routine sets the data between the limits upper and lower to zero. Then inverse transforms it, and places it in the complex structure 'pm'.

void bswap(char *b, int length) Does a byte swap for 4 byte numbers.

char * next_file(char *fn) Changes the fn to the standard next file name.

char ** read_cal_list(f_ptr, f_name) Reads a list of calibration file names, or if it is a cal file returns that.

char * select_baselines() A routine to setup the usage array.

Appendix C

The Geminga Pulsar

The latest Russian low frequency observation of great interest is a flux measurement of the Gamma ray pulsar Geminga, previously believed to be radio quiet, in the radio band; explicitly $\sim 100\text{mJy}$ at 102MHz with the LPA telescope (Kuzmin and Losovsky, 1997), although there are rumours that it is more like 30mJy (Malofeev and Malov, 1997). Geminga radiates mainly in the Gamma ray band so is of great interest as its high efficiency constrains the allowable models of emission. Obviously this radio observation is of great interest as the radio emission would presumably be a side product of the gamma ray production, thus we can reject any model which does not produce the radio emission at the same time (Romani and Yadigaroglu, 1995). However the observation has immediately become controversial as so many other observatories have done deep searches for this source (Bignami and Caraveo, 1996). For example a recent Ooty (at 327MHz) observation put an upper limit of the emission at $< 0.5\text{mJy}$, requiring a spectral index of greater than 5 (Deshpande and Ramachandran, 1997). Other observations that failed to detect the emission from Jodrell and Effelsburg at 400MHz and 1.4GHz . It is notable however that for about 93% of the LPA observations Geminga was not observed. This could be due to flaring, often seen in nearby pulsars (such as PSR0437-6715 (Johnston et al., 1993)), as it is only 157 pc away. In which case the signal could be lost in the averaging of the other observations, therefore a more reasonable spectral index maybe possible. Therefore a long term dedicated observation program would be needed.

MRT has the low frequency and the observer interest to undertake such a program but it is poorly placed to observe Geminga, as the source has a zenith angle of $+37^\circ$ and falls outside the normal observing range of the helices primary beam. The sensitivity to a pulsar is

$$R_{SN} = \frac{A_e S_{av}}{2k_b T_{sys}} \sqrt{\Delta\nu\tau} \sqrt{P - W/W}$$

Where P is the pulsar period and W is the width of the pulse. Therefore $P \cdot W/W$ is effectively the amplification due to the on over the off state.

This signal to noise ratio is about 5 in that case of MRT ignoring the primary beam losses. These however are large, so other options were considered.

The VSWR (see figure 2.6) of the antenna has sweet spots at 125, 140 and 150 MHz, the first bandpass filter has half power points at 127MHz to 151MHz; so theoretically there would be little change in sensitivity with changing the LO from 121MHz to 96MHz. A investigation of this should be simple to perform. The primary beam changes from 20dB down to 10dB down with the new frequency, from equation 2.1 (Kraus, 1988). The total signal to noise is therefore 0.5, and with just one week's observation the signal could become significant.

Therefore we could make an observation, but is it worth it? Taking a pessimistic view, where one is lead to by disagreement within the Russian group, we would only be trying to add another lower limit, and not a good one at that. It will be hard to jump to another frequency, where we have never observed before, and be confident in any negative results. Some considerable period of time would be required to confirm the telescope as functioning, and observing other pulsars. From being one of the keenest for this observation to be made, I have moved into the "its a distraction" camp.

Appendix D

A search for Fossil Radio Lines

Another possible observing opportunity was recognised in that it might be possible to look for emission due to fossil recombination lines. The theoretical existence of recombination lines from the reionization era (circa $z=1500$) has long been recognised. Dubrovich and Stolyarov (Dubrovich and Stolyarov, 1995) have improved the calculation of strength of these lines over the cosmic microwave background, $\Delta T/T$. Their results are from the numerical solution of the non-equilibrium Saha equation, which is a function of H , Ω and the hydrogen to total mass ratio (Ω_B). Thus observations of these lines would severely constrain these crucial quantities.

The wavelength of the line for the transition of an Hydrogen electron from i to j is;

$$\lambda_{ij} = \frac{912 \times 10^{-8} i^2 j^2}{i^2 - j^2} \text{ cm}$$

and this transforms to, for the present epoch;

$$\lambda'_{ij} = \lambda_{ij} z_{recombination}$$

Assuming a recombination era of $z=1500$ and that $i = j + 1$, the nearest line for MRT would then be 193 cm, or 155MHz. That is $j = 30$. The next is 213 cm, 20cm away, but the expected line width, given a recombination period Δz of 0.14, is 28 cm, so the line contrast is reduced by about a half, or possibly more if the era of recombination is longer than expected; i.e. the separations more or less close up by the time a wavelength of 2 meter's has been reached.

The fact that the lines blur into a continuum alters the spectrum from that of the perfect black body. Referring to figure D.1 part a we see here the dependence of the contrast, $\Delta T/T$ with wavelength. Unfortunately the separation between different models is not significant (10%) until wavelengths of 400cm are reached. We have considered the possibility of observing at

these frequencies at a later stage in the MRT program, and if we do we should bear the possibility of observing this effect in mind. We'd be looking for an accuracy in $\Delta T/T$ of about 2×10^{-5} for λ of 4m. The major difficulty with this approach would be that we probably would not be able to separate T_{CBB} from the foreground sources. This is a complex problem as the spectral index of the confusing sources are not well constrained. We could try looking towards the poles where the problem is less but, with our present setup that is not possible and we would be blinded by our own Galaxy before we could reach the accuracy which we require.

The advantage of the recombination lines is that these features have a much greater discriminatory power. The modelled lines are shown in figure D.1 part b. There are no¹ other processes that can produce lines in this fashion; also the details of the lines are very sensitive to the parameters in the models. However the lines have a typical contrast of 10^{-8} , a factor of 10^3 less. To observe these at 150 we need a signal to noise ratio of

$$R_{SN} = \frac{T_{ant}}{T_{sys}} \sqrt{\tau \Delta\nu}$$

T_{sys} for MRT is 300K, T_{ant} due to the CMB is 2.7K, with a 3MHz band width and 48 antennas we get a signal to noise of 10^6 in 2 and a half years!

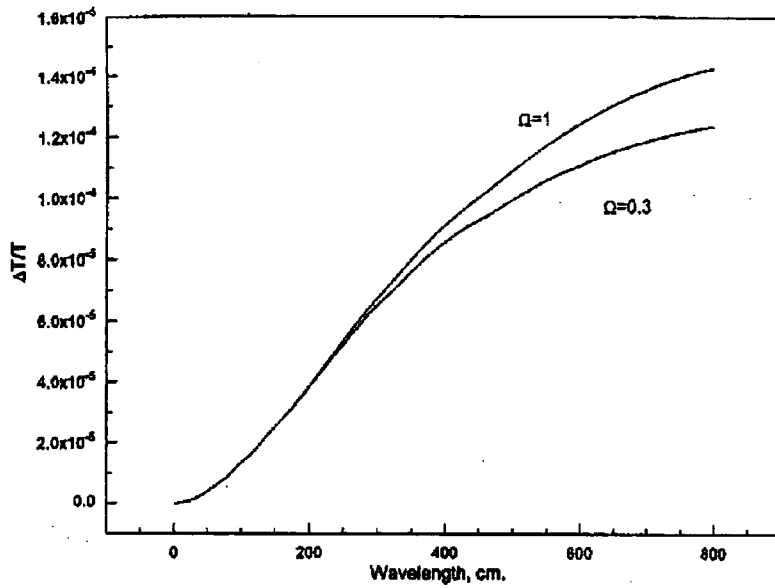
Given that this is impossible we now move on to what we could do, but not using the MRT. The first improvement has to be to cool the first stage electronics in liquid helium, as is commonly done for GHz astronomy. T_{sys} then becomes $3K^2$. However the T_{ant} for the foreground is still \sim to 300K. Therefore I would propose siting a set of very basic³ antennas in the snow in an isolated area at the south pole. There one would be viewing far from the plane (-30°), and would not have the galaxy in view. If a correlator similar to the pulsar machine is available, it could be set up and left running quietly in a corner, with the only maintenance being the topping up of the Helium. Given a large band width (3-10 MHz) and a large set of independent dipoles (200) we can bring the observing time down to about a week to reach 10^7 on each band centre. One would also choose a more ideal frequency with a fresh setup, say 1 GHz or 30 cm, where one would have better line contrast. Here we would also have a lower T_{ant} due to the foreground emission. At 1 GHz the temperature⁴ of the south galactic pole is about 1.6 K making the cooling of electronics to such temperatures worthwhile.

¹in principle the hydrogen 21cm line at $z=100$ would be a source of confusion. However unless the sources of this were of a size the order of 30 Mpc or greater a beam of 1 degree in extent would wash out the contributed power.

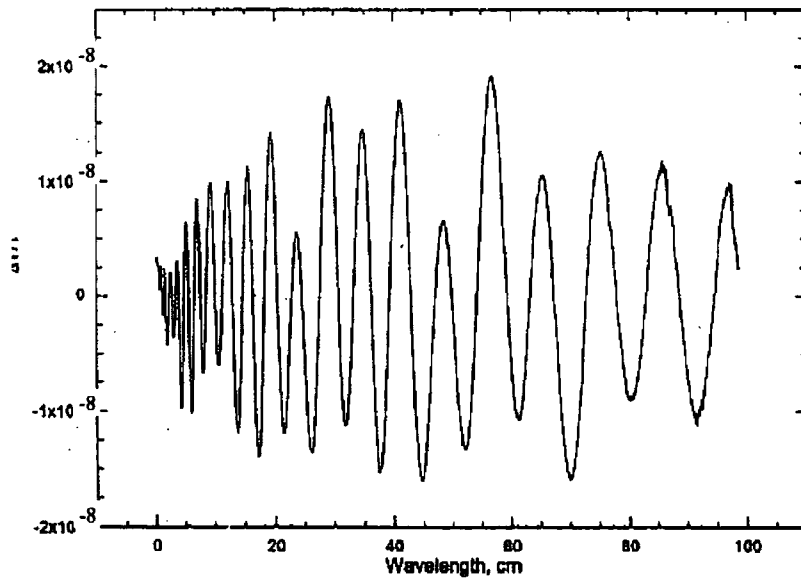
²This is in fact totally wrong, 30K is about as low as one can go

³Broad bandwidth is the only requirement, as there is no need for a high directivity as the CMB is isotropic in all directions. In fact as stated we DON'T want directivity which could introduce other sources. We need just enough to not see our own galaxy if we point away. Let us say 10° for now.

⁴27K at 408MHz and 0.013 at 4.85GHz



(a)



(b)

Figure D.1: Part a) Line to continuum contrast. Part b) The lines with wavelength. From Dubrovich et al. 1995

The frequency coverage required is very large, a single line would cover over 150MHz, however this will allow an increase in the band width allowable. Taking 5 points over the line we are allowed 30MHz. In all likelihood a 30MHz band pass would not be possible. This would have to be controlled by local conditions.

References

- Baldwin, J. E., Boysen, R. C., Hales, S. E. G. and Jennings, J. E., Waggett, P. C., Warner, P. J., and Wilson, D. M. A.: 1985, *Mon. Not. R. astr. Soc.* **217**, 717
- Becker, R. and Helfand, D.: 1985, *Nature* **313**, 115
- Becker, W., Brazier, K. T. S., and Truemper, J.: 1995, *Astron. Astrophys.* **298**, 528
- Bignami, G. and Caraveo, P.: 1996, *Ann. Rev. Astron. Astrophys.* **34**, 331
- Blandford, R. and Romani, R.: 1988, *Mon. Not. R. astr. Soc.* **234**, 57
- Bowers, F. and Klinger, R.: 1974, *Astr. Astrophys. Suppl.* **15**, 373
- Bowers, R. and Deeming, T.: 1984, *Astrophysics*, Jones and Bartlett
- Braun, R., Goss, W. M., and Lyne, A. G.: 1989, *Astrophys. J.* **340**, 355
- Brazier, K. and Becker, W.: 1997, *Mon. Not. R. astr. Soc.* **284(2)**, 335
- Caswell, J., Kesteven, M., Milne, D., Haynes, R., Stewart, R., and Wilson, S.: 1987, *Mon. Not. R. astr. Soc.* **225**, 329
- Caswell, J. and Murray, J. and Rodger, R.: 1975, *Astron. Astrophys.* **45**, 239
- Chin, Y. and Huang, Y.: 1994, *Nature* **371**, 398
- Clark, D., Green, A., and Caswell, J.: 1975, *Aust J Phys Astrophys. Suppl.* **37**, 75
- Clark, D. and Stephenson, F.: 1977, *The Historical SNe*, Pergamon
- Clemens, D.: 1985, *Astrophys. J.* **295**, 422
- Clifton, T. R. and Lyne, A. G.: 1986, *Nature* **320**, 43
- Cordes, J.: 1986, *Astrophys. J.* **311**, 183
- D'Addario, L., Thompson, A., Schwab, F., and Granlund, J.: 1984, *Radio Science* **19(3)**, 931
- Dame, T. M., Ungerechts, H., Cohen, R. S., De Geus, E. J., Grenier, I. A., May, J., Murphy, D. C., Nyman, L. A., and Thaddeus, P.: 1987, *Astrophys. J.* **322**, 706
- Danziger, J. and Gorenstien, P. (eds.): 1982, *Observations of G320.4-1.2*, Vol. Supernova Remnant and their X-ray emission of *SNRs Congresses*, IAU, D.Reidel
- Deshpande, A. and Ramachandran, R.: 1997, *Personal Comm*

- Du Plessis, I., De Jager, O. C., Buchner, S., Nel, H. I., North, A. R., Raubenheimer, B. C., and Van Der Walt, D. J.: 1995, *Astrophys. J.* **453**, 746
- Dubrovich, V. and Stolyarov, V. A.: 1995, *Astron. Astrophys.* **302**, 635
- Erickson, W., Mahoney, M. J., and Erb, K.: 1982, *Astrophys. J. Suppl.* **50**, 403
- et al., R. P. (ed.): 1989, *Synthesis Imaging in Radio Astronomy*, ASP conference, Springer-Verlag
- Feymann, R., Leightman, R., and Sands, M.: 1963, *Feyman Lectures Vol I*, Addison Wesley, 4th edition
- Fich, M., Blitz, L., and Stark, A.: 1989, *Astrophys. J.* **342**, 272
- Finley, J. and Ogelman, H.: 1994, *Astrophys. J. Letters* **434**, L25
- Frail, D.: 1997, *Personal Communication*
- Frail, D., Cordes, J., Hankins, T., and Weisberg, J.: 1991, *Astrophys. J.* **382**, 168
- Frail, D., Goss, W., and Whiteoak, J.: 1994a, *Astrophys. J.* **437(2)**, 781
- Frail, D., Kassim, N., and Weiler, K.: 1994b, *Astr. J.* **107(3)**, 1120
- Frail, D. and Kulkarni, S.: 1991, *Nature* **352**, 785
- Frail, D. and Scharringhausen, B.: 1997, *Astrophys. J.* **480**, 364
- Gaensler, B. and Johnston, S.: 1995a, *Mon. Not. R. astr. Soc.* **275**, L73
- Gaensler, B. and Johnston, S.: 1995b, *Proc. Astron. Soc. Australia* **12**, 76
- George (ed.): 1991, *The use of redundancy interferometry - A comparison of redundancy and selfcal.*, Vol. 131, Astronomical Society of the Pacific
- Georgelin, Y. and Georgelin, Y.: 1976, *Astron. Astrophys.* **49**, 57
- Golap, K.: 1996, *Master's thesis*, Faculty of Science, Univ of Mauritius
- Golap, K.: To submit in 1997, *Synthesis Imaging at 151.5 MHz using the MRT*
- Golap, K., Dodson, R., and Udaya Shankar, N.: 1995a, *Astron. Soc. of India. Bulletin* **23**, 574
- Golap, K., Issur, N., Somanah, R., Dodson, R., Modgekar, M., Sachdev, S., Shankar, N., and Sastry, C.: 1995b, *Astrophys. Sp. Sci.* **228(1-2)**, 373
- Golap, K., Issur, N., Somanah, R., Dodson, R., Modgekar, M., Sachdev, S., Shankar, N., and Sastry, C.: 1995c, *Journal of Astrophysics and Astronomy, Supp.* **16**, 447
- Green, D.: 1991, *Publs. astr. Soc. Pacif.* **103**, 209
- Green, D.: 1996, <http://www.mrao.cam.ac.uk/surveys/snrs/>
- Gupta, Y.: 1995, *Astrophys. J.* **451**, 717
- Gupta, Y., Rickett, B., and Lyne, A.: 1994, *Mon. Not. R. astr. Soc.* **269(4)**, 1035
- Gwinn, C. R., Taylor, J. H., Weisberg, J. M., and Rawley, L. A.: 1986, *Astr. J.* **91**, 338
- Harrison, P., Lyne, A. G., and Anderson, B.: 1993, *Mon. Not. R. astr. Soc.* **261**, 113

- Helfand, D. and Becker, R.: 1985, *Nature* **313**, 118
- Huang, Z., Thuan, T., Chevalier, R., Cordon, J., and Yin, Q.: 1994, *Astrophys. J.* **424**, 114
- Jacoby, G. and Barnes, J. (eds.): 1996, *XSPEC: The First Ten Years*, Vol. 101, VASP conf. series
- Johnston, S., Lorimer, D. R., Harrison, P. A., Bailes, M., Lyne, A. G., Bell, J. F., Kaspi, V. M., Manchester, R. N., D'Amico, N., and Nicastro, L.: 1993, *Nature* **361(6413)**, 613
- Johnston, S., Lyne, A. G., Manchester, R. N., Kniffen, D. A., D'Amico, N., Lim, J., and Ashworth, M.: 1992, *Mon. Not. R. astr. Soc.* **255**, 401
- Kaastra, J., Asaoka, I., Koyama, K., and Yamauchi, S.: 1992, *Astron. Astrophys.* **264**, 654
- Kaspi, V.: 1996, in S. Johnston, M. Bailes, and M. Walker (eds.), *Pulsars: Problems and Progress, IAU Colloquium 160*, p. 375, Astronomical Society of the Pacific
- Kaspi, V. M., Manchester, R. N., Siegman, B., Johnston, S., and Lyne, A. G.: 1994, *Astrophys. J. Letters* **422**, L83
- Kassim, N.: 1992, *Astr. J.* **103(3)**, 943
- Kassim, N., Hertz, P., Schuyler, D., and Weiler, K.: 1994, *Astrophys. J. Letters* **427**, L95
- Kassim, N., Hertz, P., and Weiler, K.: 1993, *Astrophys. J.* **419**, 733
- Kassim, N. and Weiler, K.: 1990, *Astrophys. J.* **360**, 84
- Katwaroo, M.: 1997, *Master's thesis*, University of Mauritius
- Koribalski, B., Johnston, S., Weisberg, J., and Wilson, W.: 1995, *Astrophys. J.* **441(2)**, 756
- Kraus, J.: 1988, *Antennas*, McGraw-Hill, 2nd edition
- Kulkarni, S. and Heiles, C.: 1980, *Astr. J.* **85**, 1413
- Kuzmin, A. and Losovsky, B.: 1997, *to appear in Astronomy Letters*
- Lang, K.: 1978, *Astrophysical Formula*, Springer-Verlag
- Lyne, A. and Graham-Smith, F.: 1990, *Pulsar Astronomy*, Cambridge Astrophysics, CUP
- Lyne, A. and Lorimer, D.: 1995, *J. Astrophys. Astro.* **16**, 97
- Lyne, A. and Smith, F.: 1982, *Nature* **298**, 825
- Lyne, A. G., Kaspi, V. M., Bailes, M., Manchester, R. N., Taylor, H., and Arzoumanian, Z.: 1996, *Mon. Not. R. astr. Soc.* **281**, L14
- Malofeev, V. and Malov, O.: 1997, *in preparation*
- Manchester, R., D'Amico, N., and Tuohy, I.: 1985, *Mon. Not. R. astr. Soc.* **212**, 975
- Manchester, R. N. and Taylor, J. H.: 1981, *Astr. J.* **86**, 1953
- McAdam, W., Osborne, J., and Parkinson, M.: 1993, *Nature* **361**, 516
- Milne, D., Caswell, J., and Haynes, R.: 1993, *Mon. Not. R. astr. Soc.* **264**, 853

- Nicastro, L., Johnston, S., and Koribalski, B.: 1996, *Astron. Astrophys. Letters* **306**, L49
- Nugent, J., Pravdo, S., Garmire, G., Becker, R., Tuohy, I., and Winkler, P.: 1984, *Astrophys. J.* **284**, 612
- Odegard, N.: 1986, *Astr. J.* **92**, 1372
- Payne, H. and Hayes, J. (eds.): 1995, *Representaion of celestial coordinates in FITS*, Vol. 77
- Pfeffermann, E. amd Aschenbach, B. and Predehl, P.: 1991, *Astron. Astrophys. Letters* **246**, L28
- Press, W., Flannery, B., Teukolsky, S., and Vetterling, W.: 1992, *Numerical Recipes*, Cambridge Univ. P., 2nd edition
- Radhakrishnan, V., Goss, W., Murray, J., and Brooks, J.: 1972, *Astrophys. J. Suppl.* **24**, 49
- Rees, M. and Gunn, J.: 1974, *Mon. Not. R. astr. Soc.* **167**, 1
- Rickett, B.: 1977, *Ann. Rev. Astron. Astrophys.* **15**, 497
- Romani, R. and Yadigaroglu, I.: 1995, *Astrophys. J.* **438**, 314
- Rosado, M., Ambrocio-Cruz, P. amd Le Coarer, E., and Marcelin, M.: 1996, *Astron. Astrophys.* **315**, 243
- Rughoobur, P.: 1996, *The Fast Control and Data Acquisition System For MRT*, Technical report, Faculty of Engineering , Univ of Mauritius
- Rybicki, G. and Lightman, A.: 1979, *Radiative Processes in Astrophysics*, Wiley
- Ryle, M.: 1952, *Proc. Roy. Soc. A.* **211**, 351
- Sachdev, S.: 1997, *Master's thesis*, Faculty of Science, Univ of Mauritius
- Sachdev, S. and Udaya Shankar, N.: 1995, *Astron. Soc. of India. Bulletin* **23**, 574
- Sanders, D., Clemens, D., Scoville, N., and Soloman, P.: 1986, *Astrophys. J. Suppl.* **60**, 1
- Schaefer, B.: 1993a, *Vistas in Astronomy* **36(4)**, 311
- Schaefer, B.: 1993b, *Publs. astr. Soc. Pacif.* **105**, 1238
- Schaefer, B.: 1995, *Astr. J.* **110(4)**, 1793
- Schaefer, B.: 1996, *Astrophys. J.* **459**, 438
- Sedov, L.: 1959, *Similarity and dimensional methods in Mechanics*, Infoscience Ltd.
- Seward, F., Harnden, F., Szymkowiak, A., and Swank, J.: 1984, *Astrophys. J.* **281**, 650
- Shakespeare, W.: 1603, *the tragedy of Hamlet, prince of Denmark*
- Shull, J.: 1982, *Astrophys. J.* **262(1)**, 308
- Stephenson, F.: 1997, *Personal Communication*
- Strom, R.: 1994, *Mon. Not. R. astr. Soc.* **268**, L5
- Tamura, K., Kawai, N., and Yoshida, A.: 1996, *Pub. Astro. Soc. Japan* **48**, L33

- Taylor, J. and Cordes, J.: 1993, *Astrophys. J.* **411**, 674
- Thompson, A., Moran, J., and Swenson, G.: 1986, *Interferometry and Synthesis in Radio Astronomy*, Wiley and Sons
- Thorsett, S. E.: 1992, *Nature* **356(6371)**, 690
- Trussoni, E., Massaglia, S., Caucino, S., Brinkmann, W., and Aschenbach, B.: 1996, *Astron. Astrophys.* **306**, 581
- Udaya Shankar, N., Dodson, R., and Osborne, J.: 1997, in *Proc. 25th Int. cosmic ray conf., Durban*, No. 3, pp 197-200
- Van Den Bergh, S. and Kamper, K. W.: 1984, *Astrophys. J. Letters* **280**, L51
- Verschuur, G. and Kellermann, K.: 1988, *Galactic and Extragalactic radio astronomy*, Springer-Verlag, 2nd edition
- Westerlund, B.: 1969, *Astr. J.* **74**, 879
- Winkler, P. and Clark, G.: 1974, *Astrophys. J. Letters* **191**, L67
- Woltjer, L.: 1972, *Ann. Rev. Astron. Astrophys.* **10**, 129
- Wright, A. and Otrupcek, R.: 1990, *The Parkes Catalogue 1990 (PKSCAT90)*, The Southern Radio Source Database, Australia Telescope National Facility
- Yu-shan., H.: 1955, *Elements of Chinese Historiography*, W.M. Hawley, Hollywood
- Zealey, W. J., Elliott, K. H., and Malin, D. F.: 1979, *Astr. Astrophys. Suppl.* **38**, 39

